Spring 1-1-2016

Buried Explosive-Induced Blast Characterization by Geotechnical Centrifuge Modeling

Curt Benjamin Hansen
University of Colorado at Boulder, cbhansen@colorado.edu

Buried Explosive-Induced Blast Characterization By Geotechnical Centrifuge Modeling

Curt Benjamin Hansen

B.S. Mechanical Engineering, Colorado School of Mines,

2008

M.S. Mechanical Engineering, University of Colorado at Boulder,

2010

A thesis submitted to the

Faculty of the Graduate School of the

University of Colorado in partial fulfillment

of the requirements for the degree of

Doctor of Philosophy

Department of Mechanical Engineering

2016

This thesis entitled:

Buried Explosive-Induced Blast Characterization By Geotechnical Centrifuge Modeling

written by Curt Benjamin Hansen

has been approved for the Department of Mechanical Engineering

_____

Professor Ronald Y.S. Pak

_____

Professor Richard Regueiro

Date_____

The final copy of this thesis has been examined by the signatories, and we find that both the content and the form meet acceptable presentation standards of scholarly work in the above mentioned discipline.

Hansen, Curt Benjamin (Ph.D., Mechanical Engineering)
Buried Explosive-Induced Blast Characterization By Geotechnical Centrifuge Modeling
Thesis directed by Professor Ronald Y.S. Pak

Abstract

A comprehensive experimental regime was conducted to advance the understanding of the mechanistic phenomena of buried, explosive-induced soil responses using geotechnical centrifuge modeling. To address experimental gaps in the current literature, this research documents the high-rate dynamic soil behavior under explosive loads with parametric variations of charge size, burial depth, and g-level in conjunction with post-detonation static measurement of blast-excavated craters. The novel integration of a high-speed imaging system into the centrifuge domain, placed in close-proximity to the blast, enabled a rigorous in-flight characterization of the transient, multiphasic soil blast mechanics including initial soil deformation, early soil disaggregation, gas-particle interactions, and soil dome evolution. The results indicate that initial soil surface motions appear progressively later, post-detonation, with elevated acceleration. Furthermore, the data demonstrates that gravity-induced confining stresses reduce the temporal and spatial soil disaggregation flow kinematics. Crater dimensions, measured by a laser profilometer, exhibit a gravity-dependent decrease and a new, dimensionless coupling function correlates the physical ejecta dynamics to the crater dimensional statics evident in the buried blast phenomena. Piezoelectric sensors, embedded coincident to the test-specified burial depth and recorded simultaneous to soil ejecta kinematics, measure ground shock transmissivity as a function of radial distance from the charge, with parametric variations in explosive mass and in-situ soil conditions. This research also developed a computational model of the buried, blast event in a dry soil medium within an advanced, 3-dimensional, multi-material, arbitrary Lagrangian-Eulerian (ALE)

framework and implemented in an explicit finite element solver. The empirically-determined soil ejecta velocities and crater dimensions demonstrate reasonable correspondence to the numerical model. Significantly, the ground shock peak accelerations and stresses data exhibit close agreement to the numerical predictions. An in-depth analysis compares this study's empirical scaling relationships, in both dimensional and dimensionless form to a compilation of past field and centrifuge results and demonstrates their favorable correlation to full-scale explosive events.

The parametric study of soil ejecta kinematics and crater morphology progressed to an in-depth investigation of buried, explosive-induced kinetic energy transfer to an overlying target. To address experimental gaps in the current literature, this research documents the near-field resultant force impacts and rigid-body dynamics under explosive loads, instead of the conventional discrete measurement methods, with parametric variations of target height, explosive mass, burial depth, g-level, target geometries, and in-situ soil conditions. The design and fabrication of a novel, laboratory-scale blast impact device, the Blast Impact Response Gage (BIRG), integrated into the centrifuge domain, enabled a rigorous characterization of the aboveground blast environment. The results from over 150 experiments demonstrate the BIRG's unique capability to directly measure the complex, non-uniform, temporal and spatial distribution of the blast loading mechanisms and subsequent impulse transferred to the target. The BIRG's tri-symmetric sensor configuration, mounted on the rigid target plate, effectively resolves the applied blast stresses and consequent out-of-plane rotational motions under both centric and eccentric explosive loads. Significantly, the BIRG measurements delineate the arrival times and magnitudes of the extremely transient *early* shock impact phase in conjunction with the complex, interfacial gas-soil ejecta loading mechanisms in the *primary* shock impact phase of longer duration. The comparative data analyses of the arrival times and magnitudes quantify the constitutive load mechanisms in both energy

transfer phases and collectively substantiate that gas-soil ejecta impacts transmit most of the kinetic energy to the overlying target. Furthermore, the systematic integration of a second high-speed video camera into the centrifuge domain, also positioned in close-proximity to the blast, captured at 84,054 frames per second, the multiphasic soil blast mechanics including early soil disaggregation, gas-soil ejecta interaction, soil dome heave expansion, and consequent impact on the BIRG target surface. These highly-resolved, rate-dependent video images simulate the same impact phenomenon apparent in full-scale blast events. The analytic synthesis of the BIRG's tri-sensor data with substantive correlation to coincident high-speed imaging results effectively characterized soil blast kinematics and kinetics. Furthermore, an analysis of conventional centrifuge scaling relationships substantiates their suitability to upscale model blast impulse to full-scale conditions. A new dimensionless, constitutive scaling term, η, derived from this study's empirical data, includes target height and burial depth dependence, and allows direct comparisons across studies of different material types and test configurations. The accurate, well-documented experimental results from the buried, explosive-induced soil ejecta kinematics, crater morphology, and blast impact investigations, establish a high-fidelity, repeatable database for future parametric experimental studies and provides a sound physical basis for parametric calibration and validation of computational, iterative simulations of full-scale soil blast mechanics.

Dedication

This dissertation is dedicated in loving memory to my late grandmother, Joan Barnett, who always joked she hoped to live long enough to see me receive my Ph.D., and she almost did;

and

My beloved mother, Cynthia Hansen, for her unconditional love, support, and encouragement throughout my entire life, making this achievement possible.

Acknowledgments

I would like to express my sincere appreciation to my advisor and committee chair, Professor Ronald Pak, for the opportunity to participate in this research and apply my mechanical background to the geotechnical field, a very worthwhile learning experience. I am forever grateful for your thoughtful contributions and support during this study, always stressing the importance to take this research to a higher level of excellence, and allowing me the independence to do so with your guidance. Our tireless in-depth discussions, work related and beyond, will always be remembered. Thank you for setting a high standard of excellence as a researcher, mentor, and role model for me to emulate in the future.

I would like to thank members of my dissertation committee Professors Richard Regueiro, Mark Rentschler, Rong Long, and Jeffrey Knutsen for their time, tremendous support, and guidance during this research; your discussion, ideas, and feedback have been invaluable. Additionally, I would like to extend my gratitude to all participant professors, representative members of the Defense Department, and graduate students who contributed to this MURI research project.

A special thanks to Dr. William Cooper of the Air Force Research Laboratory for his expertise and participation in this investigation. Your knowledge, attention to detail, and dedication were critical to this research effort. I am extremely fortunate to have worked with you and I am grateful for the strong friendship that ensued. I would also like to thank Officer Edward Quayle of the Boulder Police Department Bomb Squad for his generous support and assistance.

I offer a sincere thanks to my colleagues Pierce Jarrell, Thomas Borden, Tyler Leigh, Leyla Safari, and Aditi Tiwari for their invaluable centrifuge laboratory assistance, data compilation, and

sustained devotion during testing that rendered the endless hours spent in the centrifuge pit tolerable.

To my family, thank you for always allowing me to follow my ambitions and dreams, and instilling in me the confidence that I am capable of doing anything I put my mind to. Your endless support, enduring love, motivation, guidance, and sacrifice has been essential to my success in life. I could not have done this without you.

To my best friend and teammate, Stephanie Blankemeier, thank you for the constant encouragement, love, and support throughout this entire journey.

Funding for this research provided by an Office of Naval Research Multidisciplinary University Research Initiative (MURI) Grant N00014-11-1-0691 is gratefully acknowledged.

TABLE OF CONTENTS

TABLE OF FIGURES

LIST OF TABLES

Chapter 1 Introduction

1.1 Overview of Soil Blast Mechanisms

Landmines, buried in a network across a beach in saturated sand, or improvised electronic devices (IEDs) buried along a roadside in dry soil, silently await their targeted victims. Easily designed, cost-effective, and difficult to detect, these indiscriminate killers inflict optimal damage against superior conventional military forces [1]. IEDs caused an estimated 50% of all U.S. troop fatalities and injuries in Iraq and Afghanistan [2]. The use of IEDs against crowds of people in public places seems increasingly commonplace in recent years. The success and notoriety of IEDs in theaters of conflict now creates a transnational, lethal threat to civilian populations as combatants adopt these weapons for their signature causes and agendas, turning urban areas into killing zones. The elevated complexity and proliferation of IEDs signifies a persistent challenge to the worldwide community to research and develop technologies to counter these highly effective weapons systems [1].

The detonation of an explosive device, such as an IED or landmine, produces extremely transient (μsec) and high magnitude, interactive, non-uniform blast loads on an overlying structure, such as a vehicle chassis. The detonation of a buried explosive device transmits a high-amplitude stress wave through the explosive medium and causes an immediate chemical reaction that releases energy into the soil matrix. The amount of total energy released depends on the explosive mass and type [3]. When the applied stress wave amplitude increases beyond the material strength, the shear strength decreases relative to the confining stress and a shock wave propagates into the soil medium severely compressing the soil skeleton [4]. In general, the initial shock wave propagates at sonic speeds and creates two zones of large compressive and shear soil distortion: the plastic

zone and the rupture zone (Figure 1.1) [4–6]. Proximate the explosive detonation, in the crushed zone, the shock wave front plastically deforms the soil due to extreme pressure; in the rupture zone, wave rarefactions cause fissures extending approximately five times the explosive charge radius [4] and a blast-excavated crater forms. Subsequent shock wave passage through the explosive, within 5-10 μs [4], combustion transforms the explosive charge into extremely hot-pressurized gases with initial temperatures and pressures adjacent to the charge reaching 6,000 C and 200,00 atmospheres, respectively [3,4,7]. The hot pressurized gases, or detonation products, expand radially with subsequent volumes several hundred times greater than the initial explosive charge volume [8] to reach a pressure equilibrium. The shock wave and detonation products impart kinetic energy with consequent soil spallation. The pressurized gases perform continued mechanical work on the blast-excavated crater, and the radially expansive gases jet through the soil, followed by soil ejecta and eventual soil dome heave kinematics. Soil ejecta fallback forms the crater lip and completes crater morphology. These mechanisms, shock wave, detonation products, and soil ejecta intermix to create complex, non-uniform, highly transient, multiphasic soil blast mechanics.

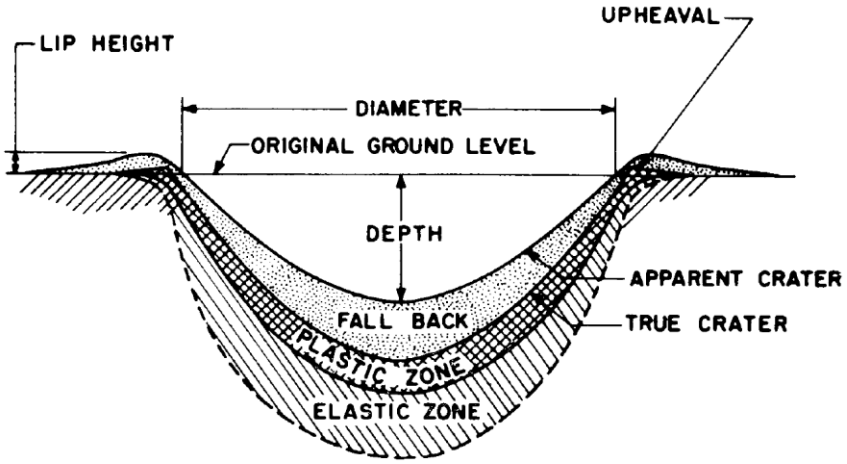

Figure 1.1. Blast-excavated crater terminology [6].

The energetic release from an explosive device typically impacts the target with pronounced eccentricity. This asymmetric momentum transfer induces highly non-linear structural dynamics and the resultant elevated angular momentum coupled with the severe structural compressive stresses and material deformations jeopardize the vehicle's viability and stability (Figure 1.2). As a result, the occupants remain vulnerable to lethal and life-threatening injuries from blast overpressure, fireballs, high-rate shock loads, hot-pressurized gases, sonic soil throw, and vehicle rollovers.

Figure 1.2. Mine Resistant Ambush Protected Vehicle (MRAP) subjected to IED [9].

These casualty mechanisms inflict serious physical trauma: compressed spinal cords, paralysis, shrapnel wounds, penetrative brain injuries, first and second degree burns, broken bones, loss of limbs, sight and hearing [2]. Blast injuries from an IED typically combine penetrating, blunt, and burn injuries. The IED shrapnel from nails, ball-bearings, etc. can cause so many small puncture wounds to exsanguinate the victim [2].

1.2 Background

The complex challenge to characterize the dynamic soil response under blast loading remains an on-going field of interest in applied mechanics and geotechnical engineering. Understanding explosive-induced geomaterials' behavior has diverse applications including mining and liquefaction [10,11], planetary impacts and cratering [12–15], ground surface instabilities [16], forensic engineering [5,17,18], flood risk management [19,20], and earthquake simulations [21–23].

In addition to these applications, a thorough understanding of soil blast mechanics remains a necessary prerequisite to develop effective predictive and preventative technologies to counter the threat of buried IEDs and landmines. Accurate and consistent experimental results that quantify soil ejecta flow, crater morphology, and delineate the multiphasic, buried explosion-induced load impact mechanisms to an overlying target are essential for both applied and theoretical progress. The high-fidelity, repeatable, experimental database provides a physical basis for parametric calibration and validation of constitutive models that simulate iterative full-scale configurations of an explosive event. Thus, this comprehensive experimental platform contributes to the development of armoring technologies and forensic engineering, used at the blast-excavated crater site. Due to the urgency to protect human lives and infrastructures, many past studies have investigated explosive detonation in soil using three primary experimental methodologies: full-scale field tests, laboratory-scale tests, and the centrifuge modeling technique. The Multidisciplinary University Research Initiative (MURI) project defined the purpose of this thesis: provide a well-documented, physical basis for computational model validation in order to simulate with predictive capabilities the buried, explosive-induced soil blast mechanics. Therefore, theoretical studies are not addressed in detail.

Field tests use large quantities of explosives and provide direct simulation of the high-rate, soil ejecta impact on overlying structures and the subsequent crater formation. For example, Ehrgott fabricated a massive piston assembly that measured impulse generated by detonating a 2.27 kg C4 charge at surface-tangent and shallow burial depths, in a testbed backfilled with three different soil types [8]. To capture the Impulse Measurement Device (IMD) motion, the three independent measurement methods: an accelerometer, displacement measurement gage (yo-yo gage), and high-speed video cameras at 8,000 frames per second (fps), often failed to record displacement and velocity data. Similarly, another experimental technique [24] developed a two-frame testing apparatus that measured blast pressure, comprised of an array of Hopkinson Pressure Bars (HPBs) threaded through a target, with affixed strain gages, to record temporal variations at discrete points. A finite element method corrected dispersion effects of the propagating stress pulse in the HPBs, evidenced by oscillations in the recordings that diminished experimental data clarity. A numerical interpolation routine estimated the spatial load distribution over the target face inferred from the discrete point measurements. Furthermore, a proof-of-concept experimental test used an array of inexpensive steel tubes with a single strain gage attached to each perimeter, referred to as displacement timer pins (DTP), to measure the temporal, single point contact of the explosively loaded plate with the DTPs [25]. Pickering et. al [26] examined rigid and deformable target responses under explosive loads with parametric variations of charge size, burial depth, and stand-off distance using a vertical ballistic pendulum. The vertical displacement of the pendulum recorded by four tracing pens determined the impulse. Bergeron et al. examined the mechanisms of a mine blast event and quantified the explosive output of a 100 gram C4 charge at burial depths ranging from 0 cm to 8 cm in a small, sand-filled tank [27]. Their flash x-ray photography provided snapshots of the early gas-soil interaction and high-speed film captured soil dome expansions. The

study further explored soil type and moisture content effects on mine output, employing an explosively loaded horizontal pendulum method. The maximum angular displacement value of the pendulum swing arm, related to momentum conservation and energy principles, yielded the induced impulse with the assumption that blast loading occurred before any significant pendulum motion [4]. A study conducted by the US Army Corp of Engineers detonated subsurface charges ranging in size from 12 to 116 kg in dry and moist soils, measured the resultant apparent crater size and shape, and investigated the influence of bedrock on crater formation [28]. Drake et al. compiled ground shock data from more than one hundred surface-tangent and buried explosive tests, conducted in various soils, using charges ranging from 453 grams to 1000 kg [29]. Vortman detonated 450 kg, 18,143 kg, and 453,000 kg TNT charges in desert alluvium sand and basalt rock at burial depths ranging from 2.92 m to 17.7 m [6]. The studies cited above, with variant explosive mass, burial depths, test bed size, soil conditions, and measurement methods, reflect the general consensus: full-scale parametric studies are not feasible. These physical tests remain impractical, laborious and costly to set up, and require large quantities of explosives. In addition, the lack of control over in-situ soil conditions and the exposure to unpredictable natural elements limits data replication and verification. Thus, parametric analysis to establish fundamental relationships and accurately characterize the multiphasic constituents of an explosive event, i.e. air shock and gas-soil eject mechanisms, remains difficult, if not impossible. In spite of the wide variability and uncertainty in field test conditions, their test results quantify full-scale explosive yields and blast loads imparted to an overlying structure. Therefore, the data remains important to small-scale laboratory test validation and prediction of the prototype condition using suitable scaling relationships.

In contrast, investigation by small-scale laboratory experiments at normal gravity offers more realistic parametric study through its economy and direct control of soil properties. Previous works used shallow-buried, gram-sized charges and controlled test parameters to quantify pressure variations above a soil blast and also impulse imparted to subscale free-flying or fixed target plates using various experimental techniques [7,30–32]. Taylor et al. detonated gram-sized charges in saturated soil to determine pressure as a function of time and position on a fixed target plate [31]. The tests used two different configurations of Kolsky bars and the results demonstrated that peak pressures on the target were not repeatable from shot to shot. Furthermore, the data showed significant variation in pressure arrival times and distribution. Genson also detonated gram-sized charges in a saturated soil and used a high-speed camera, (8,000 fps) to capture the displacement of free-flying targets as a function of target shape, burial depth, and standoff distance to calculate impulse [7]. Soil debris and jetting water often obscured individual target corners and thus limited displacement data recording. Fox et al. [30] extend the initial work presented by Genson [7] and further investigate the effects of charge location and target shape on blast loading transmitted to a target using the same methods. In the studies cited above, the experimental technique requires empirical scaling relationships, such as Sachs or Hopkinson-Cranz, to correlate between small-scale and full-scale test results. However, Hopkinson-Cranz scaling relationships assume gravitational influence on the soil overburden to be negligible. Because geomaterials' behavior strongly depends on the in-situ stress condition, the model-scale tests' parametric exclusion of gravity generally limits this technique's applicability to air-blast or shallow burial depths. As a result, this approach typically omits the key stress similitude requirement in soil mechanics.

To satisfy this critical stress similitude issue, the centrifuge scaled modeling technique has proved to be a practical and versatile solution for small-scale laboratory experiments in

geomechanics and geotechnical engineering. It permits realistic simulations of full-scale, nonlinear geotechnical problems by reproducing gravity-induced stress levels that dictate the mechanics of the soil's response under blast loading. With suitable scaling relationships between scaled model and prototype conditions, a much smaller soil model size and amount of explosive mass can produce stresses and deformation characteristics comparable to full-scale blast events. The controlled and replicable test conditions improve test efficiency, data accuracy, extrapolation to prototype conditions, and thus enable in-depth parametric studies.

An early Soviet experimental study investigated the cratering process using buried charges within an accelerated reference frame and demonstrated that as gravity increased, apparent crater dimensions decreased, as cited in Johnson et al. [33]. Credited with first recognizing gravity's significance to blast-induced crater morphology, Chabai derived a set of scaling relationships by dimensional analysis inclusive of physical variables such as charge burial depth, gravity field strength, and explosive energy [34]. Furthermore, Johnson et al. investigated crater dependence on gravity by subjecting the soil model, installed on an aircraft, to accelerations from 0.17 to 2.5 g's. This study reported that subsequent small-scale charge detonations, apparent crater dimensions varied inversely to g-field for all burial depths considered.

Most of the initial centrifuge soil blast studies investigated the impact of increased g-level on crater formation using surface-tangent or shallow-buried explosives, emphasizing soil conditions, charge properties, and gravity level as determinant factors in apparent crater dimensions [5,35–40]. Schmidt and Holsapple extensively examined the effects of elevated acceleration on the explosive cratering phenomena and substantiated that crater size remains gravity-dependent [35,36]. Their experimental program used half-buried, gram-size charges detonated in small, cylindrical containers of dry Ottawa sand and subjected to gravity levels predominantly greater

than 300 g's. Furthermore, their similarity analysis derived dimensionless Π groups relating the crater volume, radius, and depth to the g-level, soil properties, and explosive characteristics. Their experimental results evidenced that small charge detonation at increased acceleration can simulate large explosive yields by centrifuge scaled modeling, and thus demonstrated the relevance of this technique. And finally, confirmed by on-board imaging and crater axial symmetry, their data showed that craters formed in the Ottawa sand remained stable, unaffected by ambient vibrations, Coriolis effects, or air flow during centrifuge spinning. Goodings et al. reported similar findings, specifically the absence of undesirable acceleration related scale effects at lower gravity fields (31 to 100 g, the range typical of most geotechnical centrifuges) [37].

As a result, centrifuge modeling offered potential application to extended fields of research. For example, a study by Brownell and Charlie determined that the soil's moistures content significantly impacted crater dimensions due to the matric suction in partially saturated soil [38]. An experimental program conducted by Walsh and Charlie [41] examined the effect of the soil's moisture content on shock wave characteristics using gram-sized charges buried in small sand models and accelerated to 18.9 and 26.9 g-levels. The data indicated that compaction saturation stiffened the soil matrix and increased blast-induced stress transmission efficiency, with subsequent higher peak soil stress and velocities. In addition, Kutter et al. applied the centrifuge modeling technique to study the plastic deformation response of scaled tunnel models to buried gram-size charge detonations [5]. Gill and Kuennen developed a transparent specimen container that allowed cross-sectional viewing of the blast event under elevated gravity and used a cinema camera and electronic imaging system to capture soil displacement data [39]. However, the limitations of their photographic techniques precluded the recovery of useable displacement data. Therefore, real-time, sequential imagining of soil ejecta displacements and velocity time histories

were not obtained. The work reported by Shim examined the dynamic response of saturated soil under blast loading in the free-field condition and also the soil-structure interaction problem using a model pile embedded in sand at equivalent prototype conditions [40]. An analog camera and tape recorder captured only limited, segmented sequences of the explosive event. Measurements of excavated craters entailed imprinting the apparent crater using a gypsum-water mixture, measuring the radius and diameter of the cured mold, and finally submerging the crater mold in water to measure water displacement in order to estimate the volume of soil heaved. The study adhered to a single prototype condition, which precluded an analysis of increased artificial acceleration's impact on ground motions and apparent crater formation as a function of varying charge explosive weight and burial depth.

A thorough review of the current literature in the public domain, found no previous centrifuge soil blast impact research. Clearly, the need exists to characterize the centrifuge in-flight dynamic response of a particulate medium under explosive loading in the free-field condition in conjunction with the near-field, aboveground blast environment, the focus of this research.

1.3 Scope of the Research

This dissertation presents a comprehensive, innovative experimental program that examines the mechanistic phenomena of buried explosive-induced dynamic soil responses in the free-field condition using centrifuge scaled modeling in conjunction with the near-field, aboveground blast environment, to quantify the load impact mechanisms and the dynamic, rigid-body target response. Over 200 scaled explosive tests were conducted on the 400 g-ton, 6 m radius geotechnical centrifuge at the University of Colorado, Boulder. To delineate gravity-field influence on soil ejecta flow and crater dimensions, specific to fully-buried explosives, the parametric investigation

includes various gram-sized charges embedded into a large, dry natural soil model at different burial depths and detonated at multiple g-levels. The in-depth investigation of the buried blast impact phenomenon includes parametric variation of target height, explosive mass, burial depth, g-level, target geometries, and five different in-situ soil conditions. This research seeks to accurately quantify soil ejecta kinematics, crater morphology, in-situ ground shock wave transmissivity, and the high-rate impact load mechanisms by developing novel measurement techniques that integrate state-of-the-art technologies into the experimental regime. The integration of a high-speed imaging system placed into the centrifuge domain, in close proximity to the blast, captures the transient, multiphasic, interfacial soil blast mechanics apparent in a buried, full-scale explosive detonation. A new robust blast impact measurement device, the BIRG, also integrated into the centrifuge domain proximate the explosion, documents the near-field resultant force impacts and rigid-body dynamics under explosive loads, instead of the conventional, discrete point measurement methods. The BIRG's unique design configuration allows direct measurement of the complex, non-uniform, temporal and spatial distribution of the blast loading mechanisms and subsequent impulse transfer to the target. The analytic synthesis of the BIRG's applied force data correlated to coincident high-speed imaging results, enables a rigorous characterization of complex, interactive blast load mechanisms and subsequent kinetic energy transfer to the target, specific to the many different test parameters.

An analysis of the centrifuge scaling relationships compares this study's empirical relationships in both dimensional and dimensionless form to a compilation of past field and centrifuge results and demonstrates their favorable correlation to and prediction of full-scale explosive conditions. Computational predictions from an arbitrary Lagrangian-Eulerian (ALE) finite element simulation show strong correlation to buried, dry soil blast experimental data. Furthermore, without

comparable centrifuge blast impact studies, an analysis of this study's model scale, blast peak impulse results demonstrates favorable correlation to full-scale impulse data using centrifuge scaling relationships. The results further substantiate that small charge detonation at increased acceleration can simulate and predict large explosive yields by centrifuge scaled modeling. The high-fidelity, repeatable database establishes a benchmark for future parametric investigations into soil ejecta kinematics, crater morphology, ground shock peak magnitudes and attenuations, and aboveground blast impact mechanisms. The analyses provide a physical basis for parametric calibration and validation of computational models that simulate iterative configurations of soil blast mechanics in prototype scale.

Chapter 2 Experimental Technique

The research and development of the novel experimental platform required a detailed assessment of centrifuge capabilities, specifically *in-flight* explosive detonation under elevated gravity. The integration of advanced technologies to measure explosive-induced soil blast mechanics entailed extensive pre-test planning and design considerations to ensure all components (procured and fabricated), assemblies, and interactive systems functioned simultaneously without adverse explosive and accelerated gravity effects within the spatial confinement of the centrifuge domain. Concurrently, a lengthy process to certify the CU Boulder geotechnical centrifuge facility and personnel compliance to State of Colorado and Federal Regulations, in addition to approval from the Fire Marshall, Campus Police, and Dept. of Environmental Health and Safety at CU, preceded any explosive testing. As the Colorado State Licensed Blaster, the author supervised all explosive operations and individuals assisting, prepared and initiated all experiments, and managed explosive inventory and blast records.

2.1 Centrifuge Facility

The explosive tests were conducted on the 400 g-ton geotechnical centrifuge at the University of Colorado at Boulder (Figure 2.1) and used various gram-size charges embedded into a large natural soil model at different burial depths and detonated at multiple gravity levels. The design of the centrifuge asymmetric rotor arm incorporates a swinging payload platform that accommodates a variety of test specimens. At the opposite end, a fixed counterweight tank filled with tungsten carbide balances the net centrifugal tensile forces transmitted to the centrifuge arm (Figure 2.2). The radial distance from the center of rotation to the payload platform surface in-flight measures 5.49 m. The long rotor arm in conjunction with the relatively shallow soil model

minimize nonlinear stress distributions in the particle medium with depth subsequent increased gravity. Centrifugal acceleration, a_c, depends on the radial distance from the model to the center of rotation, r, and the angular velocity of the centrifuge, ω, defined as:

$$a_c = r\omega^2 \tag{2.1}$$

At a maximum centrifugal acceleration of 200 g's, this centrifuge, driven by a 900 horse-power (684 kW) DC electrical motor, accommodates 1.2 m x 1.2 m x 0.9 m models weighing 2 metric tons. During centrifuge spin-down, the DC motor generates power by electromagnetic induction that supplies the CU campus electrical grid.

Figure 2.1. University of Colorado at Boulder 400 g-ton Geotechnical Centrifuge Facility with soil model installed on the payload platform.

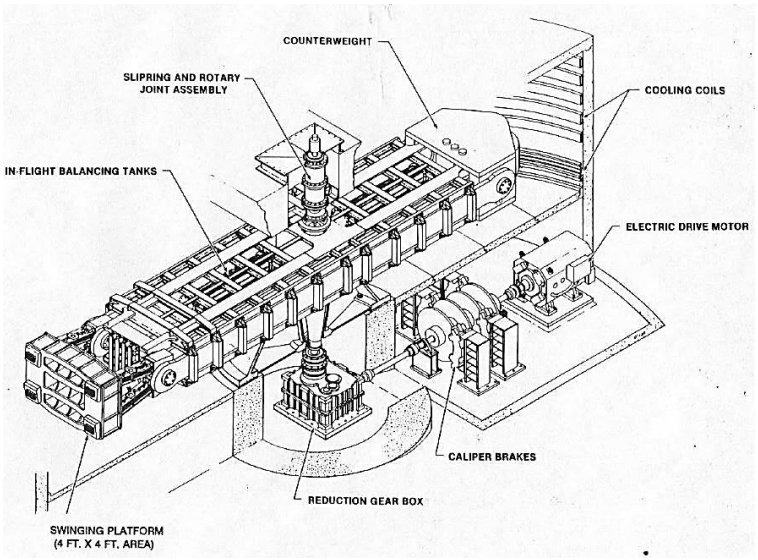

Figure 2.2. Schematic of the CU Boulder centrifuge [42].

2.2 Centrifuge Scaled Modeling

The centrifuge modeling technique has proved to be a practical and versatile solution for small-scale laboratory experiments in geomechanics and geotechnical engineering. It permits realistic simulations of full-scale, nonlinear geotechnical problems by reproducing gravity-induced stress levels that dictate the mechanics of the soil's response under blast loading. With suitable scaling relationships between scaled model and prototype conditions, a much smaller soil model size and amount of explosive mass can produce stresses and deformation characteristics comparable to full-scale blast events. This scaling technique assumes dynamic similitude, or in other words, a 1/N scale model subjected to a constant gravitational field at *N* g accurately scales and models the prototype behavior at standard earth gravity (Figure 2.3).

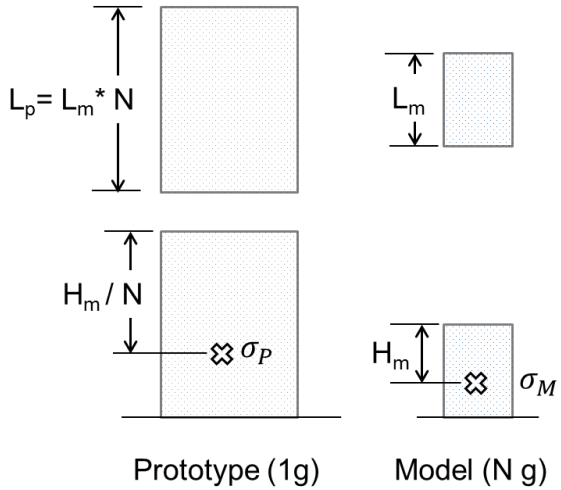

Figure 2.3. Schematic of stress similarity.

Centrifuge scaling relationships enable small, gram-sized charges to simulate blast energy typical of a full-scale, explosive field test, by scaling the explosive mass (N^3) as model charges accelerate to *N* g [35–37,43]. For example, a 1 gram model charge accelerated to 50 g's simulates a 0.14 ton explosive in the field at prototype scale. Strict adherence to gravity scaling would

require a significant reduction in model aggregate size to simulate prototype sand, and thus change the constitutive properties of the particulate medium. This study's smaller particulate size relative to adjacent structural elements minimizes adverse grain size scale effects and ensures similarity in the soil behavior and physical blast phenomenon between model and prototype. Table 2.1 lists the conventional centrifuge scaling relationships derived from a dimensional analysis or governing differential equations.

Table 2.1. Scaling relationships for dynamic centrifuge tests.

Quantity	Prototype	Model at $N\,g$
Length	N	1
Time	N	1
Area	N^2	1
Volume	N^3	1
Velocity	1	1
Acceleration	1	N
Mass	N^3	1
Force	N^2	1
Stress	1	1
Impulse	N	1
Energy	N^3	1

2.3 Centrifuge Soil Container and Components

In order to integrate the experimental components into the centrifuge domain and to physically simulate a half-space condition, a large, rectangular steel container was designed and fabricated with planar dimensions of 1.2 m by 1.0 m and a height of 0.61 m (Figure 2.4). Stress wave absorbing panels, composed of a viscous, oil-based putty (Duct Seal), lined the soil container's

four walls to mitigate incident wave reflections and dynamic boundary effects present in a finite domain [44,45]. An outer aluminum frame supports the 35 mm thick Duct Seal panels to lessen material creep during gravitational forcing (Figure 2.5). A high-strength aluminum plate (1.12 m x 0.98 m x 0.038 m thick), instrumented with piezoelectric accelerometers, placed under the soil stratum and cushioned by three, 13 mm thick elastomeric neoprene pads, simulates a rigid bedrock and effectively measures the blast-induced soil base vertical response (Figure 2.6). Table 2.2 summarizes the soil model components.

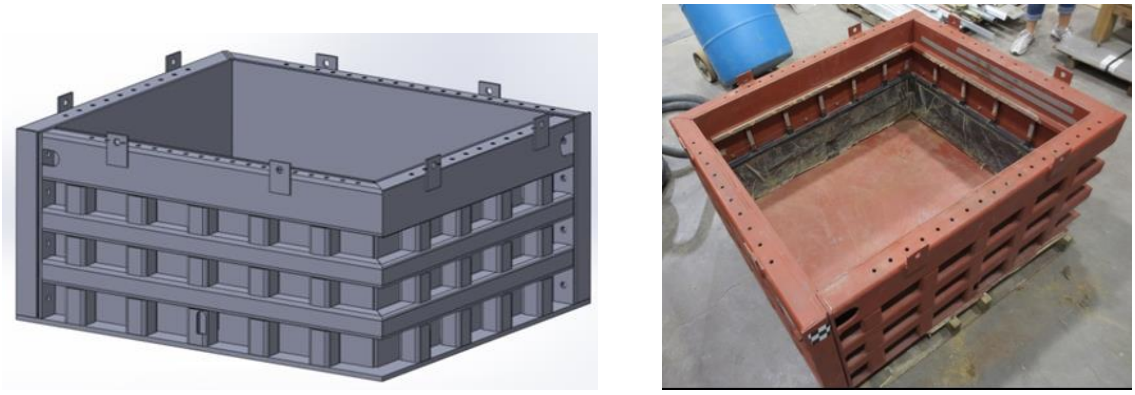

Figure 2.4. CAD model (*left*) and fabricated (*right*) soil container lined with Duct Seal.

Figure 2.5. CAD model (*left*) and fabricated (*right*) Duct Seal support frame.

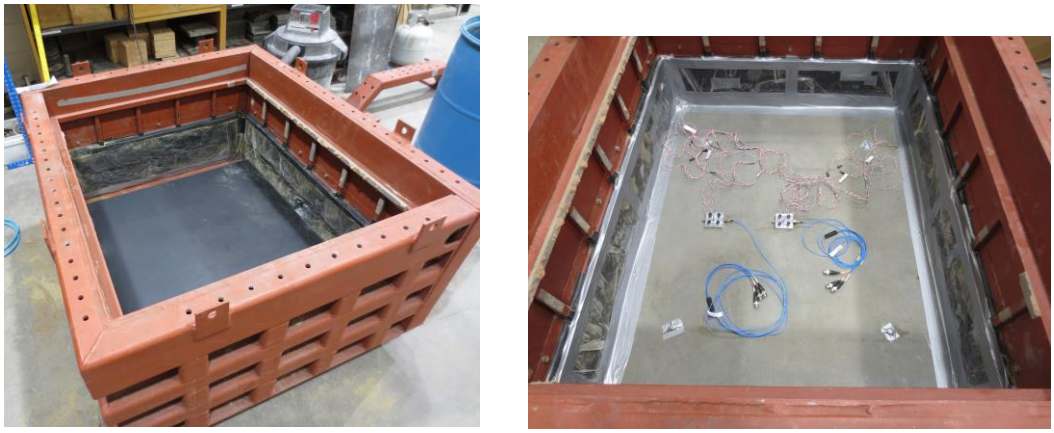

Figure 2.6. Elastomeric pads (*left*) and instrumented aluminum base plate (*right*).

Table 2.2. Soil container and components.

	Dimension	Material
Soil container	1.00 m x 1.20 m x 0.61 m	Mild steel
Elastometric pads (3)	0.80 m x 0.80 m x 0.013 m	Neoprene
Base plate	1.12 m x 0.98 m x 0.038 m	Al. 6061-T6
Absorbing boundary	35 mm thick	Duct Seal

2.4 Soil Model Properties and Preparation

In-situ soil conditions, including soil type (cohesive versus cohesionless), density, moisture content (partially saturated versus saturated), play a formative role in the buried blast phenomenon. To examine soil condition effects, this study detonated explosives in primarily two natural soil conditions. First, a homogenous soil stratum configuration consisted of dry, Colorado Mason sand, obtained from a quarry in Longmont, Colorado, classified as a cohesionless, poorly-graded sand (SP), with a specific gravity of 2.62 [46,47]. Prior to use, the soil was washed, oven-dried, and filtered through a #10 sieve to remove all non-geologic media. A sieve analysis on the soil

confirmed a diverse particle size distribution: particle diameters ranged from 200 to 3000 microns, as depicted in Figure 2.7.

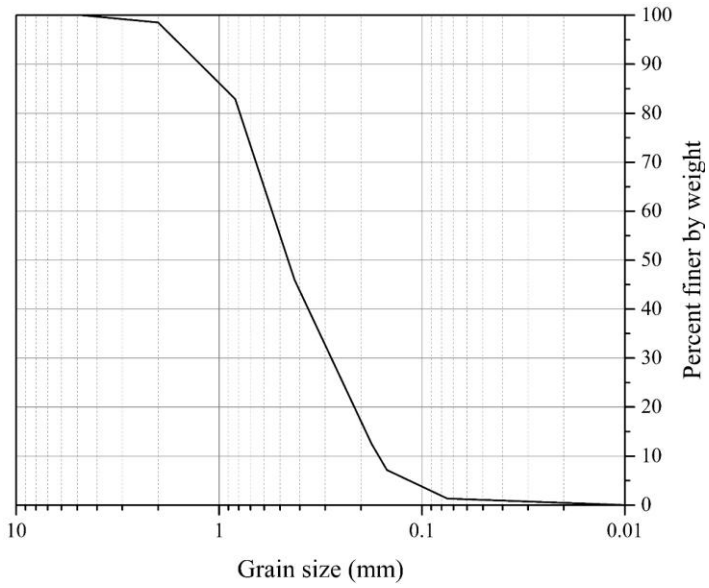

Figure 2.7. Particle size distribution for Colorado Mason sand.

Preparation of the soil model by natural sand deposition, or pulviation (Figure 2.8) from a calibrated free-fall height of 1.65 m, yielded a uniform dry density of 1735 kg/m^3, correlating to a relative density of 88% and a void ratio of 0.54. A chosen soil depth of 0.29 m resulted in width-to-depth and length-to-depth ratios of 3.1 and 3.8, respectively.

Figure 2.8. Soil model preparation by pluviation through a hopper.

To simulate a natural geologic residual soil medium, the second soil model constituents included Colorado Mason sand mixed with a low-plasticity clay obtained from the CU Boulder campus. First, sample preparation of this heterogeneous soil entailed processing the oven-dried clay through an electric grinder (Figure 2.9, *left*) to break-up clay aggregates into separate grains until the maximum clay grain measured 1.18 mm, or passed through a #16 sieve size. Next, carefully predetermined mass fractions of dry Mason sand and clay were synthesized by an industrial mixer (Figure 2.9, *right*). Spraying the two dry constituents with distilled water prior to mixing prevented loss of smaller particulates to air-borne dust. After thorough mixing, the uniformly distributed mixture was placed in sealed containers for a minimum of 24 hours to allow permeation of water into the clay particulates. All sand-clay testbeds prepared in this investigation contain a target water content of 10% by weight (wt.).

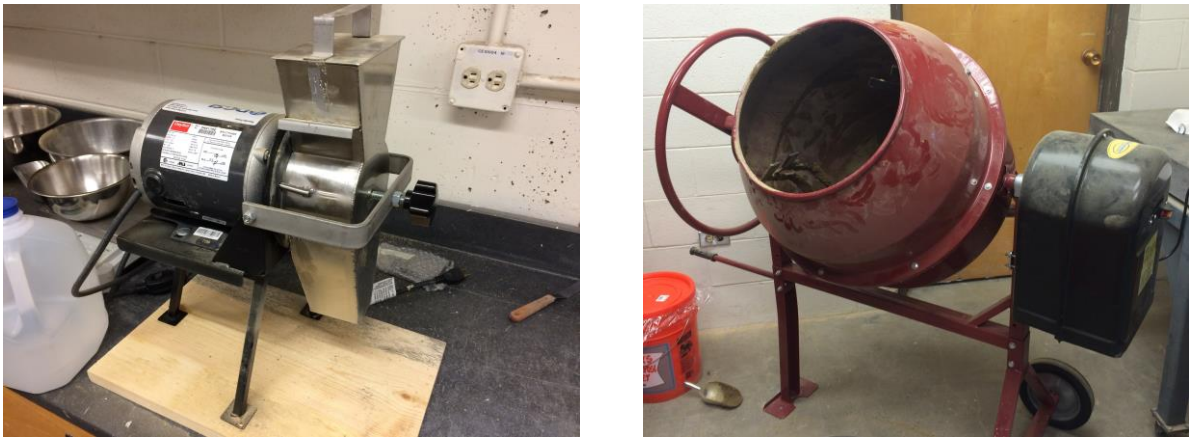

Figure 2.9. Laboratory-scale soil grinder (*left*) and industrial aggregate mixer (*right*).

After this consolidation period, the noticeably cohesive mixture precluded model preparation by pluviation, and thus, required a natural deposition backfill and compaction process. For each soil specimen, five equivalent lift heights of 4.8 cm, were backfilled individually and compacted manually between lifts, using a steel tamper (Figure 2.10). A chosen soil model depth of 0.24 m yielded a wet density of 1960 kg/m^3 for the 80% sand and 20% clay mixture with 10% saturation, denoted 80s20c10w. A comparison of the dry sieve analysis between this heterogeneous mixture and the dry Mason sand depicts the relative increase in fines attributed to the clay constituent (Figure 2.11). A study by Mun (2015) provides additional soil characteristics relevant to these soils types [47].

Figure 2.10. Prepared 80% sand and 20% clay model with 10% saturation (80s20c10w). Steel tampers compacted the centrifuge soil model.

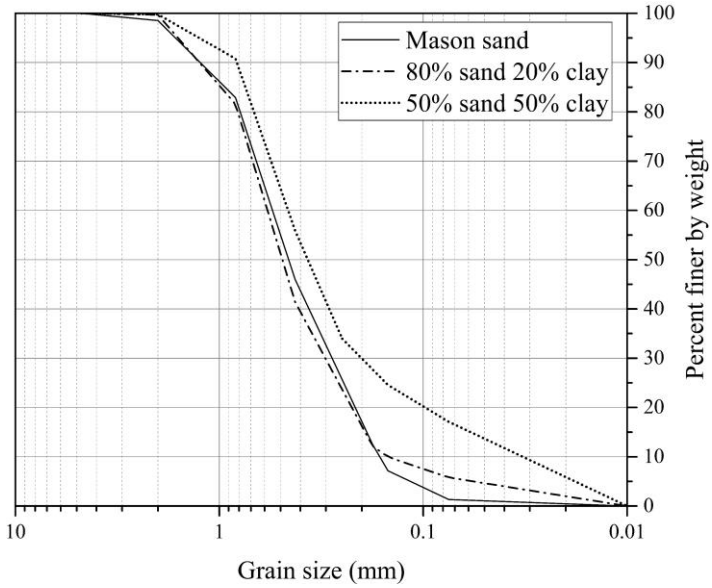

Figure 2.11. Grain size distribution from dry sieve analysis for: 80% sand and 20% clay; 50% sand and 50% clay (by wt.). Results for dry Mason sand included as a reference.

Furthermore, a series of experiments systematically varied the clay constituent and moisture content to delineate their relative role on the aboveground blast momentum transfer. Specifically, the additional testbeds included 50% sand and 50% clay with 10% saturation (50s50c10w), and two sand testbeds with 10% and 20% saturation. Table 2.3 summarizes the backfill materials and their respective Standard Proctor densities.

Table 2.3. Soil properties determined by Standard Proctor compaction.

	Initial Compaction Density (kg/m^3)
Dry Mason sand	1735
80% sand, 20% clay, 10% saturation (80s20c10w)	1960
50% sand, 50% clay, 10% saturation (50s50c10w)	2010
Mason sand with 10% saturation	1748
Mason sand with 20% saturation	2017

2.5 High-Explosives

This study used three different sizes of pentaerythritol-tetranitrate (PETN) and RDX-based exploding bridgewire detonators (EBWs), manufactured by Teledyne Reynolds, which functioned either as primary explosives or secondary initiating detonators: RP-87, RP-80, and RP-81 with respective explosive masses, 69 mg, 203 mg, and 530 mg [48] (Figure 2.12).

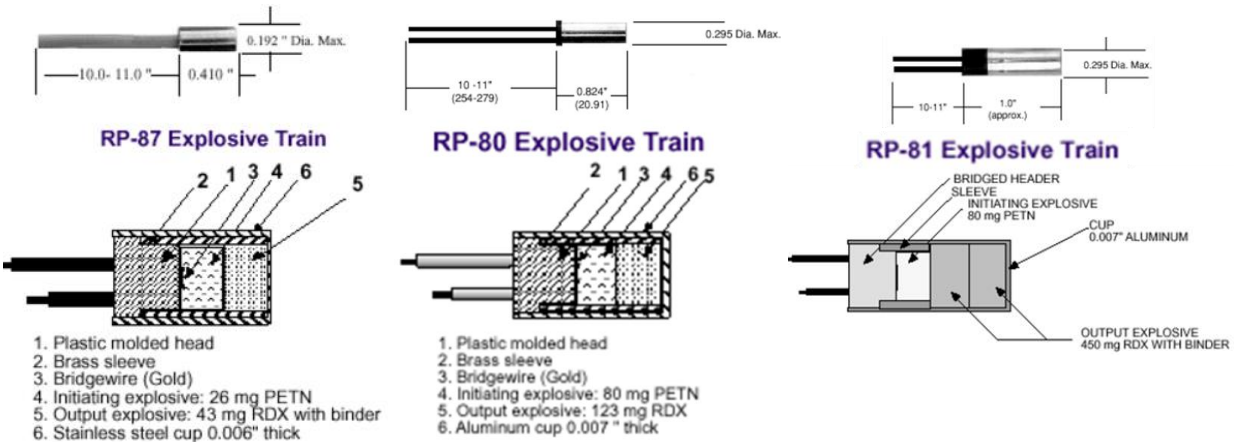

Figure 2.12. Exploding bridgewire detonators from Teledyne RISI [48].

Additionally, this study fabricated and detonated two different composite, cylindrical charges (Figure 2.13). The first charges, synthesized with plastic explosive Detasheet C (63% PETN, 29% plasticizer, 8% nitrocellulose) coupled with a Teledyne RP-87 EBW, consistently resulted in total explosive masses of 500 mg and 1000 mg, average density of 1.42 gm/cm^3, with aspect ratios 1.01 and 1.88, respectively. The second fabricated charge, synthesized with 880 mg plastic explosive Composition C4 (91% RDX, 9% plasticizer) and a Teledyne RP-80 EBW, consistently resulted in a total explosive mass of 1000 mg, an average density of 1.57 gm/cm^3, and an aspect ratio of 1.05.

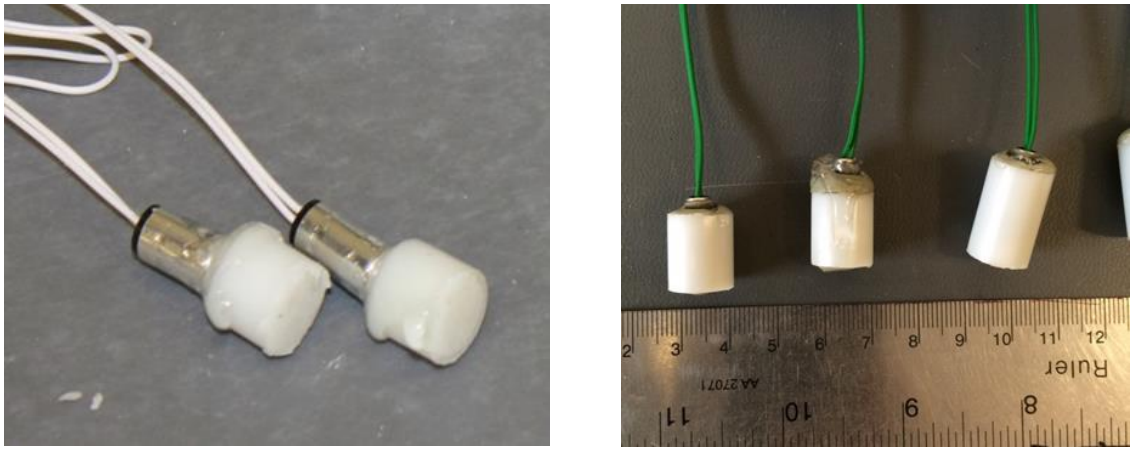

Figure 2.13. Fabricated composite charges synthesized with EBWs coupled to plastic explosive: (*left*) Composition C4 and RP-80; (*right*) Detasheet C and RP-87.

To fabricate the composite charge, a predetermined amount of plastic explosive was tamped into a thin-walled Delrin sleeve using a brass dowel, forming a disk-shaped charge. Next, the EBW detonator's free end was firmly pushed approximately 4-5 mm into the center of the cylindrical bulk explosive disk and then secured to the Delrin sleeve and the composite charge using a high-strength epoxy, completing the composite charge assembly.

2.6 Centrifuge Operation and Experimental Procedure

Centrifuge operation during an explosive event entailed: spinning the centrifuge to the prescribed g-level, detonation of the charge, and decelerating to a complete stop. Video surveillance in the centrifuge pit, in addition to a small digital camera mounted on the soil container, provided continuous monitoring of the experiment during flight. Figure 2.14 illustrates the static and *in-flight* orientation of the centrifuge payload platform and denotes imposed gravity and rotational vectors.

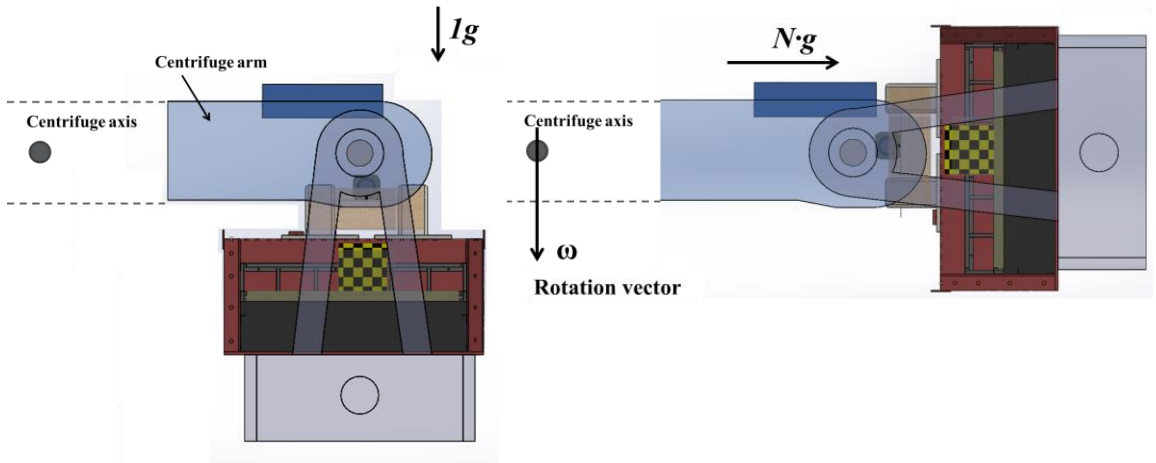

Figure 2.14. Schematics of the centrifuge payload platform and soil container illustrate the freely swinging payload platform during centrifuge operation: (*left*) static; (*right*) rotating at *N* g. Rotational trajectories and gravity vectors are shown from side-view perspective. Figures are *to-scale*.

Due to the inherent directionality of EBWs, the prescribed charge placement, with its longitudinal axis oriented vertically and its distal end nearest to the soil surface (Figure 2.15), maximized soil heave volume, as determined in preliminary investigations of buried charge orientation. Furthermore, the charge buried eccentric to the soil model's planar geometric center mitigates adverse resonant mode shape effects caused by reflected standing elastic waves. This vibrational energy phenomenon, or drumhead effect, typically occurs in finite, two-dimensional membranes and induces *monopole and dipole* behavior.

A plummet, or plumb bob, provided a physical reference and verified charge placement. Digital calipers verified the precise charge depth of burial (DOB), measured from the soil surface to the explosive output surface terminal. The DOBs varied according to test parameters with a majority of tests conducted at burial depths: 1.3 cm; 2.5 cm; 5.1 cm; and 7.6 cm.

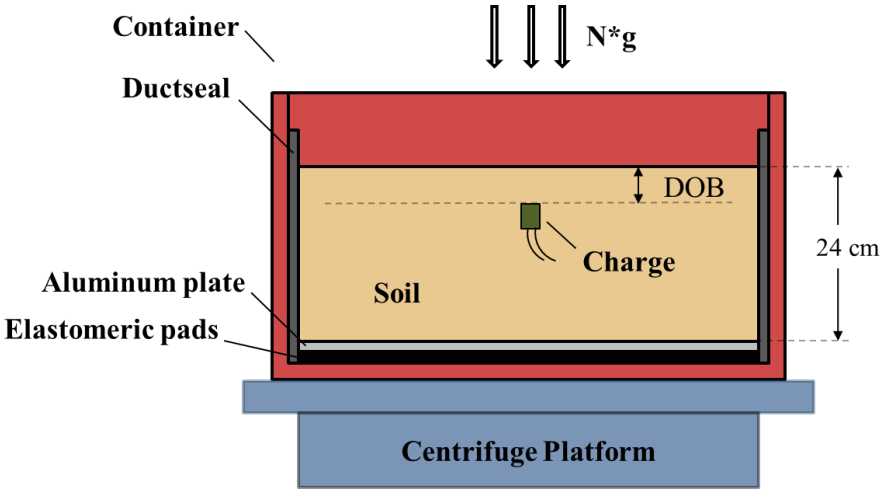

Figure 2.15. Schematic of the soil container, components, and buried explosive.

To position the explosive charge and prevent caving of the cohesionless dry soil walls during excavation, a thin, aluminum sheet configured in a C-shape roughly 20 cm in diameter, was gently inserted into the prepared soil model to the desired DOB. After the aluminum sheet's positioning,

undesired sand particles were vacated from the interior, permitting charge insertion. Next, the soil was pluviated to backfill the hole to ensure charge placement integrity, and the aluminum sheet then withdrawn. Soil regions adjacent to the explosive charge were manually tamped using an aluminum block to void existent air pockets, thus readying the charge for detonation. Saturated sand and clay-sand testbeds facilitated charge embedment because the soil matrix's cohesive strength prevented caving of the surrounding material.

Subsequent charge detonation at the prescribed g-level and centrifuge spin-down to rest, post-test static measurements and photographs ensued, designed to supplement real-time data collection. After each detonation, a line gage and digital calipers extracted crater dimensions. In later test series, a LMI Technologies Gocator surface laser system generated 3-D profiles of excavated craters with improved precision and efficiency over point-wise contact methods (Figure 2.16). The Gocator surface profilometer (laser line resolution 1,280 points/line), integrated into a monorail system and connected to a pinon gear rotary encoder and rack assembly, captured cross-sectional profiles at 51 μm intervals along the travel axis. These discrete scans stitched sequentially together permit visual upscaling of 2-D planar crater profiles into highly-resolved, 3-D computer-generated surfaces.

Figure 2.16. (*left*) Laser profilometer system and (*right*) laser line projection on excavated crater during 3D scan.

Before the next test sequence, soil specimen preparation required the removal of all explosive debris and pulverized sand within a zone that extended at least 51 cm laterally and 12 cm in-depth from the previous charge location, or longitudinal axis of the excavated crater. Specific to partially-saturated substrates, careful extraction of small samples at multiple testbed locations immediately followed each experiment. The soil sample's post-detonation and oven-dried weight determined the degree of desaturation. In general, the soil's before and after explosion in-situ water content varied insignificantly despite exposure to gravitational forcing and hot, highly-pressurized explosive combustion gases.

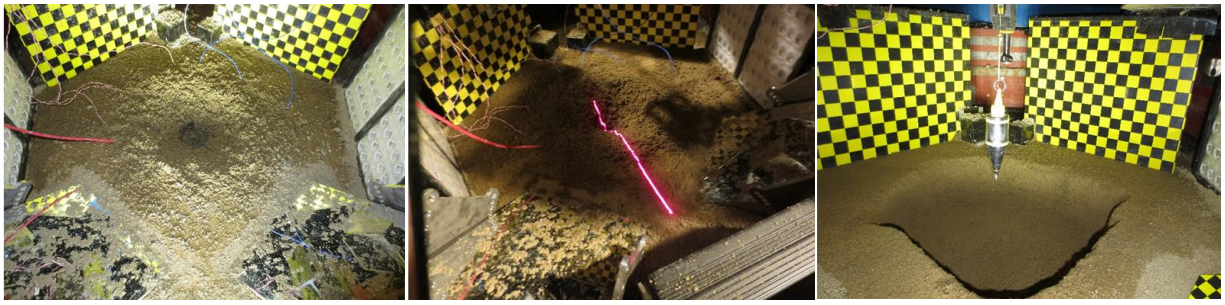

Figure 2.17. Test environment (*left*) post-detonation; (*middle*) laser profilometer scan of final crater surface; and (*right*) excavated testbed and overlying plumb bob readied for testing.

2.7 Experimental Systems Integration

The complex and highly transient nature of soil blast loading dictated extensive pre-test evaluation of systems instrumentation designed to optimally capture initial soil deformation, early charge-gas-soil ejecta interactions and expansive heave; and simultaneously measure the soil's dynamic response in both the near and far-fields. Furthermore, all integrated systems had to be installed and tested within the dimensional constraints of the centrifuge platform and be able to withstand accelerated g-level forces. The systems instrumentation, selected to provide critical qualitative and quantitative insight in to the highly transient, buried soil blast phenomenon are detailed below.

2.7.1 High-speed Imaging System

The initial high-speed imaging system characterized soil ejecta kinematics in the free-field condition. The second high-speed imagining system integrated a second camera and additional instrumentation to delineate soil blast mechanisms and the overlying target's dynamic response during soil blast momentum transfer in the near-field environment. Both imaging systems included the following interactive components: color CMOS sensor, megapixel v710 Vision Research Phantom high-speed video cameras; high-intensity LED flood panels; and optically flat mirrors (Figure 2.18).

Figure 2.18. High-speed imaging system including: (*left*) a color v710 Vision Research Phantom high-speed camera and (*right*) high-intensity 29,580 Lumen LED flood light panels.

A Vision Research Phantom v710 high-speed, g-rated camera captured sequentially, in real-time, initial soil deformation, early gas-soil ejecta expansion, and target impact specific to the soil ejecta kinematics and blast loading investigations. The camera outfitted with an acrylic protective screen and particulate filters recorded blast images from 41,013 frames per second (fps) to 90,007 fps dependent on test configuration. The use of a color high-speed camera delineated the diverse shades of soil particles existent in Colorado Mason sand and the subsequent multi-dimensional, visual image improved particle tracking. The extreme dynamic range (EDR) imaging technique, implemented at burial depths less than 2.5 cm, augments image resolution and particle tracking. At shallower DOBs, the immediate, bright luminance at detonation, attributed to the blast thermodynamics, obscures particle distinctiveness. However, EDR diminishes pixel light oversaturation and thereby improves tracking clarity. When choosing a suitable camera lens, the considered variables included: aperture, depth of field, field of view, and spatial constraints. The Canon EF f/1.4 wide-angle lens best adhered to design parameters, specifically the transient nature of buried blast loading and centrifuge spatial confinements.

2.7.1.1 Single High-Speed Camera System

A single camera high-speed imaging system to characterize soil ejecta kinematics included the following interactive components: a v710 Vision Research Phantom high-speed camera; dual high-intensity, white-light emitting diodes (LED) flood bars; and two optically flat mirrors. This specific test configuration allowed blast recordings at 41,013 fps, which in turn prescribed a maximum allowable resolution of 400 x 304 pixels and a 4 µs shutter speed. The high-speed video camera mounts on a support cross-channel suspended directly over the buried charge at a calculated distance of 56 cm above the soil surface to avoid potential damage and vibrations induced by soil blast loading (Figure 2.19).

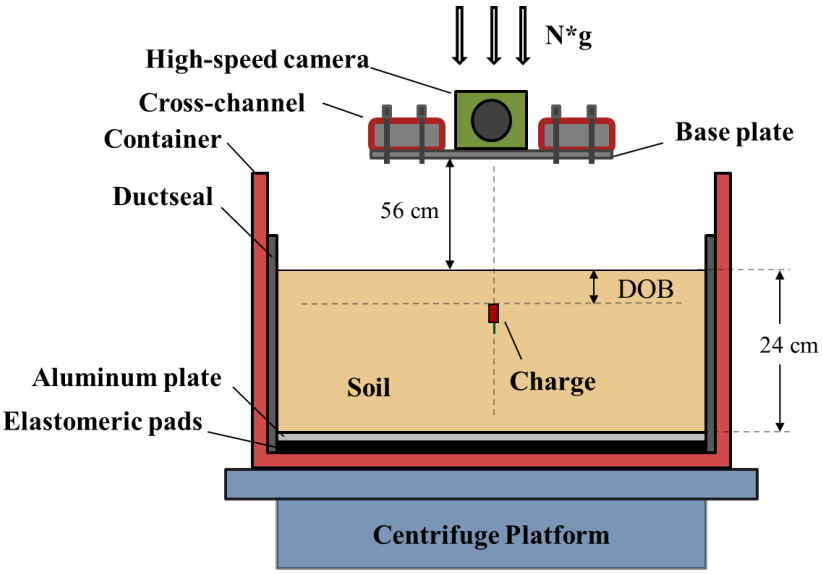

Figure 2.19. Schematic of the single camera configuration.

The camera's unique location required the specular reflection of the blast image from the two mirrors. The mirrors, bolted to the soil container's sides and oriented 90° relative to one another, maintain an equal angle of incidence and reflection, and thereby establish a horizontal, ground-surface view of soil ejecta. This imaging technique elongates the distance from the camera lens to

the region of interest, and thus increases the depth of focus and enhances resolution, an important consideration when designing a system to image a radially evolving, multidimensional gas-soil dome heave during crater excavation. And finally, a checkerboard backdrop provides contrast and serves as a spatial reference. Figure 2.20 depicts the single camera systems integration into the centrifuge domain. The single camera's position presents a unique perspective within the centrifuge rotating reference frame. From the camera field-of-view, after explosive detonation, soil particles eject radially from the model *in-flight* to the ambient free space towards the centrifuge central axis as illustrated in Figure 2.21.

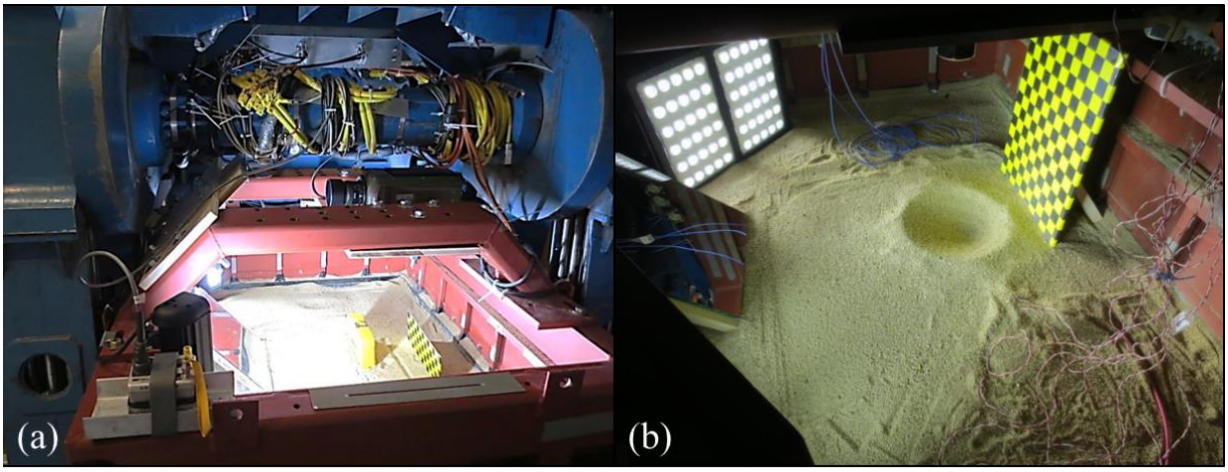

Figure 2.20. (a) Soil container and integrated components on 400 g-ton centrifuge at UCB. (b) In-box perspective.

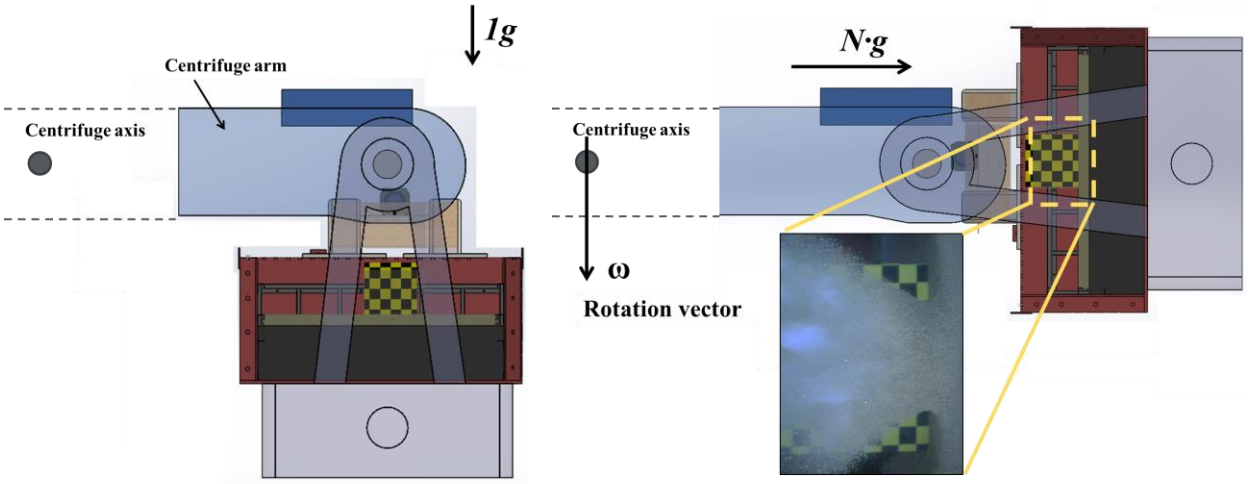

Figure 2.21. Schematics of the centrifuge payload platform and soil container illustrate the single high-speed camera's perspective during centrifuge operation. Figures are *to-scale*.

2.7.1.2 Dual High-Speed Camera System

To augment visual resolution and measurement of the buried, explosive-induced impact phenomenon in the near-field, the high-speed imaging system integrated a second Phantom v710 high-speed camera, three high-intensity LED flood panels, and four optically flat mirrors. This upgraded imaging system recorded soil blast mechanics at a maximum 90,007 fps and a 1.5 µs shutter speed. The stereo video cameras captured sequentially, in real-time, the blast loading mechanisms including initial soil deformation, gas-soil ejecta heave evolution, and subsequent impacts on overlying targets under accelerated gravity.

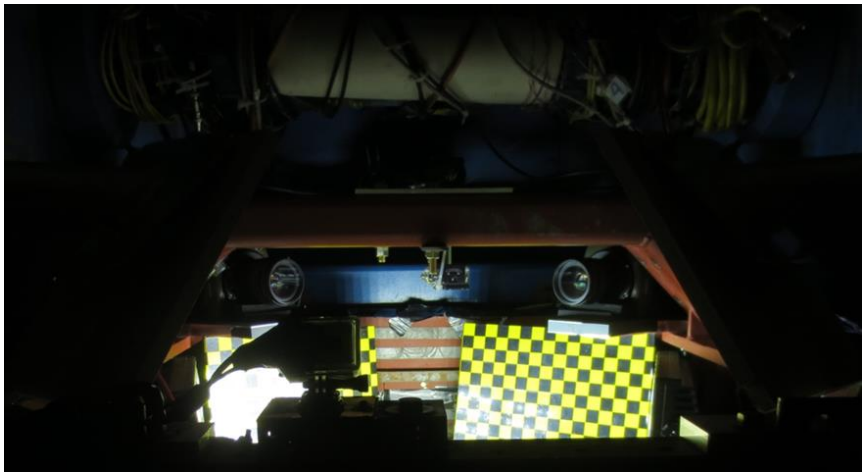

Figure 2.22. Dual camera integration.

The dual, stereo imaging system required additional design modifications and component-assembly fabrication. For example, a versatile, custom-designed assembly, comprised of a camera mount-base plate (Figure 2.23a) and stage (Figure 2.23b) allowed precise, incremental camera adjustment to refine the high-speed image. The camera and stage, securely fastened to the cross-channel base and thick steel cantilever, suspends 30 cm directly above the soil surface to avoid potential damage by explosive detonation (Figure 2.23c, d). The assembly's robust design attenuates camera vibrations caused by explosive detonations.

(a)  (b) 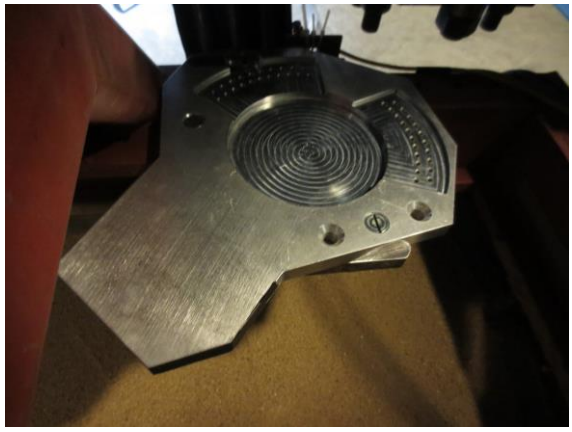

(c)  (d) 

Figure 2.23. (a) Camera mount base plate and corresponding (b) stage installed and overlying soil model; (c) side-view of the camera mount assembly attached to the soil container; (d) cross-channel base plate and camera mount base plate support beam.

In addition, the dual cameras' unique positions within the dimensional constraints of the centrifuge domain required the specular reflection of the blast image from two additional mirrors (*upper* and *lower*). This required the design and fabrication of two different mirror mount assemblies a left and right (Figure 2.24 and 2.25) to secure the fully-adjustable rigid mounts to the soil container. The mirror mounts' translational and rotational functionality enables a wide range of incidence angles for a multifaceted view of the soil ejecta evolution.

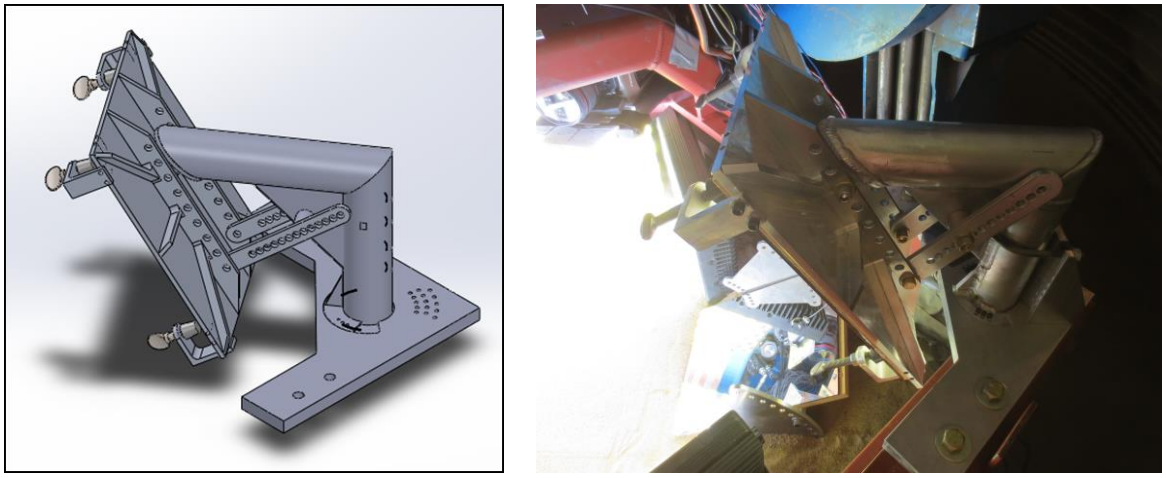

Figure 2.24. CAD model (*left*) and fabricated (*right*) upper mirror mount.

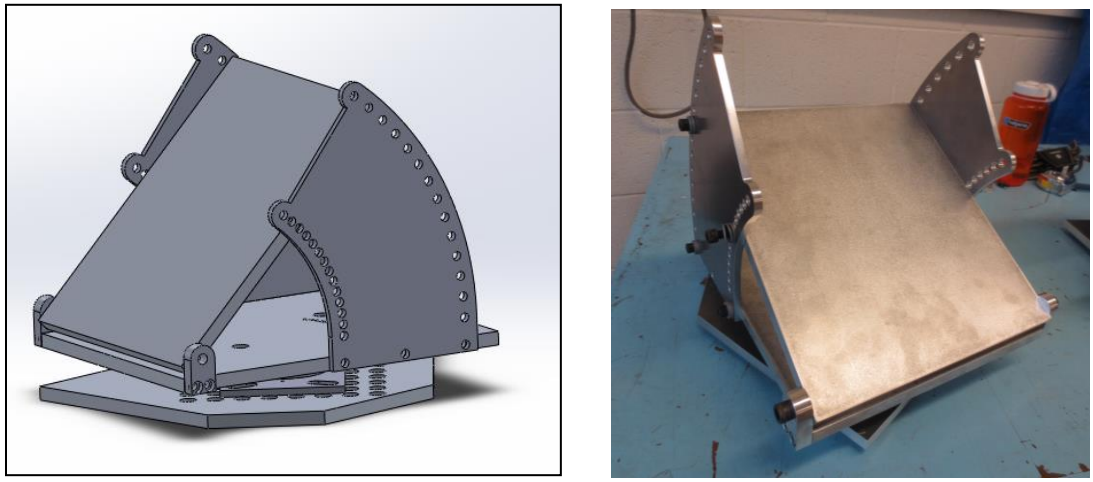

Figure 2.25. CAD model (*left*) and fabricated (*right*) lower mirror mount.

The close-range and full-field perspectives of the centrifuge experimental setup (Figure 2.26 and 2.27) detail the integration of the high-speed stereo imaging system within the soil container domain. Clearly, the spatial limitations required the systematic arrangement of all interactive components to ensure seamless mobility void of any physical or optical interference.

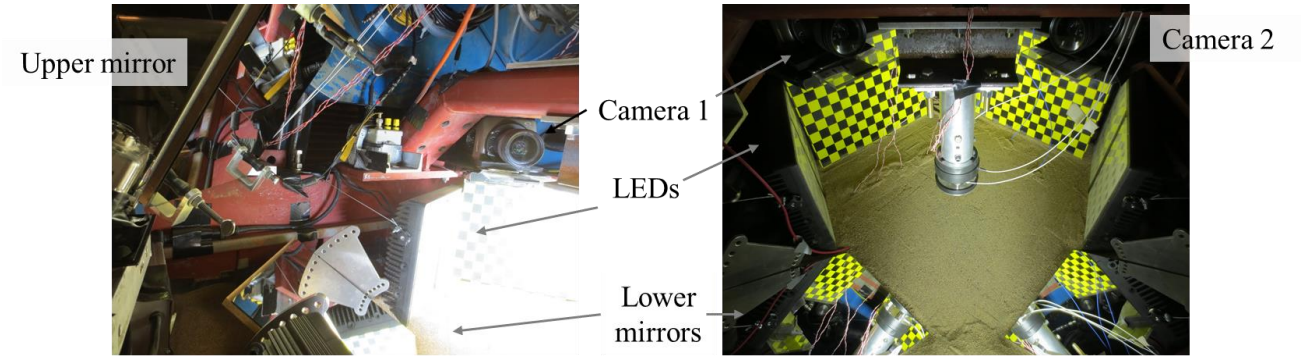

Figure 2.26. In-box perspective of integrated components in the soil container.

Figure 2.27. Wide-angle view of the soil model installed on the centrifuge illuminated by (*left)* natural light and (*right*) in-box high-intensity LED light.

2.7.1.3 Soil Ejecta Tracking Methods

The high-speed imaging system, in conjunction with a motion analysis software distributed by Vision Research, allows quantitative measurement of the evolving soil ejecta front during blast crater excavation. This motion analysis method measures the in-plane deformation rates of the soil dome heave instead of tracing single material points. In general, a soil blast experiment yields 400-2,000 high-speed video frames, dependent on internal camera settings and specific test parameters, for subsequent data analysis. The two-dimensional point-wise tracking program first requires the calibration of the digital image reference scale (unit length/pixel) in-plane relative to the buried explosive. Next, a prescribed origin set at the soil-air interface defines the x-y

coordinate system. The user selects a search area of interest, i.e. initial soil deformation, that encompasses the first tracked point and the software subsequently detects the linear translation of the particle in sequential images (Figure 2.28). This in turn, quantifies the temporal and spatial soil ejecta heave.

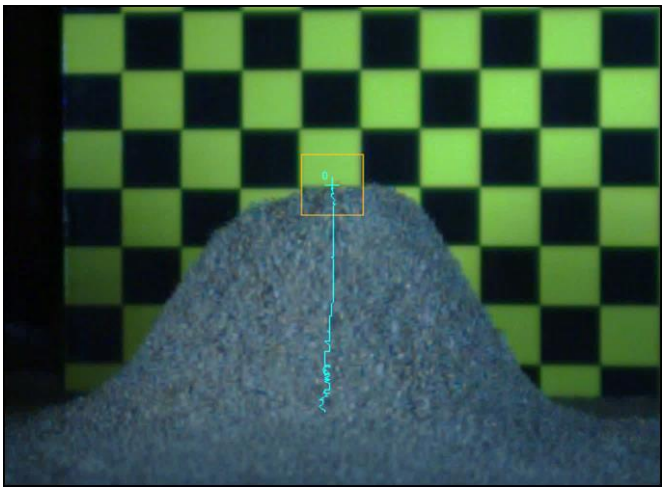

Figure 2.28. Software tracing marker superimposed on soil ejecta dome during crater excavation.

2.8 Piezoelectric Shock Instrumentation

As discussed above, the high-speed imaging system in conjunction with the motion analysis software quantifies soil ejecta kinematics. In addition, this research integrated instrumentation to measure the ground shock response and soil blast kinetics. Significantly, the artificial gravitational field governs the physical domain and response of the model, in addition to the instrumentation. Therefore, to avoid adverse sensor interference with blast impact measurements, this study selected light-weight, rugged miniaturized piezoelectric sensors that functioned without inadvertently affecting the overall blast phenomenon. Rugged, miniature shock accelerometers (PCB Model 350B24), fabricated with minimal intrinsic damping and a high resonant frequency, measure high-g accelerations (± 5000 g), and therefore allowed proper characterization of shock

wave transmissivity and dynamic soil blast target impact (Figure 2.29a). In addition, small 22.7 gm shock load cells (PCB Model 208CO5), with a compressive range ±22.4 kN, measures the transient, axial forces imparted to the overlying target by blast load impacts (Figure 2.29b). Specific shock sensor implementation is detailed in a following section.

(a) (b) (c)

Figure 2.29. PCB Piezotronics shock sensors: (a) accelerometer (Model 350B24); (b) load cell (Model 208C05); (c) pressure transducer (Model 102B).

Small, high-frequency pressure transducers (PCB Model 102B) measure the transient, radial compressive stress wave transmittal through the soil across particulate contacts (Figure 2.29c). Sensor insertion into the soil model adheres to the charge placement methodology described in Section 2.6. The sensor's burial depth coincides to the test-specified charge DOB (Figure 2.30). Furthermore, to properly characterize the propagating shock wave, the sensor's diagram aligns parallel to the cylindrical, charge centerline.

To evaluate shock stress measurement repeatability and minimize sensor cross-talk within the spatial confinement of the soil domain, the sensors were carefully positioned after the first sensor, r_1, placement from the charge center (Figure 2.30). This r_1 sensor records the first ground motion response. The remaining sensors. arranged at increments of r_2, r_3, and r_4, measure residual shock wave intensity and ground motion attenuation (Figure 2.30). Gauge wires travel behind the sensor, secured to the above cross-channel along the shortest path to minimize undesired cable interference with the propagating shock wave.

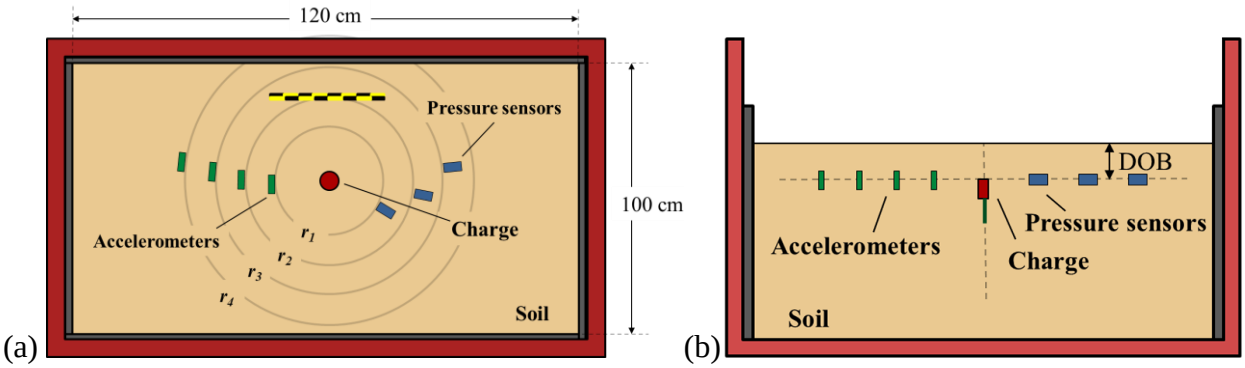

Figure 2.30. Schematic illustrating shock sensors embedded in soil and relative location to buried charge: (a) top view; (b) side view.

2.9 Data Acquisition System

The data acquisition and real-time sensor control system, a National Instruments (NI) PXI-1042 chassis paired with two high-accuracy, 8-channel NI PXI-4496 modules, mounted near the centrifuge rotor, conditioned, amplified, and recorded data at a rate of 200 kHz. This ideal sample rate enabled highly-resolved, time-histories that effectively quantify the soil blast mechanics. An optimized NI-DAQmx Labview code, configured with digital trigger functionality, seamlessly gathered and stored real-time blast data throughout the entire experimental program.

2.10 Digital Pulse Generator and Fire set

A Berkeley Nucleonics Corp. (BNC) digital pulse/delay generator (Figure 2.31) synchronized and triggered all experimental components, including a Reynolds Teledyne FS-43 firing system (Figure 2.32), the high-speed cameras, and data acquisition system (DAQ). The first two channels on the BNC 575 pulse generator were customized with a high voltage (35 V), dual-channel module to comply with the FS-43 fire set's 19 V trigger threshold requirement. The remaining BNC channels output the standard 5 V TTL signal, the requisite trigger specification for the high-speed

cameras (3 µs pulse width) and DAQ (0.2 µs pulse width). A prescribed 5 ms pulse delay to the high-speed cameras and DAQ provided a visual and time-history record of the pre-blast test environment.

Figure 2.31. BNC 575-8C digital pulse/delay generator.

The electrical connection from the FS-43 firing system control unit (Figure 2.32, *left*) to the buried explosive charge passed through one of 64 centrifuge slip ring channels (Figure 2.33). Importantly, the separation of the control unit from the firing module (Figure 2.32, *right*), specific to the FS-43 model, allowed the proper electrical current transmission through the slip rings within the 10 Amp current limit per slip ring pair. This precludes electrical overload and potential damage to the slip ring system from the FS-43 firing unit's high volt (4000 V) detonation pulse. Additionally, the FS-43 model allowed manual arming and charge detonation sequencing remotely from the near-by centrifuge control room. And finally, all essential power and signal transmitting wires were double-shielded and grounded to avoid undesired electrical crosstalk and electro-mechanical noise. As a result, no charge misfires occurred throughout the duration of this study. The wiring diagram in Figure 2.34 details the experiment setup and configuration.

Figure 2.32 The Teledyne RISI FS-43 EBW (*left*) firing system Control unit and (*right*) Firing module (installed on centrifuge soil container).

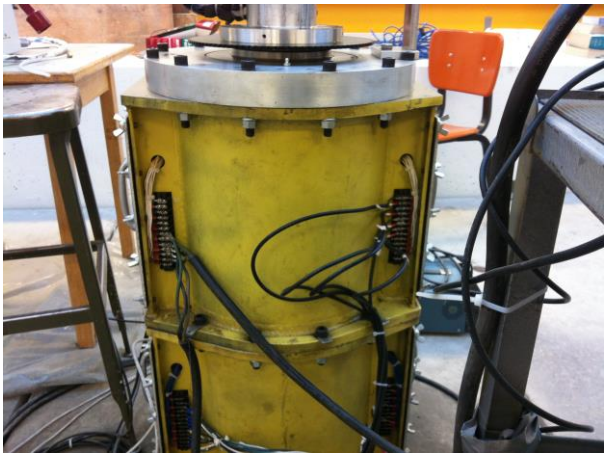

Figure 2.33. Centrifuge slip ring system.

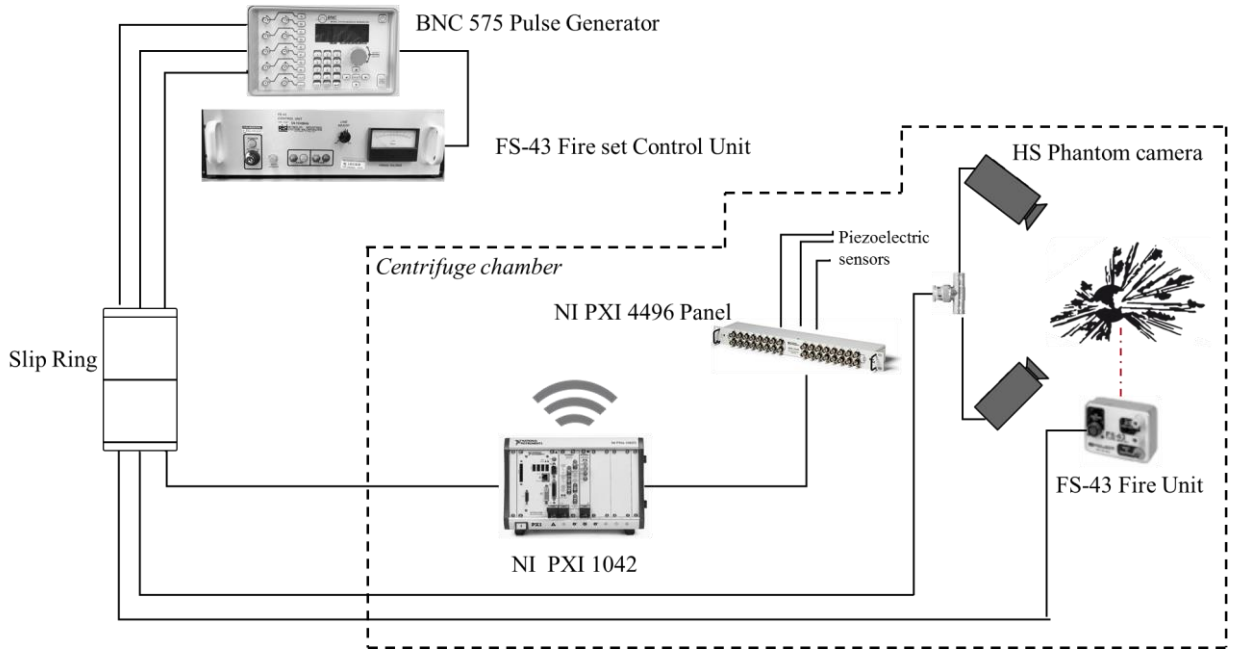

Figure 2.34. Experimental component wiring diagram.

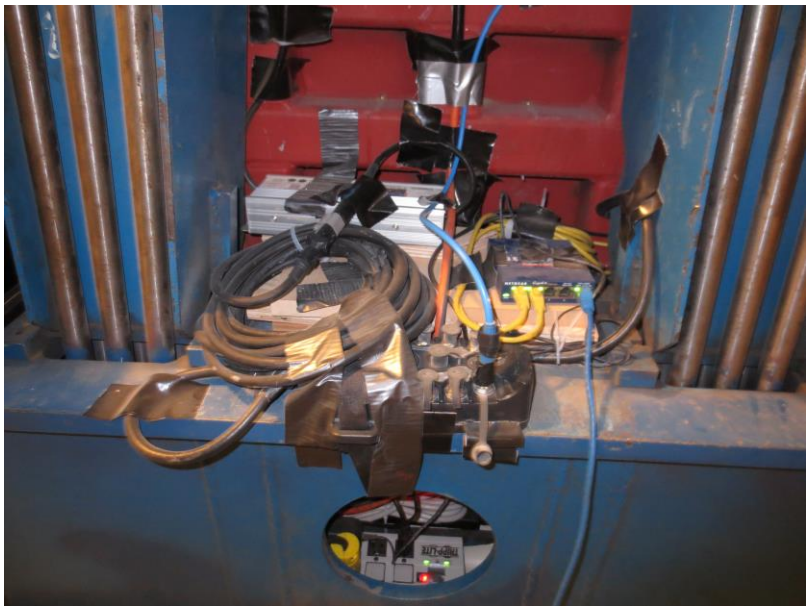

Figure 2.35. A subset of the instrumentation package installed on the centrifuge payload platform.

2.11 Blast Impact Response Gage

To quantify the near-field resultant force impacts and rigid-body dynamics, under explosive loads beyond conventional discrete measurement methods, this research designed and fabricated a novel, robust laboratory-scale measurement device, specifically the Blast Impact Response Gage, or BIRG. The BIRG, integrated into the centrifuge domain, enables a simultaneous and accurate characterization of the complex, multiphasic, interfacial soil blast impact mechanisms under elevated gravity.

2.11.1 Structural Support Design

The structural support system addressed the need to mitigate undesired macro-scale displacements and vibrations post-explosive detonation that may adversely influence measurement and data interpretation. In addition, the design considered structural fatigue resistance due to repeated centrifugal forcing. Thus, the cross-channel was fabricated from high-strength carbon steel to ensure structural rigidity (Figure 2.36).

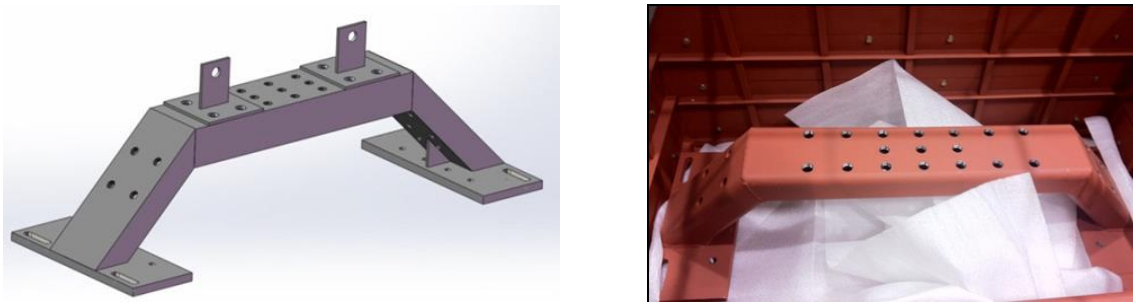

Figure 2.36. (*left*) CAD model and (*right*) fabricated cross-channel.

The cross-channel consists of three 0.95 cm thick, steel rectangular tubular sections, welded to the base plates, then bolted to the soil container. A 10.16 cm square by 20.32 cm long machined

steel I-beam connects the BIRG to the cross-channel, secured with high-strength mechanical fasteners. The experimental setup is represented schematically in Figure 2.37.

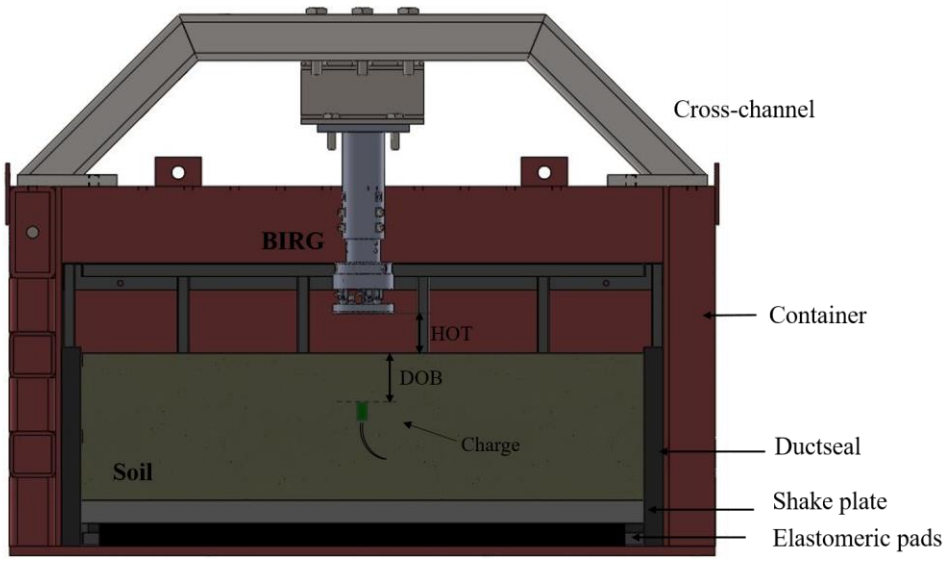

Figure 2.37. Schematic of BIRG experimental layout for buried blast tests (*to-scale*).

A finite analysis on the cross-channel with boundary conditions that prescribed full translational and rotational constraints at the cross-channel/soil container node interface predicted negligible vertical deflections for loading conditions exceeding the expected, maximum blast pressures [7,31,49]. This in turn, verified the structural integrity of the support system design. The structural support system centers the BIRG directly over the soil model and charge location. A shock accelerometer (PCB 350B24), affixed to the cross-channel, monitored support frame motions. A representative experimental response of the BIRG support system post-detonation presented in a later section validates its structural integrity.

2.11.2 BIRG Design and Methodology

Foremost design considerations, versatility and robustness, prescribed that the impact device accurately and coincidently measure both the temporal and spatial variations of the high-rate impact loads imparted to the target. Therefore, the consequent sensor configuration enables quantification of rigid-body accelerations, resultant force, and moments induced by eccentric impacts. The blast impact device with all integrated components is shown in Figure 2.38a, positioned directly over the buried explosive pre-detonation.

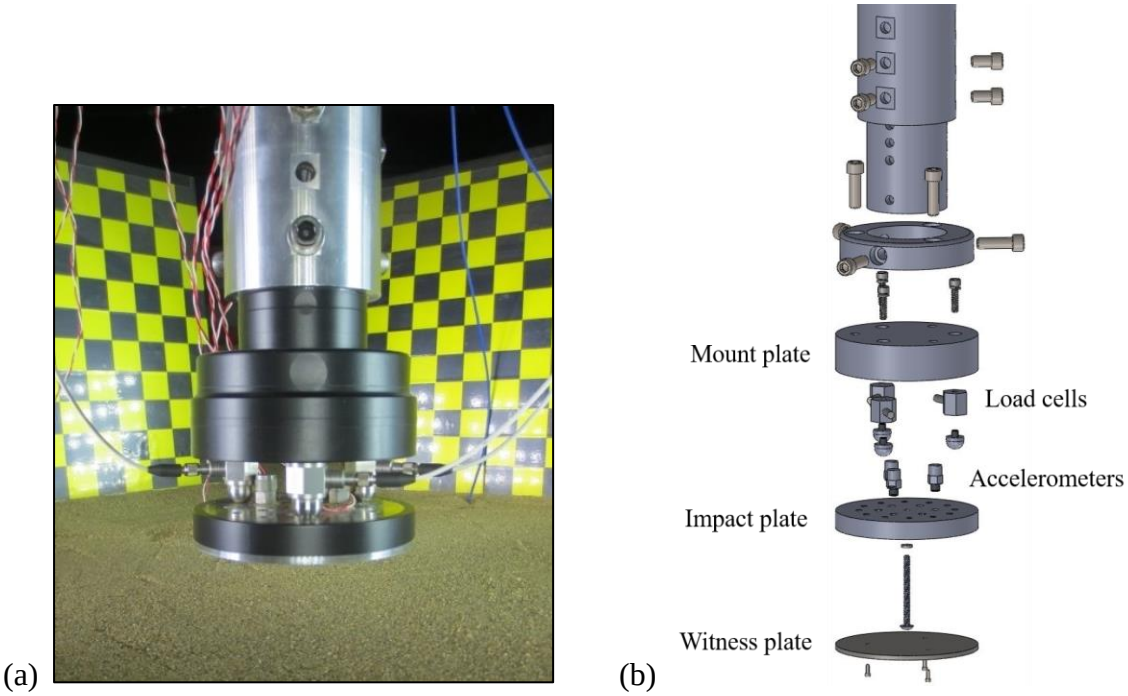

Figure 2.38. (a) The BIRG positioned directly above a buried charge pre-detonation; (b) 3-D exploded view drawing of the BIRG (*to-scale*).

The detailed 3-D exploded drawing (Figure 2.38b) depicts all interactive constituent subassemblies. The BIRG consists of three aluminum alloy plates: *mount*, *impact*, and *witness*. Three shock load cells (PCB Model 208C05), spaced radially at 3.43 cm and equidistant to each other in a tri-symmetric configuration, attach to the mount plate and measure the compressive axial

forces subsequent impact loading (Figure 2.38, 2.40a). To permit in-plane rotations and function as a load distribution mechanism, custom-fabricated miniature hemispherical cast alloy steel impact caps (Figure 2.39a), design-specific to the BIRG, affix to the sensing surface of the load cells secured by a mount stud (Figure 2.39b).

(a)  (b) 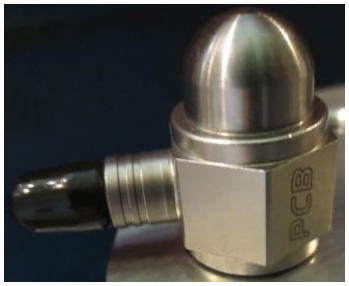

Figure 2.39. (a) CAD model and (b) fabricated hemispherical BIRG impact caps affixed to load cell.

Polyamide film placed at the interfacial boundary between these caps and the impact plate reduces high-frequency noise typical of metal-to-metal contact. Proximate and radially in-plane to the load cells, positioned 2.03 cm from the fulcrum, three high-g accelerometers (PCB Model 350B24) mounted to the impact plate, quantify the kinematics of the explosive energy transfer (Figure 2.38, 2.40b). A variation in the quantity of BIRG shock accelerometers and load cells results in an indeterminate system, the logical basis for the tri-symmetric design.

(a) 

(b) 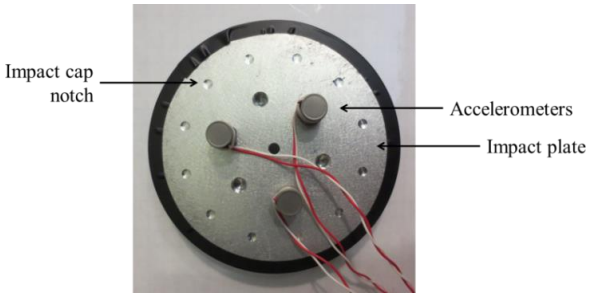

Figure 2.40. (a) Shock load cell sensors and thread-mounted hemispherical impact caps; (b) shock accelerometers affixed to the impact plate.

Furthermore, minute spherical notches on the adjoining impact plate align the load cells and accelerometers and also create a no-slip condition at the cap-plate interface (Figure 2.40b). A counter-bored center screw attaches the impact plate to the mount plate and ensures a uniform pre-stress condition on all load cell sensors. Finally, the witness plate, secured to the impact plate by small set screws, provides a flush target surface (Figure 2.38b). The plate subassemblies adjoin a telescopic module (Figure 2.38b) that permits incremental, vertical adjustments according to the experiment's prescribed height of target (HOT), defined as the vertical distance from the soil-air interface to the free-surface of the witness plate (Figure 2.38b). Table 2.4 summarizes the BIRG component specifications.

Table 2.4. BIRG assembly parameters.

Plate	Material	Diameter (cm)	Thickness (cm)	Mass (kg)
Mount	Al. 7075-T6	10.16	2.54	0.54
Impact	Al. 7075-T6	10.16	1.27	0.36
Witness	Al. 7075-T6	10.16	0.32	0.07

2.11.3 Additional BIRG Target Plates

To explore target geometries and their potential to deflect soil blast loads away from a vehicle underbody, this parametric study designed and fabricated additional flat plates and new oblique, V-shaped targets to easily conform to the preexisting BIRG design. Due to accelerated g-levels and the extreme near-field blast environment, all targets were machined from aluminum alloy 7075-T6 because of its superior fatigue strength and strength-to-weight ratio when compared to aluminum alloy 6061-T6. The three flat plates, with respective diameters of 10.16 cm, 12.19 cm, and 15.24 cm, were specifically designed with an identical diameter-to-thickness ratio of 8.0

(Figure 2.41). Therefore, different flat plate combinations simulate equivalent prototype-scaled targets by adjusting a single test parameter: gravity. The meticulous design of two dihedral 135° and 90° (included angle) targets prescribed the same masses (314.7 gm) and attachment base areas (103.23 cm^2) for both configurations (Figure 2.42). The flat plate design provides a benchmark for comparative analysis of target geometry effects. Figure 2.41 illustrates the targets assimilated into the BIRG. Table 2.5 summarizes their respective properties.

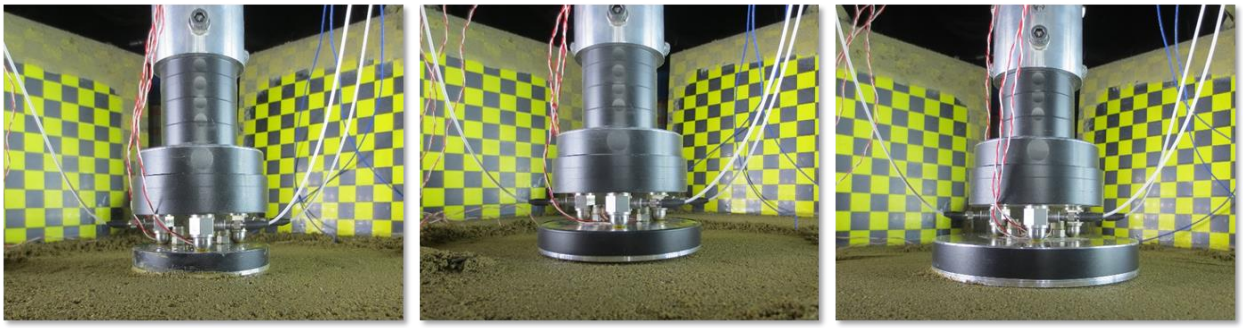

Figure 2.41. Flat targets with diameters (*left*) 10.16 cm, (*center*) 12.19 cm, and (*right*) 15.24 cm overlying a buried charge.

Figure 2.42. Dihedral targets with included angles (*left*) 135° and (*right*) 90° overlying a buried charge.

Table 2.5. BIRG target plate specifications.

Target geometry	Thickness (cm)	Mass (gm)
10.16 cm (Dia.)	1.27	286.8
12.19 cm (Dia.)	1.52	600.0
15.24 cm (Dia.)	1.91	1128.1
135° dihedral	2.10	314.7
90° dihedral	5.10	314.7

Chapter 3 Soil Ejecta Rheology

3.1 Soil Ejecta Kinematics

The key experimental results from over 50 explosive tests and their analytical synthesizes are presented in the following sections. Standard earth gravity tests included in the results augment data analysis and clarify the influence of increased gravitational forcing.

The following analysis provides critical qualitative insights into the highly transient, multiphasic soil blast mechanisms. This test series used a 1.0 gram C4 charge, under a 5.1 cm soil overburden, and detonated at 4 g-levels (1 g, 20 g, 30 g, and 40 g-level), with model burial depths scaling to 0.05 m, 1.00 m, 1.50 m, and 2.00 m in prototype condition. The video sequences, at coincident msec intervals, effectively illustrate the gravity-induced stress-level impact on the buried blast phenomena (Figure 3.1).

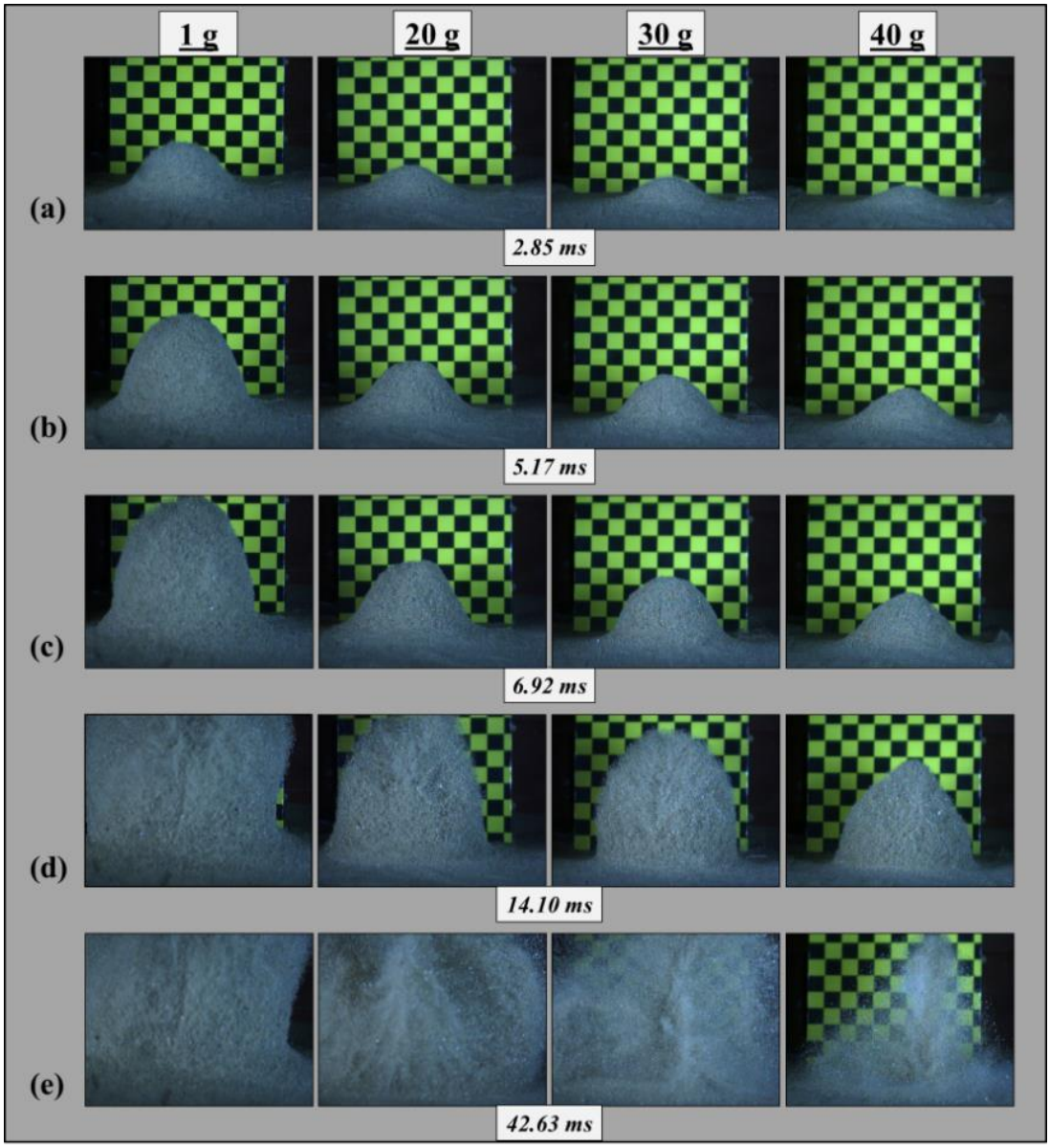

Figure 3.1. Comparison of soil deformations for 1.0 gram C4 charge detonated at 5.1 cm burial depth and corresponding gravitational accelerations: 1 g (left), 20 g (*left*-center), 30 g (*right*-center), and 40 g (*right*). Time after detonation: (a) 2.85 msec; (b) 5.17 msec; (c) 6.92 msec; (d) 14.10 msec; (e) 42.63 msec. Fiducial background square grid 2.2 cm in length.

The initial ground motions at the soil-air interface, measured by high-speed video, occurred approximately 0.214 ms post-detonation at the 1 g-level. The consequent soil surface motions appear progressively later with increased gravity: 0.415 ms at 20 g; 0.595 ms at 30 g; and finally, 0.710 ms at 40 g. It is evident that the arrival of the shock wave and pressurized gases at the soil

surface lengthen with elevated gravity-induced stress levels, and thus soil ejecta displacements occur later.

As illustrated in Figure 3.1a, the first row of high-speed video frames, recorded at 2.85 ms, reveals the opaque gas detonation products jetting through the soil at each tested g-level. This specific frame illustrates the early thermodynamic phase of a buried blast event: the immediate gas-soil particle interaction. In this stage, the heat transfer mechanism crushes and even pulverizes the soil adjacent to the charge as the shock wave passes through the soil material [27]. The pressurized gases and shock wave impart kinetic energy into the particulate medium causing the soil matrix to collapse followed by soil deformation at the surface as observed in Figure 3.1. Next, the explosive gases expand radially and initially jet past the soil cap domain, creating a dilute suspension of particles dragged upward with the detonation products, visually evidenced in Figure 3.1, especially at lower g-levels. The continuous radiating pressure impulse drives overlying soil into the air, eventually penetrating the expansive gas bubble, encasing the detonation products in a soil annulus (Figure 3.1). Then, both constituents (gas and soil) swell and rapidly accelerate in a predominantly vertical direction due to lateral soil confinement, with relatively uniform, hemispherical mound growth**.** This observed trend continues in the early stages of the blast event in all four tests (Figure 3.1a-c).

As illustrated by the video frames for the different g-levels, it is evident that elevated gravity, which led to heavier overburden loads at a constant burial depth, significantly impacts the buried blast phenomena. A closer examination of the video frames at 1 g shows a radial soil dome expansion, typical of the inverse cone (Figure 3.1a-c, 1 g). In contrast, the high-speed video frames at the 40 g-level depict a slightly asymmetrical, vertical directionality that dominates soil dome heave with increased gravity (Figure 3.1d). Here, the soil dome heave exhibits less uniformity in

surface contours, with a pointed apex and sloping, asymmetric sides**.** This can attribute to the gravity-induced increase in overburden pressure which restricts the radial flow of the detonation products and soil ejecta. The same mechanism also appears to inhibit soil mound diameter dimensions (Figure 3.1d, 40 g).

Clearly apparent, the soil dome expansion rate decreases with increased g-level. As witnessed in the 1 g test, the propagating soil dome reaches the upper boundary of the camera's high-speed image frame at 6.92 ms after detonation, preceding the 40 g, 30 g, and 20 g-level tests by 17.53, 10.29, and 6.17 ms, respectively, a significant difference within the msec time sequence of the entire blast event (Figure 3.1c). Furthermore, the soil dome heave at 1 g displays the early venting (Rayleigh-Taylor instability [31]) and soil mound disassociation in the upper portion of the gas bubble at 14.10 ms, followed by the soil fallback to form the excavated crater, as shown in the following image (Figure 3.1d). In contrast**,** at the 40 g-level, in the relatively, late-time lapse, 42.63 ms (Figure 3.1e), the soil ejecta only begins to deposit in and around the plastically deformed crater wall. In addition, this specific frame depicts thin jets of detonation products finally extruding through the stiffened soil matrix. This observation suggests that the higher effective gravity-induced soil stress proximate the charge suppresses early soil mound dissociation and confines detonation products for a longer time period when compared to lower g-levels.

Blast-excavated crater and outer ejecta lip formation at 40 g occurs 82.05 ms post-detonation. In comparison**,** the same phenomena occur at the 30 g and 20 g-level. However, the decreased gravity-induced stresses slow down final crater formation to 121.20 ms and 164.75 ms, respectively, a significant time increase of 39.20 ms and 82.70 ms. And finally, in the 1 g test, most of the soil ejecta continues to propagate radially in the late stages of the explosion beyond the field of view (Figure 3.1e, 1 g).

Because the fundamental physics of an explosive event do not change with explosive mass [3], these highly resolved, rate-dependent, sequential images of the complex, interactive soil blast mechanisms simulate the same phenomenon apparent in full-scale field tests. These results provide a sound physical characterization of the actual dynamic material behavior under buried blast loading with identification of initial soil deformations and consequent temporal and spatial ejecta flow.

3.2 Quantification of Soil Ejecta Flow

The high-speed videos combined with motion analysis software, developed by Vision Research [50], and discussed in methods, extracted rate-dependent displacement data and quantifies soil ejecta kinematics. The soil dome profiles at the same early msec intervals shown in Figure 3.2 quantify the previously observed gravity-dependent soil ejecta distribution trends illustrated in Figure 3.1. The data substantiates that increased soil overburden induced by elevated gravity significantly reduces the soil dome spatial expansion rate (Figure 3.2a-d). Also, the vertical, asymmetrical directionality evident at higher g-levels, distinctly contrasts to the 1 g profile (Figure 3.2d). And finally, as evidenced in the comparison plots, gravity restricts the radial flow of soil ejecta and therefore inhibits soil mound dimensions.

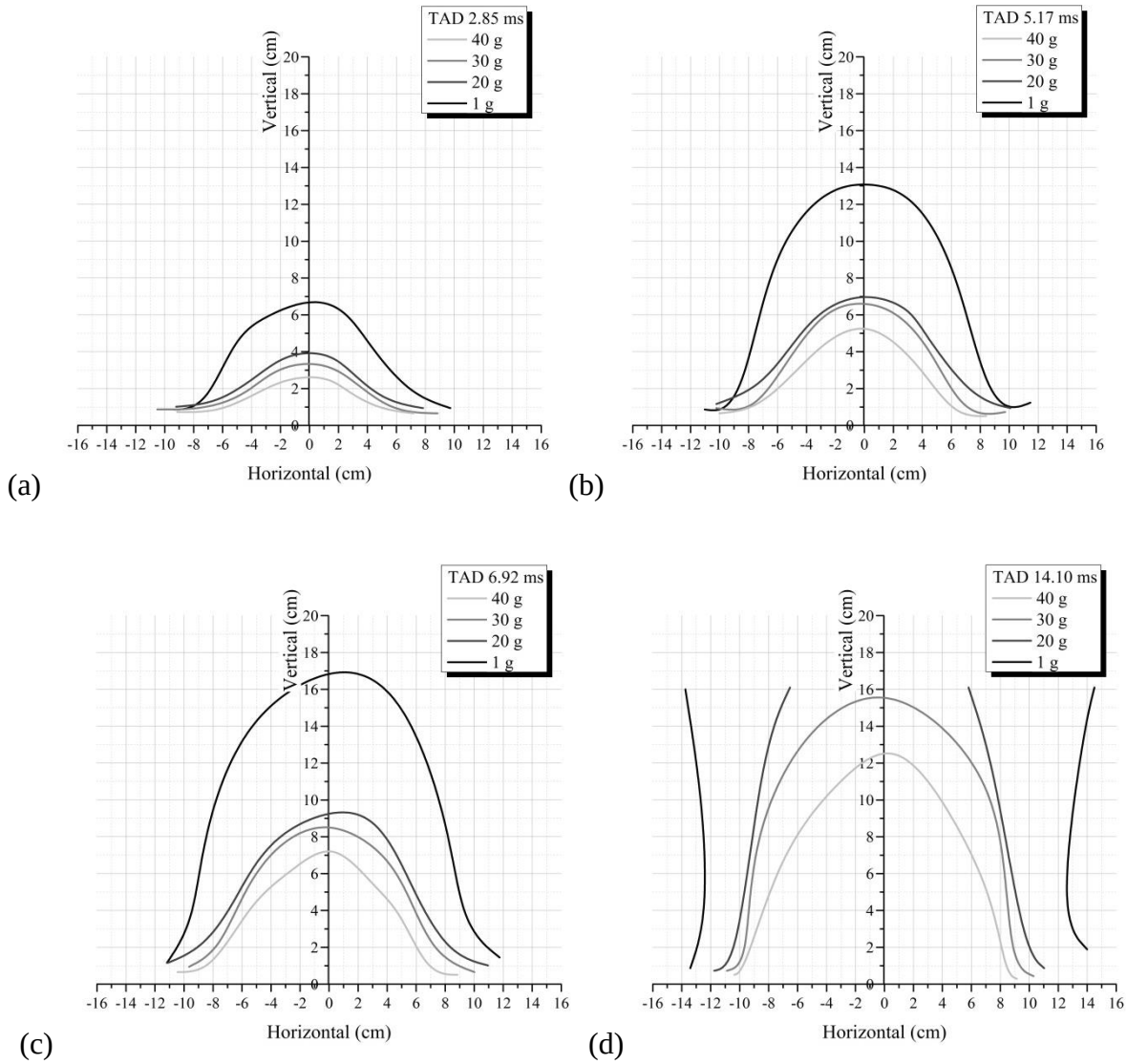

Figure 3.2. Sequential soil dome profiles as a function of time after detonation (TAD): (a) 2.85 ms; (b) 5.17 ms; (c) 6.92 ms; (d) 14.10 ms; for a 1.0 gram C4 charge buried 5.1 cm and detonated at 40 g, 30 g, 20 g, and 1 g-level.

Further data analysis determined the vertical soil dome ejecta height as a function of time post-detonation at the tested g-levels (Figure 3.3). In general, the displacement time-history plots adhere reasonably well to a linear regression throughout the examined range. Each linear regression line correlates to a range of 400 to 1000 data points specific to each g-level (Figure 3.3).

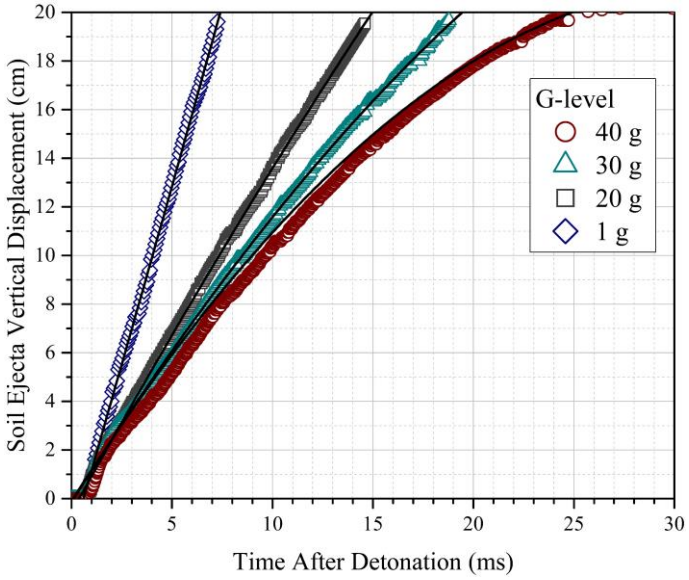

Figure 3.3. Time growth of soil dome ejecta vertical height for a 1.0 gram C4 charge buried 5.1 cm and detonated at the 1 g, 20 g, 30 g, and 40 g-level. The vertical field of view extends to 20 cm. Parabolic best-fit regression lines included (*solid-lines*).

The highly-resolved time-history plot shows that vertical soil ejecta velocities decelerate with elevated g-level (Figure 3.3), yielding a speed of 28.9 ms^{-1} at 1 g and declining to 10.7 ms^{-1} at 40 g. As the lithostatic pressure increases with g-level, more explosive energy propagates through the soil skeleton rather than dispersing to the air [37]. The stiffened soil matrix confines detonation gas expansion, delays disaggregation, and progressively attenuates soil ejecta momentum with consequent deceleration of vertical velocities, clearly observed at 40 g by the downward parabolic profile. Table 3.1 summarizes initial ejecta motion in addition to the initial and mean vertical soil ejecta velocities. The slope of a linear curve fit to the displacement data (Figure 3.3) over the first 8 cm and 20 cm defines the initial and mean vertical ejecta velocities, respectively.

Table 3.1. Summary of vertical soil ejecta velocities for 1.0 gram C4 charge buried 5.1 cm and detonated at various g-levels.

G-level *N*	DOB	Initial ejecta motion (m/s)	Initial vertical ejecta velocity (*h=8 cm*) (ms^{-1})	Mean vertical ejecta velocity (*h=20 cm*) (m/s)
1	5.1	0.214	28.9	26.5
10	5.1	0.300	21.2	20.3
20	5.1	0.415	15.3	14.4
30	5.1	0.595	13.5	10.4
40	5.1	0.710	10.7	9.8

The initial time of soil motion (t_o) gravity-dependence can be approximated by the empirical equation:

$$t_o = 0.204 + 0.006N^{1.195} \quad (3.1)$$

and indicates a nonlinear increase in initial soil surface spallation under elevated g-level, or overburden pressure. Also, a linear regression analysis determined that initial vertical soil ejecta velocities v_o best fit a power-law dependence on g-level as shown in Figure 3.4.

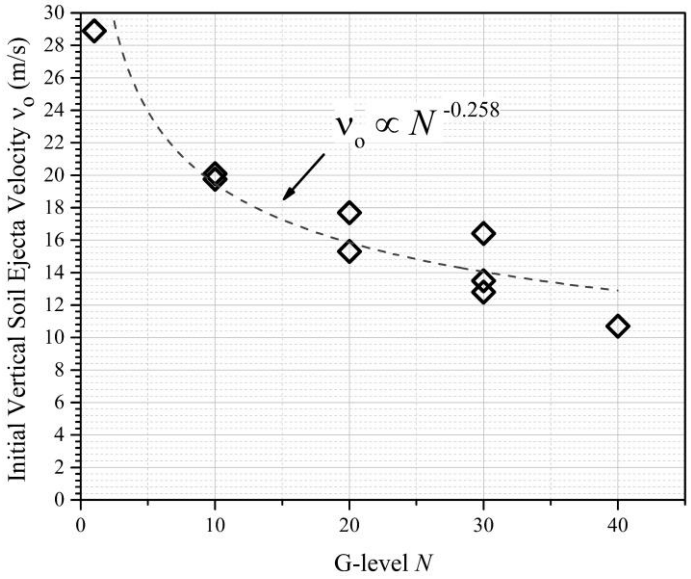

Figure 3.4. Initial vertical soil ejecta velocities as a function of g-level for a 1.0 gram C4 charge buried 5.1 cm. Included power-law regression fit (*dashed-line*). Coefficient of determination (R^2) measured 0.849.

The derived relationship between initial vertical ejecta velocities and gravity forcing is

$$v_o \propto N^{-0.258} \tag{3.2}$$

and evidences that initial vertical soil ejecta velocities display a nonlinear reduction at subsequent higher gravity-induced stress levels. The data shows a significant decrease between the 1 g and 10 g-levels, followed by a gradual asymptotic decline. Furthermore, the initial vertical ejecta velocities decrease by more than 50% at the 40 g-level relative to the 1 g-level, a difference strongly attributed to the increased shear resistance of cohesionless soil to deformations under elevated gravity.

To further characterize the soil dome ejecta front, the results quantify soil dome diameters and ejecta flow angles, as presented in the following discussion. To be consistent, an arbitrary datum 3.8 cm above the soil surface functioned as the horizontal reference to measure the lateral dimension, or soil dome diameter. The included angle between the plane tangent to the soil heave at the 3.8 cm datum and the horizontal denotes the ejecta flow angle. Figure 3.5 illustrates the effect of gravity on the temporal evolution of the soil dome diameter.

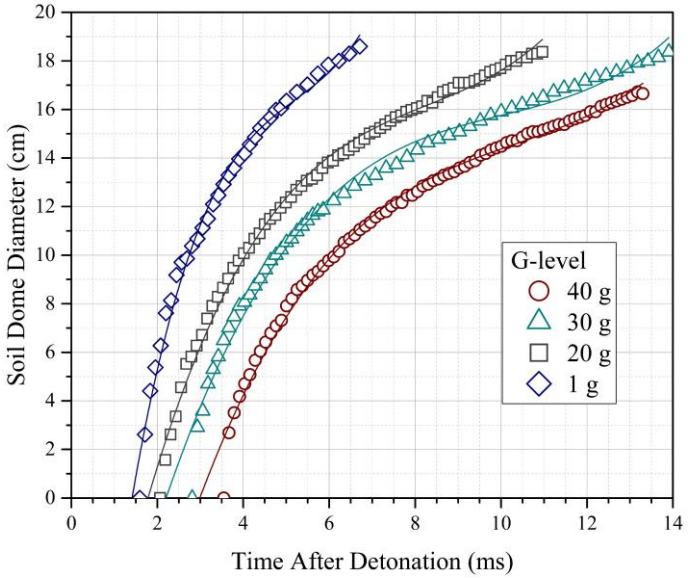

Figure 3.5. Time evolution of soil dome width for 1.0 gram C4 charge detonated 5.1 cm and corresponding accelerations: 1 g, 20 g, 30 g, and 40 g. Included cubic-polynomial regression fit (*solid-lines*).

As anticipated, the results substantiate a similar gravity-dependent trend: soil dome diameter dimensions decrease with elevated g-level and dilate at a reduced rate (Figure 3.5). The gravity-induced confining stresses strongly impede the lateral expansion rate of soil disaggregates with subsequent vertical directionality typical at higher centrifuge acceleration. This contrasts to the rapid, horizontal growth evidenced at 1 g. Specifically, the evolving soil dome diameter at 1 g measured 18.6 cm at the earliest time, 6.71 ms post-detonation. Soil dome diameter dimensions at the tested g-levels are summarized in Table 3.2. Furthermore, an analysis of the initial slopes of the curves, determined by linear regression, indicates that as time increases, soil dome diameter displacements decrease and reasonably adhere to a cubic fit (Figure 3.5).

A closer investigation of the ejecta flow field reveals that gravity plays a formative role in the time-dependent ejecta flow angle (Figure 3.6).

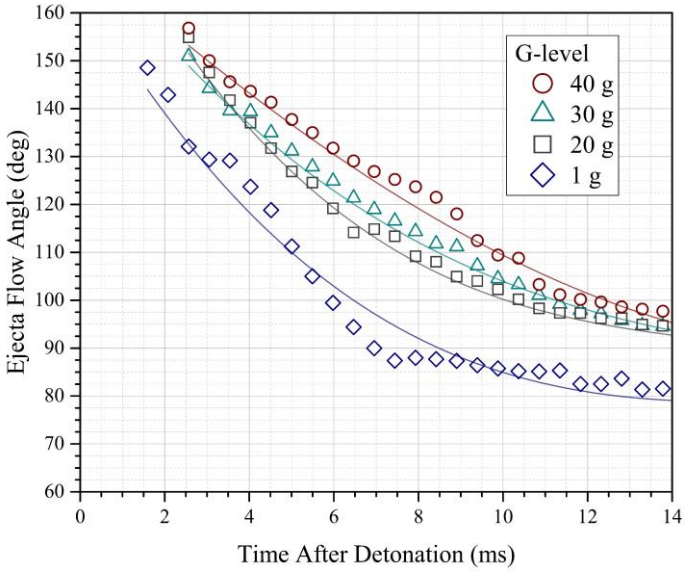

Figure 3.6. Time evolution of soil ejecta flow angle for 1.0 gram C4 charge detonated 5.1 cm and corresponding accelerations: 1 g, 20 g, 30 g, and 40 g. Included cubic-polynomial regression fit (*solid-line*).

The ejecta flow angles specific to the various centrifugal accelerations (and cubic polynomial-fit parameters) are listed in Table 3.2. The percent change between 1 g and 40 g shows the greatest increase of 21.5% in the included ejecta angle. At first, the 1 g-level soil dome heave exhibits rapid radial expansion with eventual soil ejecta flow typical of the inverse cone (Figure 3.1d, 1 g) and an included angle of 79.5° (Table 3.2). Gravity-induced confining stresses slow down the expansion rate of the detonation gases and restricts radial flow of ejecta, redirecting the blast momentum in the upward, vertical direction Figure 3.1d, 20 g, 30 g, 40 g-level) with resultant angular increases (Table 3.2). The blast momentum decays, and hence soil ejecta flow angles at elevated gravity approach a horizontal asymptote near 94° at 12 ms.

Table 3.2. Summary of soil ejecta dome diameters and flow angles for 1.0 gram C4 charge buried 5.1 cm and detonated at the 1 g, 20 g, 30 g, and 40 g-level.

		Soil Dome Diameter d (cm)						Soil Dome Ejecta Angle θ (deg)				
G-level N	DOB (cm)	d(t=6.7 ms) (cm)	d_0 (m/s)	$d(t), \theta(t) = A + B_1 t + B_2 t^2 + B_3 t^3$								θ(t=14.7 ms) (deg)
				A	B_1	B_2	B_3	A	B_1	B_2	B_3	
1	5.1	18.6	106.2	-19.83	18.20	-3.24	0.21	165.80	-15.02	0.85	-0.02	79.5
20	5.1	14.5	81.3	-13.62	9.38	-1.05	0.04	188.99	-17.12	1.05	-0.02	93.5
30	5.1	13.1	58.0	-14.62	8.22	-0.78	0.03	175.94	-11.93	0.57	-0.01	94.1
40	5.1	11.1	39.1	-19.83	8.77	-.079	0.03	172.56	-7.88	0.13	0.00	96.5

Note: d_o = initial soil ejecta diameter expansion rate.

3.3 Burial Depth Effects on Ejecta Rheology

To gain insight into the burial depth impact on disaggregation flow kinematics, a comparison of high-speed video images at three different burial depths (2.5 cm, 5.1 cm, and 7.6 cm) and a constant 30 g-level, are shown in Figure 3.7. Clearly apparent, soil dome heave expansion rates decrease significantly as burial depth increases.

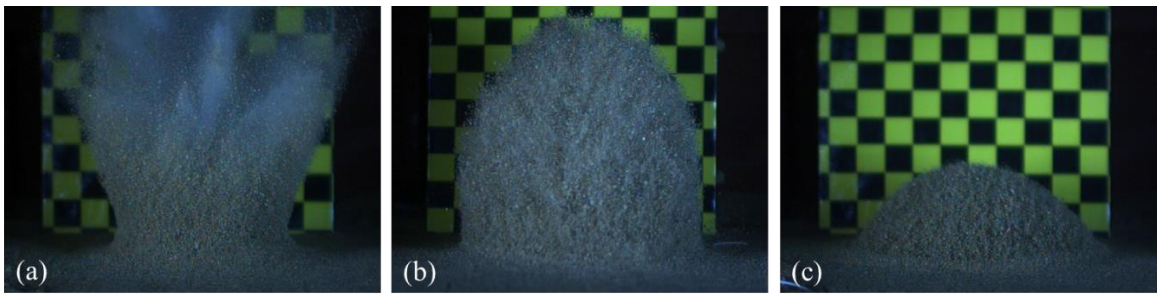

Figure 3.7. Comparison of soil deformations for 1.0 gram C4 charge detonated at the 30 g-level and buried (a) 2.5 cm (Time after detonation (TAD)=2.93 ms); (b) 5.1 cm (TAD=16.4 ms); and (c) 7.6 cm (TAD=23.7 ms).

The pronounced interaction of jetting gas-products (Rayleigh-Taylor instability [31]) and soil particulates appear significantly sooner at 2.93 ms after detonation for the shallowest 2.5 cm burial depth (Figure 3.7a). In contrast, at the 5.1 cm and 7.6 cm burial depths, the soil ejecta confines

the expanding gas products within an annulus at the later times 16.4 ms and 23.7 ms post-detonation, respectively (Figure 3.7b, c). Also noteworthy, the soil disaggregation and ejecta distribution observed at the 2.5 cm burial depth appears highly irregular and stochastic when compared to the deeper burial depths. At the 5.1 cm and 7.6 cm DOB, the soil dome heaves exhibit a more uniform, hemispherical contour and pronounced asymmetric, vertical flow directionality. In contrast, the ejecta flow field evidenced in the shallowest detonation (Figure 3.8a) exemplifies the classic inverted cone profile. These same *burial depth* dependent trends correlate to the previously discussed *gravity* dependent trends (Figure 3.1).

To further characterize the soil ejecta rheology and to differentiate between gravity and depth of detonation effects, initial vertical soil ejecta velocities are examined for a 1.0 gram C4 charge as a function of both test parameters (Figure 3.8).

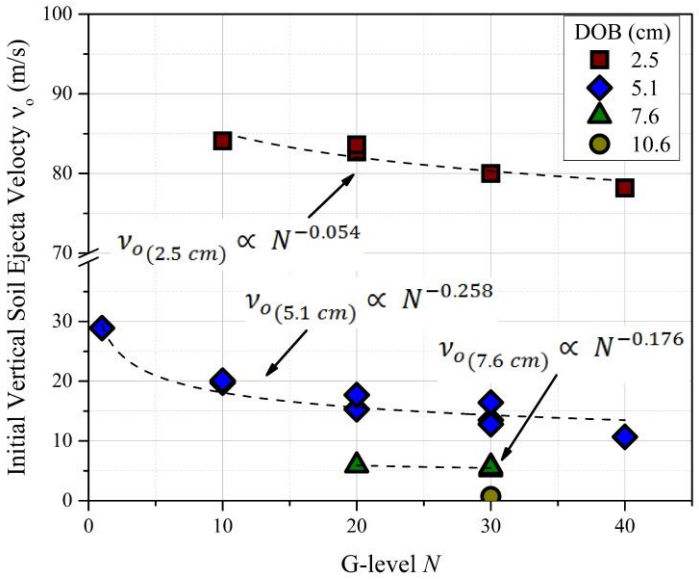

Figure 3.8. Initial vertical soil ejecta velocities versus g-level for a 1.0 gram C4 charge buried 2.5 cm, 5.1 cm, 7.6 cm, and 10.6 cm and detonated at multiple gravity levels. Initial vertical soil ejecta velocities derived by linear regression fit (*dashed-line*) to temporal evolution of vertical soil ejecta displacement over 3 ms interval.

As discussed previously, the initial vertical soil ejecta velocities decline as a function of increased g-level for a 1.0 gram C4 charge buried at 5.1 cm and best fit a power-law model (Figure 3.4). A comparison of the 5.1 cm results to the 2.5 cm and 7.6 cm DOB data sets exhibits the same trend: initial vertical soil ejecta velocities gradually decrease as a function of increased g-level independent of burial depth (Figure 3.8). A regression analysis determined the initial vertical soil ejecta velocity gravity-dependence at the 2.5 cm and 7.6 cm DOBs, are approximated by the following equations:

$$v_o(DOB = 2.5\ cm) \propto N^{-0.054} \tag{3.3}$$

$$v_o(DOB = 7.6\ cm) \propto N^{-0.176} \tag{3.4}$$

Furthermore, at the 10.6 cm burial depth and 30 g-level, the in-situ vertical stress level, comparable to a 0.32 m depth at normal gravity, results in the complete confinement of the blast phenomenon with minimal surface spallation. In this case, the explosion transmits kinetic energy to the soil matrix and forms a camouflet, encompassed by pulverized grains and highly-compressed soil. Table 3.3 summarizes mean initial vertical soil ejecta velocities for a 1.0 gram C4 charge as a function of burial depth at varying g-levels.

Table 3.3. Mean initial vertical soil ejecta velocities as a function of burial depth (DOB) and g-level for a 1.0 gram C4 charge detonation.

G-level	Burial Depth (cm)			
	2.5	5.1	7.6	10.6
1		28.9		
10	84.1	21.1		
20	83.6	15.3	5.9	
30	80.0	13.5	5.5	0.1
40	78.2	10.7		

Note: inset mean initial vertical soil ejecta velocity values have units of ms^{-1}.

As expected, the results substantiate that shallow-buried charges consistently induce higher initial vertical soil ejecta velocities compared to deeper burial depths for all g-levels tested. Within the data sets, the results evidence less variance as a function of g-level and fixed DOB when compared to the significant difference in ejecta velocities between data sets for a constant g-level and varied DOB. Here, the data confirms the trend that initial vertical soil ejecta velocities decrease as a function of increased g-level, independent of burial depth. The data also shows that gravity's impact on initial vertical ejecta velocities remains less significant when compared to burial depth effects in the tested g-level range.

Chapter 4 Crater Morphology

The experimental results of multiple test series clarify gravity's influence on the cratering phenomenon. Blast-excavated crater morphology strongly depends on soil overburden pressure, explosive energy released, and in-situ soil cohesion and strength. Soil ejecta fallback, soil density, burial depth, and charge orientation constitute second-order effects on the final crater. Figure 4.1 effectively illustrates the gravity, or soil confinement, effects on blast-excavated cratering for a constant charge size (1.0 gram C4) and burial depth (5.1 cm) at 1 g, 20 g, 40 g, and 50 g-levels.

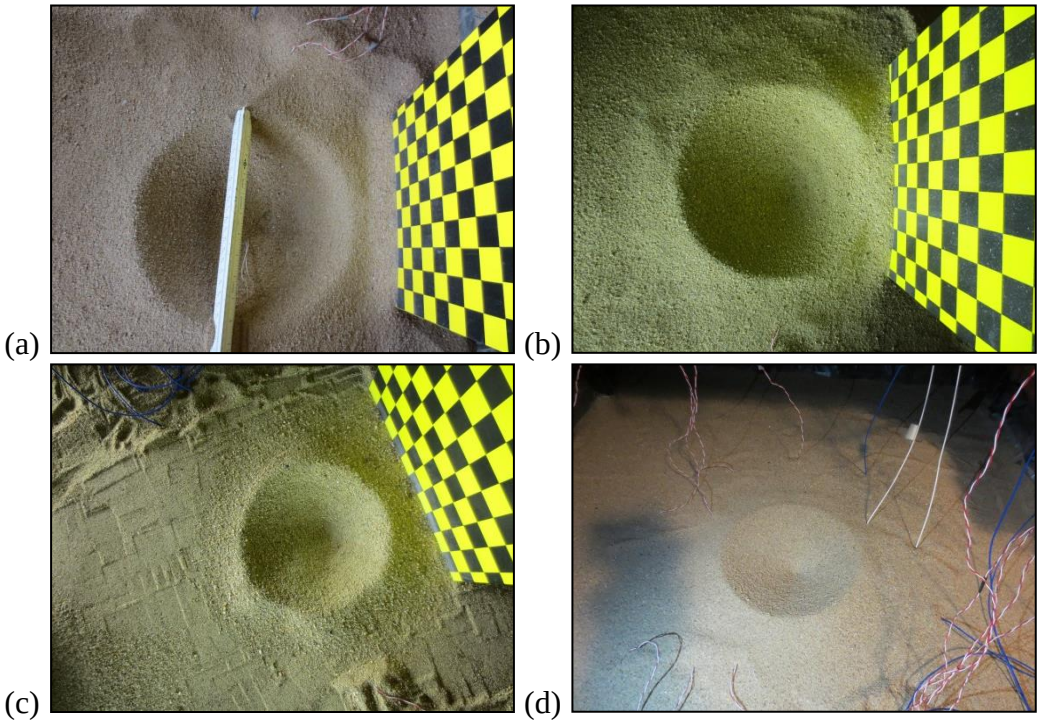

Figure 4.1. Top view of blast-excavated final craters for 1.0 gram C4 charge buried 5.1 cm and detonated at g-levels: (a) 1 g; (b) 20 g; (c) 40 g; (d) 50 g.

The crater profiles illustrate that peak crater dimensions occur at 1 g and decline with increased gravity imposed overburden stress. All the observed final craters shown in Figure 4.1a-d resemble inverted right cone geometries and consistently maintain that shape throughout each test,

independent of g-level. The observed dimensional changes in crater formation, as a function of gravity, can attribute to the in-situ variation of gravity-induced shear resistance in dry soils.

The LMI Gocator surface profilometer representative laser measurement scans (1,280 points/line), as shown in Figure 4.2, correspond to a specific test delineated above (1.0 gram C4, 5.1 cm DOB, 50 g (Figure 4.1d)).

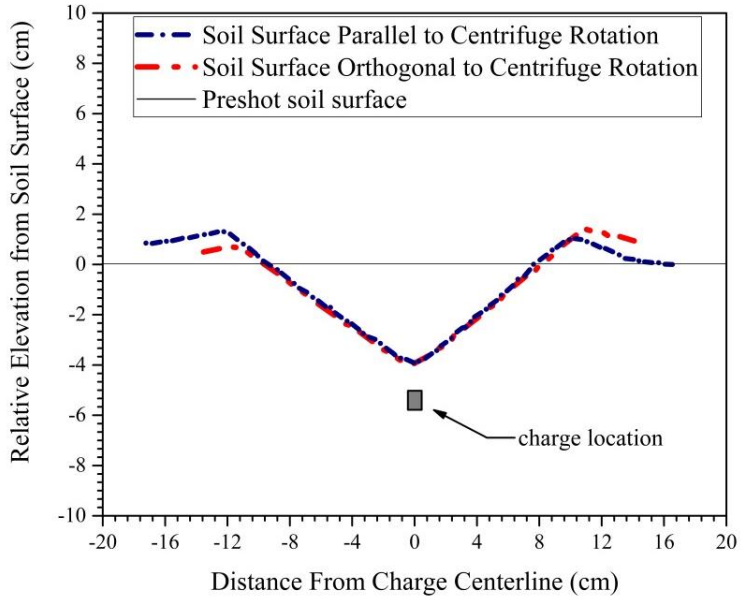

Figure 4.2. Cross-sectional scan employing laser line profilometry of a final crater subsequent 1.0 gram C4 charge buried 5.1 cm and detonated at the 50 g-level.

The consequent final crater outlines display a distinct V-shape, hyperbolic profile with a slightly rounded apex. By superimposing the scans of the cross-sectional splices, one imaged parallel and the other orthogonal to the direction of centrifuge rotation, the two crater profiles show minimal variation only in the crater lip region. The slight horizontal skewness between the two profiles varied nominally 8.4 mm. The difference between the crater lip heights varied by only 2.7 mm. The congruent final crater included angles both measured 66.3° at 50 g's. The coincident profiles strongly convey axisymmetric final craters.

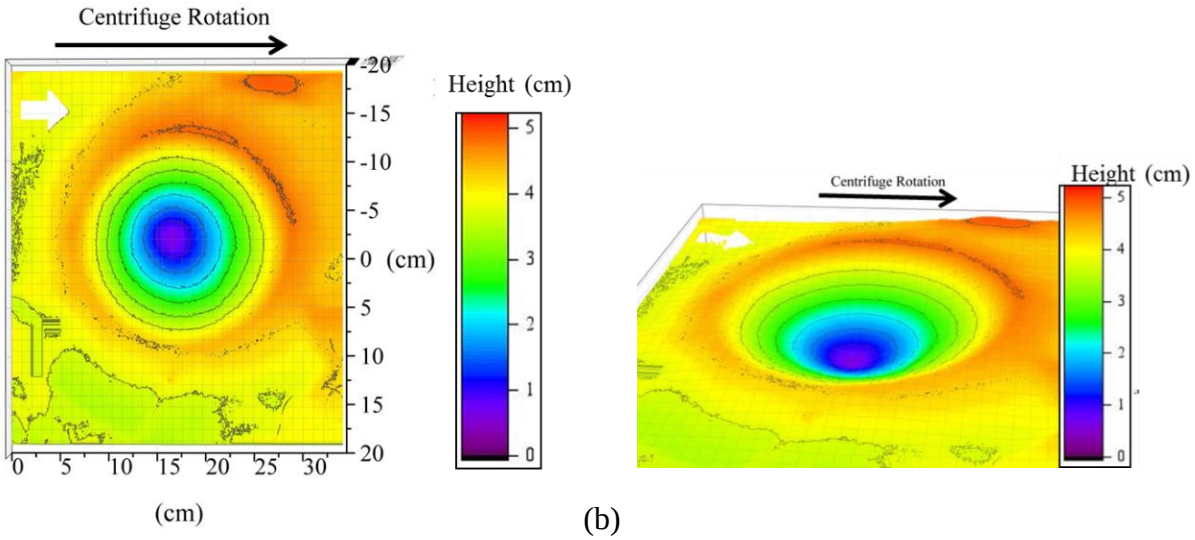

(a) (b)

Figure 4.3. Measurement scans employing laser line profilometry of a final crater subsequent 1.0 gram C4 charge buried 5.1 cm and detonated at the 50 g-level. Views: (a) perspective from axis of centrifuge rotation *in-flight*; (b) oblique. Arrow points towards the direction of laser travel and centrifuge rotation.

Furthermore, cross-sectional profiles captured at 51 μm intervals along the profilometer's travel axis and stitched sequentially together, permitted visual upscaling of 2D planar crater profiles into a highly-resolved, 3D space (Figure 4.3a, b). The topographic view (Figure 4.3a) reveals concentric elevation changes with only minor deviations. In addition, the isometric projection (Figure 4.3b) displays smooth gradients with rounded contours, and further confirms final crater axial symmetry. In most cases, final craters exhibited axial symmetry and defined slopes, despite changes in charge size, g-levels, or burial depth. A numerical integration of the 3D crater surface area by a trapezoidal iteration method yields a final crater volume of 419.7 cm^3. The axisymmetric crater profiles in this research indicate that centrifugal air flow, ambient vibrations, and Coriolis effects remain negligible in crater formation within the tested g-level range. To dynamically assess crater stability post-detonation, a compact video camera positioned above the buried charge, monitored final craters in real-time, subsequent blast excavation and centrifuge spin-down. As

expected in a granular, cohesionless soil, crater slopes appeared stable with no discernable settling or slumping during centrifuge deceleration.

A quantitative analysis of model-scale final crater volume *V,* radius *R*, and depth *H* as a function of elevated g-level, for a constant charge size (1.0 gram C4) and burial depth (5.1 cm), confirms the previously discussed initial vertical soil ejecta velocity trends: gravity-induced confining stresses also significantly impact blast-excavated crater formation. The data again approximates a power-law dependence on g-level as plotted in Figure 4.4.

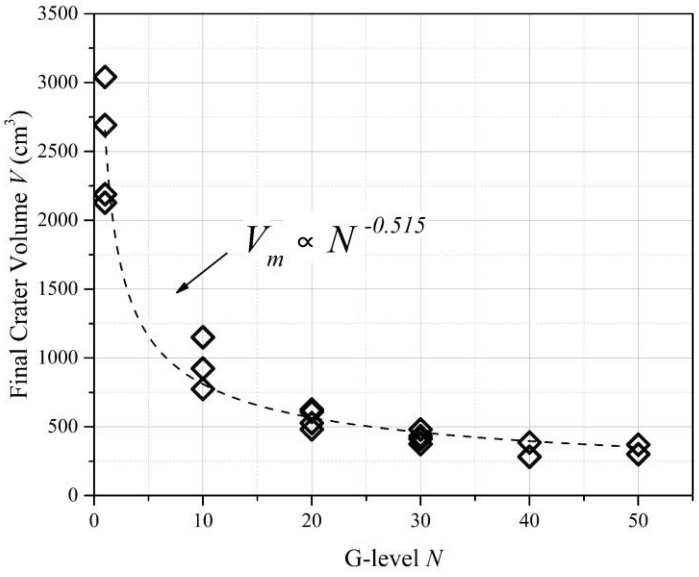

(a)

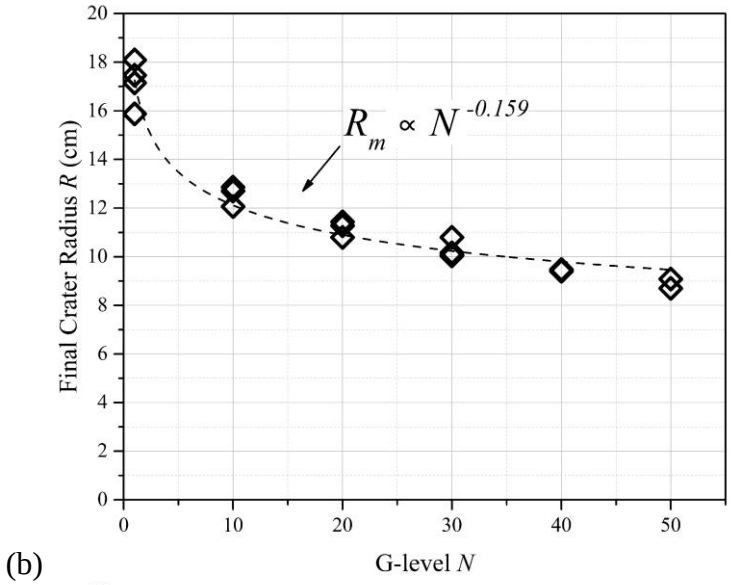

(b)

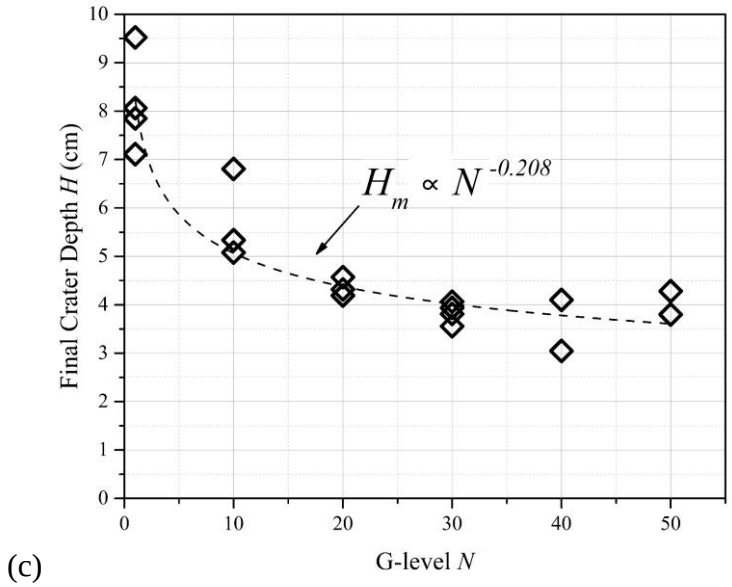

(c)

Figure 4.4. Model-scale final crater dimensions (a) volume; (b) radius; and (c) depth as a function of g-level subsequent detonation of 1.0 gram C4 charge buried 5.1 cm. *Dashed-line* represents best-fit derived from power-law regression analysis. Coefficients of determination (R^2) measured: 0.955 (volume), 0.964 (radius), and 0.886 (depth). Plots comprised of seventeen tests.

Observed in all three plots, as g-level increases, crater dimensions decrease, indicating a monotonic inverse relationship. Furthermore, final crater measurements evidence considerable repeatability throughout the g-level range tested (Figure 4.4). This repeatability, statistically quantified by 95% confidence intervals (Table 4.1), shows nominal deviation of final crater

measurements from the sample mean and validates test methods. The results demonstrate better reproducibility on the centrifuge when compared to the apparent scatter exhibited in the 1 g-level test series (Figure 4.4).

The derived relationships between model final crater dimensions and g-level *N* are:

$$V_m \propto N^{-0.515} \quad (4.1)$$

$$R_m \propto N^{-0.159} \quad (4.2)$$

$$H_m \propto N^{-0.208} \quad (4.3)$$

and demonstrate that final crater dimensions also display a nonlinear reduction subsequent higher gravity-induced stresses. The data again shows a significant decrease between the 1 g and 10 g-levels, followed by the expected gradual asymptotic decline.

Mean crater dimensions for the g-level dependent tests (Table 4.1) include model and prototype scale with uncertainties of two standard deviations.

Table 4.1. Summary of mean blast-excavated final crater dimensions in *model* and *prototype* scale subsequent 1.0 gram C4 charge buried 5.1 cm and detonated at corresponding g-levels: 1 g, 10 g, 20 g, 30 g, 40 g, and 50 g.

	Mean Final Crater Dimensions								
	Model Scale				*Prototype* Scale				
G-level *N*	Radius *R* (cm)	Depth *H* (cm)	Volume *V* (cm^3)	Slope (α)* (deg)	Charge size (kg)	Burial Depth (m)	Radius (m)	Depth (m)	Volume (m^3)
1	17.1 ± 0.92	8.1 ± 0.99	2480.3 ± 425.01	25.3					
10	12.5 ± 0.48	5.7 ± 1.06	932.7 ± 213.87	24.6	1.0	0.51	1.3	0.6	1.1
20	11.0 ± 0.43	4.4 ± 0.21	557.5 ± 66.53	21.8	8.0	1.02	2.2	0.9	4.6
30	10.3 ± 0.52	3.8 ± 0.21	422.2 ± 43.16	20.3	27.0	1.53	3.1	1.1	11.1
40	9.4 ± 0.07	3.8 ± 1.03	351.6 ± 100.94	20.0	64.0	2.04	3.8	1.5	22.7
50	8.9 ± 0.37	3.9 ± 0.47	323.5 ± 66.63	23.7	125.0	2.55	4.5	2.0	42.4

* Slope refers to the crater wall angle with respect to the horizontal.
± *95% confidence interval*

The results show that the maximum model-scale final crater dimensions significantly decrease as a function of gravity-induced overburden stress. Mean final crater volumes decrease 87% from 1 g to 50 g, radius and depth by 48% and 52%, respectively. The crater parameter depth gradually decreases consequent increased acceleration up to the 30 g-level. At this point, increased gravity appears to have a nominal impact on crater depth. The known sensitivity to confining pressure on the dynamic in-situ shear modulus can explain this observed behavior. The final crater wall angles, defined as $\tan \alpha = H/R$, progressively decrease until the 50 g-level and exhibit an inverse relationship with g-level.

Assuming dynamic similitude and equivalent soil constituent properties, the model-scale charge (1.0 gram C4), burial depth (5.1 cm), and crater dimensions extrapolate to prototype conditions via centrifuge scaling relationships as shown Table 4.1. The results evidence self-consistency and verify the expected trend that charge size and crater dimensions vary proportionally in prototype scale. In a later section, a comparative analysis of this study's empirical scaling relationships to past field tests demonstrates that small-scale laboratory tests using centrifuge scaled modeling simulates larger physical explosive yields.

Table 4.2 summarizes the derived power-law exponents relating model-scale final crater dimensions to g-level plotted in Figure 4.4. The table also includes the functional relationships between final crater dimensions and gravity reported by Schmidt and Holsapple [35] and Goodings et al. [37].

Table 4.2. Comparison of power-law relationships for model-scale final crater dimensions subsequent centrifuge soil blast excavation.

	Current Study (2016)	Schmidt and Holsapple [35] (1978)	Goodings et al. [37] (1988)
$V_m \propto N^{-\gamma}, \gamma$	0.515	0.472	0.48
$R_m \propto N^{-\alpha}, \alpha$	0.159	0.159	0.14
$H_m \propto N^{-\alpha}, \alpha$	0.208	0.164	0.17

Note: Subscript *m* stands for model-scale; *N* denotes g-level.

The power-law relationships for model-scale crater dimensions derived in this study that used fully buried charges, different explosive types and in-situ soil conditions, still demonstrate close agreement to those reported by Schmidt and Holsapple [35] and Goodings et al. [37]. This suggests the absence of gravity related scale effects over a wide range of g-levels (1 g to 451 g) and further substantiates the ability of the centrifuge scale modeling technique to alter crater morphology by changing a single parameter, *gravity*.

4.1 Burial Depth Effects on Crater Morphology

To gain further insight into soil blast mechanics, the parametric analysis includes charge burial depth. The gravity-scaled crater volume comparison plot (Figure 4.5) demonstrates the expected trend: as gravity-scaled explosive mass increases, scaled crater volumes also increase. The highest dimensional values correspond to the largest scaled explosive mass. In addition, at a fixed charge size, the burial depth dependence displays parabolic-like curves, in contrast to the monotonic, inverse gravity-dependent curve as shown in Figure 4.4.

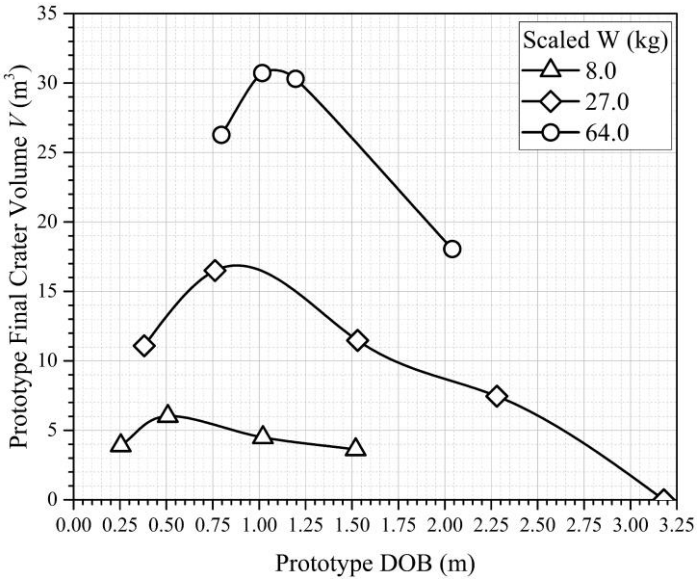

Figure 4.5. Prototype final crater volumes as a function of prototype burial depth and explosive mass for a model-scale 1.0 gram C4 charge.

As anticipated, at the shallowest buried depths, charges with less overlying soil and confining pressure eject a smaller volume of soil and thus yield reduced crater dimensions when compared to deeper burial depths. As the distance from the charge to the soil-interface gradually increases, less energy dissipates to the air and more propagates through the medium [37]. This energy transfer mechanism results in greater cratering efficiency up to a transitional point. At the apex of the curve (Figure 4.5), maximum mean crater volumes correspond to a test specific, intermediate, or "optimum" scaled burial depth, approximately 0.5 m, 0.9 m, and 1.1 m with increasing scaled explosive mass.

Subsequent this optimum burial depth, the amount of spallation diminishes as the blast energy (compressive shock wave and expanding detonation products) rapidly decreases and appears progressively ineffective relative to the increasing soil overburden pressure. As a result, mean crater dimensions significantly decrease as a function of increasing burial depths (Figure 4.5), in contrast to the asymptotic gradual decline as a function of gravity alone (Figure 4.4). At the

deepest burial depth (3.18 m, 27 kg), the blast loading no longer exceeds the tensile strength of the overburden pressure and thus induces a camouflet with minimal soil-surface disturbance.

4.2 Soil Ejecta Kinematics Coupled to Final Crater Dimensions

A dimensional analysis, performed to better understand the interrelated *physical dynamics* and *statics* intrinsic to soil blast mechanics, correlates initial vertical soil ejecta velocity to blast-excavated crater morphology. The derived dimensionless relationships coupling soil ejecta velocity (v_o) to crater volume (V), radius (R), and depth (H), inclusive of gravity (g), burial depth (D), initial soil density (ρ), and charge mass (W), are represented by the following equations:

$$\frac{v_o}{\sqrt{g}}\left(\frac{\rho}{W}\right)^{1/6} = F_V\left(\frac{V}{D^3}\right)^{m_V} \tag{4.4}$$

$$\frac{v_o}{\sqrt{g}}\left(\frac{\rho}{W}\right)^{1/6} = F_R\left(\frac{R}{D}\right)^{m_R} \tag{4.5}$$

$$\frac{v_o}{\sqrt{g}}\left(\frac{\rho}{W}\right)^{1/6} = F_H\left(\frac{H}{D}\right)^{m_H} \tag{4.6}$$

The coefficients (F) and exponents (m), determined by regression analysis, denote a simple, new coupling function to the specific experimental results. A synthesis of the data for various charge sizes, burial depths, and g-levels, in nondimensional, log-log scale (Figure 4.6 a-c) adheres best to a power-law fit.

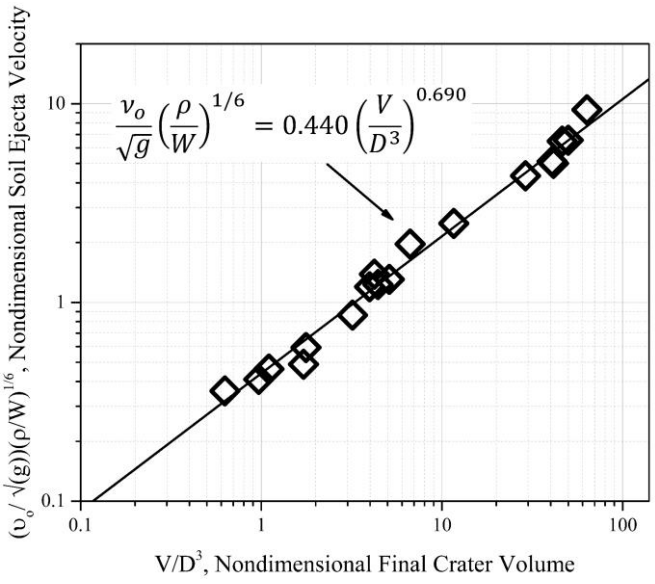
$\frac{v_o}{\sqrt{g}}\left(\frac{\rho}{W}\right)^{1/6} = 0.440\left(\frac{V}{D^3}\right)^{0.690}$
$(\upsilon_o/\sqrt{(g)})(\rho/W)^{1/6}$, Nondimensional Soil Ejecta Velocity
V/D^3, Nondimensional Final Crater Volume
0.1
1
10
100

(a)

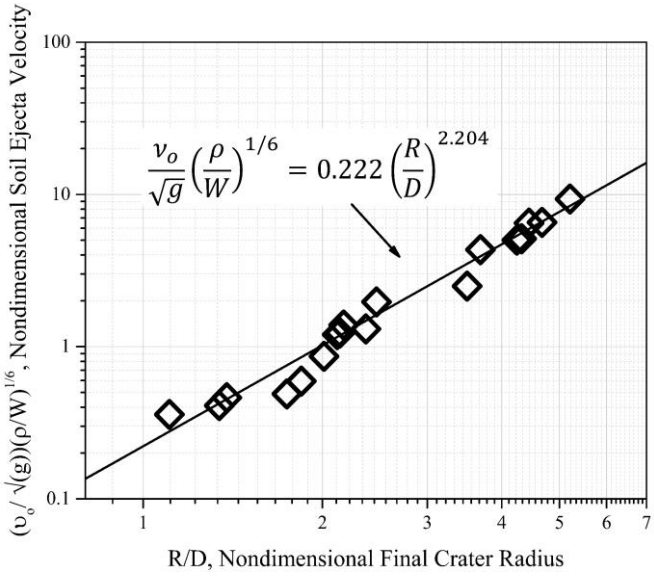
$\frac{v_o}{\sqrt{g}}\left(\frac{\rho}{W}\right)^{1/6} = 0.222\left(\frac{R}{D}\right)^{2.204}$
$(\upsilon_o/\sqrt{(g)})(\rho/W)^{1/6}$, Nondimensional Soil Ejecta Velocity
R/D, Nondimensional Final Crater Radius
0.1
1
10
100
1
2
3
4
5
6
7

(b)

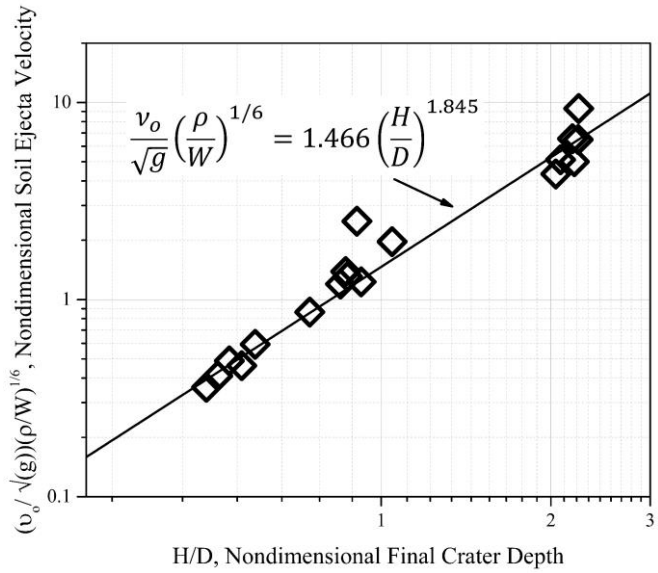

(c)

Figure 4.6. Dimensionless comparison of initial vertical soil ejecta velocities and final crater (a) volume; (b) radius; and (c) depth, for multiple gram size C4 charges buried and detonated at various depths and g-levels in log-log scale. Best-fit regression lines included (*solid-line*).

The data clearly shows the expected trend: at a fixed g-level and burial depth, crater dimensions vary proportionally to initial vertical soil ejecta velocities. The self-consistency and similarity in soil behavior between the dynamic and static relationships to the data indicates the suitability of these dimensionless functional relationships (Eqns. 4.4-4.6) to physically characterize both soil ejecta velocities and final crater dimensions concisely.

4.3 Analysis of Dimensional and Dimensionless Scaling Relationships

The cratering dimensional dependence on explosive mass is analyzed using the empirical cube-root scaling relationship with scaled explosive mass normalized to TNT equivalents [51]. The test parameters include multiple explosive weights (69 mg, 203 mg, 530 mg, and 1.0 gram C4), detonated at varying g-levels (1 g to 50 g) under different soil overburdens (1.3 cm to 7.6 cm) with soil conditions and explosive type constant.

This study's empirically derived, power-dependent relationships between prototype (*'p'*) crater dimensions (meters) and charge weight *W* (kg) are:

$$V_p \propto W^{0.829} \tag{4.7}$$

$$R_p \propto W^{0.282} \tag{4.8}$$

$$H_p \propto W^{0.269} \tag{4.9}$$

These empirical relationships and this study's data presented in Figure 4.7 depict the expected monotonic relationship: crater volume, radius, and depth increase as a function of gravity-scaled explosive mass. Furthermore, to analyze the suitability of conventional cube-root energy scaling methods to predict full-scale crater efficiency, the field test series Ehrgott, Bergeron et al., and Vortman were selected as a suitable set of comparable data because their works also used fully-buried charges detonated in a dry sand [6,8,27]. Rooke et al. field test series were also chosen to compare cratering in moist sand [28].

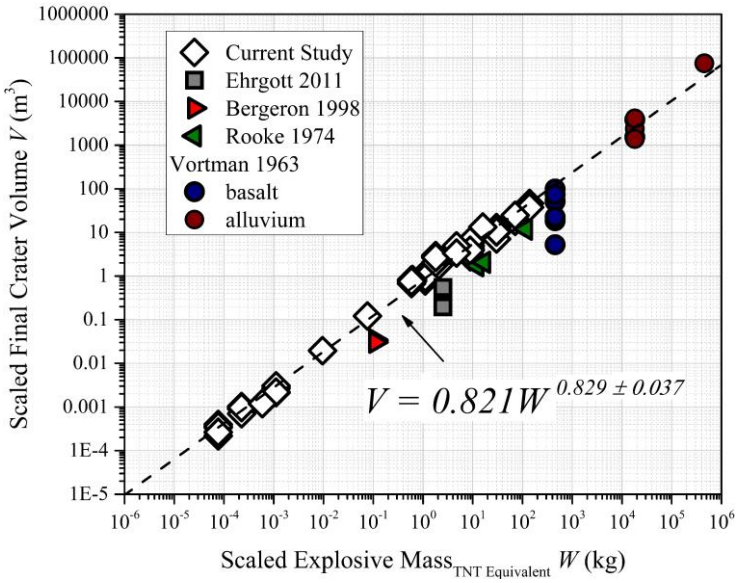

(a)

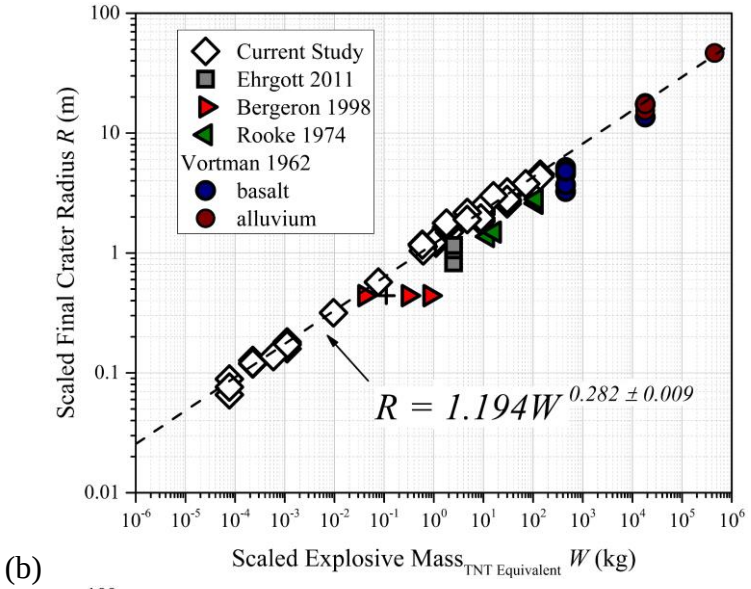

(b)

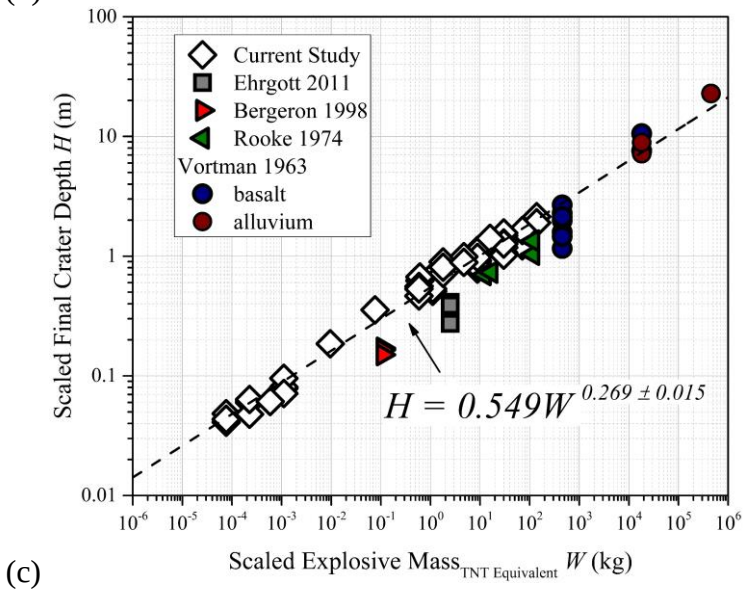

(c)

Figure 4.7. Comparison of scaled final crater (a) volumes *V*, (b) radii *R*, and (c) depths *H*, as of function of scaled TNT mass equivalent to past larger scale soil blast works plotted in *log-log* scale. Power-law regression best-fit curves derived from this study's measurements shown as *dashed-lines*.

As shown in all three comparison plots (Figure 4.7a, b, c), this study's results evidence close adherence to the included power-law regression curves, and thus, demonstrate self-consistency throughout the range of scaled explosive masses spanning six orders of magnitude. This repeatability, quantified by coefficients of determination (R^2) values (crater volume, radius, and depth: 0.992, 0.993, and 0.978, respectively), indicates nominal variance from the statistical mean.

Furthermore, the cratering dimensional dependence on explosive mass from this study's experimental data in prototype scale displays reasonable agreement to the past field tests (Figure 4.7). For example, Vortman detonated 450 kg, 18,143 kg, and 453,000 kg TNT charges in desert alluvium sand and basalt rock [6]. This full-scale test series defines the upper explosive mass limit and yields the maximum final crater dimensions. In spite of geologic differences, excavated crater profiles in desert alluvium soil (Vortman [6]) and bedrock (Rooke [28]) closely approximate this research's regression line. In addition, Ehrgott [8] and Bergeron et al. [27] used a single charge size (2.27 kg and 100 grams C4, respectively) and their findings correlate reasonably well to this work's mid-range data cluster. The apparent data scatter between the respective field tests and their dissimilarities to this study's results can attribute to differences in explosive mass and chemistry, soil conditions, burial depths, and measurement methods.

The power-dependence on explosive mass derived from this study's experimental data (Eq.4.7-4.9) is compared to the past centrifuge and field test yield exponents '*n*' (Figure 4.7).

Table 4.3. Comparison of scaled yield exponent, *n*, for buried blasts in soil.

	Current Study (2016)[a]	Brownell et. al (1992)[a]	Goodings et. al (1988)[a]	Schmidt et al. (1978)[a]	Rooke et al. (1974)[b]	Vortman (1962)[b]	
	Mason sand, dry	Beach sand, dry	Ottawa sand, dry	Ottawa sand, dry	sand, moist	basalt, dry	alluvium, dry
$V_p \propto W^n$	0.829	0.831	0.84	0.842	0.874	1.018	1.072
$R_p \propto W^n$	0.282	0.297	0.29	0.280	0.302	0.305	0.317
$H_p \propto W^n$	0.269	0.279	0.28	0.279	0.237	0.381	0.326

Note: Subscript *p* stands for prototype; Test environment: [a]centrifuge; [b]field

Clearly, the conventional method of cube-root energy scaling to predict larger scale yields approximates the cratering phenomenon quite well. However, as shown in Table 4.3, the cube-

root scaling relationships, in all centrifuge studies, underestimate the power dependence on crater radius and depth. Furthermore, all linear crater dimension exponents appear consistently higher than the quarter-root, gravity scaling method. This research's data indicates that radius and depth power-dependence on the buried charge's weight more closely approximates $W^{1/3.5}$ and $W^{1/3.7}$, respectively, due to the inclusion of lithostatic pressure effects on cratering mechanics.

Next, the dimensionless Π groups are evaluated for performance and applicability to the buried blast cratering phenomena [35,36]. Their dimensionless crater dependent π terms, or cratering efficiency, are:

$$\pi_V = \frac{V\rho}{W} \tag{4.10}$$

$$\pi_R = R\left(\frac{\rho}{W}\right)^{\frac{1}{3}} \tag{4.11}$$

$$\pi_H = H\left(\frac{\rho}{W}\right)^{\frac{1}{3}} \tag{4.12}$$

where ρ and W denote the initial soil density and charge mass, respectively.

In addition, the dimensionless, independent gravity-scaled yield parameter π_2, dependent upon explosive properties, g-level, and charge weight, can be expressed as:

$$\pi_2 = \left(\frac{g}{Q}\right)\left(\frac{W}{\delta}\right)^{1/3} \tag{4.13}$$

where g denotes g-level; $Q$and δ represent the explosive's specific heat and density, respectively. This π group enables comparisons of non-similar experiments to different scaled yields for a given charge size and explosive type. This study's data in dimensionless form demonstrates reasonable adherence to a power-law fit as shown in Figure 4.8. The empirical relationships reveal the

expected inverse proportionality: as gravity scaled yield (π_2) increases, volume cratering efficiency (π_V) decreases.

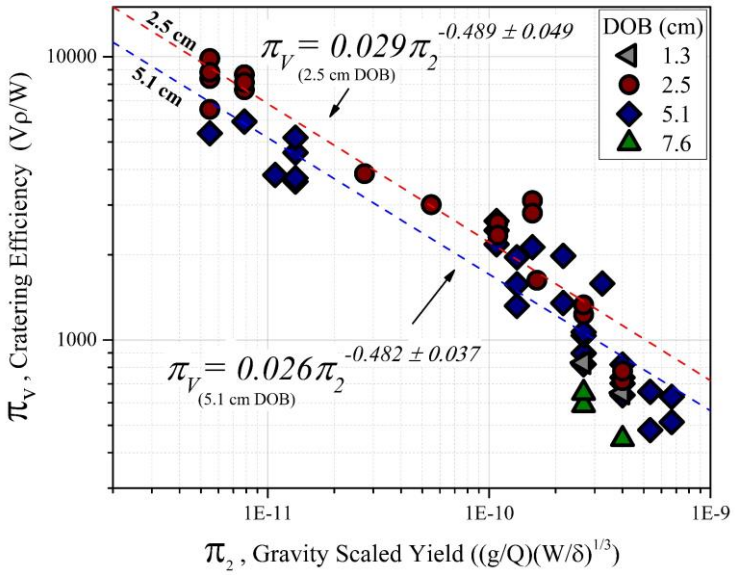

Figure 4.8. Volume crater efficiency π_V as a function of gravity scaled yield π_2 in *log-log* scale. Data corresponds to buried charge detonations of various gram size C4 charges at multiple g-levels. Power-law regression curves included (*dashed-lines*) for burial depths 2.5 cm (R^2=0.924) and 5.1 cm (R^2=0.863). For all tests, δ = 1770 kgm^{-3} and Q = 6.19 x10^6 m^{2}s^{-2}.

The two power-law regression curves appear nearly parallel, substantiated by the closeness of the power exponents: -0.489 and -0.482 for the 2.5 cm and 5.1 cm burial depths, respectively. The 2.5 cm DOB data line represents the highest volume cratering efficiency for all values of π_2, and the deeper 5.1 cm DOB corresponds to lower cratering efficiency values. This trend continues with the deepest 7.6 cm burial depth equating to the lowest crater volume efficiencies for π_2=2.5E-10 and π_2=4E-10. The soil behavior can attribute to the gravity-induced increase in shear strength consequent matrix stiffening which inhibits crater volume expansion. Note that the shallowest burial depth (1.3 cm) and equivalent π_2=2.5E-10 and π_2=4E-10, π_V shows intermediate values relative to the 2.5 cm and 5.1 cm burial depths and indicates that the crater efficiency dependence on burial depth is not monotonic. The DOB can be altered to optimize the volume of soil ejected

from the crater with resultant increased cratering efficiency [4,33]. The self-consistency observed in the examined gravity scaled yield regime suggests negligible adverse scaling effects and the relevance of the dimensionless π_2 parameter.

Table 4.4 summarizes the power-law exponents (α) and constants (c) derived from a regression analysis of the 2.5 cm and 5.1 cm burial depth results (Figure 4.8) and includes the experimentally determined π relationships reported by Schmidt and Holsapple [35] and Goodings et al. [37].

Table 4.4. Comparison of the π-group first order, least-square fit parameters α and c.

	Current Study (2016)				Schmidt and Holsapple [35] (1978)		Goodings et al. [37] (1988)	
	2.5 cm DOB		5.1 cm DOB		half-buried		half-buried	
	α	c	α	c	α	c	α	c
$\pi_V {\pi_2}^{\alpha} = c$	0.489	0.029	0.482	0.026	0.472	0.194	0.452	0.023
$\pi_r {\pi_2}^{\alpha} = c$	0.166	0.351	0.143	0.575	0.159	0.765	0.147	0.409
$\pi_h {\pi_2}^{\alpha} = c$	0.158	0.222	0.196	0.074	0.164	0.154	0.220	0.023

In all three studies, the crater dependent yield exponents demonstrate close correspondence and thus indicate similar soil blast mechanics and consequent crater formation despite varying test parameters, specifically lithostatic pressure, which can explain the variation between the exponents reported in this study compared to Schmidt and Holsapple [35] and Goodings et al. [37].

The previous dimensionless analysis of the classical Π term relationships derived for surface-tangent burst in past studies (Table 4.4) compared favorably to this work's empirical relationships and further confirms the suitability of the Π terms to simulate larger explosive yields. Here, a new dimensionless parameter, π_κ, written in the form

$$\pi_\kappa = \pi_V + \pi_D \tag{4.14}$$

refines the volume cratering efficiency parameter, π_V (Equation 4.10), to incorporate soil overburden effects through inclusion of a constituent term, π_D, defined as

$$\pi_D = N \left(\frac{D}{a_W}\right) \tag{4.15}$$

The addition of the gravity scale factor, N, explosive diameter, a_W, and burial depth, D, a key parameter in the dimensionless analysis, allows an enhanced characterization of sub-surface detonations at elevated gravity. For surface blast excavations, the classical volume cratering efficiency term, π_V, remains unchanged, as π_D equals zero and π_κ simplifies to π_V. An empirical relationship between π_κ and π_2, derived from a power-law regression fit to this study's empirical data, approximates the following equation

$$\pi_\kappa \pi_2^{0.446} = 0.074 \tag{4.16}$$

The power-law relationships, summarized in Table 4.4, in conjunction with and the new dimensionless term, π_κ (Equation 4.14), are plotted in Figure 4.9 which now includes the data reported by Brownell and Charlie [38], Gill and Kuennen [39], and Shim [40].

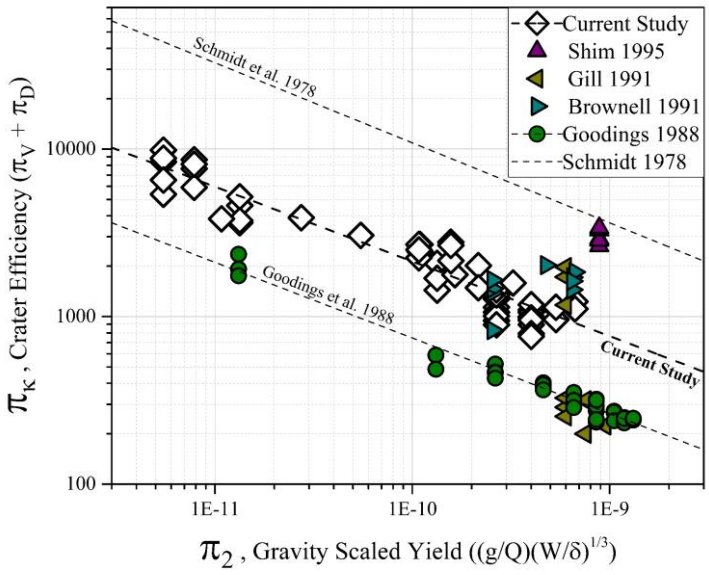

Figure 4.9. Comparison of volume cratering efficiency π_κ as a function of π_2 in *log-log* scale for multiple centrifuge soil blast studies. *Dashed-lines* indicate power-law regression curves.

The comparison plot (Figure 4.9) depicts this compilation of centrifuge soil blast data extending roughly four orders of magnitude of gravity-scaled yields. In general, the data shows progressively smaller values of π_κ as π_2 increases, consistent with the cratering efficiency dependent trend characterized in Figure 4.8. As anticipated, due to the close correspondence evidenced in the power-law exponents (Table 4.4), the Schmidt and Holsapple [35] and Goodings et al. [37] best fit lines appear nearly parallel to this study's regression curve. However, the Schmidt and Holsapple line corresponds to higher crater efficiencies for equivalent gravity-scaled yields when compared to all the other represented centrifuge studies. This can attribute to the higher g-levels and charge sizes included in their π_2 calculations as well as differences in their soil's unit weight. Gill and Kuennen [39] also measured blast excavated craters in a dry soil using surface-tangent charges and three subsurface charges. Their subsurface tests are in close agreement to this study's data, reflecting similar DOBs and g-levels. Similarly, the dry sand crater efficiencies reported by Brownell and Charlie [38] remain coincident to this study's regression line. However, the matrix

suction in their partially saturated soil induced slightly higher crater efficiencies relative to this study. Moreover, Shim [40] reported that final crater dimensions measured greater in a saturated soil, hence, their volume cratering efficiencies remain consistently higher when compared to this research. The new π_κ term refines the classical π_V parameter to include lithostatic effects and provides direct comparisons across studies of different material types and test configurations.

4.4 Final Crater Modeling of Models Analysis

The experimental validation of the previously examined scaling relationships to confirm their suitability can be established by direct comparisons of the model and full-scale conditions. However, these larger scale tests evidence unavoidable data scatter. A viable alternative method, known as 'modeling of models', facilitates scaling validation by testing models of different scales in a controlled environment that physically simulate the same prototype performance via functional scaling relationships (Table 2.1, Eqns. 4.10-4.14). Dynamic similitude requirements dictate that soil constitutive properties remain constant with quantitative agreement between the independent terms π_2 and π_3 for all models tested, thereby yielding similar values of π_V [36]. Schmidt and Holsapple [36] and Goodings et al. [37] performed modeling of models experiments to validate scaling relationships (Π groups) for final crater dimensions. However, in both studies, the DOB-dependent parameter π_3 remained constant and zero. Therefore, an experimental gap exists in the dynamic similitude analysis that includes soil-confined charges. To address this void, the experimental results of two test series verify this study's adherence to modeling of models for non-zero DOBs. The systematic analysis involved experiments of distinctly different and

arbitrarily-chosen burial depths, explosive masses, and g-levels that effectively model the same prototype condition.

The first test series used a 69 mg C4 charge buried 2.5 cm and detonated at the 20 g-level. To satisfy the similitude criterion for the independent parameters π_2 and π_3, the second test consisted of a 530 mg C4 charge buried 5.1 cm and detonated at 10 g's. The resultant volume cratering efficiency π_V with increasing charge size measured 2437.4 and 2386.6, yielding a difference of 2.8%. This lies within an admissible variance and thus confirms dynamic similitude. A second set of tests designed to confirm the dynamic similarity requirements specific to the burial depth dependent parameter π_3 varies explosive chemistry by using Detasheet charges instead of C4. The first test parameters: 1.2 gram charge, 5.6 cm burial depth, and 30 g's, dictated the second test variables: 2.8 gm charge, 7.5 cm burial depth, and 22.3 g's to ensure similitude compliance. For this test series, volume crater efficiency π_V equaled 1259.5 (1.2 gm) and 1290.2 (2.8 gm), a difference of 2.3%. Once again, the results validate dynamic similarity between two distinctly different buried-blast tests within minimal experimental deviation.

Table 4.5 summarizes the specific experimental parameters and the corresponding π_V, π_2, and π_3 values. Figure 4.10 illustrates the coherence between test series.

Table 4.5. Summary of π group dynamic similitude analysis.

Test	Charge size (gm)	DOB (cm)	G-level	Charge Comp.	$\pi_V = \frac{V\rho}{W}$	$\pi_2 = \left(\frac{g}{Q}\right)\left(\frac{W}{\delta}\right)^{1/3}$	$\pi_3 = DOB\left(\frac{\rho}{W}\right)$
1	0.07	2.5	20	C4	2368.6	1.1 *E-10*	7.3
	0.53	5.1	10	C4	2437.4	1.0 *E-10*	7.5
2	1.2	5.6	30	Detasheet	1259.5	4.2 *E-10*	6.3
	2.8	7.5	22.3	Detasheet	1290.2	4.2 *E-10*	6.3

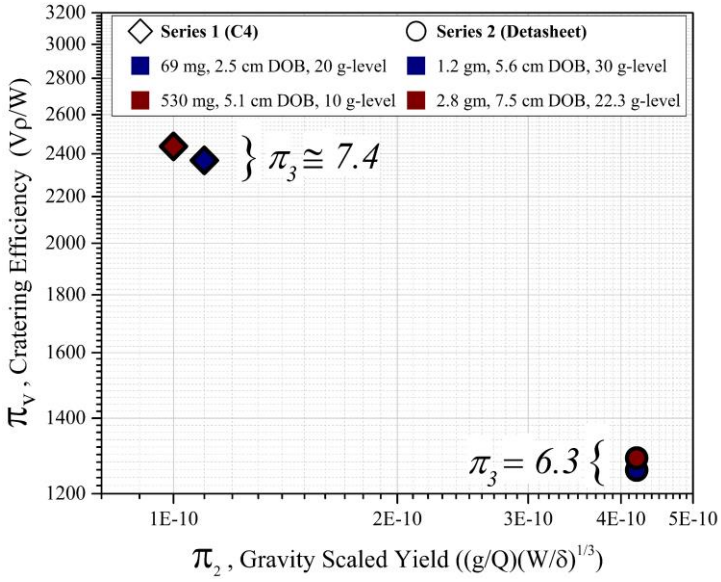

Figure 4.10. Comparison of the similitude analysis in *log-log* scale.

This confirmation of dynamic similitude in the two test series, inclusive of the π_3 parameter, allows meaningful extrapolations from model-scale buried explosive-induced craters to larger, gravity-scaled yields. In addition, the absence of detectable scale effects arising from variations in g-level and charge properties (size and chemistry) validates this study's test methodology. Significantly, the agreement observed in the modeling of models experiments substantiates the effectiveness of Π group scaling relationships to simulate a single prototype condition via models of differing physical scale.

Chapter 5 Ground Shock Characterization and Computational Developments

5.1 Ground Shock Measurements

The integration of advanced technologies into the experimental platform enabled a rigorous characterization of soil ejecta kinematics and crater morphology. To simultaneously examine buried, explosive-induced ground shock and stress wave attenuation, this study also inserted piezoelectric sensors into the testbed. As previously discussed, elevated gravitational forcing significantly influences the experimental domain and thus requires careful consideration in systems design and placement into the centrifuge. Therefore, this study selected light-weight, miniaturized piezoelectric accelerometers and pressure transducers to accurately measure in-situ responses at homologous, point-wise locations within the soil domain.

5.2 Computational Model

To numerically simulate soil blast mechanics, this study developed a computational model of the buried, explosive charge detonation in a dry soil medium including realistic boundaries, within an advanced, 3-D, multiphasic, arbitrary Lagrangian-Eulerian (ALE) framework and implemented in an explicit finite element solver, LS-DYNA [52] (Figure 5.1). The ALE method couples the fluid and soil constituent advection or flow across element domains and allows the computational mesh to move independent of material mass transport, which prevents unstable mesh distortions. This contrasts to a pure Lagrangian treatment suitable for solid mechanics, and a Eulerian technique appropriate for large fluid displacements, i.e. air and explosive detonation gases. The axial symmetry typical of a buried explosive detonation allowed one-half of the experimental domain to be modeled in the computer-aided design (CAD) program SolidWorks. Abaqus, a

finite-element software, applied a user-defined ALE mesh to the CAD model. In the near-field, the area of interest proximate the buried charge, a refined mesh element size measures 3.91 mm (vertical) by 8.13 mm (horizontal). In the far-field, a prescribed coarser mesh region reduced computational time and cost. Applied boundary conditions include: a plane strain condition on the model's cross-section surface and a non-reflective outer boundary to mitigate incident wave reflections. To simulate contact between material domains, the nodes merge at their respective material interfaces. Tracer nodes and elements, placed systematically throughout the domain, extracted acceleration and radial stress time-history data, respectively.

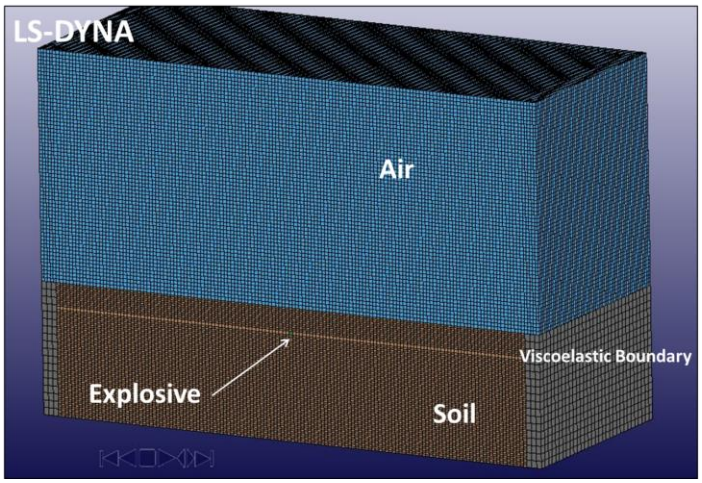

Figure 5.1. Three-dimensional finite element model of the soil, explosive, air, and outer viscoelastic boundary.

The empirically-derived Jones-Wilkin-Lee (JWL) Equation of State (EOS) defines the blast pressure (p) as a function of relative volume (V), or the volume ratio of detonation reaction products to the initial explosive volume, and energy per unit volume (E) subsequent high-explosive detonation, represented as

$$p = A\left(1 - \frac{\omega}{R_1 \cdot V}\right)e^{-R_1 V} + B\left(1 - \frac{\omega}{R_2 \cdot V}\right)e^{-R_2 V} + \frac{\omega E}{V} \tag{5.1}$$

where A, B, R_1, R_2, and ω are constants fit to experimental data for different explosive types [53]. These parametric values, summarized in Table 5.1, in conjunction with the Chapman-Jouget (C-J) pressure state parameters (ρ_o, P_{CJ}) and the explosive detonation velocity, D, describe the reaction product behavior for Composition C4 [51].

Table 5.1. C-J and JWL EOS parameters for Composition C4.

	*MAT_HIGH_EXPLOSIVE_BURN C-J Parameters			*EOS_JWL JWL Equation of State Parameters						
C4	ρ_o	D	P_{CJ}	A	B	R_1	R_2	ω	E	V
	kg/m^3	m/s	GPa	GPa	GPa	-	-	-	GPa	-
	1601	8190	28.0	597.4	13.9	4.5	1.4	0.25	8.7	1

An inviscid two invariant geologic cap model describes the explosive-induced dry soil behavior [54]. This constitutive model includes nonlinear kinematic hardening and prescribed dilatancy induced by shear loading, more representative of soil blast mechanics than comparable constitutive models, such as Drucker-Prager and Mohr-Coulomb (Figure 5.2). The cap model provides numerous parameters generally determined by empirical curve fitting to experimental data, such as mass density ρ_o, bulk modulus (K) and shear modulus (G) for the soil's elastic response, failure envelope parameters (α, θ, γ, β), cap hardening parameters (D, w, X_o), and tension cutoff surface, T. Table 5.2 summarizes the parameteric values in this soil blast simulation. Chen and Baladi [55] and the LS-DYNA user manual [52] provide additional cap model fitting guidelines.

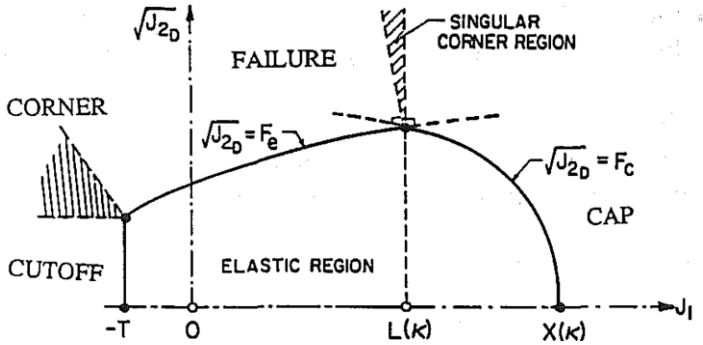

Figure 5.2. Geologic cap model yield surface illustrating tension cutoff (-T), elastic zone, hardening cap surface (F_c), and failure envelope (F_e) [54].

Table 5.2. Geologic cap model material parameters.

	*MAT_GEOLOGIC_CAP_MODEL										
Soil	ρ_0	K	G	θ	α	β	R	D	W	X_0	T
	kg/m^3	MPa	MPa	rad.	MPa	MPa^{-1}	-	MPa^{-1}	-	MPa	MPa
	1720	60.1	22.0	0.250	6.25e-2	0.360	5.0	0.00725	0.25	0.4	7.0e-3

A linear polynomial EOS for an ideal gas with Newtonian viscosity defines the ambient air pressure, P, as a function of the initial internal energy, E, represented as

$$P = C_0 + C_1\mu + C_2\mu^2 + C_3\mu^3 + (C_4 + C_5\mu + C_6\mu^2)\,E \tag{5.2}$$

The polynomial equation coefficients C_0-C_6 and volumetric parameter, $\mu = \frac{\rho}{\rho_o} - 1$ (where ρ and ρ_o denote the current and reference density, respectively), are listed in Table 5.3.

Table 5.3. EOS parameters and material model for ambient air.

	*MAT_NULL	*EOS_LINEAR_POLYNOMIAL							
Air	ρ_o	C_0	C_1	C_2	C_3	C_4	C_5	C_6	E
	kg/m^3	Pa	Pa	Pa	Pa	-	-	-	MPa
	1.225	-1.0E-6	0.0	0.0	0.0	0.4	0.4	0.0	0.25

This analysis simulates a 1.0 gram C4 charge buried 5.1 cm in dry sand. The sequential computational frames at millisecond intervals demonstrate the multi-material interaction and time-dependent evolution post-detonation, including soil deformation, gas expansion, and blast-excavated crater formation (Figure 5.3). The finite element method averages material physics at element nodes and treats granular flow behavior as a continuum, and therefore particulate disaggregation is not delineated in the visual representation. The initial ground motions, simulated by the computational model (Figure 5.3, *left*), occur at 1.15 ms. The highly pressurized gases arrive at the soil-air interface and impart kinetic energy into the particulate medium, causing the soil matrix to collapse, followed by soil deformation. Furthermore, as illustrated in Figure 5.3 (*middle*), the expanding detonation products vent to the atmosphere and jet past the soil dome heave at 5.09 ms, with soil ejecta dragged upward. This phenomenon coincides with the onset of blast-excavated crater formation. And finally, in the *late-stages* of the blast event, the expansive gas products approach the upper finite element domain at 7.42 ms (Figure 5.3, *right*). The soil ejecta heave displays the classic inverted cone profile (Figure 3.7a), and the distinct, hyperbolic-shaped final crater profile (Figure 5.3, *right*). These same soil blast mechanistic simulations correlate well to the experimental results (Section 3.1, Figure 3.1).

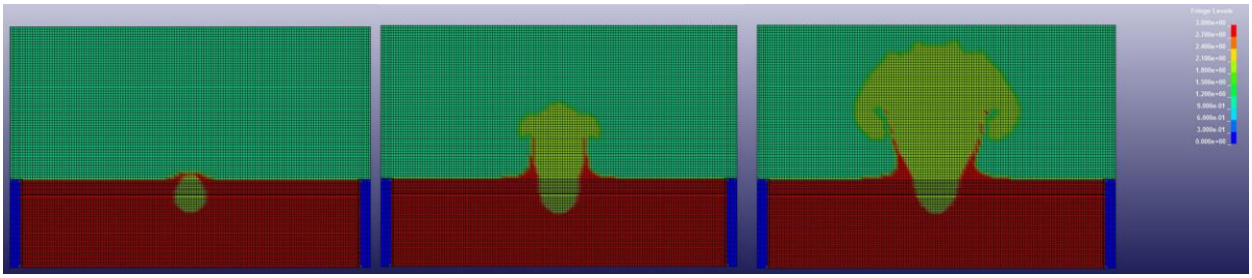

Figure 5.3. Computational results of progressive blast-induced crater formation for a 1.0 gram C4 charge buried 5.1 cm in dry sand. Material domains and corresponding color: soil (*red*); explosive detonation gases (*yellow*); ambient air (*green*).

To validate the model, predictions of soil ejecta kinematics (Figure 5.4a) and final crater morphology (Figure 5.4b) are compared to the experimental data. The ALE model effectively simulates gas-soil ejecta expansion and demonstrates close agreement to experimental soil dome measurements. Specifically, the high-speed imaging system records an approximate 19 cm soil heave front at 6.30 ms, yielding a vertical soil ejecta velocity of 29.9 ms^{-1}. In the coincident, 6.30 ms simulation frame, the model demonstrates an expansive front 3 cm higher relative to the experimental data, corresponding to a 15.4% accelerated vertical soil ejecta dome. The soil ejecta kinematics in both the experimental results and the simulation display the expected buried, blast-induced symmetric vertical flow directionality.

The crater morphology simulation also demonstrates the observed experimental trend: both crater profiles exhibit the expected inverted right cone geometries with the slightly rounded apex (Figure 5.4 b). The model under-predicts the experimental crater diameter and depth by 9.9 cm and 3.18 cm respectively. This variance can attribute to the manual use of a digital caliper for this specific crater measurement before integration of the more accurate laser profilometer. In general, the similar temporal and spatial gas-soil ejecta kinematics and crater morphology between the experimental and numerical results demonstrate reasonable correspondence and thus validate this study's simulation methodology and ALE multi-material formulation.

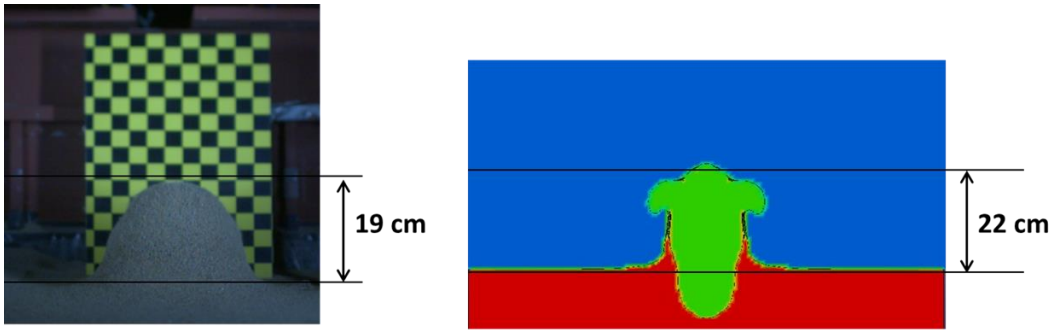

(a)

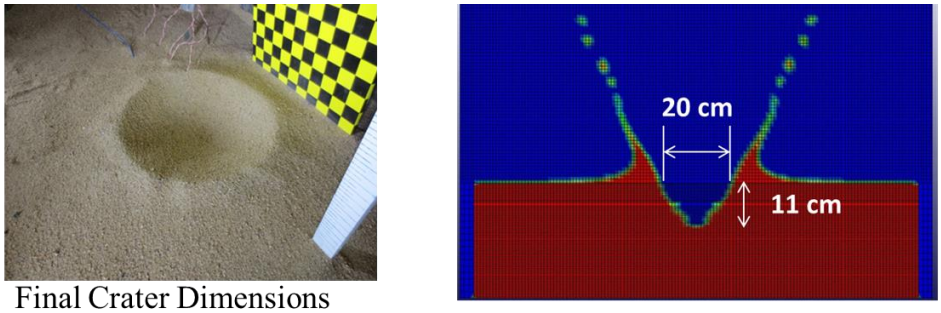

Final Crater Dimensions
DIA. 29.9 cm; Depth 7.82 cm

(b)

Figure 5.4. Comparison of experimental (*left*) and computational (*right*) results for a 1.0 gram C4 charge buried 5.1 cm in dry sand. (a) Soil deformation 6.30 ms post-detonation; (b) blast-excavated final crater.

5.3 Ground Shock Results

The experimental results quantify the soil's transient free-field response under blast loading, measured coincident to the high-speed images, and distinguish the influence of soil type (cohesionless versus cohesive) and moisture content (dry versus partially saturated) on the propagating detonation wave. Specifically, the embedded shock sensors measure the explosive-induced in-situ peak soil accelerations, stresses, and shock wave arrival times in dry sand, partially saturated sand, and clay-sand testbeds. To further validate the computational model's performance, the ground shock predictions for a 1.0 gram C4 detonation in dry sand are compared to the relevant experimental measurements.

Ground shock intensity and radial attenuation in soil strongly depends on the constitutive properties of the substrate, explosive energy, and overburden pressure [29]. An explosive

detonation generates two distinct groups of stress waves: body waves and surface waves. Shock loading typically transmits transient body, or elastic waves to the surrounding medium that spherically radiate outward from the detonation source. Body wave components include compressive waves (*p-waves*) and shear waves (*s*-waves). Compressive and shear waves induce parallel and perpendicular ground motions relative to the propagating detonation wave, respectively. Ground shock wave attenuation rates in geologic materials vary considerably due to stochastic inter-particle collisions and shear strength of the aggregate medium.

The highly-resolved soil acceleration and stress time-histories (Figure 5.5), recorded at 200 kHz, depict the dynamic soil response as a function of distance from charge (DFC). This test series used a 1.0 gram Detasheet charge buried 5.1 cm in dry soil and detonated at 10 g, with embedded shock sensors positioned radially 12.7 cm, 15.2 cm, 20.3 cm, and 25.4 cm from the explosive charge. Significantly, the waveforms represent raw, unfiltered in-soil measurements without any digital-signal processing (Figure 5.5). The data clearly evidences the expected trends: the sensor closest to the charge (12.7 cm) measures the earliest shock wave arrival time and highest peak magnitude, and the final sensor (25.4 cm) measures the latest response time and lowest peak value.

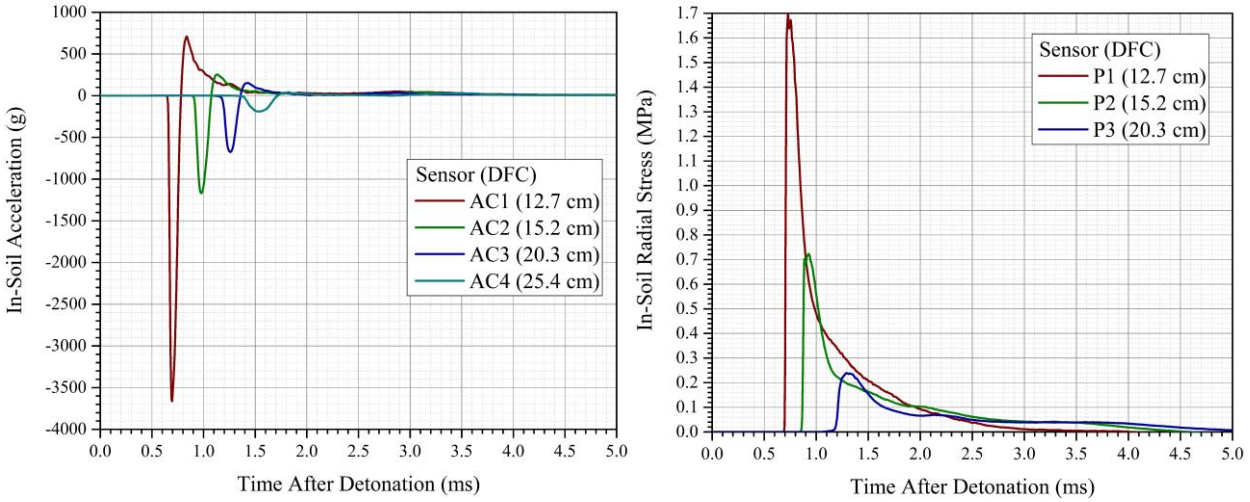

Figure 5.5. Comparison of the in-soil acceleration (*left*) and radial stress (*right*) time-histories as a function of distance from charge (DFC) for a 1.0 gram Detasheet charge buried 5.1 cm in dry soil and detonated at 10 g.

Soil accelerations and stresses exhibit a clearly defined, sharp, prominent peak extending over a sub-millisecond interval indicative of transient shock loading. All radial stress profiles resemble the classic Friedlander blast waveform, characterized by a distinct peak and narrow base, followed by a rapid decline to zero as $t \rightarrow \infty$ [51]. The data demonstrates that as the distance from the charge increases, the shock wave energy spatial attenuation causes reduced peak magnitudes and progressively less prominent peaks with broader bases, over extended time-intervals.

An accelerometer 15.2 cm away (r_1) measures the first ground motion, 0.64 ms post-detonation, followed by the pressure transducer response 30 μs later and corresponds to an initial shock wave velocity of 193.9 ms^{-1}. The propagating shock wave arrives progressively later with increased radial distance: 0.90 ms at 15.2 cm (r_2); 1.17 ms at 20.3 cm (r_3); and 1.38 ms at 25.4 cm (r_4). The shock wave arrival times, measured by all sensors, show close agreement between equivalent DFCs, with the highest, nominal variance of 0.05 ms, and thereby substantiates sensor location consistency and measurement methodology (Table 5.4).

Shock wave arrival times (t), obtained from the acceleration time-histories, display a monotonic relationship with DFC, and reasonably adhere to the parabolic fit $DFC = 126.44t^2 - 82.64t + 127.10$ $[m, s]$. The average shock wave velocity, defined as the slope of a linear curve best-fit to the arrival time data over the entire DFC range, measures 174.6 ms^{-1}. Incremental shock wave speeds decrease with radial distance, specifically 193.9 ms^{-1} at distance r_1, and decelerate to 184.1 ms^{-1} at distance r_4, or an approximate 10 ms^{-1} decline in wave velocity. This apparent trend can attribute to soil matrix energy damping. Shear modulus, density, and inter-particle contacts play a formative role on shock wave transmissivity in granular mediums. In the near-field region, the highly transient blast wave crushes and even pulverizes soil adjacent to the charge that results in soil matrix plastic deformation, with consequent higher compressional wave speeds. Beyond this rupture zone, the shock wave induces an elastoplastic constitutive soil response and thus, in the far-field region, shock waves decelerate [27,56].

As expected, the data shows that shock wave magnitudes proximate the charge measure the highest peak values, and rapidly attenuate with DFC (Figure 5.5). For example, the peak shock wave acceleration magnitude, 3643.2 g at r_1, decreases to 188.9 g at the last sensor, or an approximate 95% lower magnitude value. Distance from the charge also reduces stress magnitude from 1.68 MPa at r_1 to 0.24 MPa at r_3, an approximate 86% stress decrease (Table 5.4). After these initial peak magnitudes, a regression analysis determined that peak acceleration and stress best fit a power law-dependence on DFC. The derived relationships between peak acceleration and stress magnitudes as a function of distance from the charge, r^{-5} and $r^{-4.5}$, respectively, show the blast energy attenuation over the entire measured range ($r = DFC$).

Table 5.4. In-soil peak accelerations, stresses, and arrival times as a function of distance from charge (DFC) for a 1.0 gram Detasheet charge buried 5.1 cm in dry soil and detonated at 10 g.

	In-Soil Acceleration		In-Soil Radial Stress	
DFC (cm)	Arrival Time (ms)	Peak (g)	Arrival Time (ms)	Peak (MPa)
12.7 (r_1)	0.64	3643.3	0.67	1.68
15.2 (r_2)	0.90	1166.9	0.85	0.72
20.3 (r_3)	1.17	674.9	1.17	0.24
25.4 (r_4)	1.38	188.9		

5.3.1 Peak Acceleration versus Normalized Distance

A synthesis of this study's extensive shock wave peak soil acceleration results further characterizes the soil's free-field, dynamic response under buried blast loading. In blast mechanics, a cube-root scaling term, $R/W^{1/3}$, defines the normalized distance and relates the radial distance, R, to the explosive mass expressed in terms of TNT equivalent, W. This scaling technique enables the comparative analysis of diverse soil blast data when test parameters DFC and explosive mass vary [29]. Unless otherwise specified, the following analyses examine blast-induced ground shock as a function of normalized distance with parametric variation of in-situ soil conditions.

The compilation of 192 data points over a wide range of test parameters: charge size (0.2 gram – 1.0 gram) and type (Detasheet, C4); burial depth (1.3 cm - 7.6 cm); and g-level (1 g – 40 g), effectively characterizes the shock wave peak acceleration dependence on normalized distance in dry soil (Figure 5.6). As expected, free-field peak accelerations in a dry, cohesionless soil substrate reveal a nonlinear reduction with distance.

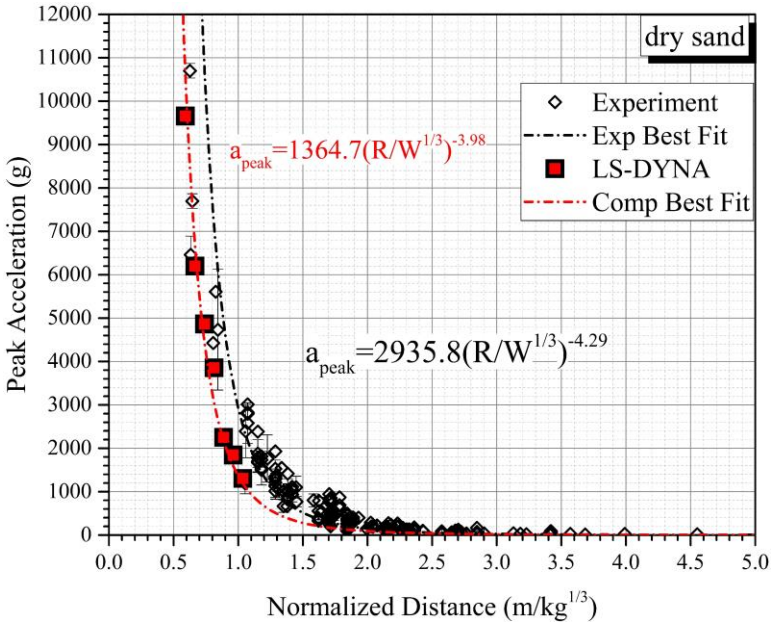

Figure 5.6. Comparison of experimental (192 data points) and computation results for in-soil peak acceleration versus normalized distance. Power law regression curves shown as *dashed* lines.

The close agreement of the experimental data throughout the wide range of test parametric variations confirms the geotechnical centrifuge modeling technique's controlled and replicable test conditions with resultant data accuracy and repeatability. As illustrated in Figure 5.6, the data delineates the pronounced spatial attenuation of the propagating shock wave in dry soil. The soil's dynamic response exhibits a highly-shocked soil medium in-proximity to the buried charge, followed by a rapid dissipation of shock wave energy with radial distance, caused by intrinsic, material damping within the soil matrix.

The predicted and experimentally measured peak accelerations mesh reasonably well and thus, indicate similar soil blast mechanics (Figure 5.6). The simulated soil accelerations remain consistently higher when compared to the corresponding experimental measurements throughout the range of normalized distance. This observed behavior likely attributes to the known sensitivity of soil constitutive parameters, i.e. damping and friction, and the consequent effect on soil blast

mechanics [57]. This study's empirically and numerically derived power-dependent relationships between dry soil peak acceleration, a_{peak}, and normalized distance, are represented by the following equations:

$$a_{peak} = 2935.8\left(\frac{R}{W^{\frac{1}{3}}}\right)^{-4.29} \tag{5.3}$$

$$a_{peak\_comp} = 1364.7\left(\frac{R}{W^{\frac{1}{3}}}\right)^{-3.98} \tag{5.4}$$

The power law, or attenuation coefficients, function as comparative indices and describe quantitatively the shock wave's transmissivity in soil [29]. For example, faster shock wave energy dissipation corresponds to higher attenuation coefficients. The empirical relationship indicates that shock wave propagation in dry sand yields a 4.29 attenuation coefficient. The numerical simulation of shock wave transmissivity yields a 3.98 attenuation coefficient, a minimal 8% variance. This comparison of the predicted and experimental attenuation coefficients quantifies the rate-dependent, close correspondence between the model and experimental data (Figure 5.6).

In addition to dry soil testbeds, the following parametric analysis provides insight into the heterogenous substrate effect on the ground shock response. Air, water, and a low-plasticity clay constituent occupy the inter-particle soil matrix air-filled void space. The experimental results from multiple test series clarify the clay constituent influence on peak soil acceleration and attenuation.

The first test series examines the explosive-induced in-situ peak acceleration as a function of normalized distance for a soil model composed of 80% sand and 20% clay with 10% saturation (80s20c10w). The compilation of 62 data points over a wide range of test parameters: Detasheet

charge sizes (0.5 gram – 1.8 gram); burial depths (2.5 cm – 5.1 cm), and g-levels (1 g – 30 g), illustrate the shock wave peak acceleration dependence on normalized distance in the cohesive soil substrate, with the expected nonlinear reduction as a function of normalized distance (Figure 5.7).

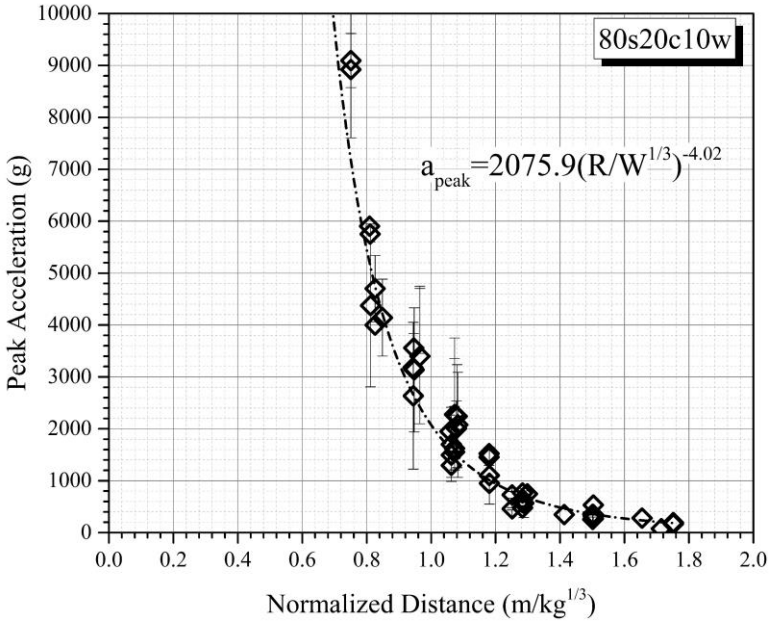

Figure 5.7. Peak soil acceleration as a function of normalized distance for buried blasts in 80s20c10w. Regression curve (*dashed* line) best-fit to 62 data points.

Despite substrate differences, the data clearly shows the same trend as dry soil: the soil's dynamic free-field response proximate the buried blast exhibits a highly-shocked particulate medium, followed by the rapidly attenuated peak soil accelerations. This study's empirically derived power-dependent relationship between the heterogenous, cohesive substrate peak accelerations, a_{peak}, and normalized distance, is represented by the following equation:

$$a_{peak} = 2075.9\left(\frac{R}{W^{\frac{1}{3}}}\right)^{-4.02} \tag{5.5}$$

As discussed, the power-law, or attenuation, coefficients quantify the shock wave's transmissivity in soil, i.e. higher attenuation coefficient, indicates increased shock wave dissipation. A comparison of the dry sand and 80s20c10w peak acceleration attenuation coefficients demonstrate the distinct differences in ground shock propagation through the two soil types. Their respective power law exponents differ by approximately 7%, with the higher value, 4.02, corresponding to the 80s20c10w series. Clay and water constituents fill the air-void space within the soil matrix and reduce the in-situ shear strength, and thereby increases shock wave transmissivity [58].

To further investigate the in-situ cohesive soil dependence on shock wave propagation, the experimental results from eight individual test series characterize peak soil acceleration and attenuation subsequent blast loading in 10% and 20% saturated soils. This test series used a 1.0 gram Detasheet charge, under 2.5 cm and 5.1 cm overburdens, and detonated at 10 g. The experimental results, shown in log-log scale, explicitly adhere to a power law relationship, independent of soil moisture content (Figure 5.8).

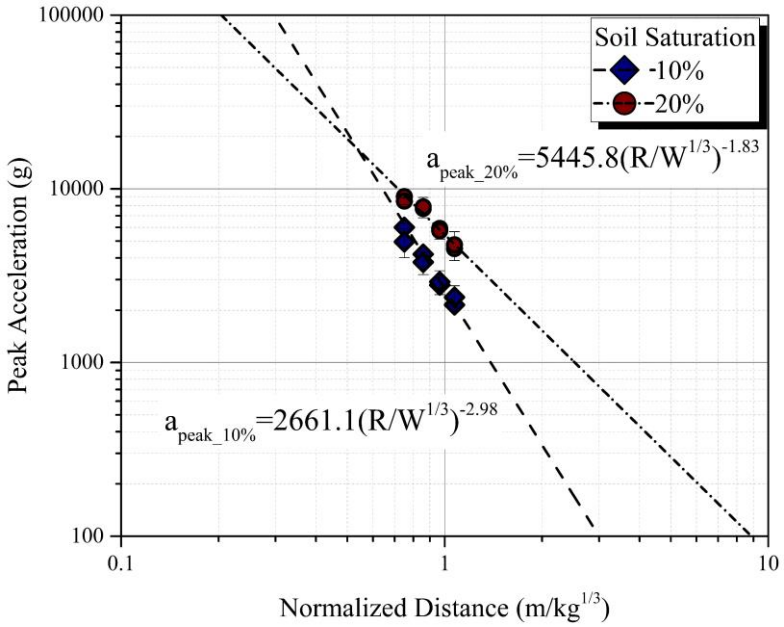

Figure 5.8. Comparison of peak soil acceleration as a function of normalized distance in *log-log* scale for buried blasts in 10% and 20% saturated soil. Regression curve (*dashed* line) best-fit to 8 data points.

Clearly, moisture content strongly influences the in-soil peak acceleration and attenuation rate. For example, peak accelerations measure 1.5 higher in 20% saturated sand at an equivalent, 0.75 m/kg$^{1/3}$, normalized distance. Likewise, at an increased, 1.02 m/kg$^{1/3}$ normalized distance, peak accelerations nearly double for the 20% saturation series compared to 10% soil saturation responses. Furthermore, the data indicates that peak acceleration attenuation varies *inversely* to in-situ moisture content: attenuation rates lengthen with increased saturation. The ground shock peak acceleration attenuation behavior, represented as:

$$a_{peak\,(10\%)} = 2661.1\left(\frac{R}{W^{\frac{1}{3}}}\right)^{-2.98} \tag{5.6}$$

$$a_{peak\,(20\%)} = 5445.8\left(\frac{R}{W^{\frac{1}{3}}}\right)^{-1.83} \tag{5.7}$$

clarifies moisture content's pronounced effect on soil blast energy dissipation. Decreasing in-situ moisture content by 10% increments shows attenuation rates consistently increase by approximately 40% (Figure 5.6 and 5.8), a considerable difference in the examined saturation range. This apparent trend can attribute to the soil skeleton's strength and stiffness. As the in-soil moisture content rises, the volume of air-filled voids declines, and the soil exhibits a stiffer dynamic response. As a result, peak shock wave accelerations increase but energy dissipation decelerates. Table 5.5 summarizes the peak acceleration regression results as a function of soil condition.

Table 5.5. Summary of the peak acceleration regression data for various in-situ conditions.

	Regression Data	
	$a_{peak} = c \cdot \left(\frac{R}{W^{\frac{1}{3}}}\right)^{n}$	
	Constant c	Attenuation Coefficient n
Dry sand	2935.8	-4.29
80s20c10w	2075.9	-4.02
10% saturation	2661.1	-2.98
20% saturation	5445.8	-1.83

5.3.2 Peak Stress versus Normalized Distance

Free-field shock wave soil stresses, measured coincident to soil accelerations, further characterize the soil's dynamic response under buried blast loading. The following analyses examine explosive-induced radial soil stresses as a function of normalized distance from the charge with parametric variation of in-situ soil conditions. The results quantify the in-situ constitutive effect on shock wave pressure magnitudes and attenuation rates.

The data compilation of radial peak stresses in a dry, cohesionless soil, derived from this study's experimental and numerical results, in addition to the full-scale field test data reported by Ehrgott [58], enables a comparative analysis of peak stress magnitudes and attenuation rates over a broad normalized distance range (Figure 5.9). This research's extensive test series varies charge chemistry (Detasheet and C4) and explosive mass (0.3 gm -1.7 gm), burial depth (2.5 cm – 7.6 cm), and g-level (1 g – 30 g). The results effectively demonstrate the peak radial stress dependence on normalized distance in dry soil (Figure 5.9). As expected, the free-field peak soil stresses in the dry soil vary inversely with normalized DFC, the same trend apparent in shock wave soil accelerations.

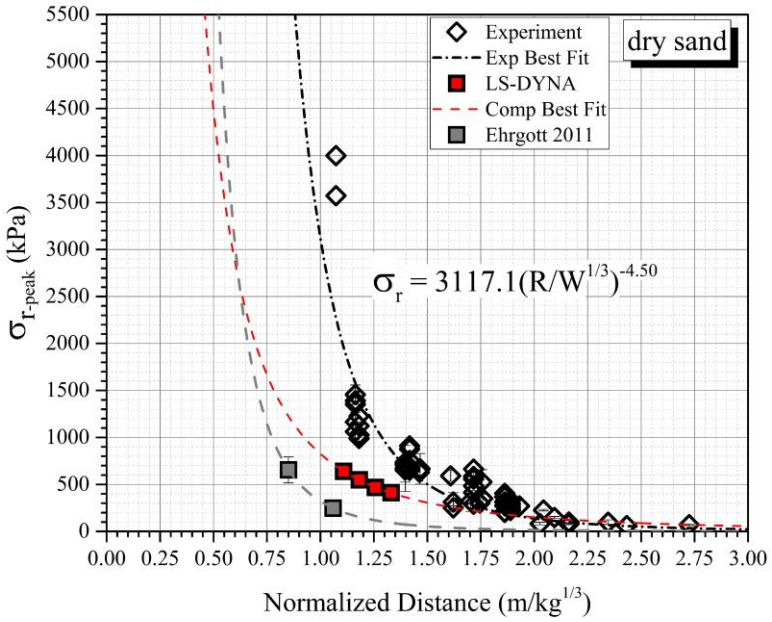

Figure 5.9. Comparison of experimental (92 data points) and computation results for radial peak soil stress in dry sand versus normalized distance. Power law regression curves shown as *dashed* lines.

As depicted in Figure 5.9, radial peak soil stresses measure consistently higher peak values at lower normalized distances and rapidly decline with increased distance. This suggests that no adverse scaling effects exist in the normalized distance range examined. The radial soil stress

experimental data and predictions coincide reasonably well, and adhere to a power law regression fit, defined respectively as

$$\sigma_r = 3117.1\left(\frac{R}{W^{\frac{1}{3}}}\right)^{-4.50} \tag{5.8}$$

$$\sigma_{r\_comp} = 824.3\left(\frac{R}{W^{\frac{1}{3}}}\right)^{-2.44} \tag{5.9}$$

Analogous to the peak soil acceleration analysis, the difference in attenuation coefficients most likely attributes to the known sensitivity of soil constituent parameters, i.e stiffness and damping, and their consequent effect on soil blast mechanics [58]. The stress measurements' variance confirms the inherent stochastic nature of in-soil blast mechanics [7,27,58]. As discussed earlier (Section 3.1), the extremely hot, pressurized detonation gases and emanating shock wave impart kinetic energy into the surrounding geologic media. The resultant shock wave induces instantaneous particle collisions and highly compressive soil matrix deformations. Thus, blast shock wave energy transmittal to the in-soil pressure sensors is a function of these complex, particle-to-particle interactions and microstructural soil responses. Also, the granular contact and their random distribution across the sensor's diaphragm, which collectively contribute to the soil stress measurement variations.

Relatively few published studies document the free-field, blast-induced ground shock soil stresses, which limits comparative analysis between this study's model-scale results and full-scale field test data. However, Ehrgott's [58] suitable dataset of peak radial dry soil stresses, included in Figure 5.9, allows meaningful comparisons to this current research. Ehrgott measured peak stresses 0.91 m, 1.2 m, and 1.5 m away from a 2.27 kg C4 charge buried in both a dry soil medium

and a partially saturated, clay-sand testbed. Their lower peak soil stresses at equivalent normalized distances relative to this study's peak soil stresses may reflect differences in soil properties and compaction conditions, instrumentation installation, and measurement technique. Despite these experimental dissimilarities, their best-fit line appears nearly parallel to this study's regression curve, quantified by the nominal 2% variance in power law exponents (Figure 5.9). Thus, the close correspondence in the attenuation coefficients confirms measurement methods and scaling techniques to simulate the same phenomenon apparent in full-scale field tests.

The following analyses from four test series further examine in-soil radial peak stresses and attenuations subsequent buried, blast loading and evaluate the soil's dynamic response to parametric variation in soil constituents. The four new testbeds include, by weight, 80% sand, 20% clay, and 10% water (80s20c10w); 50% sand, 50% clay, and 10% water (50s50c10w); and finally, 10% and 20% saturated sand.

Shock wave stresses in triphasic geologic media (sand-clay, water, air) exhibit distinct mechanistic differences when compared to dry soil responses. The first test series parameters include multiple Detasheet charge sizes (0.5 gram – 1.8 gram) burial in 80s20c10w at various depths (2.5 cm – 5.1 cm) and g-levels (1 g – 30 g). Clearly evident in the normalized distance results, the radial peak soil stresses exhibit similar spatial-dependent trends previously documented in the dry sand test series.

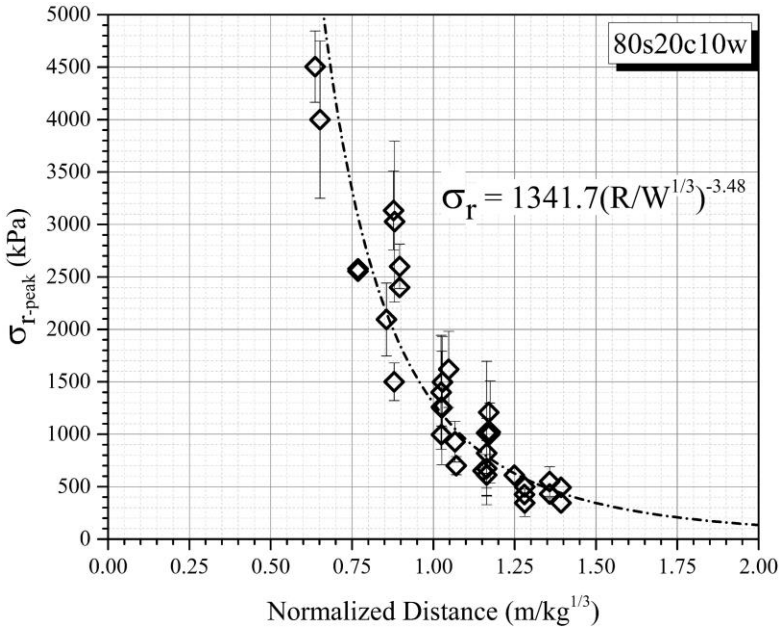

Figure 5.10. Radial peak soil stress as a function of normalized distance for buried blasts in 80s20c10w. Regression curve (*dashed* line) best-fit to 42 data points.

The data further substantiates that peak soil stresses spatially attenuate throughout the examined normalized distance. The radial peak soil stress versus normalized distance, approximated by the equation

$$\sigma_r = 1341.7\left(\frac{R}{W^{\frac{1}{3}}}\right)^{-3.48} \tag{5.10}$$

indicates a lengthened, nonlinear decline in magnitudes when compared to dry soil (Figure 5.9). Specifically, attenuation in peak stress with distance measures 25% lower in 80s20c10w than dry sand and demonstrates the substantive role clay and water constituents play on shock wave energy dissipation in granular mediums.

To further delineate clay's effect on ground shock wave pressure, a second test series measured radial peak soil stresses consequent Detasheet and C4 charge detonations in 50s50c10w testbeds. Charge size, burial depth, and g-level varied, but the majority of tests used 0.8 gram Detasheet

charges under 2.5 cm clay-sand overburdens, and detonated at 10 g. The spatial evolution of in-soil radial stresses in 50s50c10w reaffirms the previously observed trend: peak soil stresses decrease nonlinearly with normalized distance (Figure 5.11).

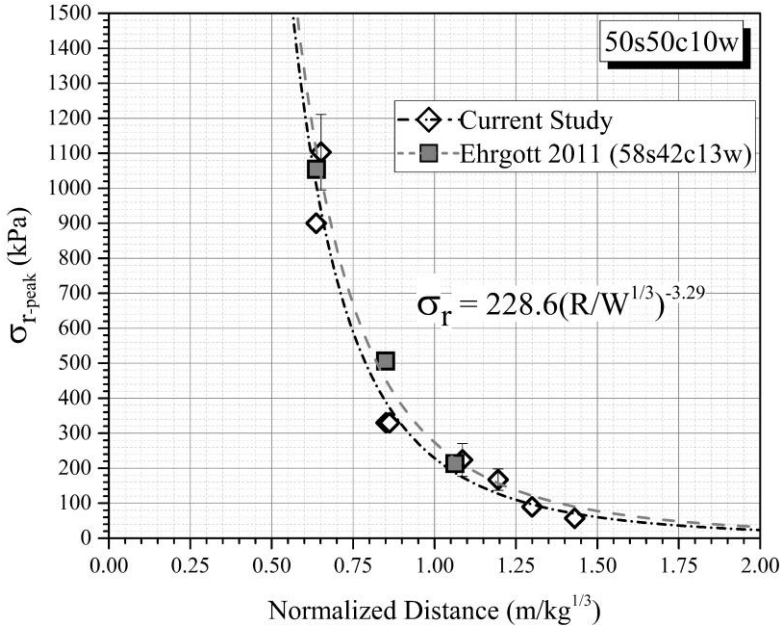

Figure 5.11. Comparison of this study's radial peak soil stress to Ehrgott [58] as a function of normalized distance for buried blasts in partially saturated, clay-sand testbeds. Regression curve (*dashed* line) derived from this study's results best-fit to 10 data points.

As shown in Figure 5.11, as normalized distance increases, radial peak soil stress decreases, indicating an inverse monotonic relationship. Furthermore, radial peak stresses in 50s50c10w evidence considerable repeatability throughout the range examined, notably difficult to achieve in clay testbeds [58]. The data shows nominal deviation from the empirically derived regression curve, defined as

$$\sigma_r = 228.6\left(\frac{R}{W^{\frac{1}{3}}}\right)^{-3.29} \tag{5.11}$$

A comparative analysis of 80s20c10w and 50s50c10w experimental results clarify the specific clay constituent effect on attenuation rates and peak soil stresses. Power law exponents measure 5.5% lower in 50s50c10w. Increasing clay mass fractions in cohesive sands decreases the soil matrix's air-filled volume, and effectively augments the medium's transmissivity. Furthermore, the added clay constituent dominates the inter-particle contact stiffness and dynamic compressibility. The 50s50c10w testbed exhibits a significantly softer mechanistic response compared to 80s20c10w at equivalent normalized distances. For example, shock waves propagating in 50s50c10w induce radial peak stresses: 1103.2 kPa, 331.5 kPa, and 108.5 kPa at corresponding distances 0.6 $m/kg^{1/3}$, 0.9 $m/kg^{1/3}$, and 1.3 $m/kg^{1/3}$. In contrast, radial peak 80s20c10w soil stresses measure over four times higher at similar normalized distances (Figure 5.10).

In addition to dry soil shock wave stress measurements, Ehrgott's [58] synthesis of in-situ data includes buried detonations in 58s42c13w, summarized in Figure 5.11. Their radial peak soil stresses and attenuation rates nearly converge with this study's data, reflecting similar DOBs and in-situ soil properties. The close adherence substantiates this study's extrapolation of subscale data to prototype condition for direct comparisons to full-scale soil blast events. Significantly, the analysis confirms that the centrifuge modeling technique enables replicable simulations of full-scale buried blast events.

The following analysis documents the moisture content's formative role on blast-induced, ground shock pressures and attenuation rates. Figure 5.12 compares radial peak soil stresses to different soil saturation levels (10% and 20%) for a given normalized distance. Test parameters charge size (1.0 gram Detasheet) and g-level (10 g) remain constant, and burial depth varies (2.5 cm and 5.1 cm). In 10% saturated soil, as normalized distance increases, radial peak soil stresses

decrease linearly in logarithmic scale with consequent lower pressures when compared to 20% soil saturation.

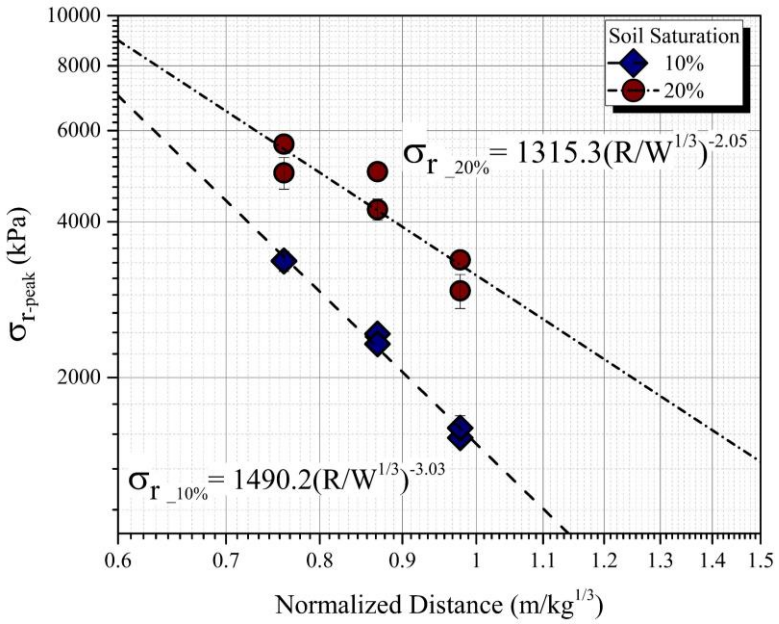

Figure 5.12. Comparison of radial peak soil stress as a function of normalized distance in *log-log* scale for buried blasts in 10% and 20% saturated soil. Regression curve (*dashed* line) best-fit to 6 data points.

The higher peak soil stresses attribute to conventional soil blast mechanics: shock waves propagate faster in saturated granular mediums and thus yield higher peak soil stresses [4,27,29,56,58]. The experimental results show reasonable adherence to a power law distribution, empirically derived for 10% and 20% saturated sand as

$$\sigma_{r\,(10\%)} = 1490.2\left(\frac{R}{W^{\frac{1}{3}}}\right)^{-3.03} \tag{5.12}$$

$$\sigma_{r\,(20\%)} = 1315.3\left(\frac{R}{W^{\frac{1}{3}}}\right)^{-2.05} \tag{5.13}$$

A comparison of regression curve slopes shown in Figure 5.12 indicate that peak stresses attenuate considerably slower in saturated sand relative to drier soils (Figure 5.7). Attenuation rates increase by 50% from dry to the lowest, 10% soil saturation. An additional 10% increase in soil saturation shows attenuation rates increase by the same approximate 50%. This apparent trend can attribute to the decreased resistance to shock wave energy propagation in water-saturated aggregates. In dry sands, stress transmits through granular contacts. In contrast, the water constituent in partially-saturated soils tends to homogenize the porous medium, and thus the blast wave effectively propagates across water filled voids.

Furthermore, the data shows that water in the soil matrix's air voids modifies blast stress transmission. Ground shock stresses measure consistently higher in 20% saturation soil when compared to 10% for a constant normalize distance. Specifically, mean radial peak soil stresses in 20% saturated soil measure 5554.3 kPa at 0.76 m/kg$^{1/3}$, 4226.2 kPa at 0.87 m/kg$^{1/3}$, and 3159.0 kPa at 0.98 m/kg$^{1/3}$. In contrast, at equivalent distances, radial peak stress subsequent buried blasts in 10% saturated soil remain consistently lower by a significant 45%. Table 5.6 summarizes the radial in-soil peak stress regression analysis as a function of soil condition.

Table 5.6. Summary of the radial peak soil stress regression data for various in-situ conditions.

	Regression Data	
	$\sigma_{peak} = c \cdot \left(\frac{R}{W^{\frac{1}{3}}}\right)^{n}$	
	Constant c	Attenuation Coefficient n
Dry sand	3117.1	-4.50
80s20c10w	1341.7	-3.48
50s50c10w	228.6	-3.29
10% saturation	1490.2	-3.03
20% saturation	1315.3	-2.05

Chapter 6 Aboveground Soil Blast Characterization

6.1 Introduction

This research documents the near-field resultant force impacts and rigid-body dynamics, under explosive loads beyond conventional discrete measurement methods, by developing a novel, robust laboratory-scale measurement device, specifically the Blast Impact Response Gage, or BIRG, integrated into the centrifuge domain. The BIRG's tri-symmetric senor configuration enables a coincident and accurate characterization of the multiphasic, interfacial blast impact mechanisms. As discussed previously, because the fundamental physics of an explosive event do not change with explosive mass [3], the highly resolved, rate-dependent video images of the complex, interactive soil blast mechanisms simulate the same phenomenon apparent in full-scale field tests. Therefore, the analytic synthesis of the BIRG results and the video data, with extensive parametric variations including target height, explosive mas, burial depth, gravity, target geometry, and in-situ soil conditions, enables a rigorous physical characterization of the buried blast impact phenomenon. The following sections present key experimental results from over 150 explosive tests.

6.2 Calculated blast parameters

An analysis of the BIRG's raw shock sensor time-history data consistently reveals a 0.3 msec electrical spike coincident explosive detonation caused by the instantaneous discharge of the fire set's microfarad capacitor. This discrete-time signal was nullified by zeroing this data over the 0.3 msec time interval. Aside from this electrical noise, the sensor recordings evidence minimal high-frequency content. Therefore, the measurements presented in the following sections remain void of frequency attenuation conversions, i.e. digital or running average filtering.

The total resultant force, $F_R(t)$, derived from the BIRG tri-load cell measurements, is expressed as

$$\mathrm{F}_R(\mathrm{t}) = \sum_{\mathrm{i}=1}^{\mathrm{N}} \mathrm{F}_\mathrm{i}\,(\mathrm{t}) \tag{6.1}$$

where $F_i(t)$ corresponds to the force time-history data for the *i*th sensor (*N=3*).

The moment resultant, $M_{o\_React}(t)$, defines the rotational component of the impact plate about its centroid subsequent eccentric loading. This term, determined by the cross product of the radial position vector r_L (measured from the center of the impact plate to the load cell) and $F_i(t)$, and written as

$$\mathrm{M}_{\mathrm{o}\_React}(\mathrm{t}) = \sum_{\mathrm{i}=1}^{3} \mathrm{r}_L \times \mathrm{F}_\mathrm{i}(\mathrm{t}) \tag{6.2}$$

quantifies the blast impact's reaction eccentricity on the target. A summation of the moment resultant and the rotational inertia tensor (I) and angular acceleration ($\alpha(t)$), defines the total rotational component of the impact plate about its mass center, or blast moment, $\mathrm{M}_{\mathrm{o}\_Blast}(\mathrm{t})$, or

$$\mathrm{M}_{\mathrm{o}\_Blast}(\mathrm{t}) = \mathrm{M}_{\mathrm{o}\_React}(\mathrm{t}) + I\alpha(t) \tag{6.3}$$

Equation 6.4, or the acceleration $\vec{a}$ at an arbitrary point on the rigid target plate, includes the plate's linear acceleration, $\vec{a}_0$, and rotational terms angular acceleration, $\vec{\alpha}$, and angular velocity, $\vec{\omega}$.

$$\vec{a} = \vec{a}_0 + \vec{\alpha}\,\mathrm{x}\,\vec{\mathrm{r}} + \vec{\omega}\,\mathrm{x}\,(\vec{\omega}\,\mathrm{x}\,\vec{\mathrm{r}}) \tag{6.4}$$

Assuming $\vec{\omega}$ x ($\vec{\omega}$ x $\vec{r}$) $\cong$ 0, the blast moment *x, y* components can be represented in matrix form as

$$\begin{bmatrix} M_{o\_Blast\_x} \\ M_{o\_Blast\_y} \end{bmatrix} = \begin{bmatrix} \frac{F_1 r_L}{2} + \frac{F_2 r_L}{2} - F_3 r_L \\ \frac{\sqrt{3} F_1 r_L}{2} - \frac{\sqrt{3} F_2 r_L}{2} \end{bmatrix} + [I] \begin{bmatrix} \alpha_x \\ \alpha_y \end{bmatrix} \tag{6.5}$$

where $F_{i\,;(i=1-3)}$ denote the load cell force measurements, and α_x and α_y define the rotational acceleration about the x and y-axis, respectively.

The inertia tensor I, defined as a function of the: target plate mass (M) and radius (R); accelerometer sensor mass, m, and radial distance to the accelerometer location, r_a; and vertical (z-direction) centroidal distance from the target plate to the accelerometer (h), can be written as

$$[I] = \begin{bmatrix} \frac{1}{4} MR^2 + 3m(\frac{1}{2} r_a^2 + h^2) & 0 \\ 0 & \frac{1}{4} MR^2 + 3m(\frac{1}{2} r_a^2 + h^2) \end{bmatrix} \tag{6.6}$$

Figure 6.1 illustrates the relative force sensor locations and the moment magnitude components: radial position vector, r, and angle, θ.

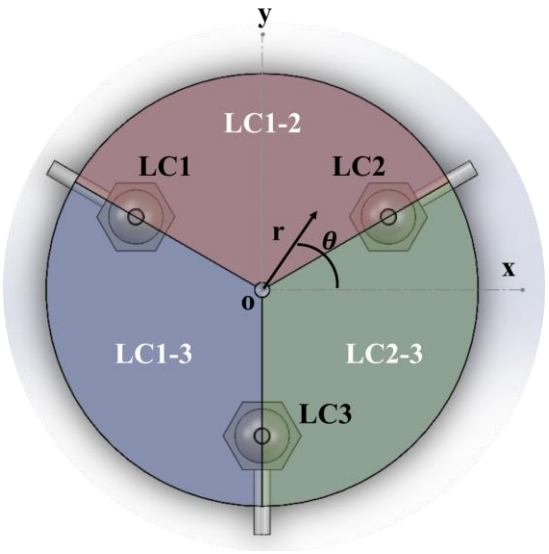

Figure 6.1. Schematic of BIRG impact plate (*top-view*) detailing proximity of load cells LC(1-3), reference coordinates, and trisections. Figure *to-scale*.

Furthermore, the product of the known target plate mass, M, and average target plate acceleration, $a(t)$, or

$$\mathrm{F_{inertia}(t)} = M\mathrm{a(t)} \tag{6.7}$$

constitutes the target plate's inertial resistance. A summation of the resultant and inertia forces establishes the total resolved force, $F_{blast}(t)$, on the BIRG impact plate, expressed as

$$\mathrm{F_{blast}(t)} = \mathrm{F_{net}(t)} + \mathrm{Ma(t)} \tag{6.8}$$

This formulation assumes rigid body plate dynamics throughout the transient event and describes the temporal distribution of the loading phase mechanisms: shock wave, detonation gas, and soil ejecta heave.

And finally, the time-integration of $F_{blast}(t)$ defines the total transferred blast impulse, $\mathcal{I}_{Blast}(t)$, on the impact plate area, *A*, for time interval *T*, and can be represented as

$$\mathcal{I}_{\mathrm{Blast}}(t) = \frac{1}{A}\int_0^T F_{\mathrm{blast}}(t)\,dt \tag{6.9}$$

6.3 Representative BIRG Measurements

The results in this section present a characteristic synthesis of the BIRG's tri-sensor shock measurements, with supportive correlation to coincident high-speed video images. This test series used a 1.0 gram Detasheet charge under a 5.1 cm overburden, detonated at 10 g, with the impact device positioned 5.1 cm above the soil-air interface. Load cell and accelerometer configurations prescribe compressive axial forces as positive and positive target velocity as vertical upward displacement (relative to the soil surface), respectively. A comparison of the acceleration and force time-histories resolves two distinct and sequential shock impact phases: the transient *early* shock (Figure 6.2, *insets*) and the *primary* shock phase of longer duration (Figure 6.2).

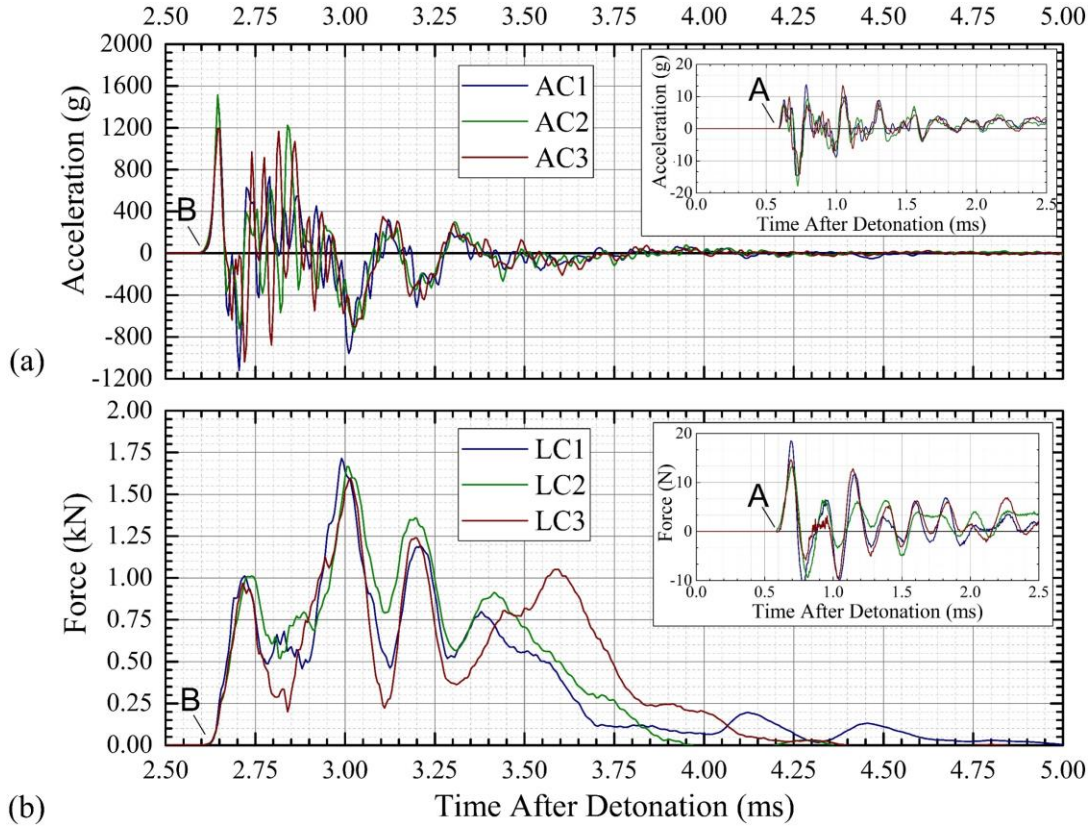

Figure 6.2. Comparision of the BIRG tri-sensor *early* (*inset*) and *primary* shock impact (a) accelerometer and (b) force time-histories subsequent detonation of a 1.0 gram Detasheet charge under a 5.1 cm overburden at 10 g. BIRG target placed 5.1 cm from the soil-air interface. AC1 and LC1 denote accelerometer and load cell sensor 1, respectively. A and B denote the arrival of the *early* and *primary* shock phases.

In general, the BIRG's sensor triad measurements exhibit close correspondence in both the respective accelerometer and load cell data throughout the blast duration. This sensor consistency indicates a predominate centric momentum transfer to the BIRG target plate (Figure 6.2). A closer examination of the two shock impact phases provides a sound physical characterization of the impact phenomenon, specifically the dynamic interaction between the shock wave and the subsequent gas-soil ejecta load mechanisms with the overlying target.

The *early* shock impact, measured by all six BIRG sensors, occurred at 0.59 ms post-detonation (Figure 6.2 'A', *insets*) and equates to an incident wave speed of 172.9 ms^{-1}. Significantly, at the

coincident 0.59 ms time interval, the nominal soil surface deformation without evidence of spallation captured by the dual high-speed video cameras (Figure 6.3a) verifies that this temporal phase clearly precedes gas-soil ejecta impacts, and thus indicates a shock wave loading mechanism. Furthermore, the accelerometers exhibit a clearly defined, initial peak at 0.62 ms post-detonation and the load cells initial peak occurs 70 μs later. The relatively low magnitudes, typical of this energy transfer phase, equate to mean acceleration and force peak magnitudes of 7.76 g and 15.46 N respectively (Figure 6.2 *inset*, Table 6.1) and can attribute to acoustic impedance which reduces shock wave intensity. The buried, blast-induced, highly transient compressive shock wave propagates radially through the particulate medium and reaches the density discontinuity at the soil-air interface. This acoustic impedance mismatch causes most of the ground shock energy to reflect back into the soil medium as a tensile wave. The remaining, energy-damped, compressive stress wave transmits upwards as an air shock, thus the evidenced lower peak magnitudes in this *early* shock impact phase (Table 6.1). Collectively, the BIRG measurement of the *early* shock arrival at 0.59 ms, with low magnitude peak values, supported by nominal coincident, visual soil spallation, provide strong evidence of a shock load mechanism.

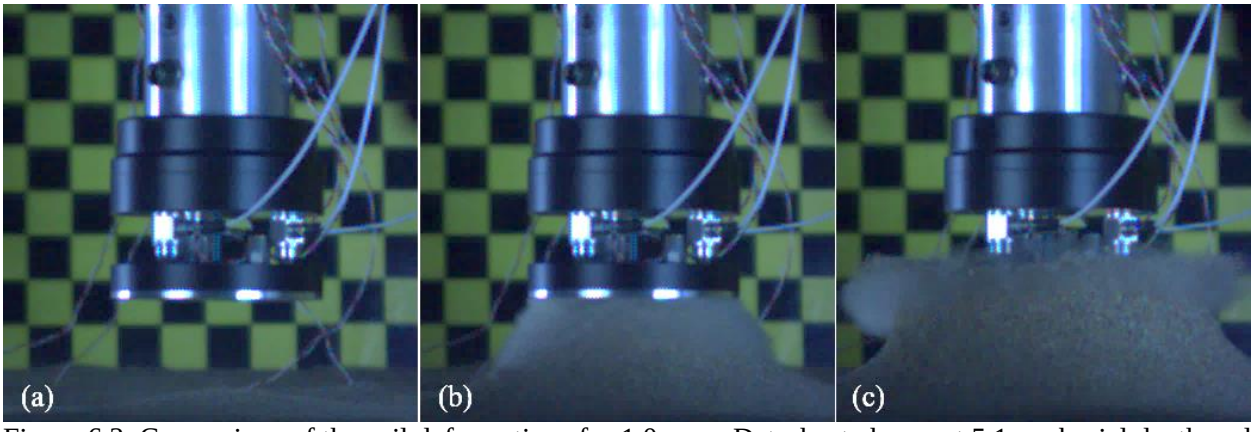

Figure 6.3. Comparison of the soil deformations for 1.0 gram Detasheet charge at 5.1 cm burial depth and detonated at the 10 g-level. Target positioned 5.1 cm aboveground. Time after detonation: (a) 0.59 ms (*early* shock, Figure 6.2, 'A'); (b) 2.60 ms (*primary* shock, Figure 6.2, 'B'); (c) 4.50 ms (*negligible* BIRG response, Figure 6.2, 'C'). Fiducial background 2.2 cm square grid.

After the initial wavelets, the time-history plots both display oscillatory decay, indicative of small residual elastic energy/shock wave reflections on the target impact plate or possibly 'wrap-around' stress effects [59] common in blast wave dynamics (Figure 6.2, *insets*). All sensor measurements decay to a nominal magnitude at 2.60 ms, which coincides with the arrival of the primary shock impact phase (Figure 6.2 B).

As anticipated, the force-time histories in the *early* shock phase drop slightly below zero, suggesting negative loading, or axial tension on the BIRG target plate. The load cell design specifications permit compressive and tensile measurements and thus 'suction', or rarefraction, can explain these negative drift anomalies in force measurements. However, a definitive cause requires further study.

To gain insight into the temporal soil dome front expansion, the vertical soil ejecta displacement data extracted from the high-speed videos, using automated motion analysis software [50], quantifies the soil ejecta kinematics prior to target impact (Figure 6.4).

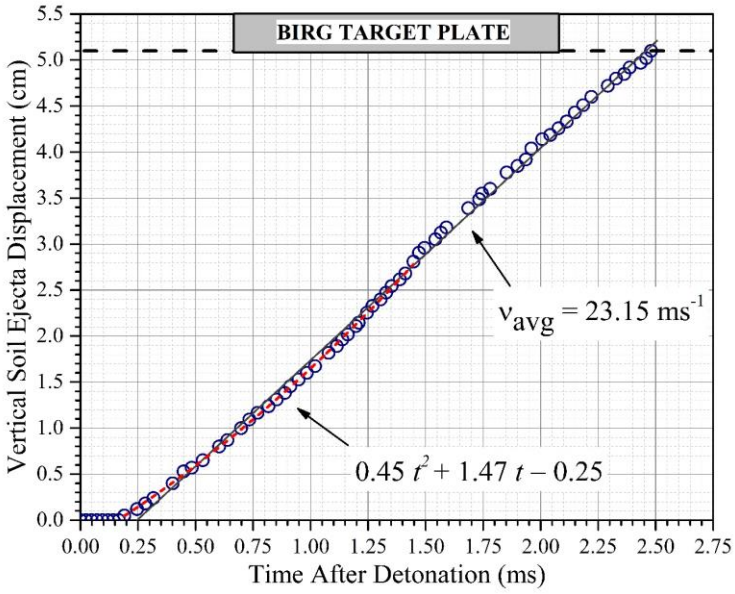

Figure 6.4. Temporal evolution of the vertical soil ejecta displacement for a 1.0 gram Detasheet charge buried 5.1 cm at 10 g. BIRG target schematic denotes a 5.1 cm HOT. Quadratic (*red dashed-line*, R^2=0.999) and linear (*black solid-line*, R^2=0.998) parabolic best-fit curves included.

The cameras' relatively high-frame rate and fast exposure time allows highly-resolved time-histories. In general, the vertical soil ejecta displacement time-history in Figure 6.4 adheres reasonably well to a linear regression fit throughout the examined range: initial soil deformation at 0.19 ms to maximum vertical tracked soil dome height at 2.52 ms. The slope of the included linear regression line, correlated to 65 data points, defines the average vertical ejecta velocity, $v_{avg} = 23.15\ ms^{-1}$. The analysis of the early vertical soil deformation slope (0.19 ms $\leq t \leq$ 1.42 ms) reveals a nonlinear, gradual rise with time, best-fit to the quadratic equation, $y(t) = \frac{1}{2}at^2 + v_o t + x_o$. The initial velocity ($v_o$) equates to 14.7 ms^{-1}, $a = 9.00$ ms^{-2}, approximately normal gravity, and the initial position $x_o = 0.25$ cm. After initial soil deformation, the data shows that vertical soil ejecta velocities progressively increase during early soil disaggregation. Following this non-linear interval at 1.50 ms, the soil dome expansion rate displays a nearly constant velocity, 21.7 ms^{-1}. For 0.08 ms, the BIRG target plate interferes with the camera's measurements. At 2.60

ms, the gas-soil ejecta front impacts the target plate, or the beginning of the *primary* shock impact phase as discussed below.

In the second, *primary* shock impact phase, subsequent the oscillatory decay, all BIRG shock sensors measured an initial spike at 2.60 ms (Figure 6.2 B) followed by a sharp, prominent peak, with a narrow base characteristic of high-rate shock loading. During this phase of the buried blast phenomenon, the nominal air shock, the pressurized expanding detonation gases, and the dense, high-velocity soil ejecta intermix and create extremely complex, stochastic interfaces (Rayleigh-Taylor instabilities [31]). These interactive load mechanisms transfer kinetic energy to the target's free surface.

Clearly evident in the comparative time-histories, the initial peak accelerations and forces measure orders of magnitude higher in the *primary* shock impact phase (Figure 6.2 B) when compared to the peak values in the *early* shock phase (Figure 6.2, *insets*). Specifically, the average initial peak acceleration and force increased from 7.76 g to 14.04 g and 15.46 N to 1.00 kN, respectively (Table 6.1). The comparative analysis of the arrival times and magnitudes quantifies the constitutive load mechanisms in both energy-transfer phases and further substantiates conventional blast mechanics: gas-soil ejecta impacts are orders of magnitude more severe than any air shock loads [26,27,56,57]**.** In the near-field, buried explosive environment, the gas-soil ejecta loads transmit most of the energy to the overlying target. The high-speed video image (Figure 6.3b) recorded simultaneous to the initial, *primary* shock spike, measured by the BIRG sensors at 2.60 ms, effectively captures and visually qualifies the gas-soil ejecta impacts on the target. Clearly apparent, a vertical flow directionality dominates the soil dome heave due to the lateral soil confinement of the buried charge.

Furthermore, the blast loading continues over an extended time period in this shock phase. After the initial peak magnitude at 2.60 ms, the force time-history exhibits a secondary peak that measured a higher 1.67 kN and a peak arrival time at 2.98 ms, followed by a progressively later third peak (Figure 6.2B, Table 6.1). These dynamic responses can attribute to the continuous flux of high-rate, soil particle impacts on the target's distal face. This mechanism can also explain the oscillations in the acceleration profile during the same time interval (Figure 6.2a, B).

Approximately 3.30 ms post-detonation, the previously in-sync acceleration and force measurements start to deviate between sensors, and 0.31 ms later, collectively attenuate rapidly toward zero, indicating a decline in soil blast energy imparted to the BIRG target plate (Figure 6.2). At this stage, the vertical directionality of the temporally and spatially evolving soil dome transitions to lateral venting across the target distal face and a dilute soil annulus encompass its circumference, observed 4.50 ms post-detonation, in Figure 6.3c. As anticipated, the soil ejecta's radial expansion beyond the target precludes kinetic energy transfer to the plate. Thus, the remaining available energy converts to kinematic soil ejecta flow. Significantly, the BIRG sensor data quantifies this energy attenuation to zero, also at the coincident 4.50 ms (Figure 6.2) and verifies the same impact phenomenon. Table 6.1 summarizes the BIRG's average early and primary shock impact peak accelerations and forces, with respective phase arrival times.

Table 6.1. Summary of BIRG average peak sensor measurements for a 1.0 gram Detasheet charge buried 5.1 cm and detonated at 10 g. Target positioned 5.1 cm aboveground.

Sensor	*Early* Shock Phase			*Primary* Shock Phase				
	Arrival Time (ms)	Avg. Peak Mag.	Peak Time (ms)	Arrival Time (ms)	Avg. Initial Peak Mag.	Initial Peak Time (ms)	Avg. 2nd Peak Mag.	2nd Peak Time (ms)
AC	0.59	7.76 g ± 0.98 g	0.62	2.60	1404.80 g ± 181.41 g	2.65		
LC	0.59	15.46 N ± 2.65 N	0.69	2.60	1.00 kN ± 0.02 N	2.71	1.67 kN ± 0.06 N	2.98

To validate the BIRG's direct measurement of the blast impact phenomenon and to ensure non-inference with BIRG sensor data, an analysis of the target plate's rigid boundary conditions compares the target plate's velocity and displacement, determined by numerical integration of the average BIRG acceleration data (Figure 6.2a).

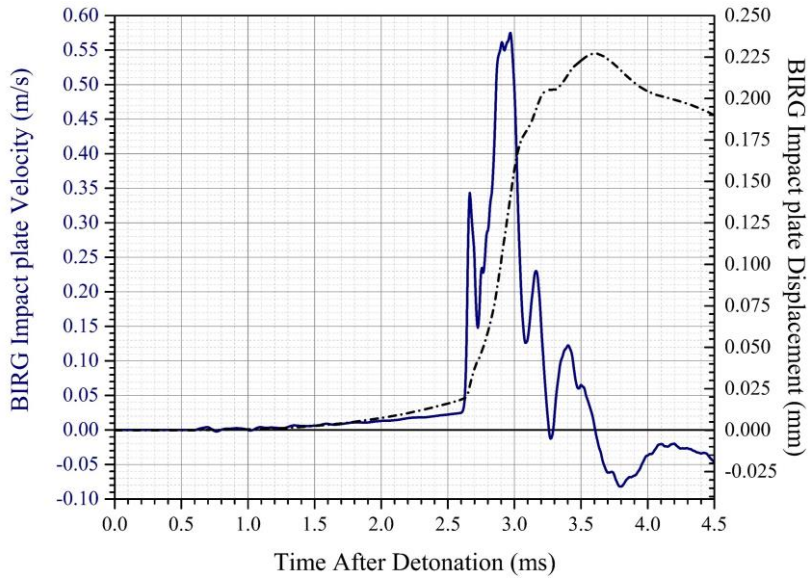

Figure 6.5. Comparisons of BIRG's target plate velocity (*solid-line*) and displacement (*dashed-line*) for a 1.0 gram Detasheet charge buried 5.1 cm and detonated at 10 g. Target positioned 5.1 cm aboveground.

The comparative velocity and displacement time-histories demonstrate that the blast loads induced nominal plate peak velocities or vertical motions (Figure 6.5). In general, the results display reasonable and consistent rigid-body dynamics with the expectant time-dependent behavior. After the 0.59 ms arrival of the shock wave impact in the *early* shock phase, the target plate velocity and displacement data show a slight, progressive increase, 0.05 ms^{-1} and 0.013 mm respectively, until the arrival of the evolving soil dome front at 2.60 ms, in the *primary* shock phase. At this point, the gas-soil ejecta impact induces an immediate dynamic response and the consequent BIRG target plate velocities and displacements rapidly increase to peak values (Figure 6.5). The target plate velocity time-history exhibits clearly defined, sharp, narrow-based profiles, and a maximum peak value of 0.57 ms^{-1} at 2.98 ms, surrounded by two shoulder peaks of lesser magnitude. Significantly, this maximum peak value at peak time 2.98 ms, directly corresponds to the maximum shock force magnitude, 1.67 kN (Figure 6.2b), measured by the BIRG load cells, also at 2.98 ms (Table 6.1). In contrast, the smooth temporal evolution of the displacement profile shows a single, rounded apex with an extremely low magnitude 227 μm, at 3.61 ms. The analysis substantiates that soil blast momentum transfer induced negligible plate peak velocities or vertical displacements, and thereby confirms a rigid boundary condition that allows direct measurement of blast impact.

Because the fundamental physics of an explosive event do not change with explosive mass [3], the highly-resolved, video images in conjunction with the high-fidelity, BIRG tri-sensor measurements provide a rigorous characterization of the same phenomena analogous to full-scale field tests. The results quantify the near-field *early* and *primary* shock impact loads to an aboveground target and delineate the respective, multiphasic, blast load constituents including the shock wave, initial soil deformation, temporal and spatial gas-soil heave evolution, and subsequent

explosive impact on the aboveground target. This analytical synthesis provides a sound physical understanding of the explosive-induced, actual dynamic behavior of the interactive explosive mechanisms and the overlying structure.

6.4 Structural Response of Support Frame

In addition to the target plate's dynamic analysis, each test series monitored the BIRG's support structure to further ensure non-interference with shock responses and to identify any structural fatigue from repeated centrifuge in-flight g-levels. To assess the rigidity of the structure, Figure 6.6 compares the target plate's average acceleration to the cross-channel's upper-midpoint acceleration in both shock impact phases. Clearly evident, the BIRG's triad accelerometers measured consistently earlier arrival times and significantly higher magnitudes in the *early* (Figure 6.6, *left*) and *primary* (Figure 6.6, *right*) shock impact phases.

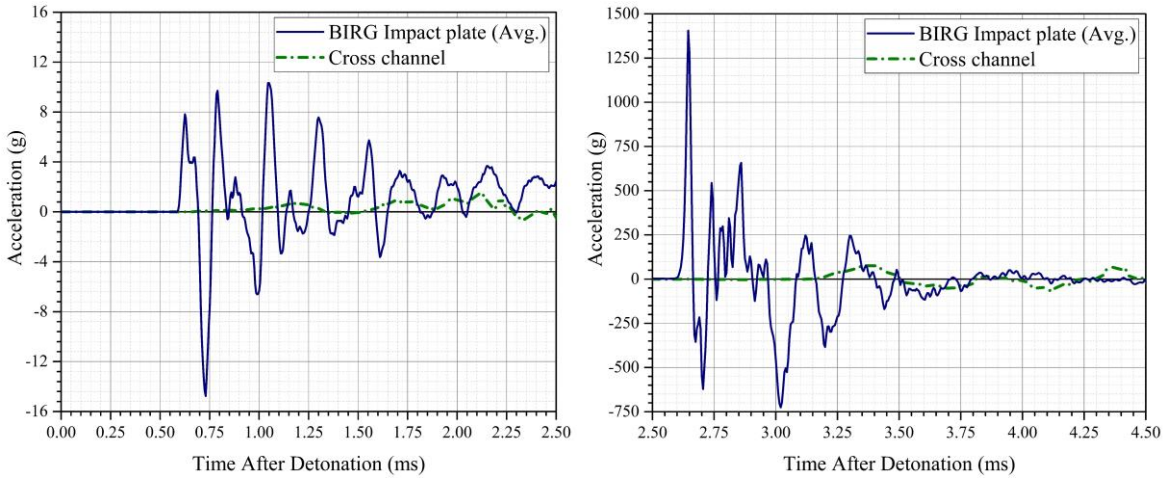

Figure 6.6. Comparison of the BIRG's impact plate average acceleration (*solid-line*) and cross-channel's upper-midpoint acceleration (*dashed-line*) during the: (*left*) *early* and (*right*) *primary* shock phases for a 1.0 gram Detasheet charge buried 5.1 cm and detonated at 10 g. Target positioned 5.1 cm aboveground.

Specifically, the support cross-channel's initial vibrational response occurred 0.11 ms and 0.53 ms later in the respective phases than the BIRG target plate responses. Furthermore, a comparison

of maximum peak values shows a significant 180% difference. And finally, the support cross-channels' maximum displacement, derived from a second-time integration of the acceleration time-history data yields a nominal peak magnitude of 70 μm. Therefore, the results substantiate the support structure's rigid design compliance and confirm that the cross-channel's global motions remain negligible without adverse effects on soil ejecta-target dynamics throughout soil blast momentum transfer.

6.5 Soil Blast Forces, Impulse, and Moments

To further characterize blast dynamics in conjunction with the temporal and spatial distribution of the load mechanisms, the results in this section quantify the force impacts over the entire target surface instead of the conventional discrete measurement methods. The analytic syntheses derived from the BIRG's load cell and accelerometer data (Figure 6.2, Equations 6.1-6.9) enable a rigorous characterization of the mechanistic blast impact phenomenon. First, a comparison of the time-dependent resultant and inertia forces (Equations 6.1 and 6.7) illustrates the interrelated kinetics and kinematics evidenced in the impact phenomenon (Figure 6.7) and demonstrates the usefulness of concurrent measurement of both forces to distinguish mechanistic trends.

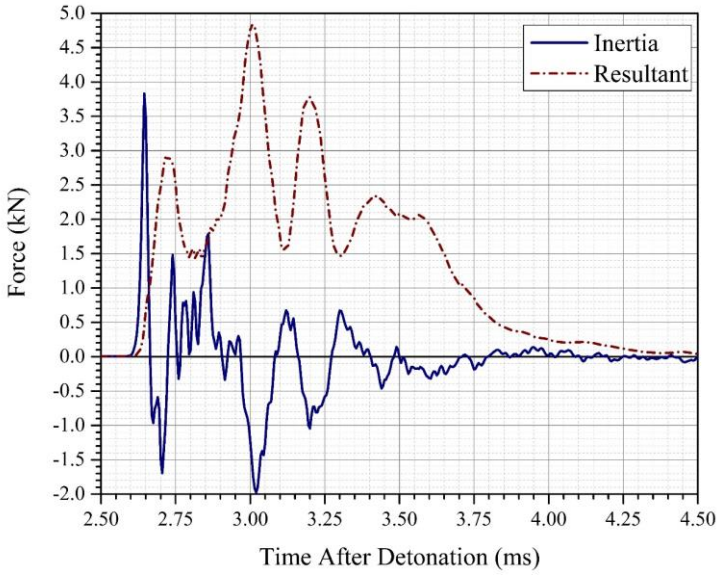

Figure 6.7. Comparison of the inertia (*solid-line*) and resultant (*dashed-line*) forces on the BIRG target during the *primary* shock phase for a 1.0 gram Detasheet charge buried 5.1 cm and detonated at 10 g. Target positioned 5.1 cm aboveground.

Subsequent the high-rate, impact of the gas-soil ejecta front 2.60 ms post-detonation, these complex, interactive load mechanisms induce an immediate BIRG target response. First, the inertia force rapidly accelerates to a clearly-defined, sharp, high magnitude peak value, 3.83 kN, coincident to the load cells' sensor element displacement (Figure 6.7). Then, the successive compressive load cell measurements, 5 μs later, yield an initial resultant force peak, with a broader base and a lower 2.93 kN magnitude relative to the inertia force.

After the initial inertia force peak, the two force profiles appear as mirrored projections about the y-axis for the remainder of the explosive event. As illustrated in Figure 6.7, the inertia force magnitude rapidly decreases from 3.83 kN to -1.70 kN at 2.71 ms, or 0.11 ms later. In contrast, during this initial decline in inertia force, the resultant force increases to its initial peak, 2.93 kN magnitude, at the same peak time. Next, the inertial force evidences a second peak magnitude at 1.98 kN and again displays a peak-to-valley transition to -1.98 kN at 3.02 ms. In the interim, this observed trend continues and the resultant force time-history exhibits the expected inverse

relationship, or valley-to-peak response. Specifically, after the initial peak, the resultant force decreases by 0.98 kN, and then increases to its second prominent peak, with the maximum 4.84 kN magnitude at 3.02 ms. At the coincident 3.02 ms, the resultant force peak magnitude mirrors the inertia force minimal magnitude value.

This mechanistic trend, the inverse relationship between the inertia and resultant force time-histories, can attribute to the continued flux of soil particle impacts from the radially expanding soil dome heave. In other words, the data indicates that the soil ejecta momentum transfer to the BIRG causes a positive rise in the target plate's inertia force that precedes the immediate increase in the resultant force. This apparent trend continues until the *late-stages* of the blast event: the loads induce a nominal dynamic response from the target plate, and the forces attenuate to zero at 4.50 ms (Figure 6.7).

Furthermore, the summation of the *inertia* and *resultant* forces via rigid-body mechanics, establishes the total resolved, blast force imparted to the BIRG's distal surface (Equation 6.8). The time-dependent blast force, normalized by the target plate's area, clearly and concisely quantifies the non-uniform, temporal distribution of the gas-soil ejecta stresses in addition to the near-field dynamic response of a rigid structure (Figure 6.8), a fundamental prerequisite for computational models.

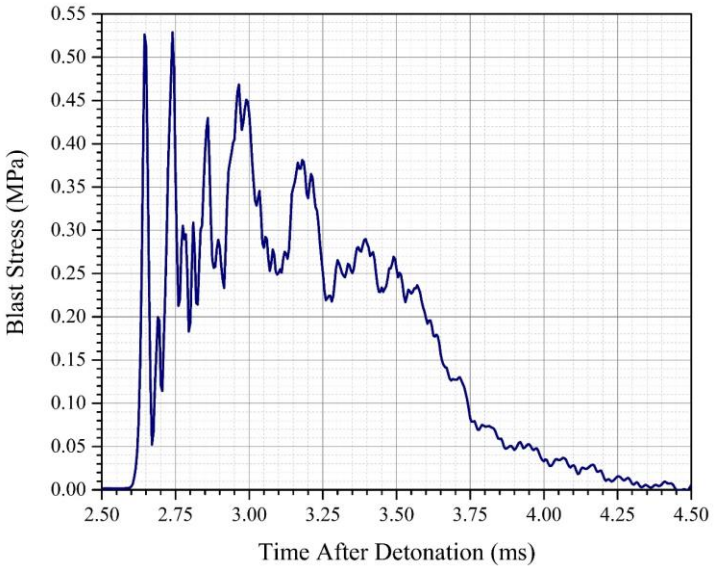

Figure 6.8. Time evolution of the blast stress on the BIRG's distal surface during the *primary* shock phase for a 1.0 gram Detasheet charge buried 5.1 cm and detonated at 10 g. Target positioned 5.1 cm aboveground.

The highly-resolved, blast stress time-history further distinguishes the gas-soil blast energy transfer to the target in the *primary* shock impact phase. In the initial, highest-pressure regime, at 2.60 ms, the two prominent, narrow peaks, both with the greatest 0.53 MPa magnitude value (Figure 6.8), depict the immediate momentum transfer from the high-rate, gas-soil ejecta loads, with the vertical directionality focusing the force impact to the BIRG rigid target plate. Then, in the second blast pressure regime, $2.90 \text{ ms} \leq t \leq 3.50 \text{ ms}$, the vertical directionality of the temporally and spatially evolving soil heave transitions to a lateral flow along the target surface. The continuous flux of soil particle impacts still transmits kinetic energy to the target for an extended period of time. However, the magnitude peak values decrease due to blast energy attenuation and a reduced soil annulus compaction density.

Instead of the conventional determination of blast energy by momentum formulation, derived from kinematics, this research resolves the blast energy by the time-integration of the blast force data (Equation 6.9) and quantifies the temporal evolution of the total blast impulse imparted to the

overlying BIRG target from the subsurface explosive detonation. The impulse time-history (Figure 6.9) clearly exhibits an immediate, rapid linear increase at 2.60 ms subsequent the arrival of the gas-soil ejecta loads, also correlated to the first high-stress impact regime.

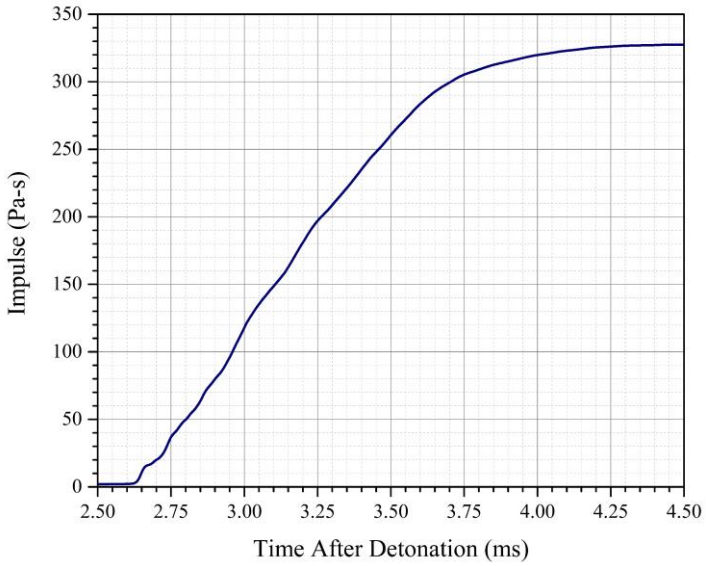

Figure 6.9. Impulse per unit area during the *primary* shock phase for a 1.0 gram Detasheet charge buried 5.1 cm and detonated at 10 g. Target positioned 5.1 cm aboveground.

After 2.60 ms, the rate-dependent blast impulse steadily increases with time, indicative of the continual gas-soil ejecta impacts. The approximate linear trend remains constant until 300 Pa-s, at 3.61 ms (Figure 6.9). As discussed in Section 6.3, this specific time 3.61 ms, post-detonation, corresponds to the decline in the blast energy transferred to the aboveground target. Next, the total blast impulse increases but at a reduced rate as it approaches a horizontal asymptote at 327.50 Pa-s, 4.50 ms post-detonation. Thus, the blast energy transferred to the target from the gas-soil ejecta impacts continued for 1.90 ms, a significant amount of time in the millisecond duration of the entire explosive event. Table 6.2 summarizes the blast stress and impulse measurements.

Table 6.2. Summary of the BIRG soil blast stress and impulse.

Charge size (gm)	DOB (cm)	HOT (cm)	G-level (g)	Blast Peak Initial Stress (*t=2.65 ms)* (MPa)	Blast Peak Impulse (Pa-s)
1.0	5.1	5.1	10	0.53	327.50

The analysis of the resultant moment provides additional insight into the soil blast mechanics (Equation 6.2). The BIRG's configuration directly measures the target plate's out-of-plane rotational motions around its mass centroid, i.e. x-y plane of symmetry, and also constrains rotations around its longitudinal axis, or torsion. The schematic (Figure 6.1) illustrates the moment magnitude components, radial position vector *(r)* and angular rotation, *(θ)*, in addition to the specific senor locations. As shown in Figure 6.10, the resultant moment magnitude and component time-histories quantify the temporal and spatial distribution of the non-uniform, gas-soil ejecta impacts in the *primary* shock phase.

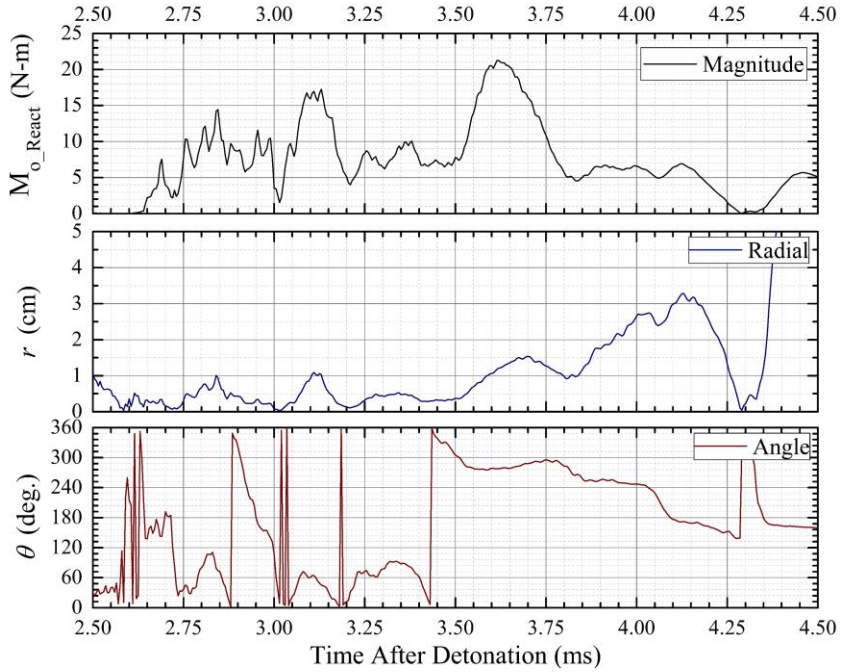

Figure 6.10. (*top*) Resultant moment magnitude, position vector (*middle*) radius and (*bottom*) angle time-histories during the *primary* shock impact phase for a 1.0 gram Detasheet charge buried 5.1 cm and detonated at 10 g. Target positioned 5.1 cm aboveground.

The results illustrate that both the resultant moment magnitude and radial position vector increase with the apparent, sporadic profile variances due to the continued flux of these load mechanisms. A closer examination of the moment time-history distinguishes three sequentially increasing peak moment magnitudes between 2.75 ms and 3.75 ms. Within this 1 ms time-interval, the first and lowest peak measured 14.4 N-m at 2.85 ms. This initial moment originates from a centric impact, measured 0.75 cm radially from the target's center to the load cell in the LC1-2 trisection (Figure 6.11a). Approximately 0.26 ms later, the second peak moment magnitude measured a 1.54 N-m increase to 16.9 N-m. Consistent with the first peak moment, the data indicates that a predominate centric impact, measured 1.09 cm from the target centroid, induced this second rotational motion, also located in the tri-section LC1-2 (Figure 6.11b). And finally, in the late stage of blast loading, the BIRG measured the highest moment, 21.2 N-m at 3.26 ms, 1.18

cm radially in the LC2-3 trisection, closest to load cell 3 (Figure 6.11c). The schematic of the three peak resultant moments' position vector component (*r, θ*) data, correlated to their respective times (Figure 6.11a-c), effectively illustrates the applied resultant force impact location on the overlying target, with the expected eccentricity even in a predominate centric load configuration.

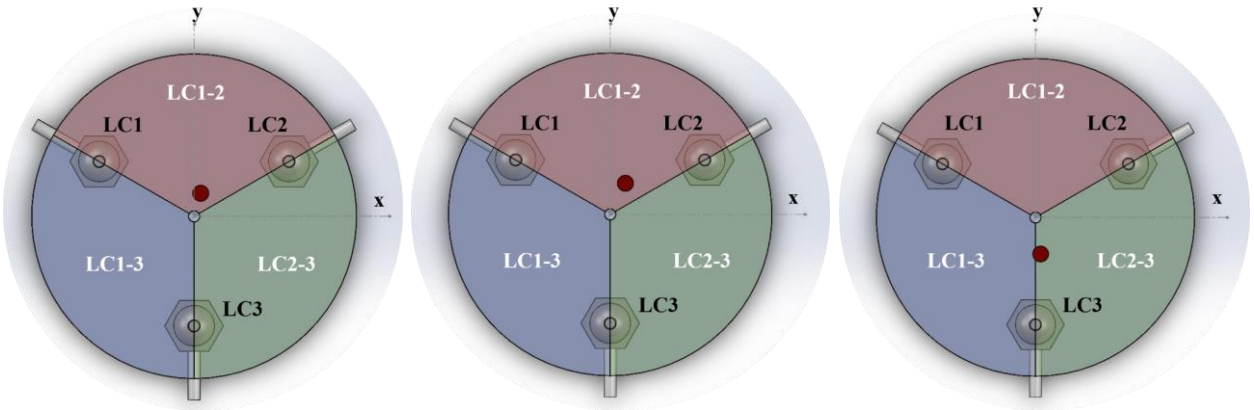

(a) TAD = 2.85 ms (b) TAD = 3.11 ms (c) TAD = 3.62 ms

Figure 6.11. Schematics (*to-scale*) of the BIRG's impact plate free-surface illustrate the eccentricity of the applied resultant force (*red-dot*) relative to the load cell sensors (1, 2, 3) determined from (a) 1st, (b) 2nd, and (c) 3rd peak moment data (Figure 6.10) for a 1.0 gram Detasheet charge buried 5.1 cm and detonated at 10 g. The test prescribed a target height of 5.1 cm. TAD denotes time after detonation.

Furthermore, the proximity of the applied resultant force to the target's mass centroid (*red-dot*) (Figure 6.11) illustrates minimal rigid-body rotations induced by the gas-soil eject mechanisms and further substantiates a predominate, *centric* load, with the defined eccentric skewness. Significantly, the results verify the test-specific, intended resultant force location. Table 6.3 summarizes the key resultant moment results.

Table 6.3. Summary of the BIRG resultant moment results for a 1.0 gram Detasheet charge buried 5.1 cm and detonated at 10 g. Target positioned 5.1 cm aboveground.

Peak Resultant		Position vector	
Time (ms)	Moment Mag. (N-m)	r (cm)	θ (deg)
2.85	14.4	0.75	74
3.11	16.9	1.09	64
3.62	21.2	1.18	278

Furthermore, the analysis of the total blast moment clearly shows that $I\alpha$ significantly influences the target's rigid body dynamics subsequent stochastic, non-uniform, gas-soil ejecta loading (Figure 6.12). Inclusion of rotational inertia effects (Equation 6.3) yield significantly higher peak moment magnitudes when compared to the moment resultant results.

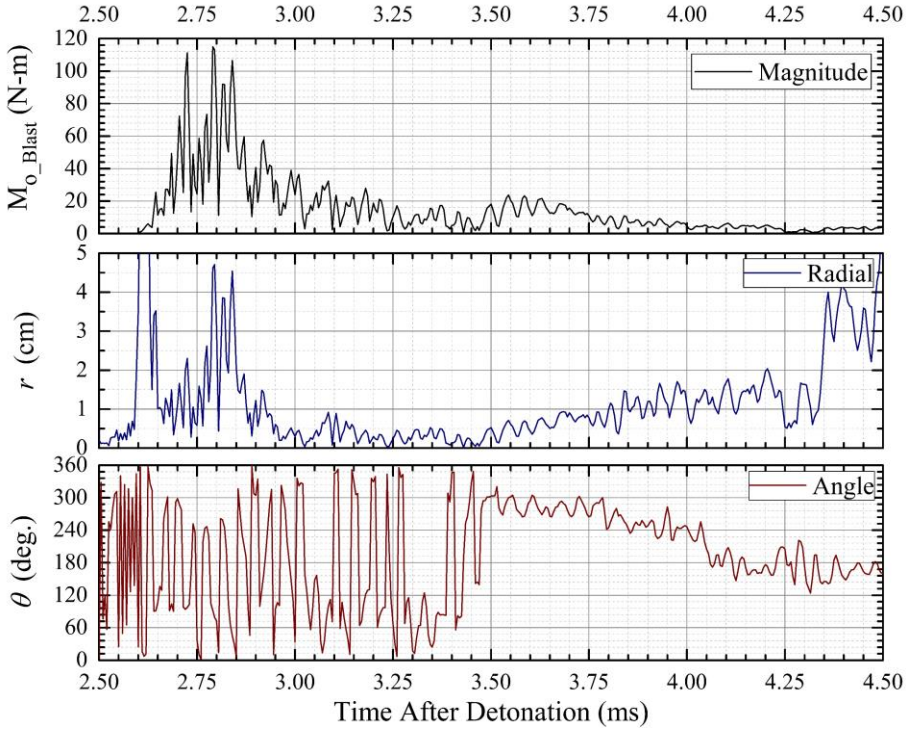

Figure 6.12. (*top*) Blast moment magnitude, position vector (*middle*) radius and (*bottom*) angle time-histories during the *primary* shock impact phase for a 1.0 gram Detasheet charge buried 5.1 cm and detonated at 10 g. Target positioned 5.1 cm aboveground.

Specifically, the peak blast moment measures 111.3 N-s at 2.73 ms post-detonation, or 7.7 times higher than the initial peak resultant moment magnitude (Table 6.3). The data substantiates this study's methods to include rotational inertia in the moment calculation because it enhances the characterization of the target's blast-induced dynamics. Table 6.4 summarizes and Figure 6.13 illustrates the initial peak blast moment results.

Table 6.4. Summary of the initial BIRG blast moment for a 1.0 gram Detasheet charge buried 5.1 cm and detonated at 10 g. Target positioned 5.1 cm aboveground.

Peak Blast		Position vector	
Time (ms)	Moment Mag. (N-m)	r (cm)	θ (deg)
2.73	111.3	2.3	102

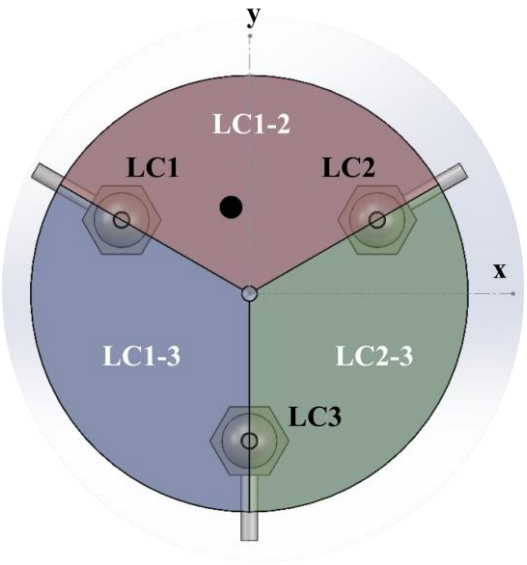

Figure 6.13. Schematic (*to-scale*) of the BIRG's impact plate free-surface illustrate the eccentricity of the applied blast force (*black-dot*) relative to the load cell sensors (1, 2, 3) determined from the blast moment data (Figure 6.12) at 2.73 ms for a 1.0 gram Detasheet charge buried 5.1 cm and detonated at 10 g. The test prescribed a target height of 5.1 cm.

6.6 Centric versus Eccentric Blast Impact

The blast resultant force imparted to an aboveground target, i.e. a triggered, buried IED striking a military vehicle, rarely coincides with the target's center of mass. Instead, the transient, non-uniform, load mechanisms typically impact the target with pronounced eccentricity. This asymmetric momentum transfer induces complex, highly non-linear structural dynamics. The resultant elevated angular momentum, in addition to severe structural compressive stresses, jeopardize the vehicle's structural integrity and increases its tendency to overturn.

The BIRG effectively characterizes these near-field, buried blast induced, rigid-body moments, as discussed previously. To further resolve asymmetric loading effects, this analytic synthesis of the BIRG shock measurements, with supportive correlation to coincident high-speed video images, compares *centric* and *eccentric* impacts. This test series used a 1.0 gram Detasheet charge under a 5.1 cm overburden, a reduced 2.5 cm target height, and gravitation forcing increased to the 20 g-level. The eccentric test's prescribed charge placement predicted predominate loading on the BIRG target plate in the LC1-3 trisection (Figure 6.1). The following comparative analysis provides critical insights into the multiphasic soil ejecta mechanisms and the stereo video images from both cameras effectively illustrate their distinct dynamic behavior under *centric* and *eccentric* blast loading (Figure 6.14).

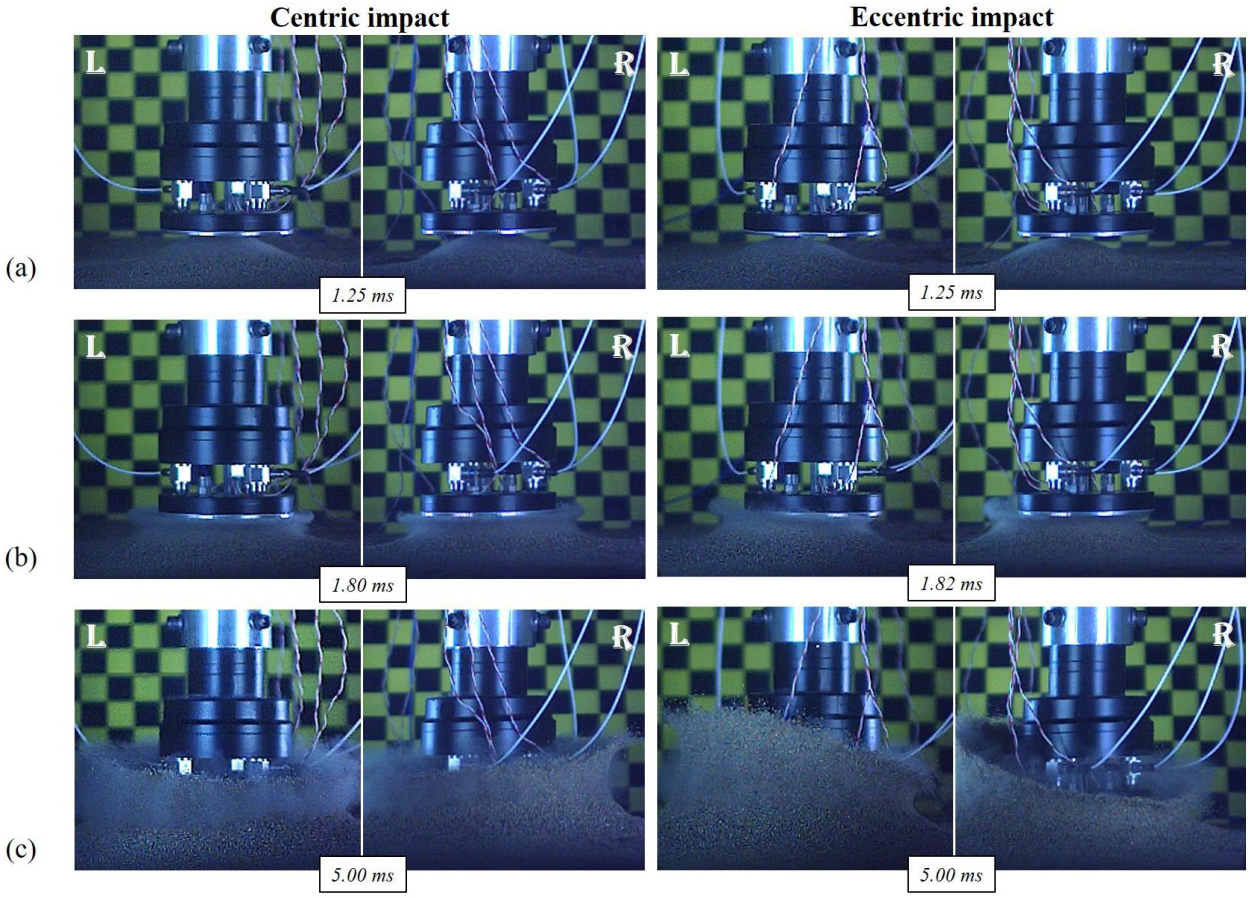

Figure 6.14. Comparisons of soil deformations and ejecta impact on the BIRG target subsequent (*left*) centric and (*right*) eccentric loading for a 1.0 gram Detasheet charge buried 5.1 cm and detonated at 20 g. Target positioned 2.5 cm aboveground. Time after detonation: (a) 1.25 ms; (b) gas-soil ejecta impact: 1.80 ms (*centric*), 1.82 ms (*eccentric*); (c) conclusion of ejecta-target interaction: 5.00 ms. Left (L) and right (R) camera images included from each test. Fiducial background 2.2 cm square grid.

The high-speed video data determined that initial soil deformation occurred approximately 0.15 ms post-detonation in both tests, and thus confirms consistency in test methodology. As evidenced at 1.25 ms, the *centric* detonation induces a gas-soil ejecta front closely aligned to the target's longitudinal axis with predominate vertical flow directionality due to the lateral soil confinement (Figure 6.14a, *left*). In contrast, at the coincident time, the *eccentric* buried charge induces an asymmetric soil ejecta flow directionality towards the target's edge, proximate load cell sensor

LC1 (Figure 6.14a, *right*; Figure 6.1). Note, the fiducial background remains visible between the target and the expanding soil dome heave at 1.25 ms (Figure 6.14a).

Furthermore, differences in their respective ejecta rheology also correlate to the BIRG's measurements of the initial gas-soil impacts on the target. In the *primary* shock impact phase, the BIRG measures the arrival of the *centric* load mechanisms, 1.80 ms post-detonation (Figure 6.14a). At the coincident time interval, the high-speed video image (Figure 6.14b, *left*) exhibits a uniform distribution of the blast loads on the target plate. In comparison, the *eccentric* detonation displays off-centered spallation with gas-soil ejecta flow skewness at the onset of the *primary* shock phase (Figure 6.14b, *right*) measured 2 μs later by the BIRG sensors (Table 6.5). After momentum transfer, the *centric* detonation yields a dispersed symmetric annulus flow around the target's circumference (Figure 6.14c, *left*). This phenomenon distinctly contrasts to the visible oblique soil ejecta curtain that encompasses the target 5.00 ms post-detonation (Figure 6.14c, *right*).

The BIRG shock measurements quantify the blast-location dependent trends, illustrated in Figure 6.14, and further resolve the resultant force imparted to the target under *centric* and *eccentric* loading. The *early* shock impact, measured by the BIRG sensors in both *centric* and *eccentric* tests occurred at 0.55 ms post-detonation and equates to an incident wave speed of 138.2 ms^{-1} (Table 6.5). Correlation to the high-speed video image (Figure 6.14a) and the BIRG data verifies that this temporal phase clearly precedes gas-soil ejecta impacts at 1.80 ms (Figure 6.14b), and thus indicates a shock wave loading mechanism, discussed in Section 6.3. Significantly, in the *eccentric* test, only LC1 measured the shock wave arrival at 0.55 ms, which preceded the LC2 and LC3 measurement by 4 μs. This can attribute to both the asymmetric detonation and consequent bow-shaped shock wave impact in the LC1 vicinity. Furthermore, the results indicate the relatively low magnitudes, typical of this early energy transfer phase, equate to a greater mean

initial force of 14.2 N at a peak time of 0.65 ms in the *centric* test, compared to the *eccentric* impact of 10.27 N at a 0.66 ms peak time (Table 6.5).

The *centric* and *eccentric* force time-histories (Figure 6.15) quantify the gas-soil ejecta mechanisms in the *primary* shock impact phase and further delineate asymmetric loading effects. In general, the BIRG tri-sensor force measurements exhibit reasonable correspondence in the *centric* load cell data.

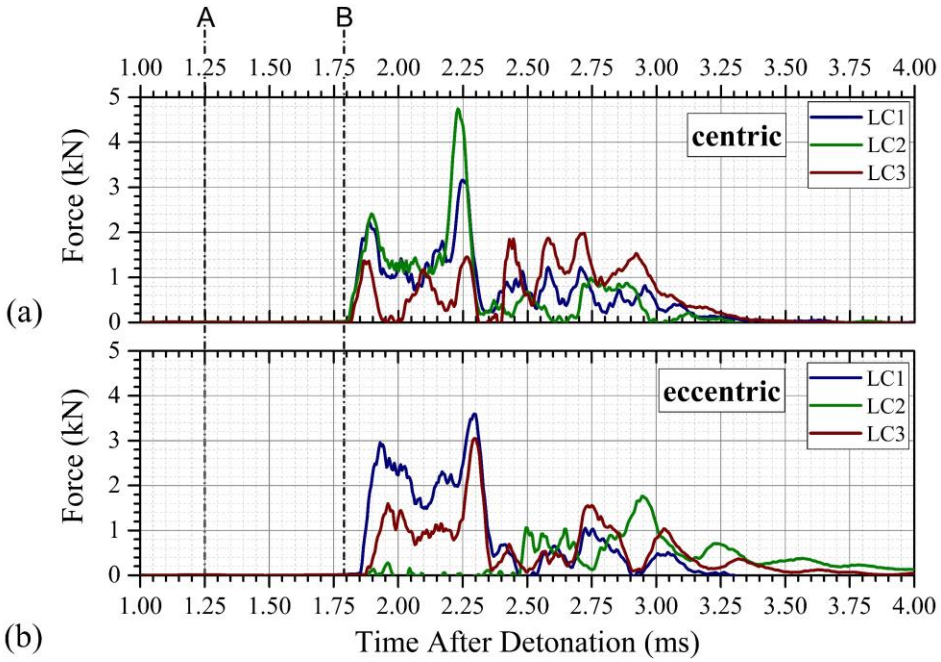

Figure 6.15. Comparision of the BIRG force time-histories subsequent (a) *centric*, and (b) *eccentric* soil blast loading during the *primary* shock phase for a 1.0 gm Detasheet charge buried 5.1 cm and detonated at 20 g. Target positioned 2.5 cm aboveground.

This sensor consistency indicates a predominate uniform momentum transfer (Figure 6.15a) as observed in Figure 6.14b (*left*). In contrast, the eccentric load cell data shows less consistency between sensors (Figure 6.15b) typical of the non-uniform, skewed distribution of the gas-soil ejecta impacts (Figure 6.14b, *right*). As expected, *eccentric* loading yielded a lower initial average peak force magnitude 1.16 kN at a later peak time 1.93 ms (Figure 6.15b), when compared to *centric* loading, 2.00 kN at 1.90 ms (Figure 6.15a). After the initial peak magnitudes,

approximately 2.25 ms post-detonation, the force time-histories both exhibit higher secondary peaks that measure 2.20 kN and 3.08 kN for the *eccentric* and *centric* blast loads, respectively. Load cells LC1 and LC3 resolve the *eccentric* resultant force imparted to the target, in contrast to the negligible force impacts at LC2. The collective data confirms the predicted *eccentric* force impact in tri-section LC1-3. The results show that average peak forces decrease with loading eccentricity, independent of the shock impact phase. Table 6.5 summarizes the mean resultant force data respective to *centric* and *eccentric* detonation loads in both shock impact phases.

Table 6.5. Summary of *centric* and *eccentric* BIRG force-time history results for a 1.0 gram Detasheet charge buried 5.1 cm and detonated at 20 g. Target positioned 2.5 cm aboveground.

	Early Shock Phase			*Primary* Shock Phase				
Impact location	Arrival Time (ms)	Avg. Initial Peak Force (N)	Peak Time (ms)	Arrival Time (ms)	Avg. 1st Peak Force (kN)	1st Peak Time (ms)	Avg. 2nd Peak Force (kN)	2nd Peak Time (ms)
Centric	0.55	14.27 ± 3.38	0.65	1.80	2.00 ± 0.58	1.90	3.08 ± 1.69	2.23
Eccentric	0.55	10.27 ± 2.15	0.66	1.82	1.16 ± 1.37	1.93	2.20 ± 1.94	2.30

To further distinguish the fundamental differences between *centric* and *eccentric* impact mechanisms, Figure 6.16 displays the accumulated impulse on the target plate under these two load configurations.

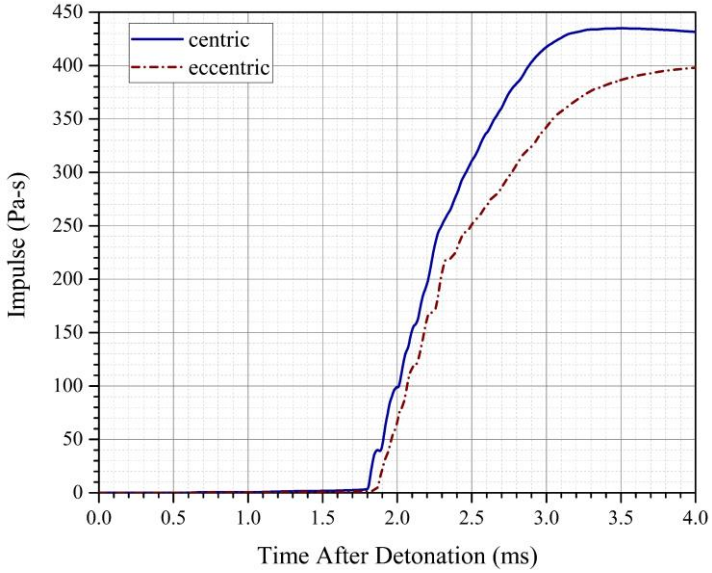

Figure 6.16. Temporal evolution of blast impulse subsequent centric (*solid-line*) and eccentric (*dashed-line*) soil blast loading during the *primary* shock phase for a 1.0 gram Detasheet charge buried 5.1 cm and detonated at 20 g. Target positioned 2.5 cm aboveground.

The comparative time-history data indicates that the *centric* loading induces the highest peak impulse, 434.7 Pa-s at 3.38 ms, when compared to the lower *eccentric* peak impulse, 397.9 Pa-s, corresponding to a 9.2% decrease. Peak blast stress magnitudes also exhibit the same impact location dependent trend: the *centric* load induces the highest peak stress, 1.00 MPa, compared to a decreased peak stress, 0.72 MPa, under *eccentric* loading (Table 6.6).

Table 6.6. Summary of the blast stress and impulse results subsequent *centric* and *eccentric* soil blast loading for a 1.0 gram Detasheet charge buried 5.1 cm and detonated at 20 g. Target positioned 2.5 cm aboveground.

		Blast Peak		
	Arrival Time (ms)	Time (ms)	Initial Stress (MPa)	Impulse (Pa-s)
Centric	1.80	3.38	1.00	434.7
Eccentric	1.82	3.99	0.72	397.9

A comparative analysis of the resultant moment magnitude and position vector components quantify the temporal and spatial distribution of *centric* and *eccentric* induced soil blast load mechanisms (Figure 6.17). After gas-soil ejecta impingement on the overlying target plate, the moment time-history exhibits two sequentially increasing peak moment magnitudes in both profiles between 1.92 ms and 2.29 ms, or an approximate 0.37 ms time interval.

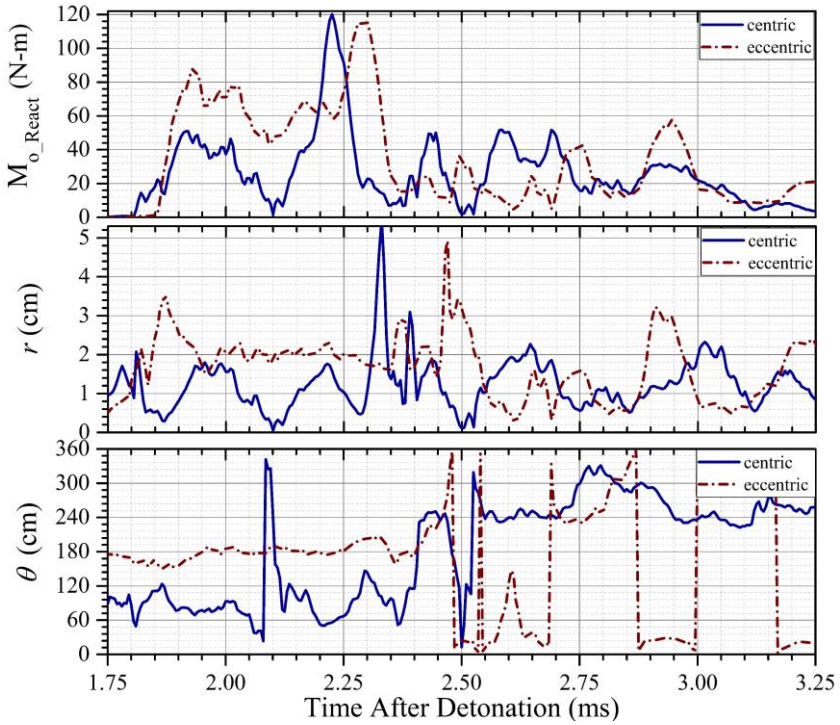

Figure 6.17. Comparisons of the BIRG (*top*) resultant moment magnitude, position vector (*middle*) radius and (*bottom*) angle time-histories for *centric* (*solid-line*) and *eccentric* (*dashed-line*) soil blast loading during the *primary* shock phase for a 1.0 gram Detasheet charge buried 5.1 cm and detonated at 20 g. Target positioned 2.5 cm aboveground.

At 1.93 ms, the eccentric load induces a greater angular momentum transfer, with a consequent initial peak magnitude of 88.3 N-m. In comparison, the initial centric induced peak magnitude at 1.92 ms, or 10 μs sooner, measured 51.0 N-m, or 1.7 times less than the eccentric peak value. As shown in Figure 6.17, both *centric* and *eccentric* profiles display a second prominent peak of increased moment magnitudes induced by the continual gas-soil ejecta impacts on the BIRG target

plate (Figure 6.14b). At 2.23 ms post-detonation, the centric peak moment increases to 120.1 N-m. The eccentric peak moment, 6 μs later, measured a slightly lower 115.6 N-m. This reduced eccentric moment can attribute to the asymmetric directly flow across the target surface, contrasted to the symmetric focus of the load mechanisms observed in the centric test (Figure 6.14b). After these second blast peak moments, the apparent lesser peak values attribute to the continual stochastic flux of gas-soil ejecta impacts on the BIRG target plate until approximately 3.0 ms (Figure 6.17). In this last phase, the blasts impact loads induce a nominal dynamic response and the BIRG target plate moments attenuate towards zero.

The schematic of the two peak resultant moment position data (r, θ), correlated to their respective peak times, depicts the typical eccentricity of the applied resultant force impact location on the target under *centric* and *eccentric* blast loading (Figure 6.18).

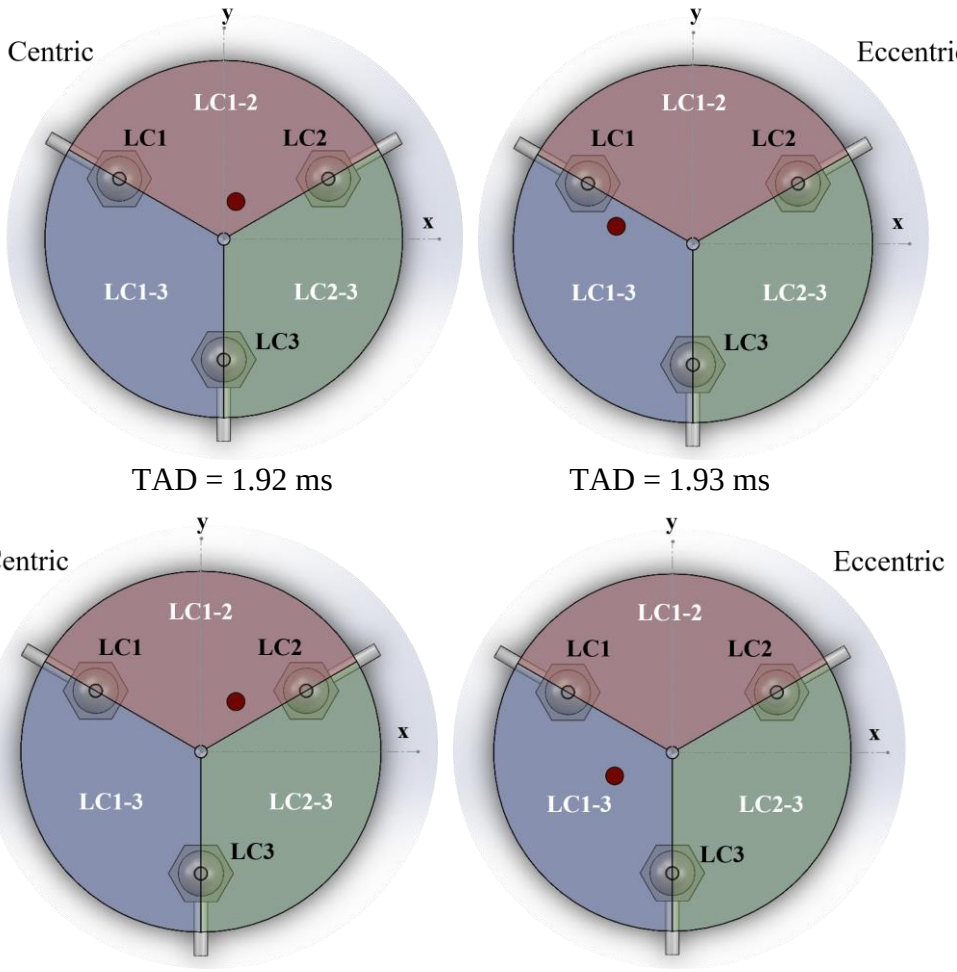

Figure 6.18. Schematics (*to-scale*) of the BIRG's impact plate free-surface illustrate the *eccentricity* of the applied resultant force (*red-dot*) relative to the load cell sensors (1, 2, 3) determined from (a) 1st and (b) 2nd peak moment data (Figure 6.17) for a 1.0 gram Detasheet charge buried 5.1 cm and detonated at 20 g. Target positioned 2.5 cm aboveground. TAD denotes time after detonation.

The initial *centric* rotational moment at 1.92 ms originates from a resultant force impact measured 1.12 cm from the axis of rotation in the LC1-2 trisection and confirms the intended centric impact (Figure 6.18a, *left*). In contrast, the *eccentric* moment originates from a resultant force impact measured 2.22 cm radially from the target center, approximately half the target's diameter in the LC1-3 trisection, proximate LC1 (Figure 6.18a, *right*) and quantifies the gas-soil ejecta impact rheology evident in Figure 6.14b. Furthermore, the results show that second peak

centric moment, at 2.23 ms, originates from a force impact measured 1.72 cm from the target's fulcrum, in the LC1-2 trisection proximate LC2. This compares to the *eccentric* induced resultant force impact at 1.77 cm from the target's mass centroid, a slight 0.05 cm difference.

In general, the *centric* and *eccentric* data demonstrates consistency in the intended force impact locations in both peak moments. As shown in Figure 6.18, both *centric* moments cause a resultant force applied near LC2, in contrast to the *eccentric* locations in-between LC1 and LC3. This indicates a nearly constant ejecta flow directionality onto the target plate during the blast momentum transfer. Significantly, the BIRG data combined with the high-speed video images, verified the test-specific intended resultant force impact location under *centric* and *eccentric* blast loading. Table 6.7 summarizes the peak moment magnitudes and times, in addition to position vector components *r* and θ.

Table 6.7. Summary of the BIRG peak resultant moment data for *centric* and *eccentric* soil blast impact for a 1.0 gram Detasheet charge buried at 5.1 cm and detonated at 20 g. Target positioned 2.5 cm aboveground.

	Impact Location	Peak Resultant		Position vector	
		Moment Mag. (N-m)	Time (ms)	r (cm)	θ (deg)
1st Peak	Centric	51.0	1.92	1.12	72°
	Eccentric	88.3	1.93	2.22	167°
2nd Peak	Centric	120.1	2.23	1.72	55°
	Eccentric	115.6	2.29	1.77	202°

A comparative analysis of blast moment dependence on gas-soil ejecta impact location evidences distinct differences in the target's rigid-body response (Figure 6.19). The *eccentric* blast loads consistently induce higher peak moments throughout the *primary* shock phase.

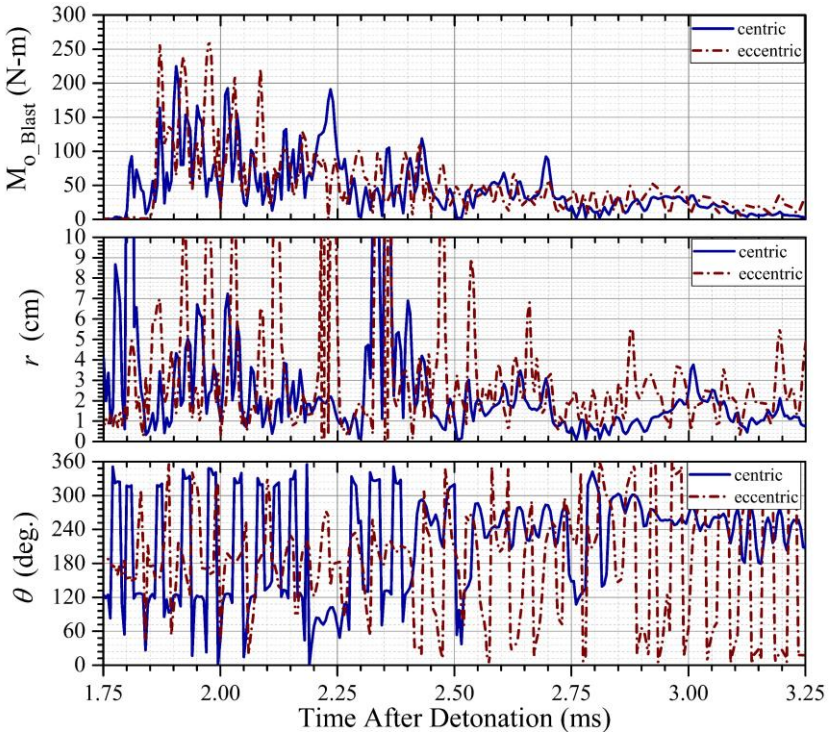

Figure 6.19. Comparisons of the BIRG (*top*) blast moment magnitude, position vector (r) (*middle*) radius and (*bottom*) angle (θ) time-histories for *centric* (*solid-line*) and *eccentric* (*dashed-line*) soil blast loading during the *primary* shock phase for a 1.0 gram Detasheet charge buried 5.1 cm and detonated at 20 g. Target positioned 2.5 cm aboveground.

Soil blast loads under *eccentric* impact induce a peak blast moment of 230.1 N-m at 1.87 ms. In contrast, the BIRG peak blast moment decreases by 29% under *centric* loading, or 163.9 N-m, at an equivalent time after detonation. Significantly, the BIRG data combined with the high-speed video image (Figure 6.14b), substantiates the test-specific intended soil blast *eccentric* impact location (proximate LC1-3) and *centric* blast loading. Table 6.8 summarizes and Figure 6.20 illustrates the initial peak blast moment results for the two load cases.

Table 6.8. Summary of the BIRG blast moment for *centric* and *eccentric* soil blast impact for a 1.0 gram Detasheet charge buried at 5.1 cm and detonated at 20 g. Target positioned 2.5 cm aboveground.

Impact Location	Peak Blast		Position vector	
	Moment Mag. (N-m)	Time (ms)	r (cm)	θ (deg)
Centric	163.9	1.87	2.1	316°
Eccentric	230.1	1.87	5.0	152°

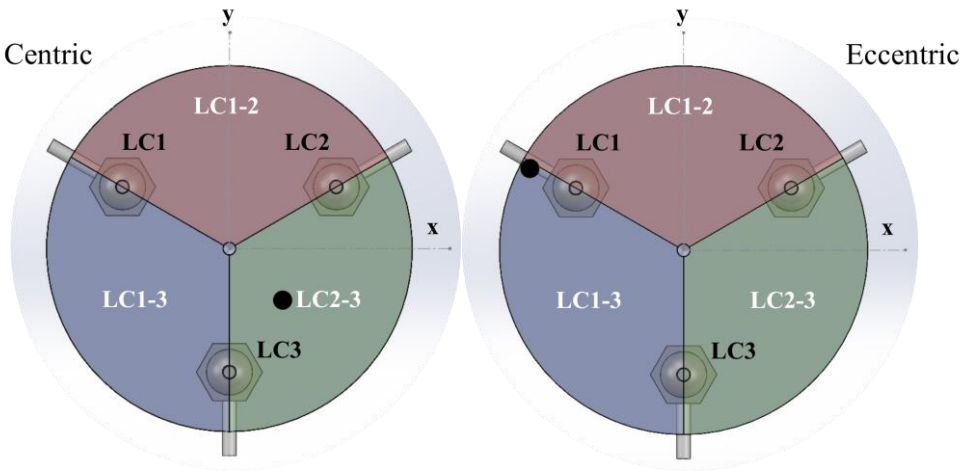

Figure 6.20. Schematics (*to-scale*) of the BIRG's impact plate free-surface illustrate the *eccentricity* of the applied blast force (*black-dot*) relative to the load cell sensors (1, 2, 3) determined the initial peak blast moment data 1.87 ms post-detonation (Figure 6.19) for a 1.0 gram Detasheet charge buried 5.1 cm and detonated at 20 g. Target positioned 2.5 cm aboveground.

6.7 BIRG Repeatability

Accurate, repeatable data strongly depends on experimental technique, specifically measurement methods. The experimental results from two test series document the BIRG's measurement capabilities to extract repeatable data consistently, independent of test configurations with distinctly different and arbitrarily chosen burial depth, charge mass, explosive type, g-level, and target height parameters.

6.7.1 Test Series 1

The first test series used a 0.5 gram Detasheet charge buried at 3.4 cm and detonated at the 30 g-level. The BIRG's free-surface positioned approximately 1 mm aboveground precluded any contact with the soil surface.

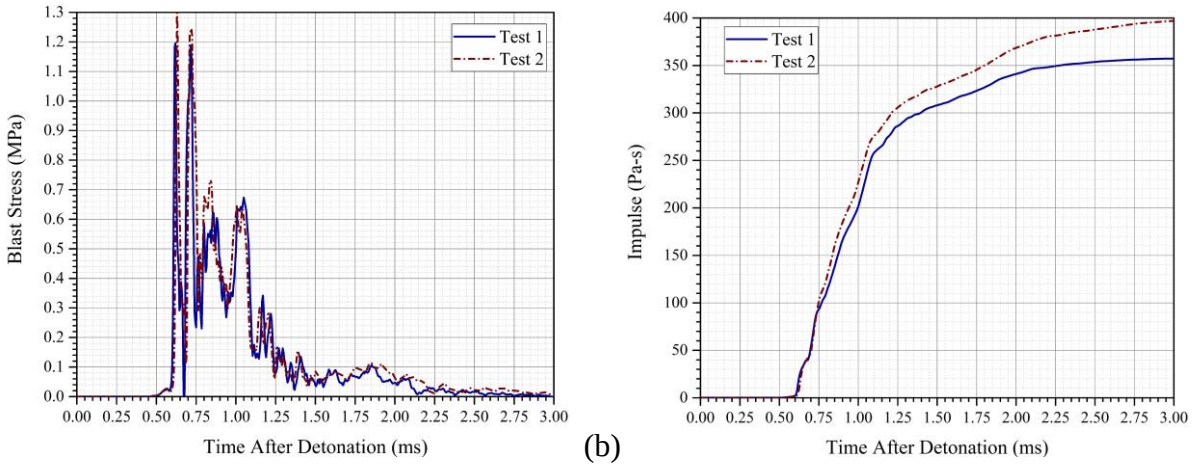

(a) (b)

Figure 6.21. Temporal distribution of (a) blast stress and (b) impulse for a 0.5 gram Detasheet charge buried 3.4 cm and detonated at 30 g. Target positioned 0.1 cm aboveground. Two repeated tests are shown distinguished by line color and style (*blue solid-line*; *red dashed-line*).

The comparison time-histories for the two tests evidence excellent data repeatability in both blast stress and impulse profiles (Figure 6.21). The initial shock impact measured by all BIRG sensors at 0.51 ms in both tests equates to an incident wave speed of 66.7 ms^{-1}. Clearly apparent in each test, the applied stress continues for an approximate 2.50 ms time-duration (Figure 6.21a). The initial and second peak blast stress values vary between tests by a nominal 7.3% and 3.3%, respectively (*relative standard deviation*, Table 6.9).

Similarly, after the high-rate impact at 0.51 ms, the impulse time-history exhibits an immediate, rapid increase with close agreement between tests (Figure 6.21b). Next, the progressive decline in blast energy consequent the gas-soil ejecta lateral flow around the target slows the impulse rate and causes a minimal 4.5% variance in impulse between tests at 1.50 ms. Furthermore, due to the

continuous flux of these stochastic load mechanism on the target and the blast energy decay towards zero at 3.00 ms, the two tests evidence a 7.5% difference in peak impulse (Figure 6.21b). Table 6.9 summarizes the peak stress and impulse results for the two independent experiments.

Table 6.9. Summary of the blast stress and impulse for two repeated tests subsequent a 0.5 gram Detasheet charge buried 3.4 cm and detonated at 30 g. Target positioned 0.1 cm aboveground.

Test	Arrival Time (ms)	1st Blast Peak		2nd Blast Peak		Impulse (*t=1.50ms)* (Pa-s)	Impulse (*t=3.00ms)* (Pa-s)
		Stress (MPa)	Time (ms)	Stress (MPa)	Time (ms)		
1	0.51	1.19	0.62	1.19	0.72	308.5	357.2
2	0.51	1.32	0.63	1.25	0.72	329.1	396.9

6.7.2 Test Series 2

A second test series further assesses the BIRG's measurement repeatability and varies the charge size (1.0 gram), burial depth (2.5 cm), target height (3.8 cm), and g-level (20 g), in addition to explosive chemistry, Composition C4 replaces Detasheet. The comparison time-histories for the two tests display data repeatability in both blast stress and impulse profiles (Figure 6.22).

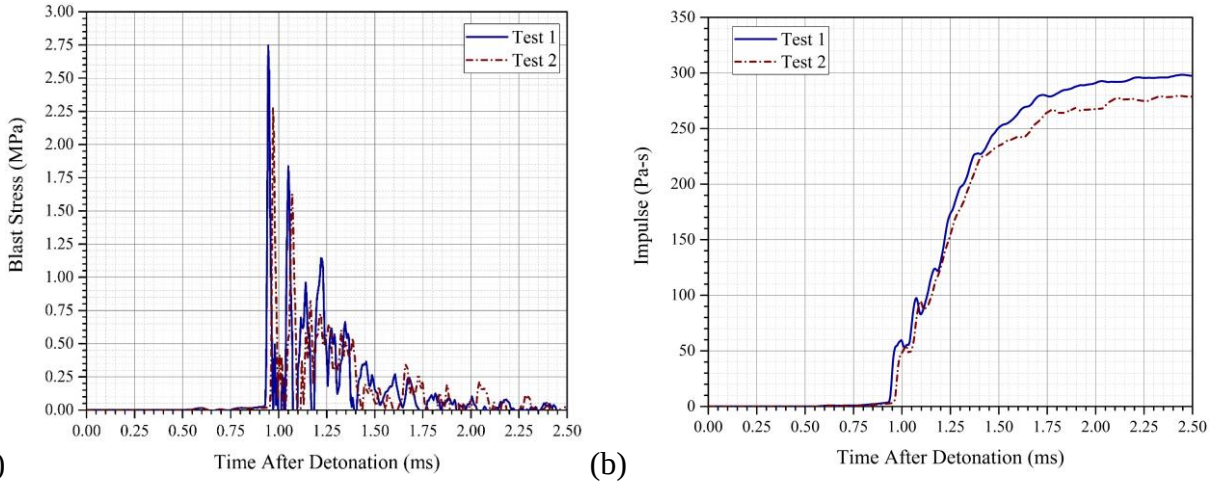

(a) (b)

Figure 6.22. Temporal distribution of (a) blast stress and (b) impulse for a 1.0 gram C4 charge buried 2.5 cm and detonated at 20 g. Target positioned 3.8 cm aboveground. Two repeated tests are shown distinguished by line color and style (*blue solid-line*; *red dashed-line*).

The initial shock impact, measured by all BIRG sensors at 0.51 ms in both tests, corresponds to an incident wave speed of 123.5 ms^{-1}. The axial compression measured by the BIRG at 0.93 ms in *Test 1*, and 20 µs later in *Test 2*, indicates the arrival of the gas-soil ejecta load mechanisms. The blast stress data demonstrates a tolerable test-retest initial peak magnitude variance of 13.2%, and the second peak blast stress values vary between tests by a nominal 8.2%. Similar to *Test 1*, coincident to the high-rate impact of the soil ejecta loads at 0.93 ms, the impulse time-histories exhibit an immediate rapid increase with close-correspondence between both tests (Figure 6.22b) and display high-fidelity data repeatability. As observed in *Test 1*, the progressive blast energy attenuation, following the gas-soil ejecta lateral flow, causes a nominal 4.5% variance between tests at 1.50 ms, the same variance at a coincident time documented in *Test 1*. At the peak impulse, 2.50 ms, the data differs by only 4.6%. Table 6.10 summarizes blast stress and impulse data for the two repeated experiments.

Table 6.10. Summary of the blast stress and impulse for two repeated tests subsequent a 1.0 gram C4 charge buried 2.5 cm and detonated at 20 g. Target positioned 3.8 cm aboveground.

Test	Arrival Time (ms)	1st Blast Peak		2nd Blast Peak		Impulse (*t=1.50ms)* (Pa-s)	Impulse (*t=2.50ms)* (Pa-s)
		Stress (MPa)	Time (ms)	Stress (MPa)	Time (ms)		
1	0.93	2.74	0.95	1.83	1.05	250.8	297.6
2	0.95	2.27	0.97	1.63	1.07	234.6	278.7

In *Test* 2, at the 2.5 cm burial depth, the high-speed video image (Figure 6.23a) recorded at 0.93 ms, or the initial gas-soil ejecta impact measured by the BIRG, illustrates the opaque, detonation products jetting through the soil cap domain creating the dilute suspension of particles dragged upward with the expanding gas cloud. These highly pressurized, hot gases visibly scorched the underside of the BIRG impact plate and etched an irregular, burn imprint (Figure 6.23b). This phenomenon indicates a predominate gas constituent load mechanism. Water removed the scorch marks prior to the next test.

(a) 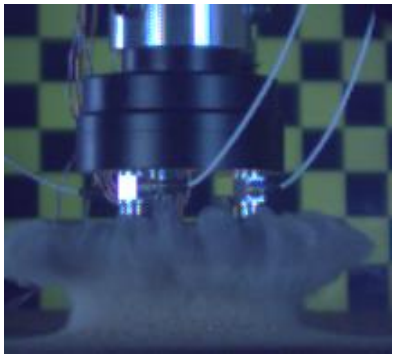 (b) 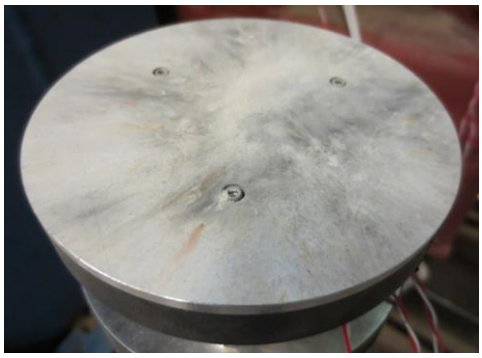

Figure 6.23. (a) High-speed video frame captured 0.93 ms post-detonation and (b) scorched BIRG distal surface for a 1.0 gram C4 charge buried 2.5 cm and detonated at 20 g. Target positioned 3.8 cm aboveground.

Collectively, the two series demonstrate a high-degree of fidelity and test-to-test repeatability. The measurement variance can contribute to the typical asymmetric ejecta flow and complex, non-uniform, gas-soil ejecta impacts induced by buried explosive loading. Past studies of the buried

blast impact phenomenon report experimental data variances between 15-50% for nominally identical tests [60–62]. Clearly evident in these two independent test series, the BIRG measurements consistently show strong correspondence, independent of test parameters. This, in turn, validates this studies experimental technique and the BIRG's capability to accurately quantify the near-field, aboveground blast environment, with test-to-test consistently below the reported 15-50% metric.

6.8 Target Height Effect

The BIRG's telescopic module readily adapts to incremental vertical translations, as detailed in the methods section. To gain insight into the target height dependence on the multiphasic gas-soil ejecta impact loads and subsequent BIRG dynamic response, this test series used a 1.0 gram Detasheet charge buried under a 5.1 cm soil overburden, detonated at 30 g, with the target positioned 0.1 cm, 1.3 cm, 2.5 cm, 3.8 cm, and 5.1 cm over the soil domain. The analytic synthesis of the BIRG's tri-sensor measurements, with supportive correlation to coincident high-speed video images at target impact times, effectively characterizes the gas-soil dome temporal and spatial distribution as a function of varied target heights (Figure 6.24).

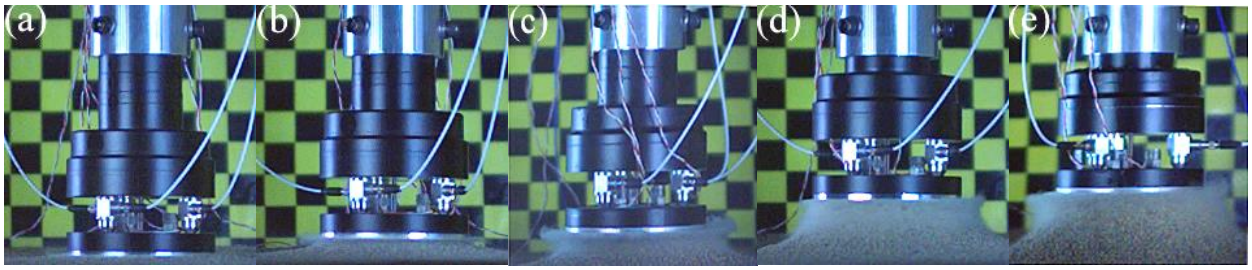

Figure 6.24. Comparisons of soil ejecta impact on the BIRG target plate with increasing distance from the soil surface for a 1.0 gram Detasheet charge buried 5.1 cm and detonated at 20 g. Target heights and corresponding *primary* shock arrival time: (a) 0.1 cm, 0.69 ms; (b) 1.3 cm, 1.35 ms; (c) 2.5 cm, 1.82 ms; (d) 3.8 cm, 2.31 ms; (e) 5.1 cm, 2.65 ms.

The average initial soil deformation at the soil-air interface measured by the dual cameras occurred approximately 0.17 ms ± 0.02 ms post-detonation. Clearly evident in Figure 6.24, the initial arrival times of the gas-soil impact appear progressively later at the elevated target heights with concurrent visual, expansion of the soil dome heave imparted to the target. For example, at 0.69 ms, the target's position 0.1 cm above the soil-air interface suppresses all soil spallation and detonation gas expansion (Figure 6.24a). Similarly, at the initial shock impact at 1.35 ms, minimal soil disaggregation and gas expansion appears at the respective 1.3 cm target height (Figure 6.24b).

The sequential video images depict the observed trend: with increasing target height, the gas-soil ejecta impacts occur progressively later and reveal an evolving soil dome heave. (Figure 6.24c-e). Also, the visual distinction between the gas-soil ejecta mechanisms becomes more evident at elevated target heights. The soil dome front at the 3.8 cm target height displays the predominate, milky-white detonation gases jetting through the soil annulus (Figure 6.24d). In, contrast, the soil dome heave at the 5.1 cm HOT clearly evidences an increased soil ejecta impact, with the soil annulus restricting the radial flow of the detonation gases across the target surface (Figure 6.24e). However, when compared to the 3.8 cm, the spatial distribution of the gas-soil mechanisms increases across the target face.

The *early* and *primary* shock impact arrival times, measured by the BIRG accelerometers, exhibit a non-linear target height dependence as shock impact arrival times lengthen with small incremental increases in HOT. In general, the data shows that *early* shock impact arrival times remain less affected by target height variance when compared to the gas-soil ejecta arrival times in the *primary* shock impact phase (Figure 6.25).

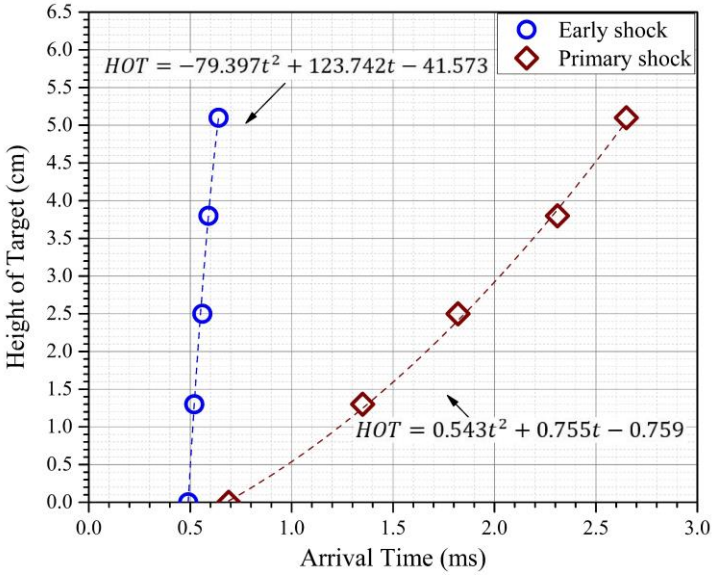

Figure 6.25. *Early* and *primary* shock phase arrival time as a function of target height for a 1.0 gram Detasheet charge buried 5.1 cm and detonated at 20 g. Included parabolic regression fits (*dotted-line*).

In the *early* shock impact phase, the high-rate detonation wave propagates through the particulate medium and impacts the BIRG's distal face, positioned 0.1 cm aboveground, at 0.49 ms, yielding an incident wave speed of 106.1 ms^{-1}. The shock wave intensity and velocity attenuate with increased distanced from the soil-air interface to the overlying target. This phenomenon causes a delayed BIRG dynamic response with consequent increased shock wave arrival times. Clearly evident, the shock wave arrival times lengthen only a nominal 15 ms, relative to the 5.0 cm increase in height of target, or 30.6 % delay between the 0.1 cm and 5.1 cm target heights respectively.

In the *primary* shock impact phase, the same mechanistic trend continues: arrival times of the gas-soil ejecta front also lengthen with elevated target height. The results quantify the previous qualitative analysis of the high-speed videos and evidence that target height dependence significantly influences the soil dome temporal and spatial distribution on the overlying target. The initial gas-soil ejecta impact measured 0.69 ms at the 0.1 cm HOT, with no visual soil

disaggregation. In contrast, at the 5.1 cm HOT, the expansive gas-soil ejecta mechanisms encompass the target plate upon impact at 2.65 ms, a 1.96 ms, or 284% delay in ejecta impact time between the 0.1 cm and 5.1 cm target heights respectively (Table 6.11).

In general, the data demonstrates that shock wave velocities decelerate with distinct 1.2-1.3 cm incremental increases in target height. (Figure 6.25). The high-rate detonation wave propagates through the soil medium and impacts the BIRG's distal face positioned 1.3 cm aboveground at 0.52 ms, yielding a wave speed of 433.3 ms^{-1}. However, as the shock wave intensity and velocity attenuates with increased distance from the soil-air interface to the overlying target, the incremental shock wave velocity decreases from 433.3 ms^{-1} to 300 ms^{-1} at the 2.5 cm and 3.8 cm target heights respectively, a 44.4% wave speed reduction. Furthermore, at the 5.1 cm target height, the shock wave velocity decelerates to 260 ms^{-1}, or a 15.4% wave speed decline. The analysis demonstrates that the shock wave velocities in the 1.3 to 5.1 cm HOT range sequentially decrease but at reduced rates (Table 6.11). Significantly, these measured shock wave speeds reach Mach ~ 1, or transonic conditions in the tested HOT range.

To further characterize target height effects, the stress wave peak magnitude (σ_{Blast}) dependence on target height can be expressed by the empirical equation:

$$\sigma_{Blast} \propto (HOT)^{-2.11} \tag{6.10}$$

and indicates a power-law reduction in peak stress with increased target height. This derived relationship from the experimental data approximates the amplitude decay of a spherically expanding compressional wave defined in elastic wave theory as r^{-2}, where r denotes the radial distance from the point source [56].

The high-speed video data, combined with particle tracking methods [63], extracted rate-dependent vertical soil ejecta displacements for these specific target heights (1.3 cm to 5.1 cm). The lack of soil disaggregation at 0.1 cm HOT precludes ejecta flow tracking and thus excludes this target height from the kinematic analysis. The average vertical soil ejecta velocities, determined by the slope of a linear regression fit to the displacement time-history data, from initial soil deformation to target impact, exhibit a monotonic relationship with HOT. Specifically, the vertical soil ejecta velocity at 1.3 cm HOT measures 12.4 ms^{-1}, and increases to 15.5 ms^{-1} at the respective 2.5 cm HOT, or a 25% increase in vertical soil ejecta velocity. This trend continues throughout the examined range: the small 1.2-1.3 cm increase in target height induces an average 23.2% increase in velocities. Collectively, the data demonstrates that a 3.8 cm increase from the 1.3 cm to the 5.1 cm target height accelerates the gas-soil ejecta front by a significant 87%. The results substantiate soil blast mechanics: the radial expansive detonation wave and pressurized explosive gases accelerate the soil ejecta heave with increased soil-target interface distance (Table 6.11).

The comparative time-histories demonstrate the target height dependence on impulse with the expected inverse proportionality (Figure 6.26). At the lowest, 0.1 cm target height and consequent the earliest arrival of the load mechanisms at 0.69 ms, the impulse profile clearly exhibits an immediate linear rise until approximately 1.3 ms post detonation. After 1.3 ms, the rate-dependent impulse steadily increases with time, but at a reduced rate as it approaches a horizontal asymptote at 3.0 ms, with the peak impulse value, 811.5 Pa-s (Table 6.11). As depicted in Figure 6.24a, at this near-surface tangent HOT, the target suppresses gas-soil ejecta expansion. The explosive energy directly impacts the target and channels the shock wave and gas-soil ejecta mechanisms to the target.

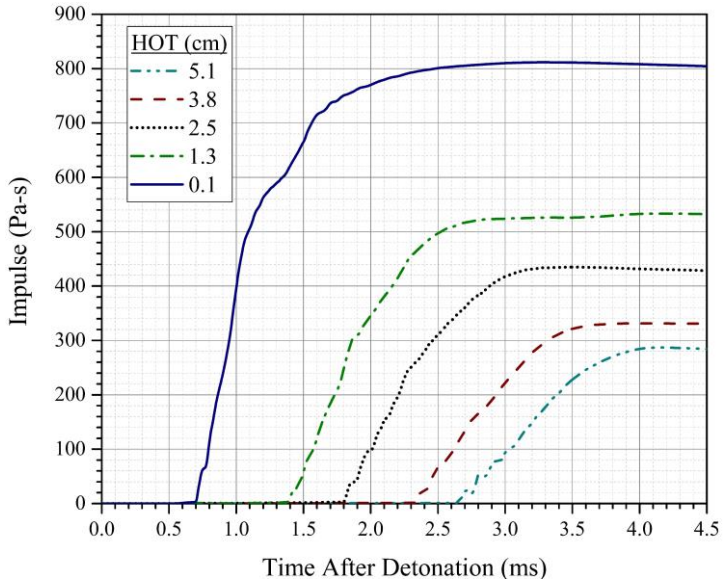

Figure 6.26. Impulse time-histories as a function of target height for a 1.0 gram Detasheet charge buried 5.1 cm and detonated at 20 g.

The results substantiate the significance of target height dependence on total blast energy transmitted to the underside of the target, such as a vehicle chassis. For example, the increase in target standoff distance from 0.1 cm to 1.3 cm, decreases the blast impulse to 533.3 Pa-s, or a 34.3% reduction in peak impulse. Alternatively, if the target height increases from 0.1 cm to 5.1 cm, the impulse decreases by more than 64%. The data evidences the same mechanistic trend throughout the tested range: as the distance from the soil-air interface to the target increases, the impact arrival times occur sequentially later and the peak impulse values decrease.

Furthermore, the rate-dependent rise to peak impulse decreases with elevated target height. Clearly apparent at the 0.1 cm HOT, the rise time to peak impulse measures the longest 2.60 ms., due to the focused, compressive stresses and longer duration of the shock wave and gas-soil ejecta impact loads at the lowest soil-air-target interface distance (Figure 6.26). In general, the rise time to peak impulse decreases with elevated target height, with a nominal 0.01 ms deviation between the 1.3 and 2.5 cm HOT, and attributes to the lower induced, peak compressive stresses and the

reduced duration of these load mechanisms as blast energy attenuates. The explosive gases and soil ejecta expand with increased disaggregation across the target thus induce lower momentum imparted to the target. The BIRG measurement of shock impact arrivals times, shock wave and soil ejecta velocities, rise to peak impulse time, and peak impulse values quantify target height dependence on the impact phenomenon and substantiate the qualitative analysis of soil blast mechanics (Figure 6.24). Table 6.11 summarizes these results.

Table 6.11. Summary of *early* and *primary* shock phase arrival times and incremental velocities, vertical soil ejecta velocities, and peak impulse for a 1.0 gram Detasheet charge buried 5.1 cm and detonated at 20 g.

	Arrival time (ms)		Incremental velocity (ms^{-1})				
HOT (cm)	*Early* shock	*Primary* shock	*Early* shock	*Primary* shock	Avg. vertical soil ejecta velocity (ms^{-1})	Rise Time to Peak Impulse (ms)	Peak impulse (Pa-s)
0.1	0.49	0.69	106.1			2.60	811.5
1.3	0.52	1.35	433.3	19.7	12.4	1.56	533.3
2.5	0.55	1.80	300.0	25.5	15.5	1.57	434.7
3.8	0.60	2.31	300.0	26.5	19.3	1.55	328.0
5.1	0.64	2.65	260.0	38.2	23.2	1.40	286.1

6.9 Explosive Mass Effect

Energetic output released by an explosive detonation remains finite and determined by explosive mass and type [27]. To examine explosive mass dependence on the dynamic response of an aboveground target, this specific test series varied charge size (0.5 gram, 0.8 gram, 1.0 gram Detasheet) for a constant 5.1 cm burial depth and target height, detonated at 10 g in dry Mason

sand. The analysis of the high-speed video images, correlated to the coincident BIRG sensor data, effectively illustrates the differences in the soil dome rheology and interactive constituents at gas-soil ejecta impact as a function of charge size (Figure 6.27).

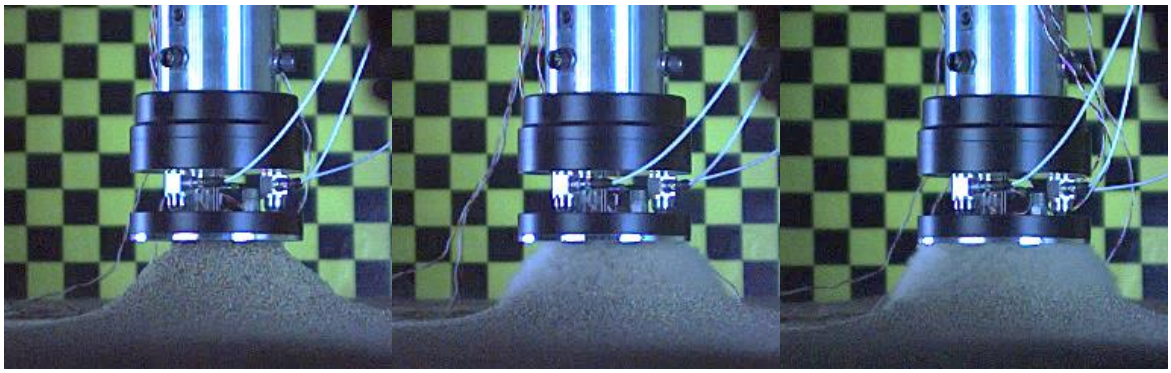

Figure 6.27. Comparisons of soil deformations for (*left*) 0.5 gram, (*middle*) 0.8 gram, and (*right*) 1.0 gram Detasheet charges buried 5.1 cm in dry sand and detonated at 10 g. Target positioned 5.1 cm aboveground. Corresponding frame (*primary* shock arrival) times with increasing charge size: 4.35 ms; 2.86 ms; 2.60 ms. Fiducial background 2.2 cm square grid.

Clearly evident, as explosive mass increases, soil dome expansion rates increase with consequent earlier blast impact arrival times. At the smallest 0.5 gram charge size and 4.35 ms target impact time (Figure 6.27, *left*), the soil dome heave displays a distinct vertical directionality, with minimal evidenced stochastic interface of the gas-soil constituents, and a predominate soil annulus aligned to the BIRG mass centroid. The soil dome rheology displays less spatial distribution across the target area relative to the increased charge size detonations. The soil annulus appears to suppress explosive gas venting and indicates initially a predominate soil ejecta load. A nominal 0.3 gram increase in explosive mass to 0.8 gram accelerates the gas-soil ejecta impact on the target to 2.87 ms, or an approximate 34% earlier target impact time (Figure 6.27, *center*). As depicted, the increased soil dome dilation disperses across the target's surface with more constituent distinction between the visible, milky-white detonation gases and soil ejecta front. The sequential increase in explosive mass to 1.0 gram decreases the impact arrival time by

0.27 ms to 2.60 ms relative to the 0.8 gram charge size (Figure 6.27, *right*). At this 2.60 ms impact, the soil dome heave displays considerable early venting (Raleigh-Taylor instability [31]) and more soil disaggregation and dispersion. In general, at the 0.8 gram and 1.0 gram charge sizes, the soil dome heave reveals increased expansion of the detonation gas and a less defined soil ejecta front, with enhanced visual resolution of the opaque, pressurized gas constituent radially permeating the air filled voids (Figure 6.27, *center* and *right*).

The experimental results from multiple test series quantify the explosive mass dependence on the buried blast impact phenomenon. In addition to test *Series 1* (5.1 cm DOB and HOT), a second test series reduced the DOB to 2.5 cm and HOT to 1.3 cm to identify mechanistic trends across different test configurations as a function of increasing explosive mass. The *early* and *primary* shock impact arrival times, recorded by the BIRG tri-sensor accelerometers, exhibit an inverse monotonic relationship with charge size (Figure 6.28).

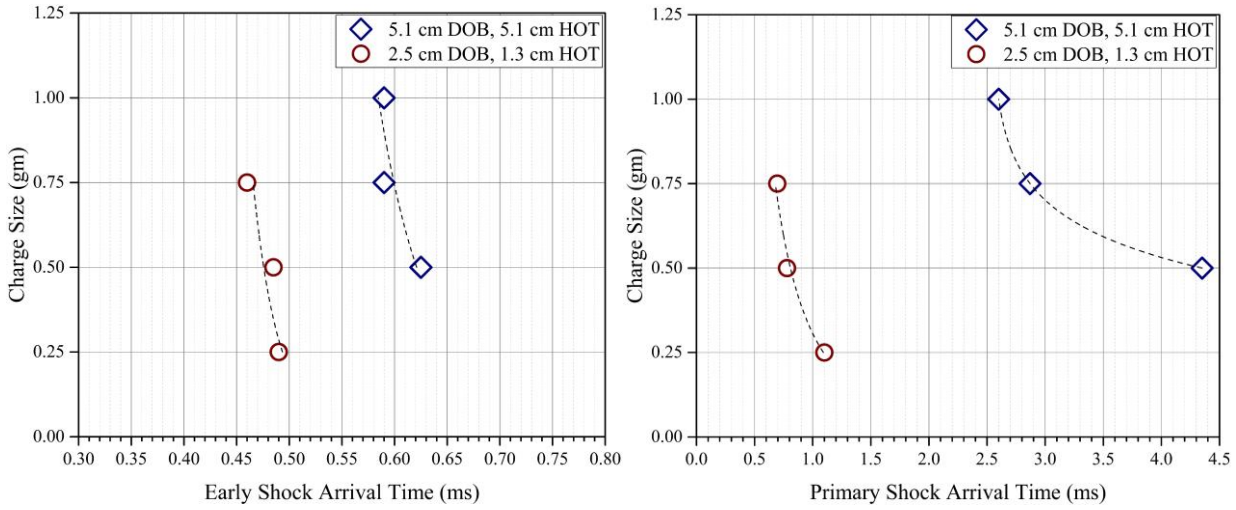

Figure 6.28. Early (*left*) and primary (*right*) shock arrival times as a function of Detasheet charge size buried in dry sand and detonated at 10 g for various burial depths and target heights.

Collectively, the data clearly documents the expected high-rate dynamic behavior: impact arrival times progressively accelerate with higher energetic output, independent of the burial depth

and target height in both shock impact phases. For example, in the *early* shock phase, the highly transient shock wave impacts the target at 0.63 ms subsequent the 0.5 gram detonation, and the shock wave arrival times shorten to 0.59 ms, and 0.58 ms with respective explosive mass increases in *Series 1*, or a nominal variance of 0.05 ms relative to the 0.5 gram explosive mass increase (Figure 6.28 *left*, Table 6.12). The shock wave arrival times equate to higher incident wave speeds of 161.9 ms^{-1} (0.5 gram); 173.0 ms^{-1} (0.8 gram); and 175.9 ms^{-1} (1.0 gram).

Furthermore, in *Series 2*, the shock wave arrival times demonstrate the same mechanistic trend and also decrease as a function of increasing charge size (Table 6.12). The shock wave target impact times occur at 0.49 ms, 0.48 ms, and 0.46 ms with the respective increasing charge sizes. Again the BIRG accelerometers measure minimal variance between shock wave arrival times. In this second test series, the shock wave arrival times equate to incident wave speeds of 77.6 ms^{-1} (0.3 gram); 79.2 ms^{-1} (0.5 gram); and 82.6 ms^{-1} (0.8 gram). With less blast energy potential, or explosive mass, the shock wave intensity and velocity decline.

The previous analytic synthesis of the high-speed videos with the BIRG measurements (S*eries 1*) delineated soil dome rheology and the complex, interfacial gas-soil ejecta loads as a function of increasing charge size at target impact time (Figure 6.27). The results confirm the previous analysis: as energetic output increases, gas-soil dome expansion rates increase and target impact times accelerate, independent of burial depth and target height (Figure 6.28, Table 6.12). In contrast to the shock wave mechanism, these loads exhibit a non-linear rate decrease as a function of reduced charge size, indicative of a greater explosive mass dependence. Clearly evident, the complex, multiphasic soil blast mechanics significantly delay gas-soil ejecta arrival times when compared to the detonation wave transmission in the *early* shock phase (Table 6.12). Furthermore, in *Series 1*, with the 5.1 cm DOB and HOT parameters, the 0.5 gram charge induces the latest gas-

soil ejecta target impact at 4.25 ms. In comparison, the 1.0 gram charge accelerates the soil dome heave (Figure 6.27, *right*) and impact occurs at 2.60 ms, a significant 1.65 ms decrease in gas-soil ejecta arrival time. Similarly, the second test series exhibits the same trend: the smallest, 0.3 gram charge, induces the latest impact time at 1.10 ms, and the 0.8 gram charge accelerates the loads to 0.70 ms (Table 6.12). The higher blast energy with increased charge size drives the overlying soil radially towards the soil surface at progressively elevated velocities and thus accelerates the gas-soil ejecta momentum transfer to the target (Figure 6.27, Table 6.12)

The same soil blast mechanics induce higher kinetic energy transfer to the target as a function of increased charge size. The comparative time-histories specific to test *Series 1* (5.1 cm DOB and HOT) quantify the temporal evolution of the blast impulse (Figure 6.29). The results indicate a significant explosive mass dependence on peak impulse throughout the examined range.

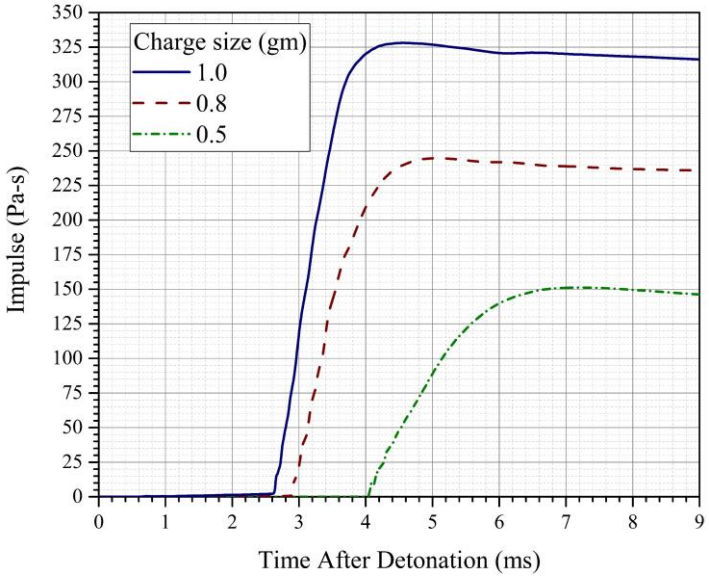

Figure 6.29. Impulse time-histories for a 0.5 gram (*dash-dot-line*), 0.8 gram (*dashed-line*), and 1.0 gram (*solid-line*) Detasheet charge buried 5.1 cm in dry sand and detonated at 10 g. Target positioned 5.1 cm aboveground.

As shown in Figure 6.29, subsequent the 1.0 gram detonation, the high-rate gas-soil ejecta mechanisms impact the target at 2.60 ms and induce an immediate BIRG dynamic response. The

impulse profile exhibits a rapid linear rise until approximately 3.80 ms post-detonation. After 3.80 ms, due to blast energy attenuation, the impulse steadily increases with time, but at a reduced rate as it approaches a horizontal asymptote at 4.50 ms, and peak impulse at 328.1 Pa-s. The results substantiate the significance of explosive mass dependence on blast energy transfer to a target. For example, with small incremental decreases in explosive mass to 0.8 gram and 0.5 gram charge sizes, peak magnitudes decline by 25% and 38.4%, respectively. Alternatively, if the charge size decreases from 1.0 gram to 0.5 grams, peak impulse decreases from 328.1 Pa-s to 151.0 Pa-s, respectively, or a 117% decline in blast load momentum transfer (Table 6.12).

Because explosive mass determines energetic output, the rise time to peak impulse consistently decreases with increasing charge size. For example, the 1.0 gram detonation induces an immediate dynamic response and the rise to peak impulse measures the lowest compressive load duration, 1.88 ms. In comparison, the 0.5 gram charge rise time to peak impulse lengthens to 3.01 ms, or a 60% increase in blast loading (Table 6.12). As shown in the high-speed video images (Figure 6.27), higher energetic release increases the temporal and spatial distribution of the gas-soil ejecta heave at target impact. The results substantiate that these load mechanisms induce higher peak magnitudes with significantly reduced compressive loading duration as a function of explosive mass.

Similar to the analysis of shock arrival times, the comparison of the two test series demonstrates that increased explosive mass consistently induces greater peak impulse magnitudes across different test configurations (Figure 6.30). The results verify that peak impulse exhibits a monotonic explosive mass dependence on target height and burial depth.

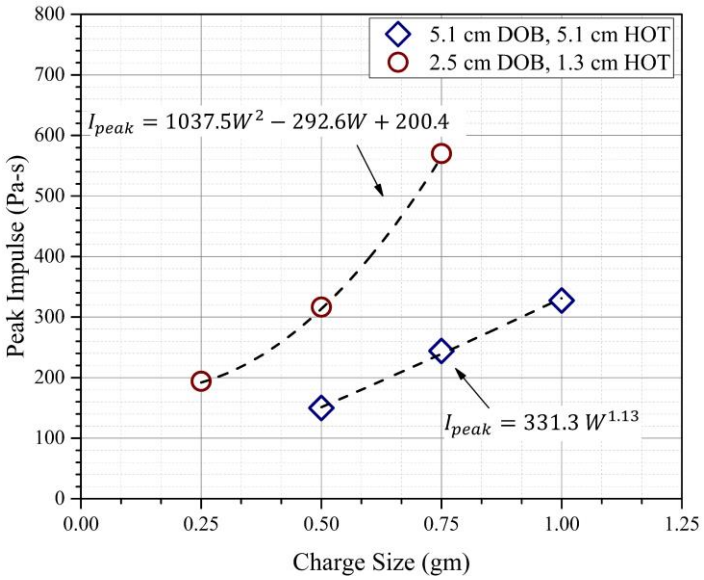

Figure 6.30. Peak impulse as a function of Detasheet charge size buried in dry sand and detonated at 10 g for various burial depths and target heights. Best fit regression lines and equations included (*dashed-lines*).

In test *Series 1*, with equivalent 5.1 cm HOT and DOB, a regression analysis determined that the data adheres best to a power-law fit as peak impulse approximates a linear relationship with charge size. As discussed previously, for this specific test configuration, peak impulse magnitudes measure significantly higher with increased energetic output. The data displays the same mechanistic trend in the second test series: peak impulse values increase with higher energetic output (Figure 6.30). Furthermore, in test *Series 2*, with a reduced soil-target interface and burial depth (HOT/DOB = 0.52), a regression analysis determined a non-linear, parabolic data fit. The results indicate that less soil overburden pressure at the 2.5 cm burial depth and closer target proximity to the charge at 1.3 cm, induces higher kinetic energy transfer to the target when comparted to test series 1, at a constant charge size. For example, a 0.8 gram charge in test *Series 1* induces a 244.7 Pa-s peak impulse compared to a significantly higher 570.2 Pa-s in test *Series 2*, or a 57% increase in momentum transfer.

Collectively the results substantiate that increased energetic release per unit volume of explosive accelerates the radiating shock wave speeds and soil dome expansion rates. Greater explosive mass transmits more energy into the soil as mechanical work and increases crater excavation, soil surface deformation, and peak pressures from the explosive gas products driving the expanding gas-soil ejecta front toward target impact. The data delineates the explosive mass dependence and evidences an increased gas-soil ejecta target impact load at an increased rate, with subsequent higher impulse magnitudes and lower compressive load duration. Table 6.12 summarizes the early and primary shock impact arrival times, rise times, and peak impulse for the two different test series.

Table 6.12. Summary of *early* and *primary* shock phase arrival times, peak stress and impulse for multiple Detasheet charge sizes buried in dry sand and detonated at 10 g.

				Arrival time (ms)			
	W (gm)	HOT (cm)	DOB (gm)	Early shock	Primary shock	Rise time (ms)	Peak Impulse (Pa-s)
Series 1	0.5	5.1	5.1	0.63	4.35	3.01	151.0
	0.8	5.1	5.1	0.59	2.87	2.11	244.7
	1.0	5.1	5.1	0.58	2.60	1.88	328.1
Series 2	0.3	1.3	2.5	0.49	1.10	2.46	194.7
	0.5	1.3	2.5	0.48	0.77	1.80	316.6
	0.8	1.3	2.5	0.46	0.70	1.21	570.2

6.10 Burial Depth Effect

To gain insight into the burial depth effect on the impact phenomenon, the BIRG sensor data, with supportive correlation to coincident high-speed video images, further delineates the complex, interfacial blast load mechanisms at target impact (Figure 6.31). This test series used a 1.0 gram

Detasheet charge buried in dry sand at increasing depths (2.5 cm, 5.1 cm, and 7.6 cm) and detonated at 10 g for a constant 5.1 cm target height.

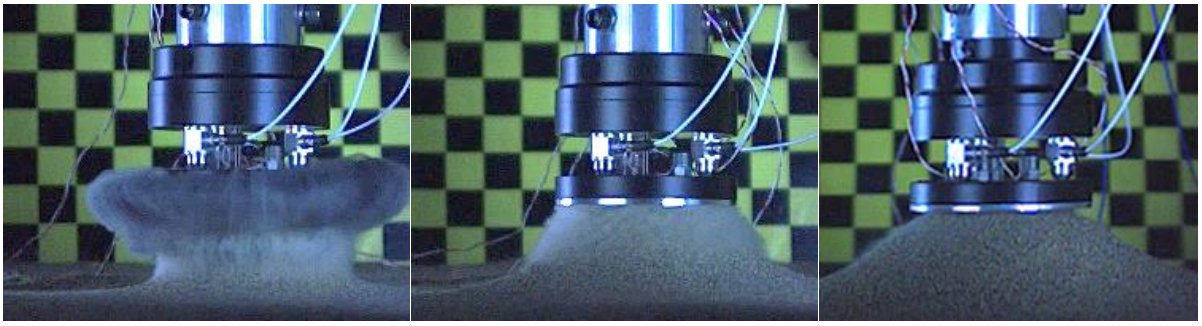

Figure 6.31. Comparisons of soil deformations for a 1.0 gram Detasheet charge buried (*left*) 2.5 cm, (*center*) 5.1 cm, and (*right*) 7.6 cm in dry sand and detonated at 10 g. Target positioned 5.1 cm aboveground. Corresponding frame (*primary* shock arrival) times with increasing burial depth: 0.88 ms; 2.60 ms; 5.20 ms. Fiducial background 2.2 cm square grid.

As shown in Figure 6.31, burial depth dependence significantly affects the soil dome rheology, expansion rate, and the constituent interfaces. At the shallower 2.5 cm burial depth and earliest 0.88 ms arrival time of the load mechanisms, the compressed opaque, explosive gases jet past the soil surface, creating the dilute suspension of soil particles dragged upward with the detonation products (Figure 6.31, *left*). The pronounced vertical flow of the expanding gas products, pushing the soil ejecta front to the overlying target, resembles a 'mushroom-cloud' profile and indicates a predominate explosive gas impact mechanism. This swirling vortex-like flow of hot, pressurized detonation gases and dense high-velocity soil ejecta turbulently intermix and create extremely complex, stochastic interfaces that wrap around and encase the target plate simultaneous to impact.

A 2.5 cm increase in the lithostatic layer delays gas-soil ejecta impact on the target to 2.60 ms, or a significant 66.2% increase in the blast load arrival time (Figure 6.31, *middle*). The higher effective lateral soil stress proximate the charge at the 5.1 cm DOB restricts the radial flow of the detonation products and soil ejecta heave for a longer time period, and thus lengthens initial soil deformation, the temporal and spatial evolution of the gas-soil ejecta front, and resultant target

impacts. Furthermore, at the 5.1 cm burial depth, the gas-soil ejecta front expands in a predominantly vertical direction, due to the lateral soil confinement, with the apparent uniform, hemispherical mound growth, not yet transitioned to the lateral flow evidenced at the 2.5 cm burial depth. Also, at target impact the soil dome heave displays the early gas venting and the interfacial constituent distinction between the gas and soil mechanisms remains less resolved because the soil annulus confines detonation gases relative to the 2.5 cm DOB.

The same soil blast mechanisms discussed above lengthen target impact at the 7.6 cm burial depth to 5.20 ms, or a 50% delay compared to the 5.1 cm DOB (Figure 6.31, *right*). With increased soil overburden, the energy transfers to mechanical work, with more soil ejected from the blast-excavated crater, and the continuous radiating pressure drives more overlying soil into air. The deeply-buried detonation induces the characteristic bell-shaped soil dome heave, with gradual, sloping sides and broad base. The comparison between the 5.1 cm and 7.6 cm DOB (Figure 6.31 *center, right*) shows that the included angle of the soil dome increases as the burial depth decreases. As evidenced in Figure 6.31 (*right*), the increased soil volume encases the explosive gases in a dense soil annulus that suppress explosive gas venting during initial target loading, and indicates a pronounced soil ejecta load mechanism with less spatial distribution of the load mechanisms across the target, relative to the 5.1 m burial depth.

The results in Figure 6.32 quantify the burial depth dependence on the *early* and *primary* shock impact phases. The multiple test series that varied both burial depth and charge size to characterize shock arrival times across different test configurations. In general, shock wave and gas-soil ejecta target impact times adhere well to an exponential regression fit throughout the examined DOB range (Figure 6.32).

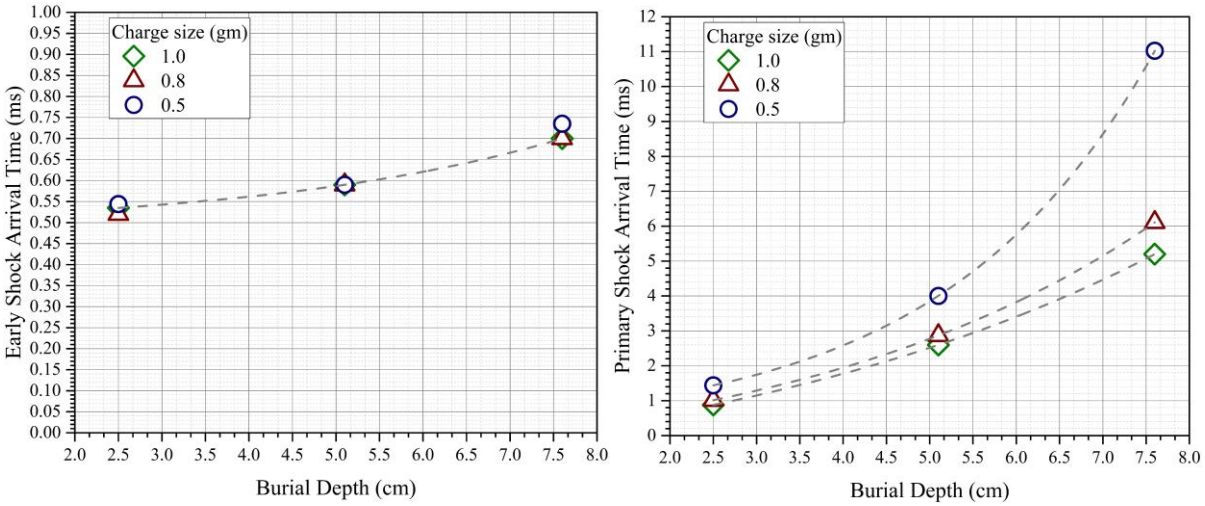

Figure 6.32. *Early* (*left*) and *primary* (*right*) shock arrival times as a function of burial depth in dry sand for 0.5 gram, 0.8 gram, and 1.0 gram Detasheet charges detonated at 10 g. Target positioned 5.1 cm aboveground. Best fit regression lines included (*dashed-lines*).

In general, shock wave arrival times lengthen with increased soil overburden, independent of charge size (Figure 6.32, *left*). In the *early* shock impact phase, as the lithostatic pressure increases with deeper burial depths, more explosive energy transfers to soil compaction and creation of soil ejecta, effectively reducing shock wave intensity and propagation rates [27]. The BIRG measurements of the shock wave impact times exhibit minimal variance between the respective burial depths throughout the tested explosive mass range in all three test series (Table 6.13). Noteworthy, at the 5.1 cm burial depth, the shock wave impact time measures consistently 0.59 ms at the 1.0 gram. 0.8 gram, and 0.5 gram Detasheet charge detonations. The highest variance, a nominal 0.04 ms occurs at the 7.6 cm burial depth when the 1.0 gram charge reduces to a 0.5 gram explosive mass.

Similarly, incident shock wave speeds exhibit minimal variance as a function of increasing burial depth and measure as follows: 142.1 ms^{-1}, 173.0 ms^{-1}, and 173.8 ms^{-1}. As anticipated, the greatest deceleration occurs between the 2.5 cm and 5.1 cm DOB, a 21.7% delay in target impact. The incremental increase in confining stress to the 7.6 cm burial depth decelerates shock wave

speed by a nominal 0.08 ms^{-1}. Furthermore, the data indicates that shock wave peak magnitudes transmitted to the overlying target decline with increasing stress confinement. For example, a 1.0 gram charge buried 2.5 cm, 5.1 cm, and 7.6 cm yielded shock wave peak magnitudes of 9.17 kPa, 6.20 kPa, and 2.61 kPa, respectively. Stress confinement at the 7.6 cm relative to the 5.1 cm DOB reduces shock wave peak magnitude by a significant 57.9%. As previously discussed, as the soil confinement increases, more explosive energy transmits through the soil skeleton rather than dispersing to the air [37]. The blast induced compressive shock wave propagates radially through the particulate medium and reaches the density discontinuity at the soil-air interface. The acoustic mismatch causes most of the shock wave to reflect back into the soil medium as a tensile wave. The remaining energy damped compressive wave then transmits upward which results in lower shock wave magnitudes with increasing burial depth (Figure 6.32, *left*).

The previous analytic synthesis of the high-speed video images with the BIRG measurement distinguishes the significantly different blast load mechanisms with increasing burial depth for the 1.0 gram detonation (Figure 6.31). The *primary* shock impact time-history now includes data from the 0.8 gram and 0.5 gram charge sizes (Figure 6.32, right). The results confirm the expected trend: gas-soil ejecta mechanisms arrive significantly later with increasing burial depth throughout all three test series (Table 6.13). However, the data also shows that between test series, less energetic release further delays impact times at a constant DOB. For example, at the 5.1 cm DOB, post-detonation of the 1.0 gram charge, the impact time measures 2.60 ms. In comparison, at the same 5.1 cm DOB, the 0.5 gram charge size induces the gas-soil ejecta front arrival time at 4.01 ms, a 35 % delay in target impact. The results indicate that explosive mass dependence on the gas-soil mechanisms target impact times remains more significant when compared to the burial depth parameter (Table 6.13).

In the preceding crater morphology analysis (Chapter 4), the results evidenced an experimentally determined 'optimal' burial depth that induced maximum crater dimensions. Here, the data indicates that the same phenomenon applies to kinetic energy transfer: an optimal burial depth maximizes the momentum imparted to an aboveground target. The comparative time-histories quantify the temporal evolution of the total blast impulse transmitted to the BIRG from the subsurface 1.0 gram Detasheet charge detonations at 2.5 cm, 5.1 cm, and 7.6 cm, and exhibit the apparent optimal DOB for the maximum peak impulse in the tested range (Figure 6.33).

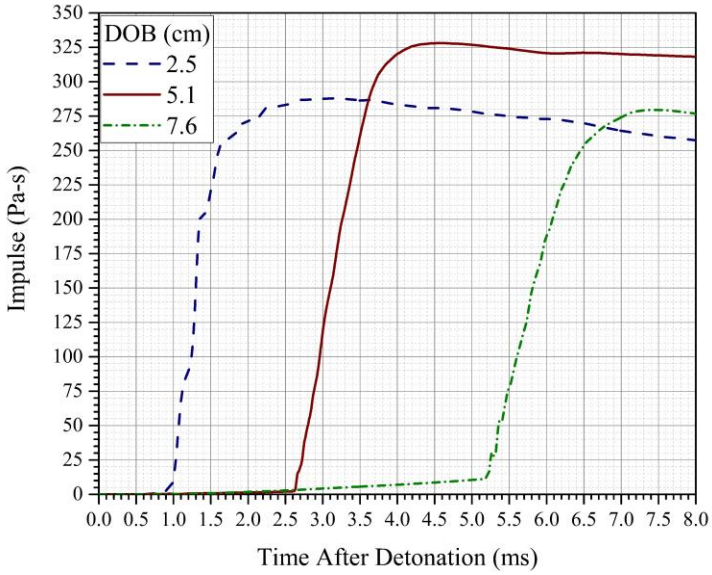

Figure 6.33. Impulse time-histories for a 1.0 gram Detasheet charge buried 2.5 cm, 5.1 cm, and 7.6 cm in dry sand and detonated at 10 g. Target positioned 5.1 cm aboveground.

As observed in Figure 6.33, the results depict the expected rate-dependent behavior: an immediate target dynamic response with the rapid linear increase in momentum transfer subsequent gas-soil ejecta impact at the respective arrival times. As illustrated in the video image, (Figure 6.31, *left*), the shallowest 2.5 cm burial depth and earliest 0.88 ms arrival time, the 'mushroom-cloud' profile indicates a predominate explosive gas mechanism at target impact. This highly transient compressive load duration measures a nominal 0.34 ms with the attendant 285.4

Pa-s peak impulse (Table 6.13). Charges detonated at shallower burial depths (2.5 cm) with less overlying soil, typically eject a smaller volume of soil [4] and thus yield lower impulse values relative to deeper burial depths.

As the distance from the explosive to the soil-air interface gradually increases, the soil's lateral confining pressure focuses the compacted, (higher packing density), gas-soil ejecta front in a predominate vertical directionality (Figure 6.31, *middle*). This burial depth effect directs the kinetic flow of the increased soil ejecta inertia force to the target [3,26]. Furthermore, the soil volume ejected from the blast-excavated crater increases with burial depth and blast load duration lengthens by 1.65 ms relative to the 2.5 cm DOB or an 82.9% longer target impingement (Table 6.13). Collectively, these soil blast mechanics induce the highest peak impulse, 327.5 Pa-s, at the intermediate 5.1 cm burial depth (Figure 6.33). The data indicates for this specific test series, the maximum peak impulse coincides with the optimal 5.1 cm burial depth. This further verifies that soil ejecta contributes a significant source of energy transfer to the overlying target. In addition, the results demonstrate that DOB is not monotonic [4] and can be adjusted to maximize peak impulse, analogous to crater dimensions [63].

Following this optimal 5.1 cm burial depth, or transition point, the peak impulse declines to 277.4 Pa-s or a 15.3% reduction in blast force impact at the 7.6 cm DOB. Due to the increased confining stress proximate the charge, more explosive energy transmits through the particulate medium and less dissipates to the soil surface [37]. This energy transfer mechanism causes compressive and shear soil distortions via grain fracture and elastoplastic soil deformation adjacent to the buried charge [4,5]. More energetic release transfers to soil compaction and soil ejecta formation [26]. As observed in Figure 6.31 (*right*), the soil annulus suppresses gas venting and the spatial load distribution across the target decreases, with a predominate soil ejecta impact. The

compressive load time lengthens to 2.70 ms, or a significant 2.35 ms increase in impact load duration compared to the 2.5 cm DOB (Table 6.13). However, the blast energy intensity attenuates as the extremely hot, pressurized gases are forced to drive more compacted overlying soil, with the consequent decrease in blast momentum transferred to the target at 7.6 cm DOB.

As anticipated, these same soil blast mechanisms induce similar burial depth effects on impulse across different test configurations. The data documents burial depth dependence on peak impulse for 1.0 gram, 0.8 gram, and 0.5 gram charge size detonations under multiple overburdens (Figure 6.34).

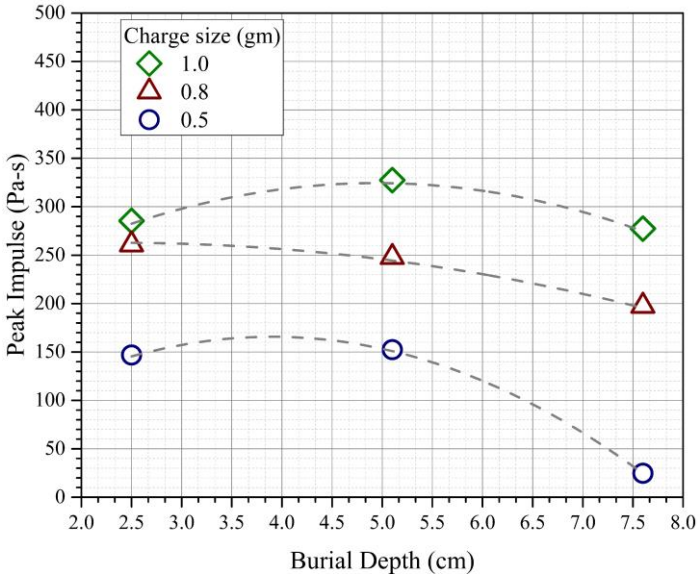

Figure 6.34. Peak impulse as a function of burial depth in dry sand for 0.5 gram, 0.8 gram, and 1.0 gram Detasheet charges detonated at 10 g. Target positioned 5.1 cm aboveground. Best-fit regression lines included (*dashed-lines*).

In general, the comparison plot evidences the same mechanistic loading trends with the apparent optimal burial depth, an approximate 5 cm, yielding maximum peak impulse values, independent of charge size. At 0.5 gram charge size, the 2.5 cm burial depth, with a predominate explosive gas mechanism and less soil ejecta loading, the peak impulse measures 146.9 Pa-s (Table 6.13). Then, the intermediate, or optimal 5.1 cm DOB, similar to the 1.0 gram charge, yields the maximum peak

impulse value, 152.4 Pa-s, consequent the increased soil ejecta impact loads. Blast energy transfers to the soil with subsequent intensity attenuation at the increased 7.6 cm soil overburden and the peak impulse declines to a significantly lower value, 24.7 Pa-s, or an 84% decrease in blast momentum transfer (Table 6.13). This data further substantiates that burial depth can be adjusted to maximize peak impulse analogous to crater dimensions.

Peak impulse displays a monotonic relationship with burial depth for the 0.8 gram charge as peak values gradually decrease with increased confinement. At the 2.5 cm DOB, the 0.8 gram charge detonation yields a 261.0 Pa-s peak impulse. Instead of the expected trend, the peak impulse value decreases at the 5.1 cm DOB by a nominal 12.8 Pa-s. This can be attributed to the complex, stochastic gas-soil ejecta interfaces with slight variances in constituent loading, i.e. an increase in detonation gas upon impact. The lowest peak impulse value, 197.5 Pa-s, correlates to the highest soil confining stress at the 7.6 cm DOB. The results demonstrate that burial depth dependence significantly affects the fluid dynamics, soil ejecta kinematics, loading constituents, impact times, and subsequent blast peak impulse. Table 6.13 summarizes the *early* and *primary* shock phase arrival times, soil blast load duration, and peak impulse for the three test series.

Table 6.13. Summary of *early* and *primary* shock phase arrival times, soil blast load duration, and peak impulse for multiple Detasheet charge sizes under various dry sand overburdens and detonated at 10 g. Target positioned 5.1 cm aboveground.

	DOB (cm)	W (gm)	HOT (cm)	Arrival time (ms) *Early* shock	Arrival time (ms) *Primary* shock	Impact duration (ms)	Peak Impulse (Pa-s)
	2.5	1.0	5.1	0.54	0.88	0.34	285.4
Series 1	5.1	1.0	5.1	0.59	2.60	1.99	327.5
	7.6	1.0	5.1	0.70	5.20	2.70	277.4
	2.5	0.8	5.1	0.52	1.02	1.73	261.0
Series 2	5.1	0.8	5.1	0.59	2.87	2.23	248.2
	7.6	0.8	5.1	0.70	6.11	3.42	197.5
	2.5	0.5	5.1	0.54	1.44	2.17	146.9
Series 3	5.1	0.5	5.1	0.59	4.01	2.70	152.4
	7.6	0.5	5.1	0.74	11.02	8.28	24.7

6.11 Centrifugal Force Effect

The prior in-depth investigation presented in Chapter 3 and Chapter 4 characterized gravity-dependence on soil ejecta kinematics and crater morphology. Furthermore, the results substantiated that small charge detonations at increased acceleration can simulate and predict large explosive yields by centrifuge scale relationships (Table 2.1). Because geomaterials behavior strongly depends on the in-situ stress condition, this analysis provides insight into the gravitational forcing effect on the kinetic energy transfer to an aboveground target. The empirically derived relationships suitable to prototype scale impacts are discussed in Section 6.17.

The first test series in this parametric study used a 1.0 gram Detasheet charge, buried 5.1 cm, and detonated at 10 g, 20 g, and 30 g-levels with model burial depths scaling to 0.05 m, 1.02 m, and 1.50 m, respectively. The 1.3 cm HOT was specifically selected to minimize gas expansion

and soil disaggregation, and thus isolate gravity dependence at impact. As shown in Figure 6.35, for the near-surface HOT, the high-speed video images coincident to the BIRG's measured arrival times exhibit minimal soil spallation with nominal detonation gases throughout the tested g-levels.

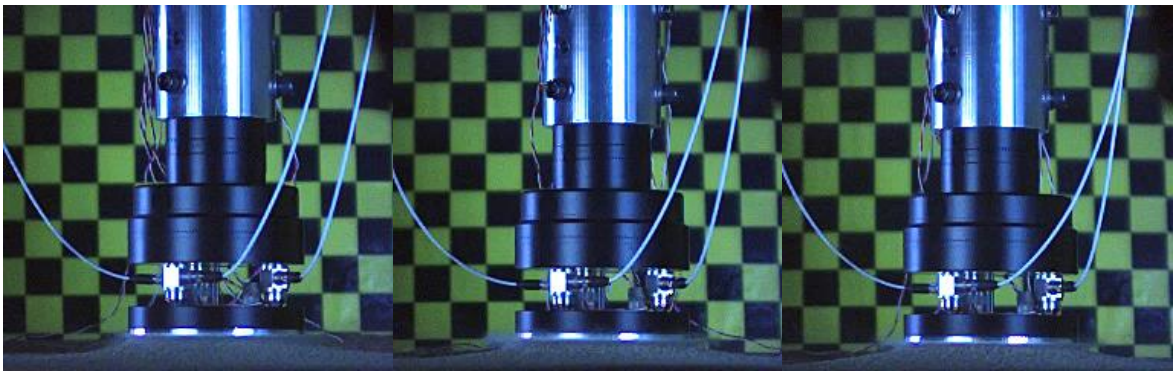

Figure 6.35. Comparisons of soil deformations for a 1.0 gram Detasheet charge buried 5.1 cm in dry sand and detonated at 10 g (*left*), 20 g (*middle*), and 30 g (*right*). Target positioned 1.3 cm aboveground. Corresponding frame (*primary* shock arrival) times with increased gravity: 1.45 ms; 1.34 ms; 1.33 ms. Fiducial background 2.2 cm square grid.

The initial shock impact in this phase, 1.45 ms at 10 g, accelerates to 1.34 ms and 1.33 ms at 20 g and 30 g, respectively, a nominal variance of 0.01 ms. The data indicates that arrival times progressively decrease with higher gravity-induced confining stresses.

To further augment data analyses, the second test series increases the target height to 5.1 cm, with the constant 1.0 gram Detahseet and 5.1 cm DOB, detonated at 1 g (normal gravity), 10 g, and 20 g-levels. The comparative time-histories demonstrate gravity-dependence on the buried blast phenomenon in both shock phases (Figure 6.36).

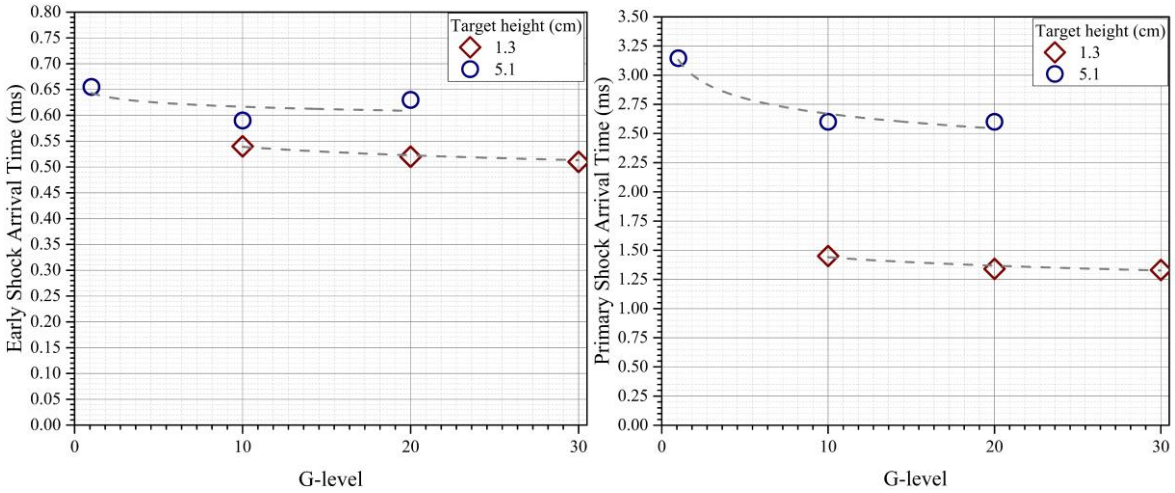

Figure 6.36. (*left*) *Early* and (*right*) *primary* shock arrival times as a function of g-level for a 1.0 gram Detasheet charge buried 5.1 cm in dry sand. Target positioned at 1.3 cm and 5.1 cm aboveground. Best-fit regression lines included (*dashed-lines*).

The earliest measured shock wave impact occurs 0.54 ms post-detonation at 10 g and accelerates progressively to 0.51 ms at the highest 30 g-level detonation. Specifically, at this 1.3 cm HOT, the shock wave velocity measures 118.5 ms^{-1} at 10 g and increases by an approximate 6.9 ms^{-1} at 30 g (Table 6.14). As expected, the increased 5.1 cm HOT delays shock wave arrival times relative to the 1.3 cm HOT (Figure 6.36, *left*). In general, impact times also decrease at the 5.1 cm target height consequent soil matrix stiffening under elevated gravity forces. The 1 g-level measures the latest shock wave arrival time at 0.66 ms, accelerates to 0.59 ms at 10 g, but increases by a nominal 0.03 ms at 20 g. This slight deviation from the expected dynamic behavior can attribute to nominal differences in charge fabrication. At 5.1 cm HOT, the shock wave velocity at the lowest 1 g-level 154.5 ms^{-1}, increases by the same approximate 6.5% increase at the highest 20 g-level similar to the 1.3 cm HOT (Table 6.14). The data indicates that shock wave speeds rise with increased material bulk modulus under elevated gravity forcing [4] (Figure 6.36, *left*).

Primary shock impact arrival times display similar gravity-dependent trends (Figure 6.36, *right*). The extremely pressurized detonation gases and high-rate soil ejecta loads transfer

momentum to the overlying target consistently sooner at higher g-levels throughout the examined range. For example, at the 5.1 cm HOT, the primary shock impact occurs at 3.15 ms at 1 g, and arrives 0.55 ms and 0.57 ms sooner at the 10 g and 20 g, respectively, a significant time period in the millisecond duration of the entire blast event (Table 6.14). The higher soil shear stresses and compressed air-filled void space within the soil matrix causes a sudden release of stored elastic energy, or an increase in burst pressure, and thus a higher ejecta flow rate and compaction density focused towards the target.

These soil blast mechanisms dictate the attendant momentum transfer to the target, as evidenced in the impulse time-histories for the 1.3 cm HOT test series (Figure 6.37). The gravity dependence on peak impulse values exhibits a monotonic relationship: higher gravitational forcing increases the impulse imparted to the target. Specifically, the peak impulse at the 10 g-level measures the lowest 525.0 Pa-s, and rises sequentially at the 20 g-level and 30 g-level by 2.4% and 10.3%, respectively (Table 6.14). In general, the profiles display similar rate-dependent behavior and vary primarily in magnitude.

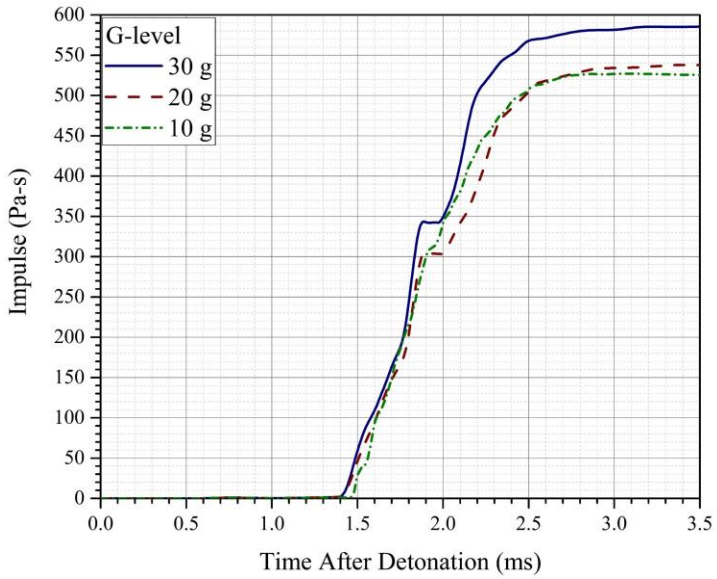

Figure 6.37. Impulse time-histories for 1.0 gram Detasheet charge buried 5.1 cm in dry sand and detonated at 10 g, 20 g, and 30 g-level. Target positioned 1.3 cm aboveground.

A comparison of the peak impulse values, inclusive of the 5.1 cm HOT data further delineates gravity's influence on peak magnitude across different test configurations (Figure 6.38). The results demonstrate the same trend: peak impulse consistently increase with gravity. At the 5.1 cm HOT, buried soil blasts subjected to elevated gravity yield an approximate 22% higher peak impulse when compared to the 1 g-level test (Figure 6.15). Furthermore, in this test series, the expected increase between 10 g and 20 g-level apparently decreases by a nominal 7.5 Pa-s. This can attribute to the stochastic interfaces of the gas-soil ejecta impacts and possible variances in charge fabrication. The comparison across test parameters substantiates that the closer target proximity to the charge at the 1.3 cm HOT yields significantly higher peak impulse values relative to the 5.1 cm HOT configuration.

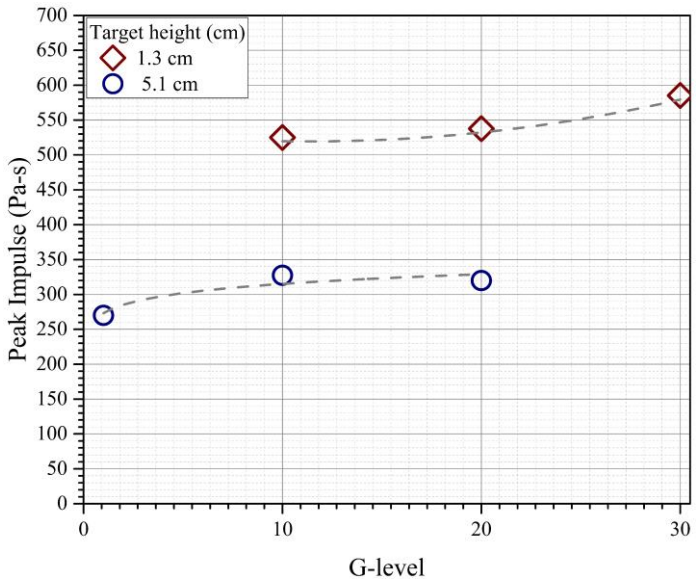

Figure 6.38. Peak impulse as a function of g-level for a 1.0 gram Detasheet charge buried 5.1 cm in dry sand and detonated at multiple g-levels. Target positioned at various heights aboveground. Best-fit regression curves included (*dashed-lines*).

Because of the soil's stress-dependent mechanical behavior, gravity-induced stress levels can produce stress and deformation characteristics comparable to full-scale blast events using the

suitable scaling relationships (Table 2.1). Gravitational forcing strongly influences soil rheology and the consequent mechanistic target loads. Buried charge detonations at higher g-levels scale to deeper burial depths, and thereby simulate similar soil blast mechanics discussed in the burial-depth dependence Section 6.10. The results confirm that the gravity-driven increase in shear strength and the lateral confinement of the buried charge collectively restricts the radial expansion of detonation gases and soil ejecta. This resultant flow directionality of blast loads channels increased energy transfer towards the target. In addition, elevated gravity, or heavier overburden pressure, reduces the air-filled voids in the soil matrix. The subsequent decrease in the soil's permeability minimizes gas venting to the ambient surroundings, and thus confines the highly-pressurized gases with elevated gravity, increasing the potential energy transferred to the overlying target. As a result, more energy transmits to the soil medium, and induces the release of stored elastic energy, or burst pressure, with consequently higher peak impulse on the target. The results demonstrate that the blast loading phenomenon can be altered by a single parameter, *gravity*.

Table 6.14. Summary of *early* and *primary* shock phase arrival times, soil blast load duration, and peak impulse for 1.0 gram Detasheet charge buried 5.1 cm in dry sand and detonated multiple g-levels. Target positioned at various heights aboveground.

G-level	W (gm)	HOT (cm)	Arrival time (ms) *Early* shock	Arrival time (ms) *Primary* shock	Impact duration (ms)	Peak Impulse (Pa-s)
10	1.0	1.3	0.54	1.45	1.66	525.0
20	1.0	1.3	0.52	1.34	1.58	537.7
30	1.0	1.3	0.51	1.33	1.77	585.3
1	1.0	5.1	0.66	3.15	1.70	270.1
10	1.0	5.1	0.59	2.60	1.99	327.5
20	1.0	5.1	0.62	2.58	1.64	320.0

6.12 Surface-Tangent Blasts

The breach of a vehicle underbody exposes the crew to the I.E.D.'s lethal blast pressure and fires from the energetic, highly luminous fireball that burns and blinds its occupants [4]. The high-speed video images simulate this explosive fireball at target impact from a surface-tangent blast (Figure 6.39). The prior in-depth analyses have consistently confirmed the significant influence of the soil mechanism in both kinematics and kinetics. As previously documented, the soil constituent in a buried explosive-induced detonation amplifies the stochastic, complex interactive load mechanisms and the resultant rigid-body response. To further clarify soil overburden effects on the impact phenomenon and energetic momentum imparted to the target, this analysis compares surface-tangent charge detonations to buried, explosive-induced soil blasts.

The first test series uses a 0.3 gram Detasheet charge oriented vertically, placed at a zero burial depth with its distal end flush to the soil surface. In these tests, the target height (5.1 cm) defines the total distance from the charge to target, or standoff distance (SOD). The dual camera imaging system recorded the surface-tangent blast at 90,066 frames per second (Figure 6.39). The sequential, high-speed video images effectively capture the combustive, interfacial turbulence and expansive detonation cloud at target impact.

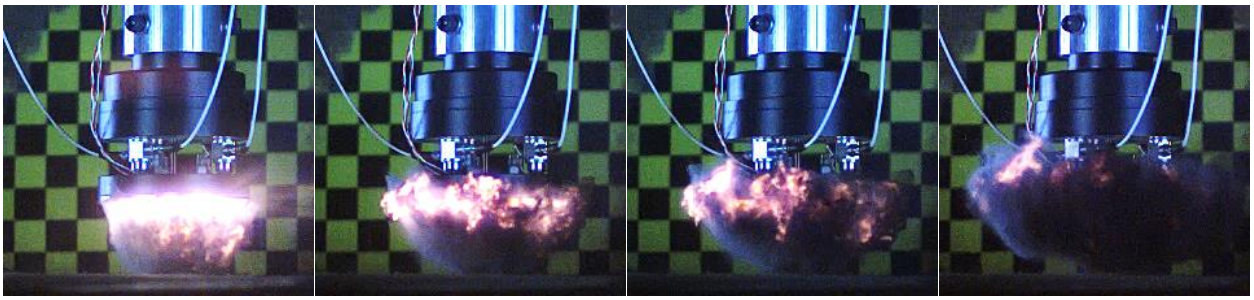

Figure 6.39. High-speed video frames for a 0.3 gram Detasheet surface-tangent detonated at 10 g. First frame recorded 0.01 ms post-detonation. The inter-frame time is 22.2 μs. Target positioned 5.1 cm aboveground.

Specifically, the first frame, recorded at 0.01 ms post-detonation, reveals the extremely bright, intense fireball bursting through the pressurized gases. The visual, sustained combustion suggests intense burning of the detonation products long after the initial detonation wave transmits through the explosive medium [3]. The flames appear to anneal the target's metallic surface (Figure 6.40), confirmed by the scorch marks visible post-detonation on the impact face (Figure 6.40, *left*). The residual soil on the target's peripheral surface can attribute to thermal updraft of the substrate material (Figure 6.40, *right*). Throughout this very short, 22.2 µs time-sequence, the videos exhibit the turbulent intermixing at the detonation cloud and oxygen interface. As illustrated, this fiery turbulent flow progressively expands beyond the target face. Temperature rapidly drops within the microsecond interval and the detonation products cool, indicated by the evolving dark cloud, moving upward toward the target as the combustion quenches.

Figure 6.40. Target surface pre (*left*) and post (*right*) surface detonation of a 0.3 gram Detasheet charge at 10 g. Target positioned 5.1 cm aboveground. Note scorch marks and soil residue on target surface after detonation.

A review of the extensive soil blast video images confirms that surface-tangent detonations exclusively evidence a fireball impact. At the 2.5 cm burial depth, the target plate exhibits a similar etched, burn imprint post-detonation (Figure 6.23b). However, the coincident video image shows the dark soil annulus encompassing the explosive gases at target impact (Figure 6.23a).

Collectively, the data demonstrates that soil overlying the explosive charge impedes the turbulent mixing of ambient air and detonation products. This precludes complete combustion in contrast to the burning fireball induced by surface-tangent explosions. In addition, the soil annulus acts as a non-conductive boundary and mitigates heat energy transfer from the fireball flames to the target.

To further delineate the soil mechanistic impact and to assess test-to test variation, this data synthesis compares three repeated surface-tangent detonations to two subsurface soil blasts, buried at 2.5 cm. The test series used a constant 0.3 gram Detasheet charge and a fixed 10 g-level acceleration. The target height for the buried explosive event varied from 1.3 cm to 2.5 cm, with the respective standoff distances 3.8 cm and 5.0 cm.

The initial target impact, measured by the BIRG's sensors in all three surface tests, occurs at 0.36 ms and corresponds to an incident wave velocity of 141.7 ms $^{-1}$ (Figure 6.41, *left*). The first video image records the fireball and explosive target impact at 0.01 ms significantly sooner than the BIRG's dynamic response at 0.36 ms post-detonation (Figure 6.39). The target plate's inertia resists the underbody blast force and explains the delayed response.

The stress time-histories compare the surface-tangent and buried blasts in the *early* shock impact phase (Figure 6.41). Throughout this investigation of the multiphasic soil blast mechanics, the results have consistently demonstrated the BIRG's capability to distinguish the highly transient shock wave, with lower force magnitude measurements, subsequent attenuation towards zero, followed by a later, major spike in force measurement of higher magnitudes and secondary peaks of longer blast duration in the gas-soil ejecta mechanistic loading phase. In the *zoomed-in* plot (Figure 6.41, *left*), at the same scale as the representative buried detonation (Figure 6.41, *right*), the data indicates that without the overlying soil constituent the BIRG measures the same 0.36 ms force arrival times in both the *early* and *primary* shock phases (Table 6.15). In contrast, the shock

wave arrival times in the subsurface charge detonations occur at 0.47 ms (1.3 HOT) and 0.51 ms (2.5 cm HOT) or a 0.10 ms and 0.15 ms deceleration, respectively (Figure 6.41, *right*). The comparative, later shock wave arrival times in the buried, explosive-induced stress profiles further substantiates the significance of the acoustic impedance mismatch at the soil-air interface (Figure 6.41, *right*). The strong difference in interfacial densities due to the overlying soil, reflects the shock wave back into the particulate medium as a compressive wave, with subsequent attenuation of shock wave velocity and intensity [4].

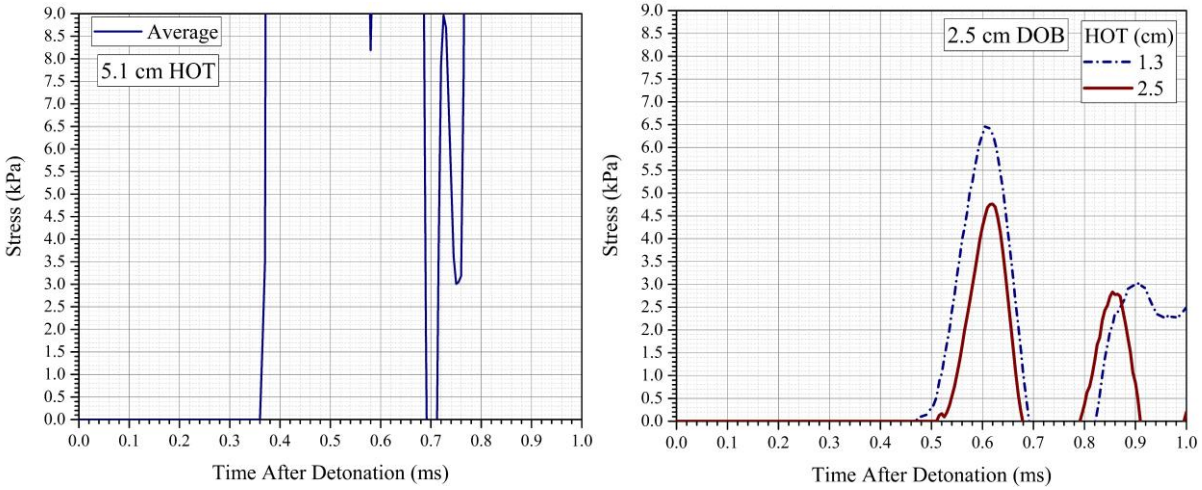

Figure 6.41: Comparisons of the stress time-histories during the *early* shock phase for a 0.3 gram Detasheet charge detonated at 10 g: (*left*) average of three individual surface-tangent blast tests, target 5.1 cm aboveground; (*right*) charge buried 2.5 cm in dry sand, target positioned 1.3 cm (*dashed-line*) and 2.5 cm (*solid-line*) aboveground.

In the *primary* shock phase, the three surface-tangent detonations exhibit excellent data repeatability (Figure 6.42). The average peak stress measures 700.3 kPa and varies between tests by a nominal 9.9% (*relative standard deviation*). Notably, the peak stress magnitudes between two of the three tests differ by only 20.7 kPa, or a nominal 2.2% variation.

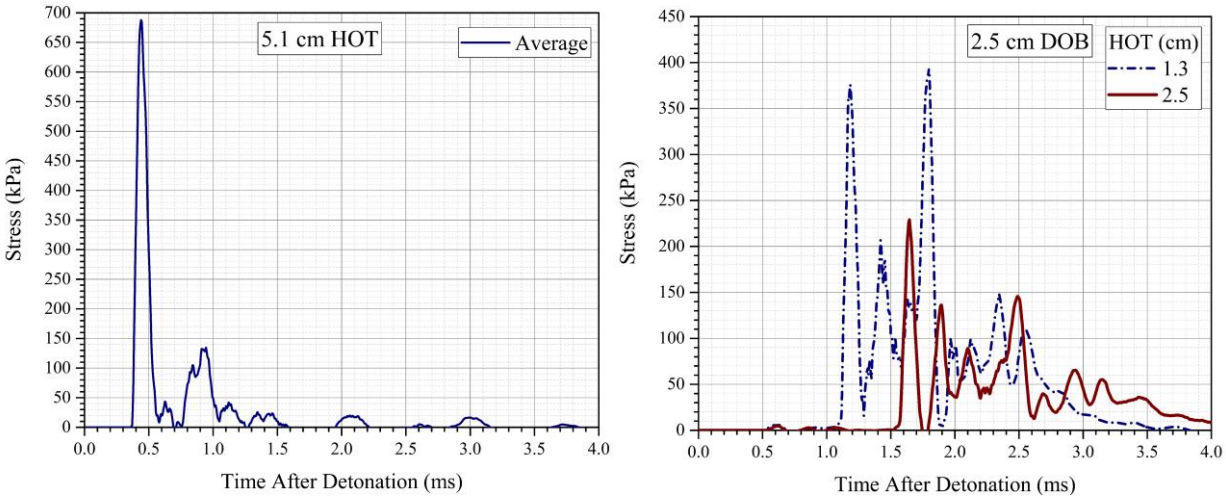

Figure 6.42: Comparisons of the soil blast stress time-histories for a 0.3 gram Detasheet charge detonated at 10 g: (*left*) average of three individual surface-tangent blast tests, target 5.1 cm aboveground; (*right*) buried 2.5 cm in dry sand, target positioned 1.3 cm (*dashed-line*) and 2.5 cm (*solid-line*) aboveground.

Without the soil overburden, the high-rate shock wave and detonation products directly impact the target. These mechanisms induce the characteristic high-amplitude, sharp peak and narrow-base profile. After the immediate rise to peak stress, 700.3 kPa, and the transient blast duration of only 0.30 ms, the stress rapidly declines after 0.60 ms, and gradually attenuates toward zero, 1.50 ms post-detonation. This correlates to the high-speed video images that depict the fireball flames quenching, with consequent heat energy dissipation.

In contrast, the subsurface profiles exhibit the characteristic, multiple peaks of lower magnitudes and longer impact durations (Figure 6.42, *right*). The BIRG sensors measure the arrival times of the gas-soil ejecta mechanisms at 1.06 ms and 1.53 ms for the respective 1.3 cm and 2.5 cm HOTs, significantly later than the 0.36 ms surface-tangent blast impact time. In this phase of the buried blast phenomenon, the nominal air shock, the pressurized expanding detonation gases, and the dense, high-velocity soil ejecta intermix and create extremely complex, stochastic interfaces [31]. The continuous flux and reflective interaction of these mechanisms impinging on the target induces the multiple oscillations observed in the soil blast stress measurements over an extended time

period. Specifically, the impact duration significantly increases to 2.44 ms and 2.47 ms at the 1.3 cm and 2.4 cm target heights respectively, when compared to the 0.30 ms impact duration of the surface-tangent load mechanisms. The variations in the soil blast test series attributes to the different target height parameters, with the expected higher 2.5 cm HOT yielding the lower blast force magnitudes. Significantly, the 2.5 cm burial depth reduces the initial peak stress by 50% (1.3 cm HOT) and 67% (2.5 cm HOT) when compared to the surface-tangent explosions (Figure 6.42, *right*).

The comparative analysis of the temporal evolution of kinetic momentum imparted to the target, further delineates fundamental differences in the surface-tangent and subsurface loading mechanisms (Figure 6.43). The flush-buried charge impulse time-history represents the average of the three individual experiments with an admissible peak impulse variation 104.0 Pa-s ± 9.6 Pa-s.

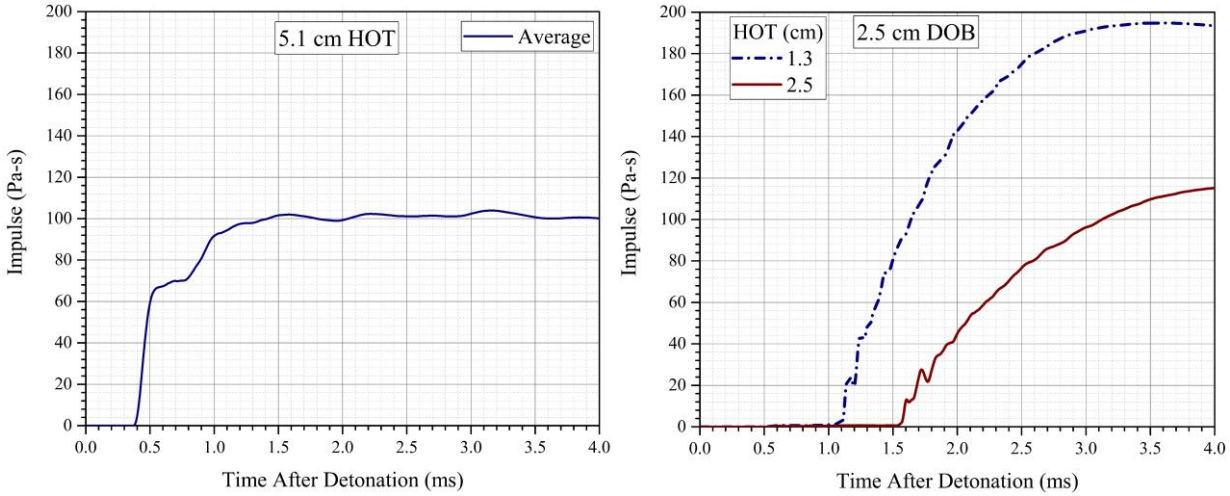

Figure 6.43. Comparisons of the impulse time-histories for a 0.3 gram Detasheet charge detonated at 10 g: (*left*) average of three individual surface-tangent blast tests, target 5.1 cm aboveground; (*right*) buried 2.5 cm in dry sand, target positioned 1.3 cm (*dashed-line*) and 2.5 cm (*solid-line*) aboveground.

The surface-tangent impulse curve displays the sharp, immediate rise to the peak impulse 104.0 Pa-s (Figure 6.43, *left*), indicative of the highly transient, energetic transfer from the shock wave

and detonation gas constituents. The energy attenuates after 1.60 ms and reaches the horizontal asymptote. This distinctly contrasts to the buried blast impulse profiles (Figure 6.43, *right*). Both tests exhibit a gradual rise to peak impulse, indicative of the continual gas-soil ejecta flow impinging on the target for a significantly longer time period. The data clearly shows that buried charge detonations yield higher peak impulse magnitudes than air blasts at the same standoff distance. Specifically, for a constant 5.1 cm SOD, the peak impulse measures 13.2 % higher for the subsurface detonation relative to the flush-buried blast (Table 6.15).

The results substantiate that buried blasts induce higher momentum transfer to the aboveground target. Energetic output released by an explosive detonation remains finite and determined by explosive mass and type [3]. The explosive mass, type, configuration and soil conditions remained constant in this test series analysis to fully distinguish the fundamental differences between surface-tangent and buried explosive events. Therefore, with the constant test parameters and higher impulse values from the buried blasts, the results suggest that buried detonations convert blast energy to kinetic energy, transmitted to the target, more efficiently than bare charge detonations. In soil blast mechanics, the soil compresses and confines the highly pressurized detonation gases momentarily. This stored potential energy rapidly releases and drives the overlying geomaterial in a predominate vertical direction towards the target. The conversion process evidences minimal energy dissipation due to the direct ground shock coupling between the explosion and adjacent soil [64]. In addition, soil ejecta momentum contributes a significant amount of the total impulsive energy transferred to the target when compared to the shock wave and detonation gas due to the higher soil ejecta mass density. Bare charge detonations omit the soil ejecta constituent, and thus, thermo-fluid dynamics govern the impulse loading transmitted to the target. The entropy production across the existing compressive shock wave front and gas

bubble components limits the availability of thermal energy for conversion to mechanical work on the target, and thus explains the lower peak impulse values [56]. Table 6.15 summarizes *early* and *primary* shock phase arrival times, soil blast load duration, and peak impulse for surface-tangent and subsurface detonations.

Table 6.15. Summary of *early* and *primary* shock impact arrival times, impact duration, and peak impulse for 0.3 gram Detasheet charge surface-tangent and subsurface detonations at 10 g. Target positioned at various heights aboveground.

Test	W (gm)	DOB (cm)	HOT (cm)	SOD (cm)	Arrival time (ms)		Impact duration (ms)	Peak Impulse (Pa-s)	% Increase from **surface blast**
					Early shock	*Primary* shock			
1	0.3	0	5.1	5.1	0.36	0.36	0.30	114.5	
2	0.3	0	5.1	5.1	0.36	0.36	0.30	101.9	
3	0.3	0	5.1	5.1	0.36	0.36	0.30	95.6	
Buried	0.3	2.5	1.3	3.8	0.47	1.06	2.44	194.7	91.4
Buried	0.3	2.5	2.5	5.1	0.51	1.53	2.47	115.2	13.2

6.13 Target Plate Inertia Effects

The previous results document the impulsive loading on an overlying target as a function of target height, explosive mass, burial depth, and gravitational forcing. In addition to these factors, target plate size and consequent mass inertia also influence momentum transfer to the target. The blast impulse calculation includes the mass inertia term, Ma (Equation 6.8). The following analysis provides insight into target plate inertia dependence and its appropriate inclusion into the blast impulse calculation. This test series used a 1.0 gram Detasheet charge, buried 5.1 cm in

80s20c10w, and detonated at 10 g. The target's aspect ratio of 8.0 (*diameter*-to-*thickness*) and the target height (5.1 cm) remained constant.

The high-speed video images capture the distinctive stages of the blast phenomenon as a function of increasing target plate diameter (10.16 cm, 12.19 cm, and 15.24 cm) and mass (Table 6.16). The sequential images illustrate an expansive soil dome heave (Figure 6.44), the attendant impact (Figure 6.45), and the *late-stage* soil ejecta flow encompassing the targets (Figure 6.46). Collectively, the heterogeneous microstructures in this clay-sand heave depict a rough, irregular, fissured surface. This cohesive soil ejecta matrix visibly restricts venting of the highly-pressurized, milky-white detonation gases.

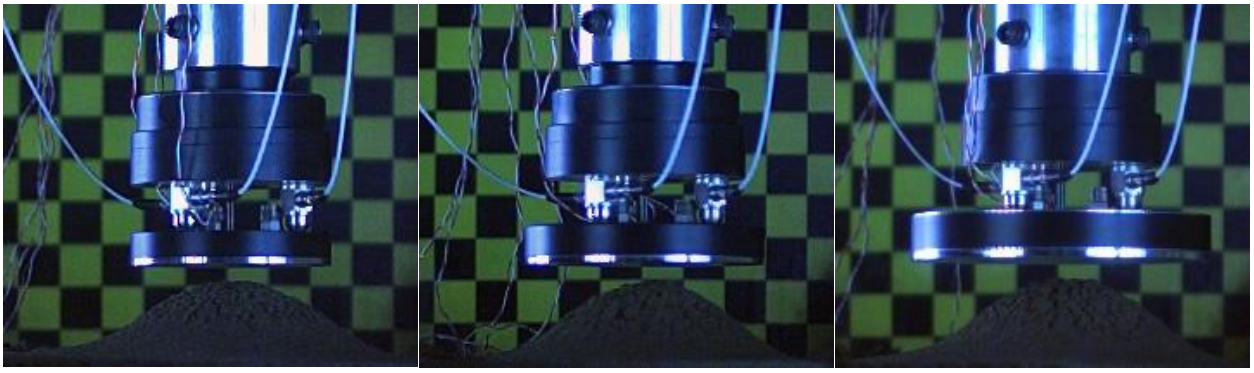

Figure 6.44. Comparisons of soil deformations for 1.0 gram Detasheet charge buried 5.1 cm in 80s20c10w and detonated at 10 g. Target positioned 5.1 cm aboveground. Soil dome height 3.60 cm at corresponding time after detonation and target diameter, respectively: (*left*) 1.43 ms, 10.16 cm; (*middle*) 1.25 ms, 12.19 cm; (*right*) 1.38 ms, 15.24 cm. Fiducial background 2.2 cm square grid.

Figure 6.45. Comparisons of soil deformations for 1.0 gram Detasheet charge buried 5.1 cm in 80s20c10w and detonated at 10 g. Target positioned 5.1 cm aboveground. Soil dome cap and target plate diameter coincident at corresponding time after detonation and target diameter, respectively: (*left*) 2.35 ms, 10.16 cm; (*middle*) 2.31 ms, 12.19 cm; (*right*) 2.85 ms, 15.24 cm. Fiducial background 2.2 cm square grid.

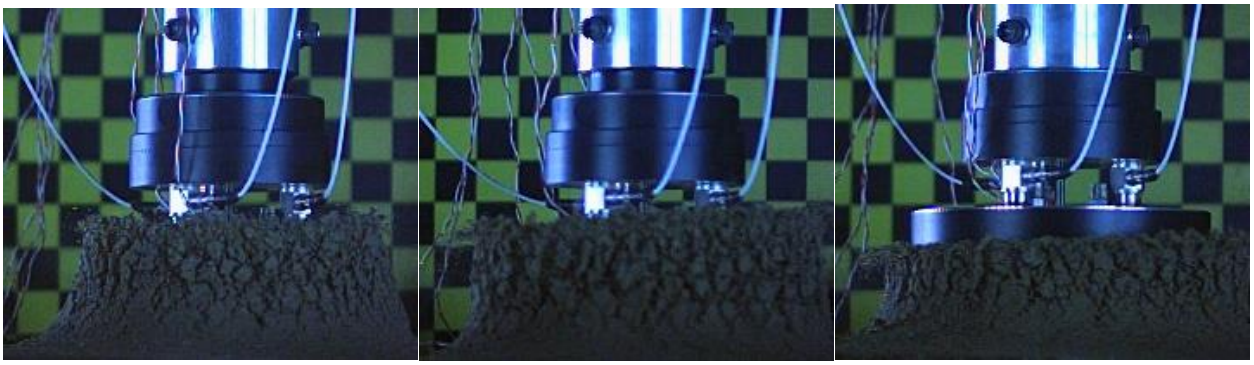

Figure 6.46. Comparisons of soil deformations for 1.0 gram Detasheet charge buried 5.1 cm in 80s20c10w and detonated at 10 g. Target positioned 5.1 cm aboveground. Time after detonation 3.61 ms for plate diameters: (*left*) 10.16 cm; (*middle*) 12.19 cm; (*right*) 15.24 cm. Fiducial background 2.2 cm square grid.

The high-speed videos demonstrate the expected trend that the *primary* shock phase progressively lengthens with increasing target plate diameter (Figure 6.44-6.46). Specifically, the blast momentum transfer duration to the widest, 15.24 cm diameter target, exceeds the 12.19 cm and 10.16 cm diameter targets by 0.67 ms and 0.74 ms, respectively, a considerable difference within the millisecond sequence of the entire blast event (Table 6.16). This observed trend can attribute to the lateral translation and continual target impingement of the gas-soil ejecta loads.

Furthermore, a comparative analysis of peak impulse dependence on target mass inertia clearly shows that plate momentum influences the kinetic energy transfer to the target (Figure 6.47). Exclusion of inertial target mass in the blast impulse integrand causes a greater peak variance

between the respective targets (Figure 6.47, *left*) when compared to the inclusion of the resistive *ma* term (Figure 6.47, *right*).

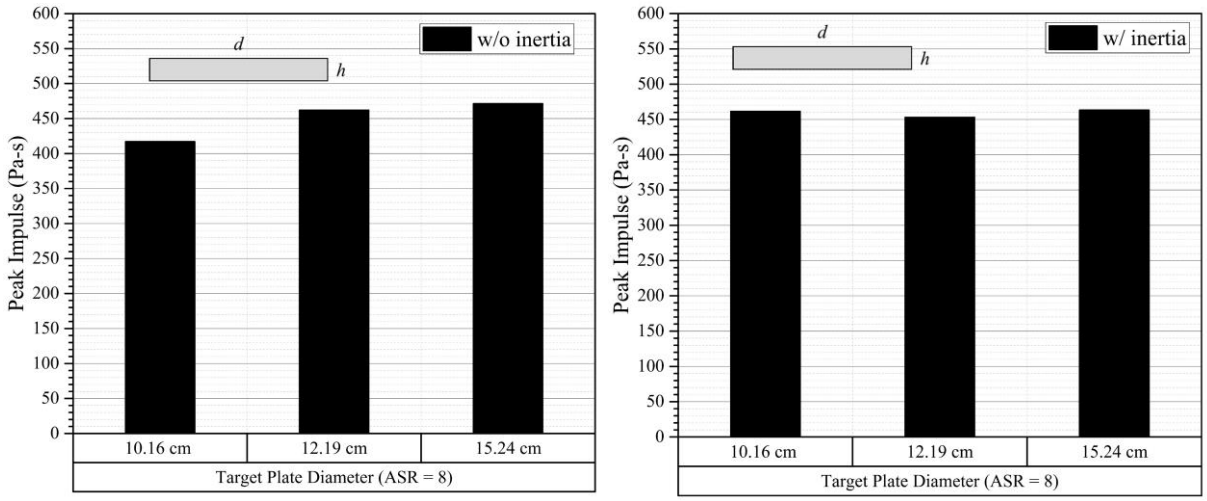

Figure 6.47. Peak impulse as a function of target plate diameter (*left*) excludes and (*right*) incorporates inertia effects for a 1.0 gram Detasheet charge buried 5.1 cm in 80s20c10w and detonated at 10 g. Target positioned 5.1 cm aboveground. Target diameter-to-thickness ratio (ASR = *d* / *h*) equals 8.0.

Specifically, the 6.4% difference in peak impulse without including mass inertia contrasts to the nominal 1.2% variance that includes mass inertia term. The data substantiates this study's method to include inertial target mass in the blast impulse calculation because it allows improved characterization of the target's blast induced dynamics. Furthermore, the close agreement in peak impulse (Figure 6.47, *right*) indicates that the range of BIRG target diameters sufficiently resolve the total blast momentum imparted to the target. Table 6.16 summarizes the blast load duration and peak impulse for the various target plate sizes.

Table 6.16. Summary of impact duration, and peak impulse excluding and including target inertia in the blast impulse calculation for a 1.0 gram Detasheet buried 5.1 cm and detonated at 10 g. Target positioned at 5.1 cm aboveground.

Target plate diameter (cm)	Plate mass (kg)	W (gm)	HOT (cm)	DOB (cm)	Peak Impulse (Pa-s) w/o inertia	Peak Impulse (Pa-s) w/ inertia	Impact duration (ms)
10.16	0.36	1.0	5.1	5.1	417.3	461.7	1.18
12.19	0.60	1.0	5.1	5.1	462.2	453.2	1.25
15.24	1.13	1.0	5.1	5.1	471.5	463.4	1.92

6.14 V-Shaped Targets

The mitigation of blast energy imparted to low-armored vehicles remains a significant area of active defensive research. One of the developed technologies to counter the IED and landmines threats, a V-shaped hull, currently integrated into combat mine-resistant vehicles, demonstrates effective attenuation of blast force impacts [65–67]. However, few studies have been published in the public domain. Due to the lack of published data, this research seeks to augment the current literature and further characterize the protective armoring benefits of dihedral target geometries. The unique, rate-dependent high-speed video images of target geometry dependence, correlated with coincident BIRG data in both shock impact phases, enables a rigorous characterization of this protective armoring technology.

Each successive test series varies the target's included angle (180° (flat), 135°, and 90°) for a constant charge size (0.8 gram Detasheet), burial depth (2.5 cm), target height (2.5 cm), and acceleration (10 g-level) with different in-situ conditions specific to the prescribed test parameters to isolate target geometry dependence on kinetic energy transfer. The BIRG's versatile design allows easy integration of the wedge-shaped plates to the underside of the pre-existing target

assembly. The following analyses defines the dihedral target's HOT as the distance from the tip of the 'V' to the soil-air interface.

In the first test series, the high-speed video images exhibit significant differences in the gas-soil ejecta expansion and the load mechanisms at target impact specific to the varied target geometries, in a dry Mason sand medium (Figure 6.48). As visually evidenced in the three video sequences (Figure 5.43a-c), the extremely hot, pressurized detonation products jet past the soil cap domain, creating the dilute suspension of particles dragged upward with the detonation products. The predominate milky-detonation gas cloud and the soil ejecta intermix to create the complex, stochastic interfaces that impact the target. Clearly evident, the angled plates (Figure 6.48b, c) deflect the focused vertical directionality of the centric impact (Figure 6.48a) to a more oblique, dispersed, spatial distribution of the load mechanisms.

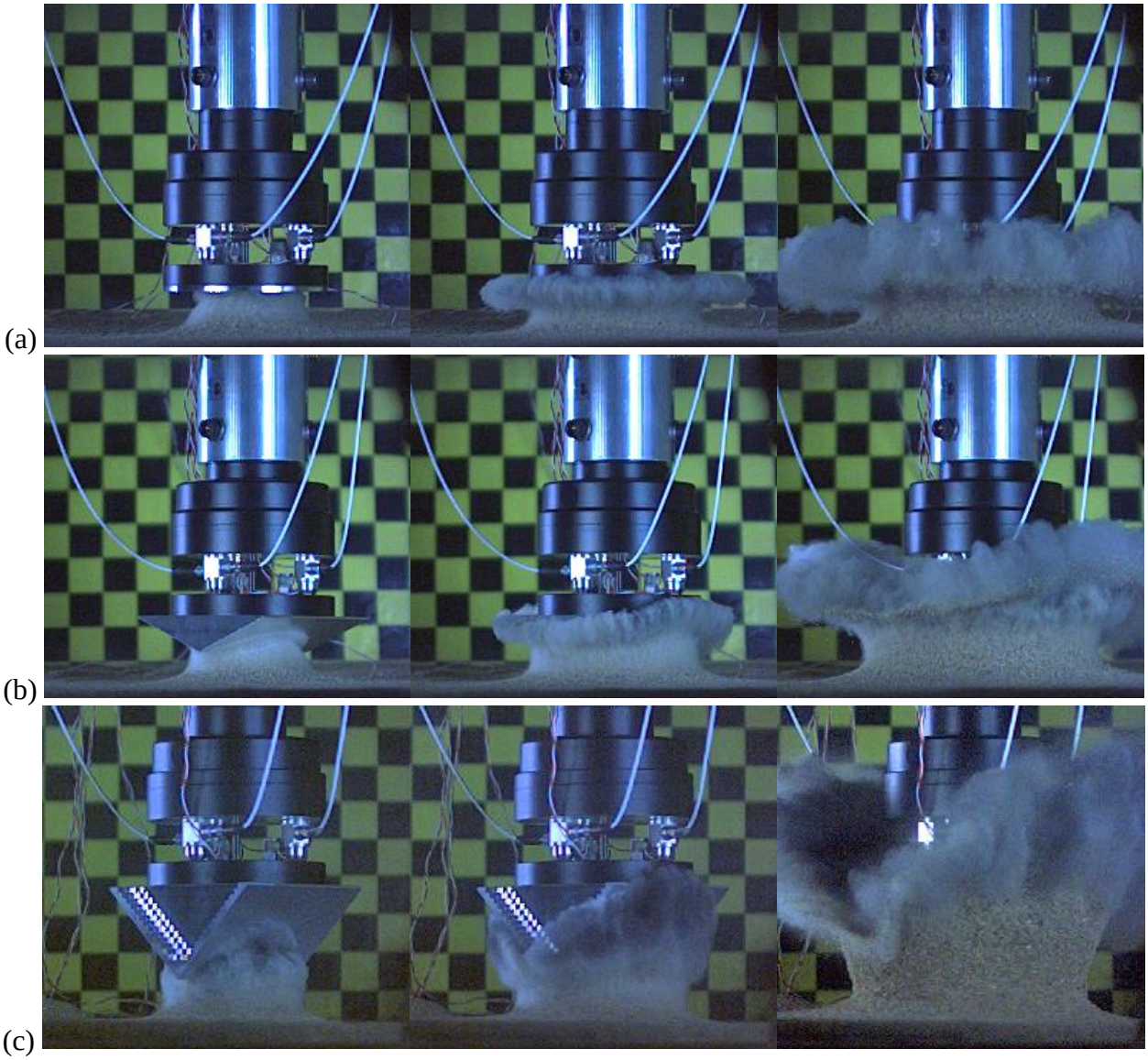

Figure 6.48. Comparisons of soil deformations for 0.8 gram Detasheet charge buried 2.5 cm in dry sand and detonated at 10 g. Target positioned 2.5 cm aboveground. Target plate included angles: (a) flat; (b) 135°; (c) 90°. Time after detonation: *(left)* 0.52 ms; (*middle*) 0.79 ms (*primary* shock arrival); (*right*) 1.90 ms. Fiducial background 2.2 cm square grid.

The soil blast mechanisms load the flat target plate in a uniform hemispherical heave, orthogonal to the target face and appear trapped beneath the target's distal face (Figure 6.48a). The flat plate geometry stagnates the flow of the load mechanisms, reduces the rate of soil dome expansion, and forces a lateral transition of the load at target impact. The flat target dependence on both the temporal and spatial evolution of the gas-soil ejecta heave, distinctly contrasts to the flow rheology

apparent in the dihedral target impacts (Figure 6.48b, c). The high-speed video images demonstrate the effectiveness of the V-shaped plates to deflect blast loads outwards and away from overlying targets, and thus reduce the focused channeling of the loads, more evident in the 90° dihedral target plate (Figure 6.48c). In contrast to the symmetric gas-soil ejecta flow (Figure 6.48a), the dihedral target geometry induces a predominate asymmetric flow with significantly increased temporal and spatial evolution. This asymmetric flow progressively accelerates beyond the BIRG with reduced included target angles due to increased target aerodynamics.

A comparison of the stress time-histories (Figure 6.49) demonstrates the distinct differences between the dynamic flat target response relative to the blast defectors under explosive loads, and quantifies the prior high-speed video analysis (Figure 6.48). The stress time-histories show that soil blast loads transmit the highest peak stress on flat plates when compared to dihedral targets in both the *early* (Figure 6.49, *left*) and *primary* (Figure 6.49, *right*) shock phases.

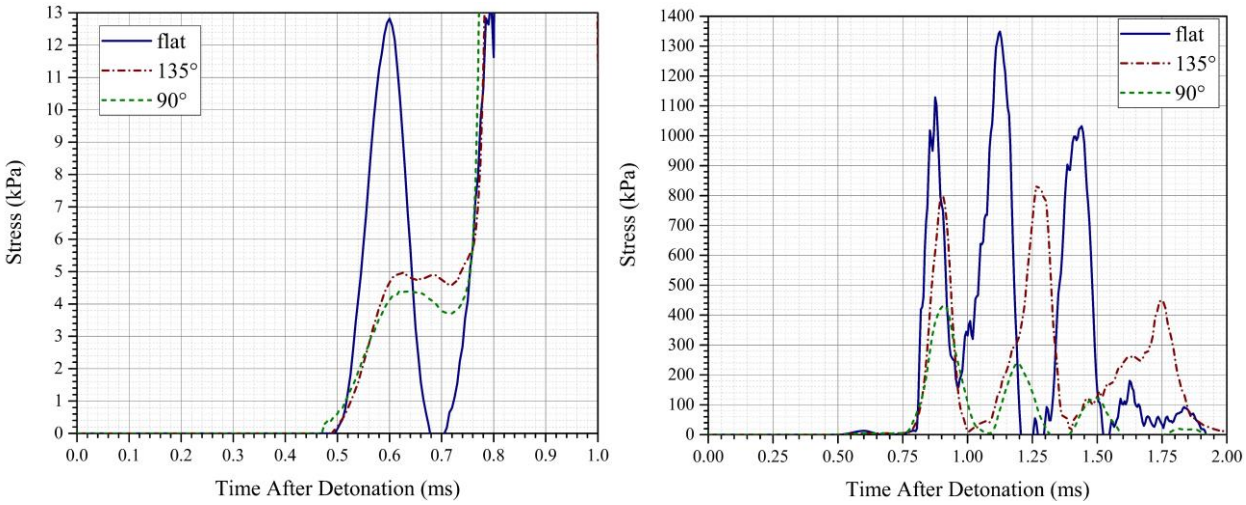

Figure 6.49. Comparisons of the stress time-histories as a function of target plate geometry for a 0.8 gram Detasheet charge buried 2.5 cm in dry sand and detonated at 10 g during the (*left*) *early* (*right*) *primary* shock phase. Target positioned 2.5 cm aboveground.

Shock wave arrival at target interface occurs 0.49 ms ± 6 µs post-detonation measured by all BIRG sensors and confirms test consistency (Figure 6.49, *left*). This equates to a shock wave

speed of 102.0 ms^{-1}. A closer examination of the *early* shock phase reveals distinctly different shock wave time-history profiles directly attributed to target geometry. The immediate BIRG flat target response evidences a clearly defined, sharp peak of magnitude 12.9 kPa with a narrow base representative of a highly transient normal impact. In contrast, the dihedral targets, subsequent shock wave impact, demonstrate distinctly different rigid-body dynamics. For example, the V-shape target shock wave profiles appear damped and show a comparative gradual rise to peak magnitude, with a rounded apex, indicative of energy attenuation (Figure 6.48 b, c). The results show that the shock wave peak stress magnitude on the flat target decreases by 61% and 66% with reduced included target angle, 135° and 90°, respectively.

This angle target dependent trend continues in the *primary* shock phase after gas-soil ejecta impact at 0.77 ms post-detonation (Figure 6.49, *right*). As demonstrated in the *early* shock impact phase, target included angle and resultant soil blast stress adhere to a monotonic relationship: reductions in target angle correspond to a decrease in peak soil blast stress. Soil blast load vectors act normal to the flat target surface, and therefore induce the highest initial peak stress, 1128.5 kN (Figure 6.49, *right*). In comparison, the 90° dihedral target design significantly deflects detonation gases and soil ejecta away from the target, quantified by the 61.7% decrease in the initial peak soil blast stress relative to the flat plate target (Figure 6.49, *right*). Because of the streamlined 90° target design and consequent deflection of blast loads, the secondary peaks, indicative of the continued flux of gas-soil ejecta impacts, also demonstrate much lower magnitudes (Figure 6.49, *right*).

These same target surface-dependent trends also occur in the blast energy transfer phenomenon. Soil blast momentum induces the highest peak impulse, 391.4 Pa-s, on the flat target, and rapidly decreases by 41.2% for the 135° target, and a significant 76.0% for the 90° angled target.

Collectively, the data substantiates that V-shaped hulls effectively attenuate blast energy impact to an overlying target in a dry sand medium. Table 6.17 summarizes initial peak blast stress and impulse as a function of target surface geometry.

Table 6.17. Summary of peak stress and impulse as a function of target geometry for a 0.8 gram Detasheet charge buried 2.5 cm in dry sand and detonated at 10 g. Target positioned 2.5 cm aboveground.

Plate geometry	W (gm)	DOB (cm)	HOT (cm)	G-level	Initial Peak Stress (kPa)	Peak Impulse (Pa-s)	% Decrease from **flat** target
Flat	0.8	2.5	2.5	10	1128.5	391.4	
135°	0.8	2.5	2.5	10	796.3	230.0	41.2
90°	0.8	2.5	2.5	10	432.2	94.3	76.0

The following experimental results from two test series further validate the performance of dihedral targets to reduce the kinetic energy transfer to the target. Furthermore, the tests evaluate the dynamic target response to in-situ soil conditions. The two new soil testbeds include, by weight: 80% sand, 20% clay, and 10% water (80s20c10w) for test *Series 1*; and 50% sand, 50% clay, and 10% water (50s50c10w) for test *Series* 2.

Clearly evident in the sequential high-speed videos, the triphasic soil deformation (soil, water, and air) and resultant target impact (Figure 6.50 and 6.51) exhibit similar rate-dependent soil ejecta rheology to the observed behavior in the dry sand test series (Figure 6.48). This observation substantiates the previous analysis that target surface geometry strongly affects the temporal and spatial gas-soil ejecta heave evolution, independent of soil condition.

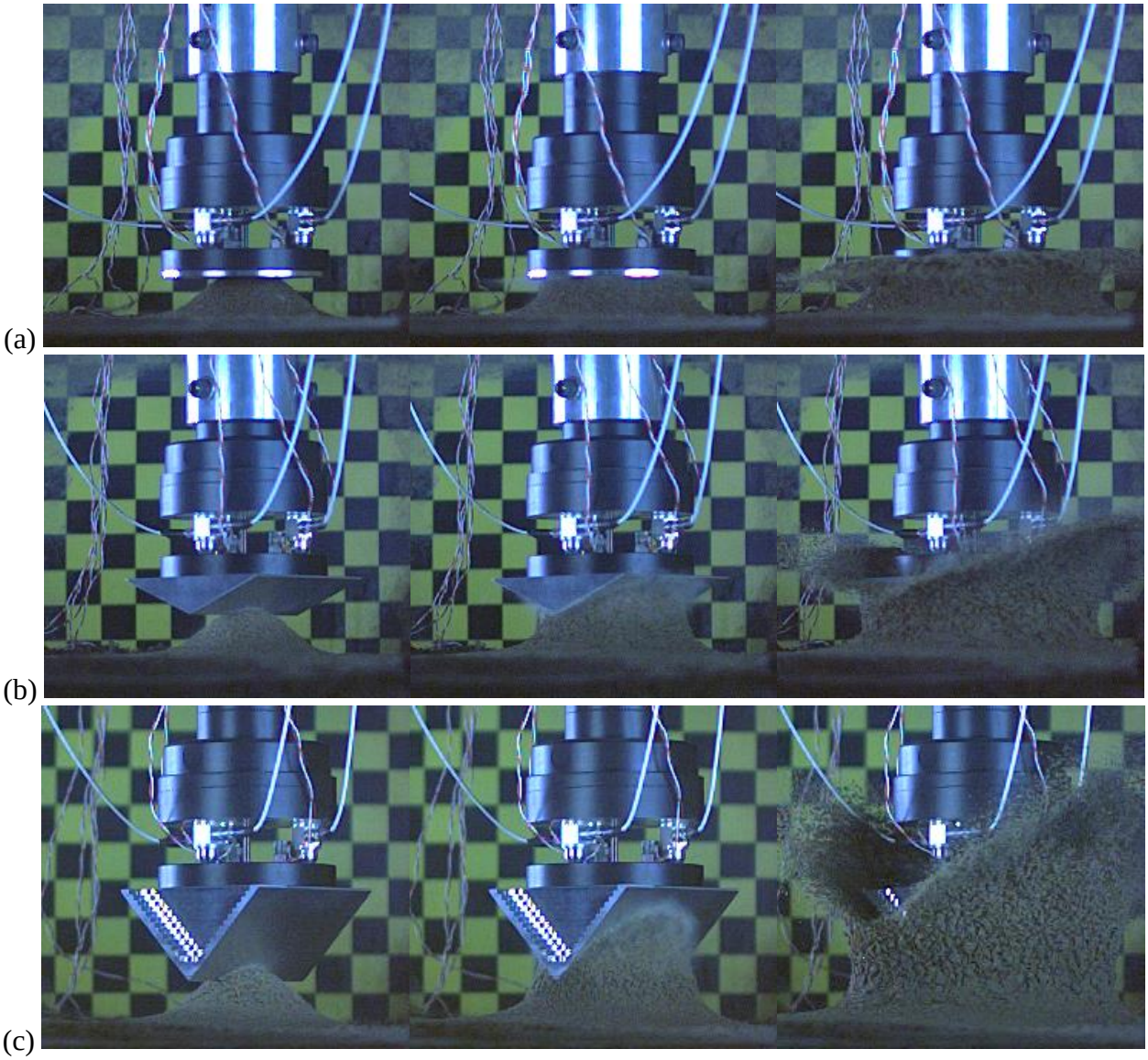

Figure 6.50. Comparisons of soil deformations for 0.8 gram Detasheet charge buried 2.5 cm in 80s20c10w and detonated at 10 g. Target positioned 2.5 cm aboveground. Target plate included angles: (a) flat; (b) 135°; (c) 90°. Time after detonation: (*left*) 0.40 ms; (*middle*) (a) 0.72 ms, (b) 0.76 ms, (c) 0.73 ms (*primary* shock arrival); (*right*) 1.81 ms. Fiducial background 2.2 cm square grid.

(a)

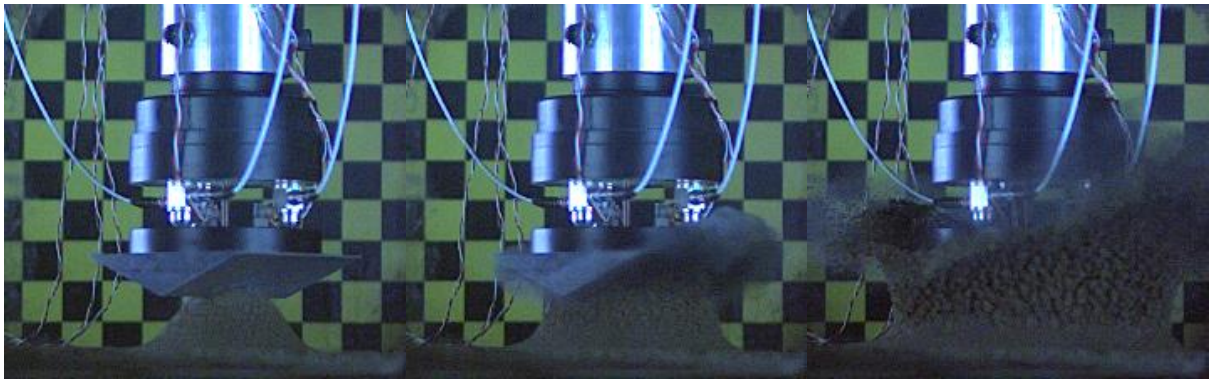

(b)

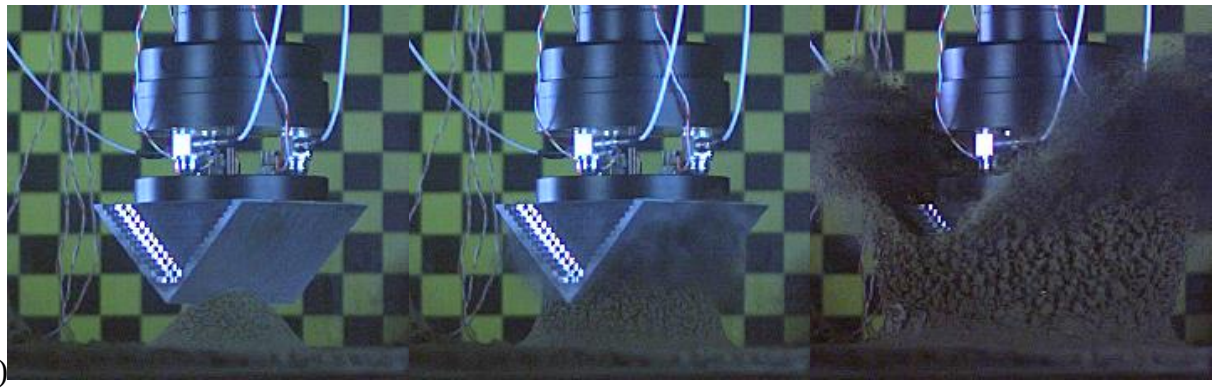

Figure 6.51. Comparisons of soil deformations for 0.8 gram Detasheet charge buried 2.5 cm in 50s50c10w and detonated at 10 g. Target positioned 2.5 cm aboveground. Target plate included angles: (a) 135°; (b) 90°. Time after detonation: (*left*) 0.40 ms; (*middle*) (a) 0.71 ms, (b) 0.70 ms (*primary* shock arrival); (*right*) 1.90 ms. Fiducial background 2.2 cm square grid.

The distinct and asymmetric cohesive granular flows across the dihedral target surfaces for both soil conditions during soil dome expansion and target impact (Figure 6.50b, c and Figure 6.51) contrasts to the symmetric, centric focus of the load mechanisms against the flat target throughout the blast duration (Figure 6.50a). The plane target surface impedes the lateral expansion of the soil disaggregates considerably. However, the angled targets visibly deflect blast constituents radially away from the BIRG. In the late-stages of the blast event, specifically the gas-soil ejecta flow after target impact (Figure 6.50 and 6.51, *right*), the clearly defined cohesive soil ejecta front, or curtain, mirrors the V-shaped contours of the dihedral targets, especially visible in the 90° angled target (Figure 6.50 and 6.51). The blast load mechanisms propagate along the target's near-frictionless plane surface, hence the analogous physical features. In the cohesionless, dry sand

medium, the interfacial gas-soil constituents, via air-filled voids (higher permeability in dry sand) obscure the BIRG target plate, and thus the profile does not delineate the specific target geometries.

Overall, the results substantiate that different target surface geometries significantly influence the post-impact soil ejecta rheology, distribution of load mechanisms, and consequent impulse imparted to the aboveground target, independent of soil conditions. Similar to the dry sand momentum analysis, the impact of the cohesive load mechanisms induces the highest peak impulse, 501.2 Pa-s, on the flat target for the 80s20c10w soil and rapidly attenuates to 209.4 Pa-s, or a 58% decrease in peak impulse due to the 90° angle target deflection of the gas-soil ejecta mechanisms (Table 6.18 and 6.19). The results substantiate the expected monolithic relationship: as the included target angle decreases, soil blast impact values significantly decline. The data indicates that in-situ soil conditions also affect the aboveground blast environment and the in-depth analysis of soil conditions presented in Section 6.16 examines this parameter's role in the target's dynamic response. Table 6.18 and 6.19 summarize peak impulse values specific to the 80s20c10w and 50s50c10w soil mediums.

Table 6.18. Summary of peak impulse as a function of target geometry for a 0.8 gram Detasheet charge buried 2.5 cm in 80s20c10w and detonated at 10 g. Target positioned 2.5 cm aboveground.

Plate geometry	W (gm)	DOB (cm)	HOT (cm)	G-level	Peak Impulse (Pa-s)	% Decrease from **flat** target
Flat	0.8	2.5	2.5	10	501.2	
135°	0.8	2.5	2.5	10	345.7	31.0
90°	0.8	2.5	2.5	10	209.4	58.2

Table 6.19. Summary of peak impulse as a function of target geometry for a 0.8 gram Detasheet charge buried 2.5 cm in 50s50c10w and detonated at 10 g. Target positioned 2.5 cm aboveground.

Plate geometry	W (gm)	DOB (cm)	HOT (cm)	G-level	Peak Impulse (Pa-s)	% Decrease from **flat** target
Flat	0.8	2.5	2.5	10	460.2	
135°	0.8	2.5	2.5	10	261.8	43.1
90°	0.8	2.5	2.5	10	163.7	64.4

The data indicates that the highly-compressive, soil blast loads head-on with the target plate repeatedly induce higher peak impulses in spite of geologic media (Figure 6.49, Table 6.17-6.19) Furthermore, the results evidence that peak impulse consistently declines with reduced included target angle. The comparison of the three tests documents that dihedral targets lessen the potential soil blast impact energy by at least 31% or as much as 76%, dependent on soil conditions, when compared to flat targets. Dihedral target geometries clearly provide a simple and effective blast deflector design.

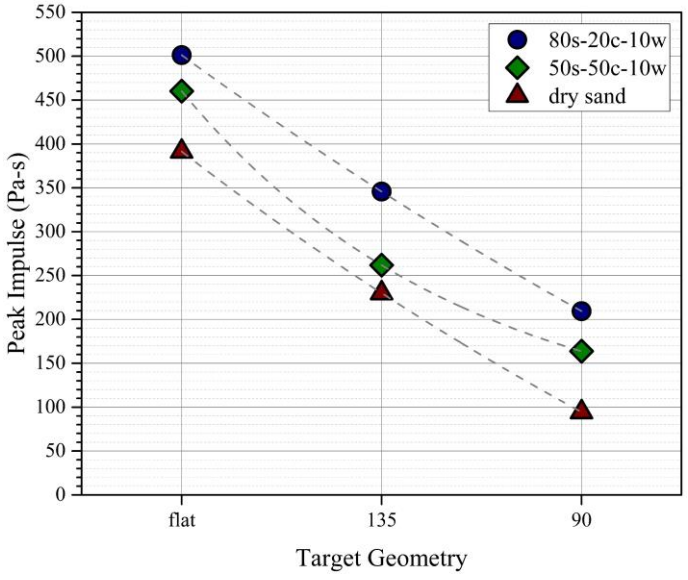

Figure 6.52. Comparisons of peak impulse as a function of target surface geometry for a 0.8 gram Detasheet charge buried 2.5 cm in various soil conditions and detonated at 10 g. Target positioned 2.5 cm aboveground. *Dashed-lines* represent best-fit curves derived from a parabolic regression analysis.

Collectively, the prior analyses indicate that low-armored vehicles equipped with an acute angled (included) V-shape hull may experience the least amount of structural damage caused by the detonation of a buried IED or landmine. From an application and design perspective, an advantageous and cost-effective approach would mount a dihedral blast deflector, with the smallest possible included angle, to the vehicle's pre-existing frame without raising the chassis, i.e. mass centroid. An elevated underbody height increases the vehicle's tendency to overturn, potentially comprises its functionality, and exposes the crew to life-threatening injuries. In addition, a consensus on the definition of target height for V-shaped targets under soil blast loads remains unresolved in this specific field of research [7,65–68]. Therefore, the following analysis further quantifies the dihedral target's performance and examines the target height metric. The experimental results from two test series document the V-shaped target and flat plate response under soil blast loading at distinctly different HOTs.

Figure 6.53 identifies the target's position relative to the soil surface. The first configuration, labeled *Case 1*, prescribes the HOT as the vertical distance from the soil-air to the target's distal surface, as defined in the previous analyses (HOT=HOT_1, Figure 6.53, *center*). The second configuration, or *Case 2*, also defines the target height, denoted HOT_2, as the distance from the soil to the flat target. However, the target's plane surface now parallels the dihedral target's mount interface (Figure 6.53, *right*). In other words, the ground clearance increases by 2.1 cm (135° target) and 5.1 cm (90° target), or the respective dihedral target's vertex.

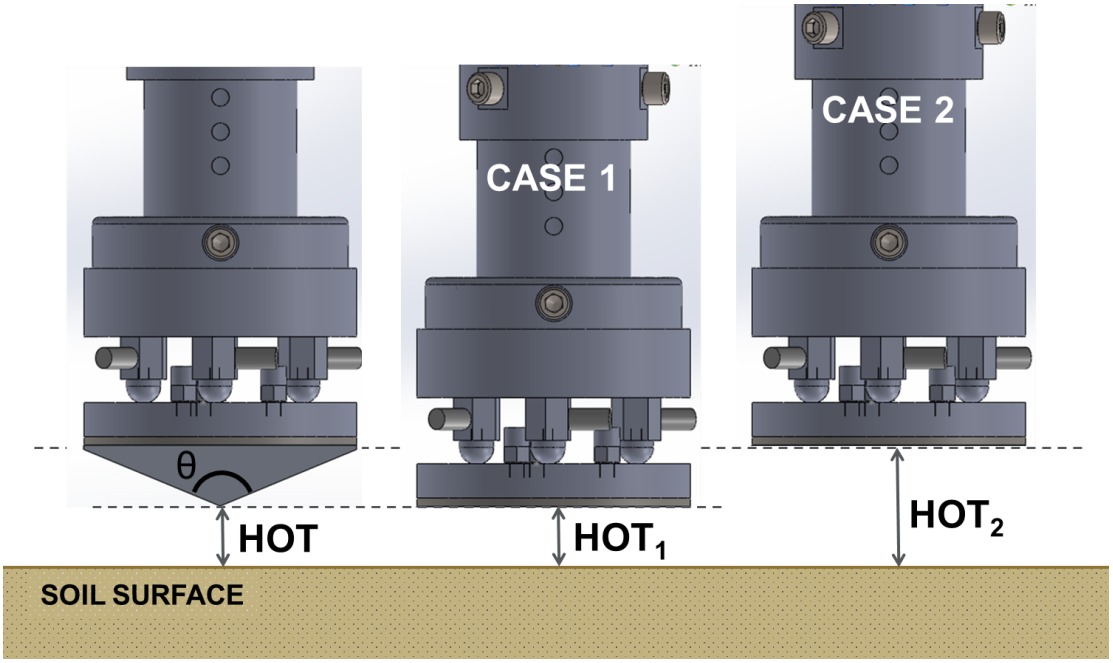

Figure 6.53. Schematic details target height for flat and dihedral target experiments.

This test series used the same Detasheet charge size (0.8 gram), burial depth (2.5 cm), g-level (10 g), soil condition (dry sand), and *Case 1* reference target height (HOT=HOT_1=2.5 cm), as summarized in Table 6.17. Table 6.20 and 6.21 restates the previous data, and lists the peak impulse values measured by the flat target for *Case 2* (Figure 6.53).

Table 6.20. Summary of peak impulse as a function of target geometry for a 0.8 gram Detasheet charge buried 2.5 cm in dry sand and detonated at 10 g. Flat target height varied relative to dihedral target.

Series 2 Dry sand	W (gm)	DOB (cm)	HOT (cm)	G-level	Peak Impulse (Pa-s)	% Increase from **135°** target
Flat plate (*Case 1*)	0.8	2.5	2.5	10	391.4	70.1
Flat plate (*Case 2*)	0.8	2.5	4.6	10	280.5	21.9
135° (HOT)	0.8	2.5	2.5	10	230.1	

Table 6.21. Summary of peak impulse as a function of target geometry for a 0.8 gram Detasheet charge buried 2.5 cm in dry sand and detonated at 10 g. Flat target height varied relative to dihedral target.

Series 2 Dry sand	W (gm)	DOB (cm)	HOT (cm)	G-level	Peak Impulse (Pa-s)	% Increase from **90°** target
Flat plate (*Case 1*)	0.8	2.5	2.5	10	391.4	315.1
Flat plate (*Case 2*)	0.8	2.5	7.6	10	215.4	128.4
90° (HOT)	0.8	2.5	2.5	10	94.3	

Soil blast loads on V-shape targets consistently induce lower peak impulse values relative to flat targets even at the redefined, higher HOT_2 (*Case 2*). For a 2.1 cm increase in the flat target HOT (2.5 cm to 4.6 cm), peak impulse decreases by more than 28%, from 391.4 Pa-s to 280.5 Pa-s (Table 6.20). In spite of the increased HOT, this impulse magnitude remains 1.2 times higher than the 135° target impulse at an equivalent 2.5 cm HOT. Likewise, a 5.1 cm increase in the distance from the soil-air interface to the flat target surface results in a significant 45% reduction in peak impulse. In comparison, the soil blast momentum imparted to the dihedral 90° target positioned 2.5 cm aboveground yields a 94.3 Pa-s peak impulse, or a 56% lower peak magnitude (Table 6.21). This further verifies the practicality and functionality of wedge-shaped hull designs to deflect more soil blast pressure away from the overlying structure. In addition, the results demonstrate the effectiveness of dihedral targets to attenuate blast impact energy regardless of the clearance offset over the range of HOTs examined.

6.15 Numerical Analysis and Comparison to Experimental Results

Direct and rigorous simulation of buried, explosive-induced gas-soil ejecta mechanisms and the attendant impact on an overlying target remains an ongoing challenge. To simulate these complex,

interactive soil blast constituents, computational models typically rely on fluid continuum approximation methods. Westin et al. [69] conducted an extensive experimental program and developed an empirically-based model to predict peak soil blast momentum transfer to rigid target plates. Tremblay [70] generalized this analytic formulation to include oblique targets and incorporated additional parameters including soil density, explosive energy, and volume. Figure 6.54 illustrates the two configurations addressed in this numerical analysis. The specific parameters and respective notations are listed in Table 6.22.

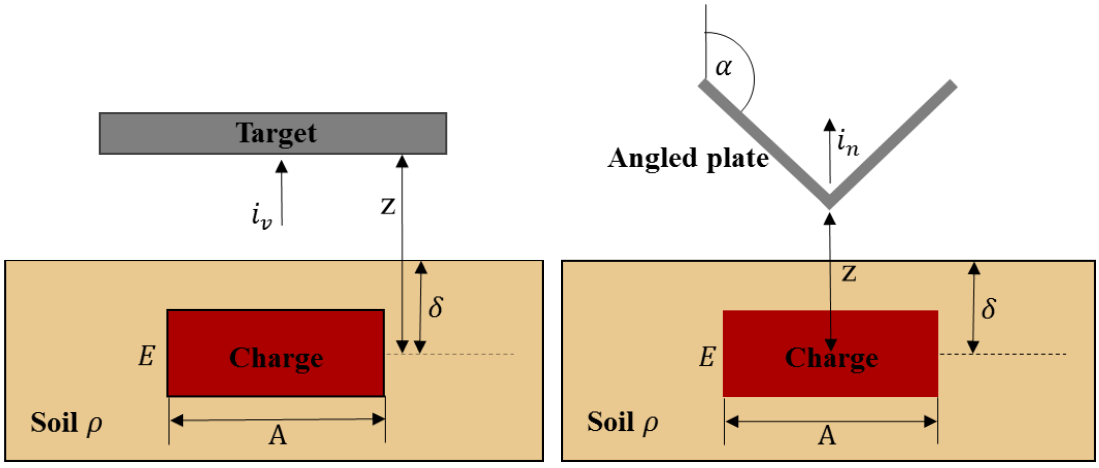

Figure 6.54. Schematic detailing parameters for a flat (*left*) and dihedral (*right*) target positioned above the buried explosive.

Table 6.22. List of parameters for Equations 6.11-6.16.

Parameter	Definition [Unit]
z	Standoff distance [m]
δ	Burial Depth [m]
ρ	Soil density [kgm^{-3}]
E	Gurney explosive energy release [J]
A	Area of the explosive [m^2]
x, y	Planar dimension of target plate [m]
i_v	Specific impulse [N-s]

The analytic solution for specific impulse i_v integrated over a *flat* target's surface area resolves the total blast impulse $\mathrm{I_v}$ on an aboveground rigid structure. Equation 6.11 represents this mechanics theorem in 2-dimensional Cartesian coordinates.

$$\mathrm{I_v} = \int_{x_0}^{x_1} \int_{y_0}^{y_1} i_v(x,y)\,dy\,dx \tag{6.11}$$

The focused blast loads on the target during the *primary* shock phase, or specific impulse i_v, discretizes favorably into the empirically-derived form written as

$$i_v(x,y) = 0.1352\,\left(1+\frac{7\delta}{9z}\right)\left(\frac{\tanh(0.9589\zeta d)}{\zeta d}\right)^{3.25}\sqrt{\frac{\rho E}{z}} \tag{6.12}$$

where $d = \sqrt{(x^2+y^2)}$ and Equation 6.13 defines the function ζ.

$$\zeta = \frac{\delta}{z^{5/4}A^{3/8}tanh\left(\left(2.2\frac{\delta}{z}\right)^{3/2}\right)} \tag{6.13}$$

Furthermore, the specific impulse on an *oblique* blast deflector surface subjected to similar soil blast load conditions, denoted i_n, can be expressed algebraically in Equation 6.14. The solution components include trigonometric parameters $cos^2\,\theta$ and $cos^2\,\beta$, in addition to specific impulse, i_v, for flat targets.

$$i_n = i_v\frac{cos^2\,\theta}{cos^2\,\beta} \tag{6.14}$$

Following mathematical manipulations, Equation 6.15 defines a ratio of trigonometric expressions in terms of the physical experimental parameters standoff distance (z) and angle (α), depicted in Figure 6.54 (*right*).

$$\frac{z^2 \sin\alpha}{(z - x\cot\alpha)^2} = \frac{cos^2\,\theta}{cos^2\,\beta \sin\alpha} = \frac{(x\cos\alpha + z\sin\alpha)^2}{z^2 \sin\alpha} \tag{6.15}$$

Substituting Equation 6.14 into Equation 6.11, the total normal impulse on a dihedral target surface, I_n, can be represented as

$$I_n = 2 * 0.1352 \int_{x_0}^{x_1} \int_{y_0}^{y_1} \left[\frac{cos^2\,\theta}{cos^2\,\beta\, sin\,\alpha} \left(1 + \frac{7\delta}{9z}\right) f(\zeta d) \sqrt{\frac{\rho E}{z}} \right] dydx \tag{6.16}$$

This study's V-shape targets include two angled plates, hence the factor of two in Equation 6.16. Tremblay's final solution [70] only considered one blast deflector plate.

A general numeric integration method implemented into a mathematical solver computed the explicit multidimensional integrands shown in Equations 6.11 and 6.16. To validate this empirical model's predictive performance, the numeric solutions derived from two distinctly different test configurations are compared to the corresponding experimental measurements (Figure 6.54).

The first series examines peak impulse on flat surface targets in dry Mason sand using a 1.0 gram Detasheet charge, 5.1 cm burial depth, detonated at 10 g, with varied HOTs (1.3 cm, 2.5 cm, 3.8 cm, and 5.1 cm). As shown in Figure 6.55, the peak impulse prediction by Tremblay's model displays a nonlinear reduction at progressively higher HOTs, identical to the experimental data.

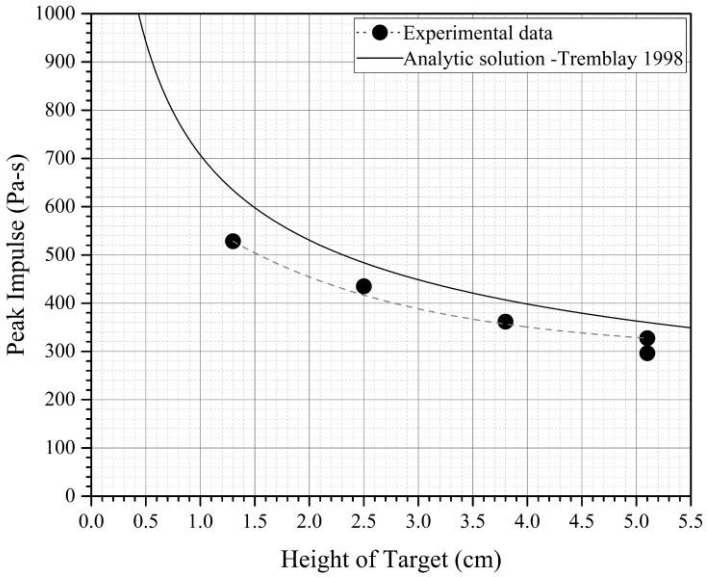

Figure 6.55. Comparison of experimental results (*discrete-points*) and analytic solution (*solid-curve*) for peak impulse on a flat plate as a function of HOT for a 1.0 gram Detasheet charge buried 5.1 cm in dry sand and detonated at 10 g. Power law best-fit curve included (*dashed-line*).

In general, the model accurately predicts the power-law dependent behavior demonstrated in the experimental data. Further comparison between the model and experimental results shows that the analytic solution consistently overestimates the BIRG's peak impulse measurements throughout the examined HOT range (Figure 6.55). However, differences vary minimally by 6.2% and 12.1% at 5.1 cm HOT and 1.3 cm HOT, respectively.

To further evaluate this empirical method's performance, a second series varies soil conditions (80s20c10w), in addition to target geometry (flat, 135°, and 90°), with all other variables charge size (1.0 gram), burial depth (5.1 cm), and g-level (10 g) fixed. Target heights ranged from 0.1 cm to 2.5 cm. As evidenced in the comparison plot, the model prediction of peak impulses demonstrates close correspondence to the BIRG's peak impulse measurements over the 2.5 cm HOT range, independent of target geometry (Figure 6.56).

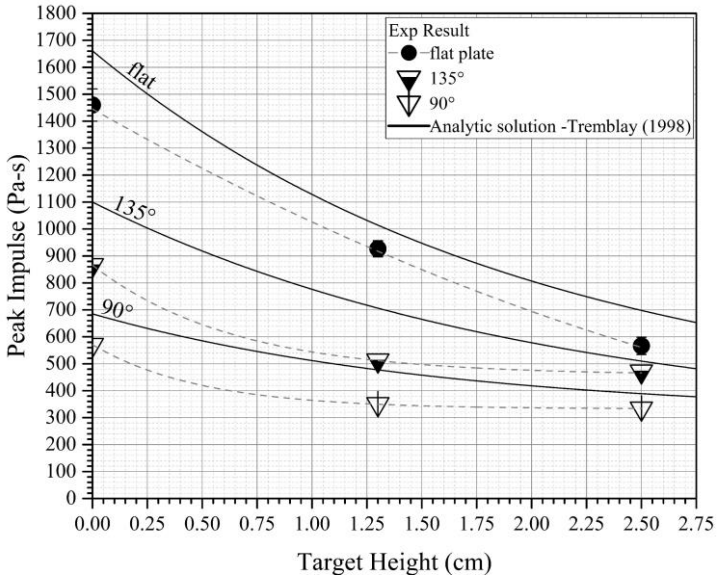

Figure 6.56. Comparison of experimental results (*discrete-points*) and analytic solution (*solid-curves*) for peak impulse on flat and dihedral targets as a function of HOT for a 1.0 gram Detasheet charge buried 5.1 cm in 80s20c10w. Power law best-fit curve included (*dashed-line*).

The analysis reaffirms that peak impulse declines exponentially with elevated target height (Section 6.8) and significantly decreases with reduced target included angle (Section 6.14). These identified physical trends, important factors for impulse determination, are evident in both the predicative model and experimental measurements (Figure 6.56). Similarly, the analytic solution over estimates the experimental data in the examined 2.5 cm HOT regime, specifically 6.1% to 8.9% (flat target), 5.9% to 17.4% (135° target), and finally 10.9% to 18.3% (90° target). The experimental impulse results exhibit closer correspondence to the theoretical curves with increased distance from the soil-air interface, specifically at 2.5 cm HOT (Figure 6.56). This can attribute to progressively higher instabilities and stochastic gas-soil ejecta behavior at lower target heights in the near-field blast environment.

For its versatility and simplicity, this empirical model shows suitable correlation to the measured vertical blast impulse on flat and dihedral target surfaces with HOT variations and captures the overall physical trends. The analytic solution's omission of thermodynamic and damping effects,

significant factors to characterize the multiphasic buried blast impact phenomenon, likely accounts for the apparent deviations to the BIRG measurements.

6.16 Soil Conditions

The analytic synthesis of the BIRG's dynamic response subsequent partially-saturated and heterogeneous gas-soil ejecta impacts, with correlation to high-speed video, quantifies the role in-situ conditions play on the aboveground, near-field blast environment. The following documents the *early* and *primary* shock phases with incremental changes in (1) *moisture content* (dry, 10% and 20% saturation), and (2) *low-plasticity clay content* embedded within a 10% saturated sand skeleton (80s20c10w and 50s50c10w). Physical soil properties are listed in Table 2.3 and References [46,47]. As specified, charge size, target height, and burial depth vary but g-level (10 g) remains constant.

6.16.1 In-situ Moisture Constituent Effect

This analyses provide qualitative and qualitative insights into the effect of in-situ moisture content on the soil heave evolution and attendant momentum transfer. A comparison of the sequential, high-speed video frames illustrates distinctive differences in gas-soil ejecta rheology and blast load mechanisms under two test configurations: 0.8 gram Detasheet charge buried in dry sand (Figure 6.57); 1.0 gram Detasheet charge buried in 20% saturated sand (Figure 6.58). The shallow 2.5 cm burial depth and 10 g-level remain fixed and the distance from the soil surface to the target measures 2.5 cm.

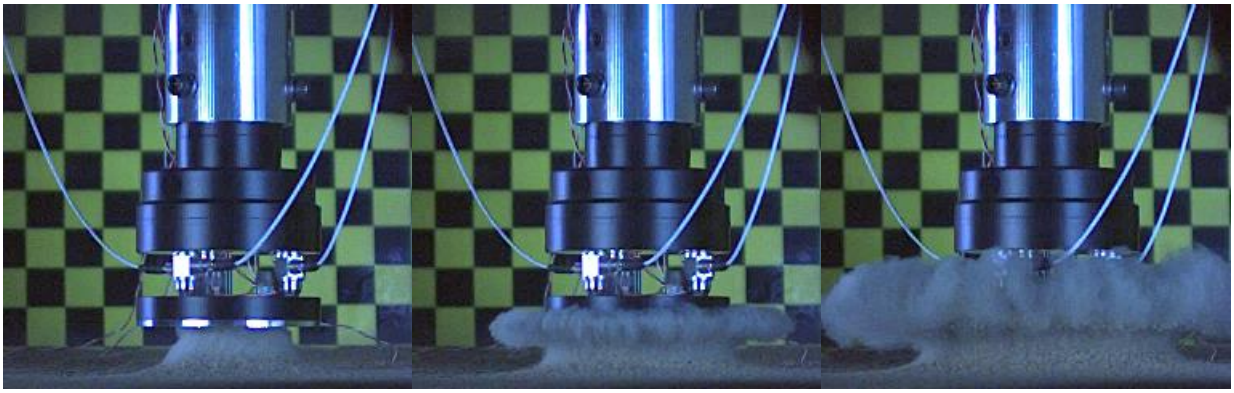

Figure 6.57. Comparisons of the soil deformations for 0.8 gram Detasheet charge buried 2.5 cm in *dry sand* and detonated at 10 g. Target positioned 2.5 cm aboveground. Time after detonation: (*left*) 0.47 ms (*early* shock); (*middle*) 0.79 ms (*primary* shock arrival); (*right*) 1.67 ms (*negligible* BIRG response). Fiducial background 2.2 cm square grid.

(a)

(b)

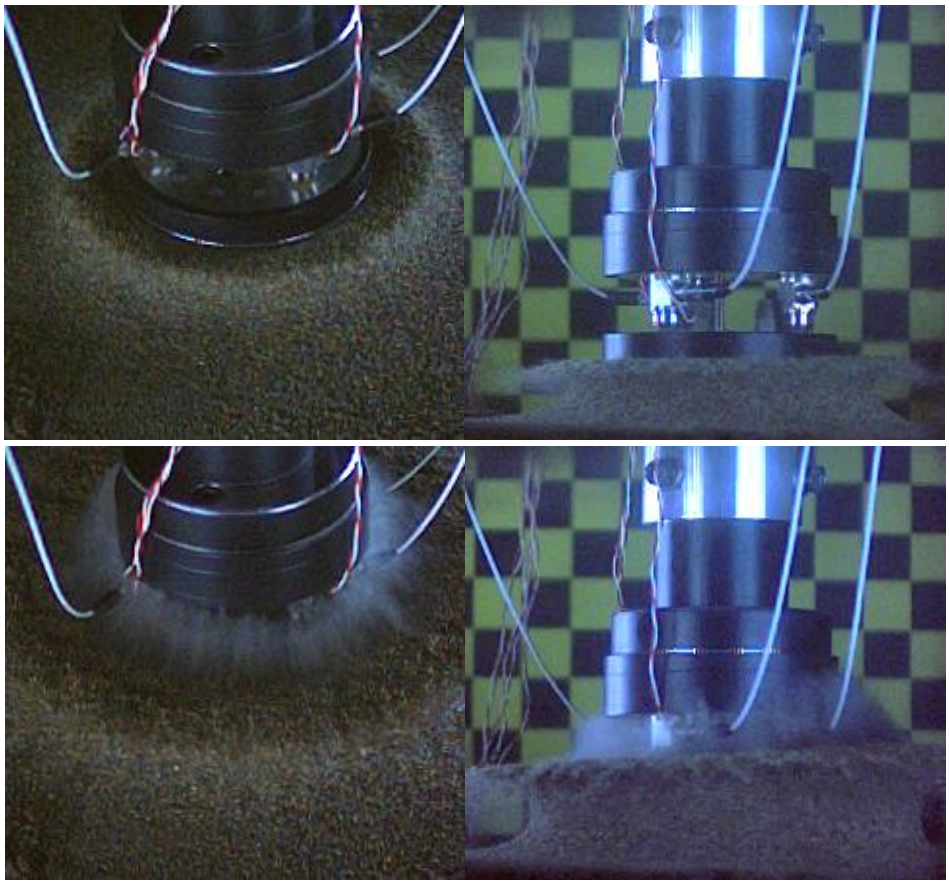

Figure 6.58. Comparison of the soil deformations for a 1.0 gram Detasheet charge buried 2.5 cm in *20% saturated sand* and detonated at 10 g. Target positioned 2.5 cm aboveground. Time after detonation: (a) 0.66 ms (*primary* shock arrival); (b) 1.75 ms (*negligible* BIRG response). Diagonal (*left*) and corresponding horizontal (*right*) views provided. Fiducial background 2.2 cm square grid.

The high-speed video images delineate fundamental physical differences in the near-field blast environment and show that moisture content governs soil ejecta rheology and the gas-soil ejecta-target interaction (Figure 6.57 and 6.58). Dry sand entrained within the prominent, milky-white detonation cloud flows radially (Figure 6.57a), impacts the overlying target (Figure 6.57b), and forms a mushroom-shaped heave (Figure 6.57c). The predominate gas constituent permeates the air-filled void space in the soil ejecta annulus and remains visible throughout the blast event. These blast mechanics distinctly contrast to the partially-saturated soil impact on the target and consequent expansion observed in Figure 6.58. The clearly defined triphasic heave (soil, water, and air) impinges on the overlying target, deforms laterally along the target surface (Figure 6.58a), and yields an initial peak stress, 3661.2 kPa (Figure 6.59). During this energy transfer, the dense, moist soil ejecta front impedes jetting of the opaque detonation cloud. As a result, the detonation products remain indistinct, confirmed by the high-speed camera's diagonal view (Figure 6.58a, *right*) until the *late-stage* of the blast event. Approximately 1.09 ms after *primary* shock arrival, the soil ejecta heave expands beyond the target surface and a small flux of detonation gases appears to 'finger', or breakthrough the soil cap domain (Figure 6.58b). Previously suppressed within the soil ejecta annulus, the combustion gases vent to the atmosphere and contact the target's distal surface. The gas pressures transmit negligible kinetic energy to target 1.75 ms post-detonation, supported by the coincident BIRG stress measurements (Figure 6.59).

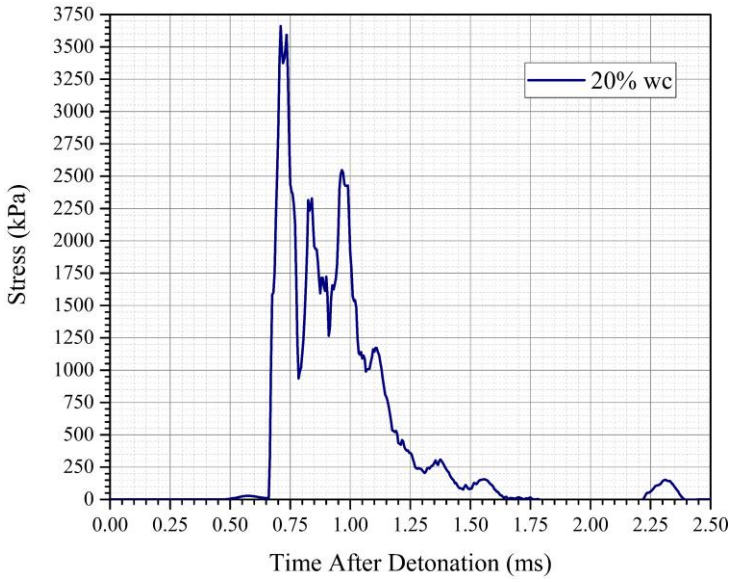

Figure 6.59. Time evolution of the soil blast stress on the BIRG's distal surface during *primary* shock phase for a 1.0 gram Detasheet charge buried 2.5 cm in 20% saturated sand and detonated at 10 g. Target positioned 2.5 cm aboveground.

In general, the data indicates that in-situ moisture content affects soil ejecta rheology and influences the significance of the specific blast load constituent. This phenomenon strongly attributes to the higher porosity in dry sand flows, contrasted to a partially-saturated soil matrix. In a partially-saturated soil matrix, the particle-to-particle cohesion reduces the loose soil ejecta flow evidenced in dry soil disaggregation. Thus, moist sand heaves behave more like an expanding continuum.

A comparison of the temporal distribution of blast stress measured by the BIRG in the *early* shock phase quantifies the shock wave physics as a function of substrate moisture content (Figure 6.60). Charge size (1.0 gram), burial depth (5.1 cm), and g-level (10 g) remain constant and target height varies by 0.1 cm (Figure 6.60, *left*) and 2.5 cm (Figure 6.60, *right*). The target's free-surface proximate the soil interface (HOT=0.1 cm) prevents interfacial contact that might adversely induce a localized stress-inclusion zone in the soil medium.

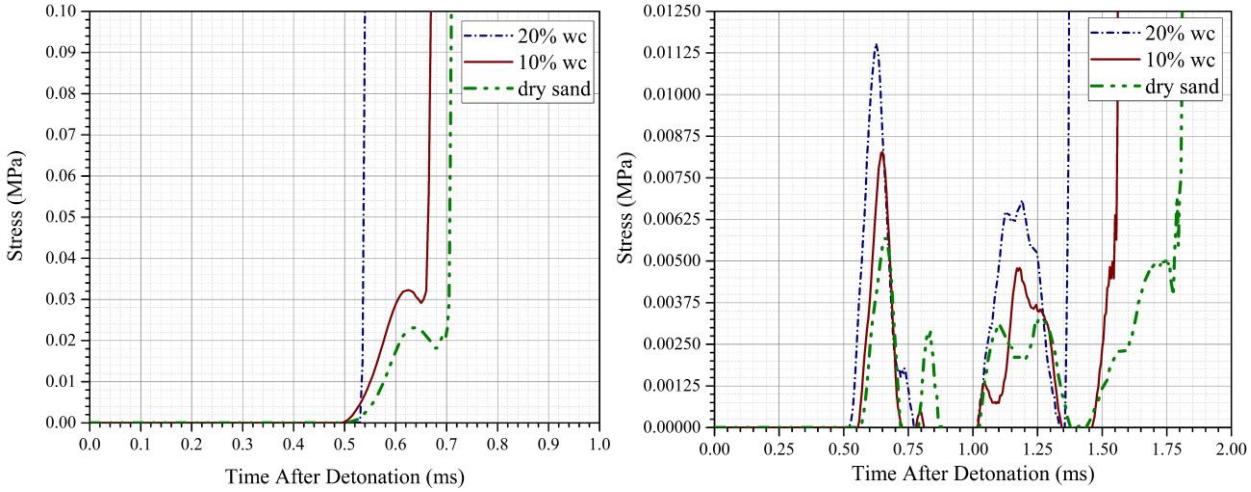

Figure 6.60. Comparison of the shock wave stress time-histories for a 1.0 gram Detasheet charge buried 5.1 cm in dry sand (*dash-dot-dot-line*), 10% saturated sand (*solid-line*), 20% saturated sand (*dash-dot-line*); and detonated at 10 g. BIRG target (*left*) 0.1 cm and (*right*) 2.5 cm aboveground.

The sharp, immediate rise in stress evidences the highly transient impact of the combined blast loads (shock wave, detonation gases, and soil ejecta) on the target positioned 0.1 cm aboveground (Figure 6.60, *left*). At this near-surface HOT, the *early* and *primary* shock impact phases converge at a coincident 0.52 ms. Figure 6.60 (*left*) displays a low-magnitude wavelet in both the dry and 10% saturated soil time-histories, 0.62 ms post-detonation. This wavelet attributes to a small fraction of the incident shock wave compressing against the target, in conjunction with a partial wave reflection back into the soil as a tensile wave, 0.1 ms prior to soil blast loading. This minimal BIRG response suggests that target height measured slightly higher than 0.1 cm for these two tests, with a consequent acoustic impedance mismatch at the soil-air interface.

A 2.5 cm increase in target height decouples the blast load mechanisms into shock wave and gas-soil ejecta impacts, and thereby enables the shock wave characterization as a function of moisture content (Figure 6.60, *right*). Clearly, moisture strongly influences the blast induced shock wave physics. The high-rate detonation wave propagates progressively faster in the soil matrix with elevated moisture. Wave propagation in 20% saturated sand demonstrates the most

efficient transmission: the shock wave impacts the overlying target first at 0.51 ms, yielding a wave speed of 149 ms^{-1}. This shock wave arrival time precedes the 10% saturated and dry sand tests by 0.02 ms and 0.04 ms, respectively (Figure 6.60, *right*). Furthermore, subsequent shock wave arrival, the shock wave stresses rapidly increase to peak magnitude and sharply decline to zero, typical of high-rate compression. Observed in the comparison plot (Figure 6.60, *right*), an increase in the in-situ moisture content induces higher shock wave peak stresses, indicating a monotonic relationship. Specifically, ground shock intensity measures twice as high in 20% saturated sand when compared to dry sand (Table 6.23).

For comparative analysis, multiple test series further distinguish the efficiency of shock wave energy transmission in dry and partially-saturated soils (Figure 6.61).

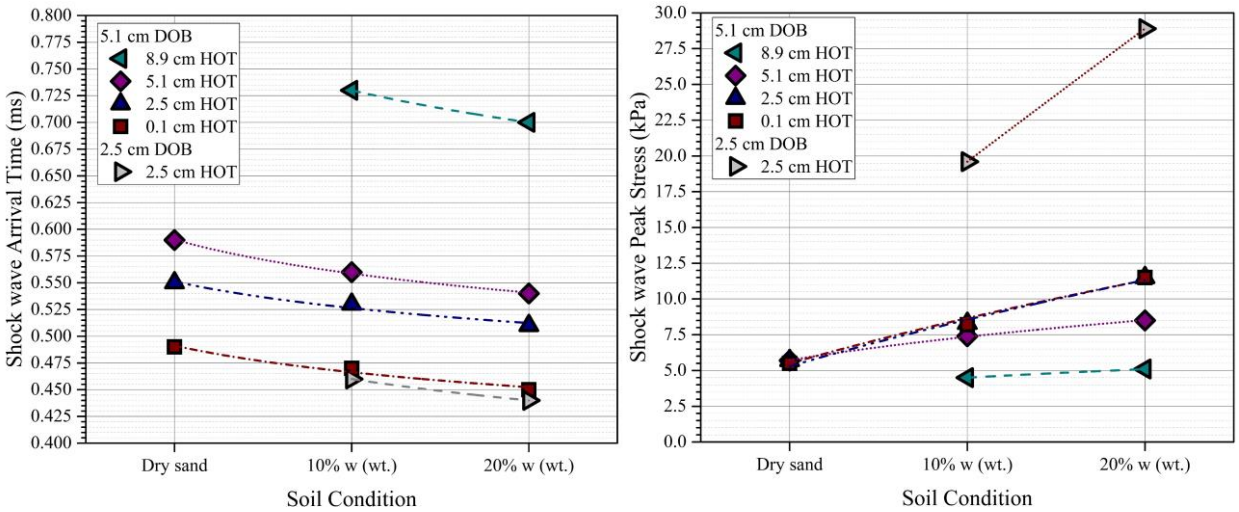

Figure 6.61. Shock wave arrival time (*left*) and peak stress (*right*) for a 1.0 gram Detasheet charge buried in dry sand, 10% saturated sand, 20% saturated sand; and detonated at 10 g. Legend details target height and burial depth.

The data substantiates the moisture-dependent trend that detonation wave speeds consistently measure the highest in 20% saturated soil, and gradually decelerate with reduced water content (Figure 6.61, *left*). In general, the shallowest 2.5 cm burial in 20% saturated soil evidences the

earliest shock wave arrival at 0.44 ms for a 2.5 cm HOT, followed by shock wave arrival in the 10% saturated soil at 0.46 ms (Table 6.23). This corresponds to a shock wave velocity of 113.6 ms^{-1} and 108.7 ms^{-1}, respectively. Approximately 0.1 ms later, the shock wave induces a dynamic BIRG response for a 5.1 cm burial in both saturated soil conditions measured 0.1 cm aboveground, in spite of substantive differences in target height and soil overburden pressure. The standoff distance, defined as the vertical distance from the charge to the target. remained 5.1 cm for both test configurations and can explain the similar arrival times. As the distance from the soil-air interface to the target's distal surface increases, shock wave arrival times lengthen, a phenomenon detailed in Section 6.8.

In addition, shock wave peak stresses vary proportionally with soil moisture content (Figure 6.61, *right*). Specifically, peak values measure consistently higher with increased moisture content, independent of the target heights and burial depths examined. Furthermore, slopes of the included regression curves indicate shock wave peak stresses appear less sensitive to soil properties with elevated HOT. For example, shock wave peak stresses increase linearly with moisture content by an approximate 43% at 0.1 cm HOT (Figure 6.61, *right*). In contrast at 8.9 cm HOT, shock wave propagation through 20% saturated soil yields a nominal 13% higher peak stress value when compared to 10% saturated sand. Elevated target height results in rapid attenuation of air shock intensity and explains these similar peak values (Figure 6.61, *right*) [56,57].

The results confirm that air shock intensity and detonation wave speed decline with reduced soil moisture content. Dry soil displays a highly dissipative mechanistic response relative to partially-saturated sand (Figure 6.61). Higher water fractions within the soil skeleton's air-filled void space augment geomaterial energy damping with consequent more efficient ground shock transmissivity.

As a result, shock wave velocities and peak impact stresses consistently increase with moisture content, attributed to the moisture-dependent decrease in the soil's shear strength and compressibility [8,47]

The contrasting BIRG target response measured 0.1 cm (Figure 6.62, *left*) and 2.5 cm (Figure 6.62, *right*) aboveground resolves the rate-dependent, partially-saturated and dry soil blast load distributions and demonstrates that in-situ moisture strongly influences soil blast stress. This comparative analysis quantifies the *primary* shock phase following *early* shock wave impact (Figure 6.60).

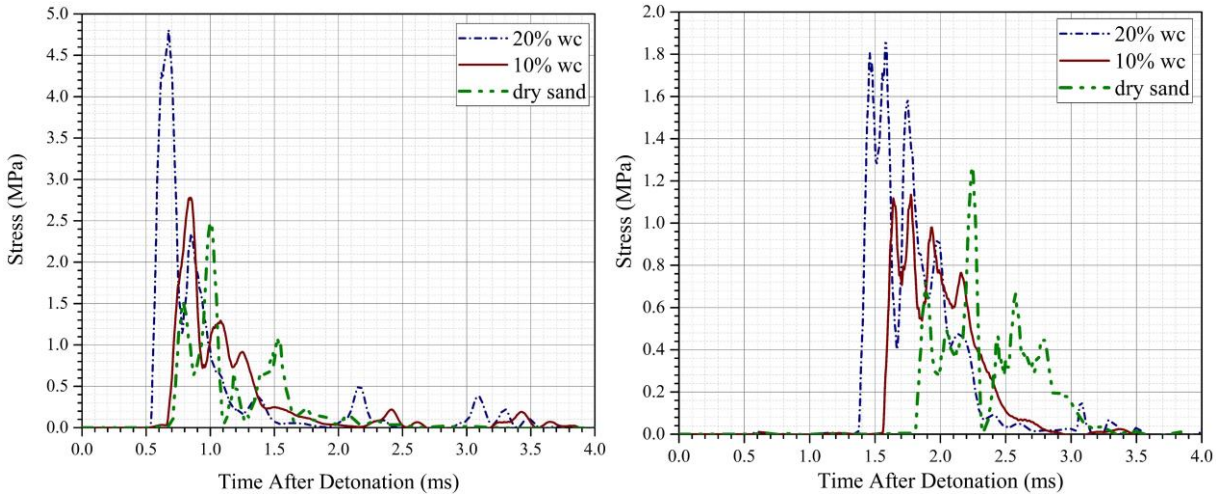

Figure 6.62. Comparisons of the soil blast stress time-histories during the *primary* shock phase for a 1.0 gram Detasheet charge buried 5.1 cm in dry sand (*dash-dot-dot-line*), 10% saturated sand (*solid-line*), 20% saturated sand (*dash-dot-line*); and detonated at 10 g. Target positioned (*left*) 0.1 cm and (*right*) 2.5 cm aboveground.

As expected, gas-soil ejecta impacts clearly induce higher stress magnitudes on the overlying target (Figure 6.62) than the shock wave constituent (Figure 6.60). The results show, however, similar moisture-dependent trends: soil blast loads occur progressively later and decline in peak value as a function of reduced soil saturation. Independent of HOT, the 20% saturated sand heave arrives at the target's distal surface first, and yield the highest initial peak stress (Figure 6.62). The

BIRG subjected to dry sand blasts exhibits the latest response time and lowest peak stress magnitudes, with intermediate values for the 10% saturated soil (Figure 6.62). Consistent in both HOT series, a 10% reduction in saturation (from 20% to 10%) decreases initial peak stress by roughly 40% (Figure 6.62). A further reduction in soil moisture content (from 10% to dry) attenuates peak soil blast stresses by 46% and 27%, measured 0.1 cm (Figure 6.62, *left*) and 2.5 cm (Figure 6.62, *right*) aboveground, respectively.

A comprehensive comparison of the soil blast load arrival times and initial peak stresses verifies the aforementioned in-situ moisture dependent trend on soil blast loading mechanics (Figure 6.63). Significantly, these *primary* shock phase measurements, in conjunction with the *early* shock impact results (Figure 6.61), quantify the initial blast impact stresses.

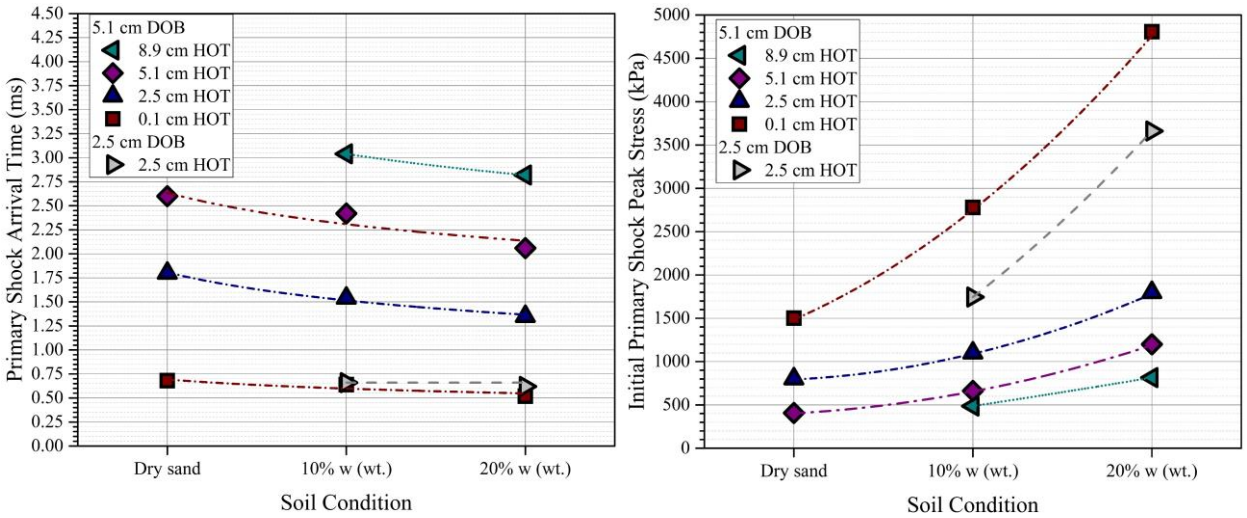

Figure 6.63. Gas-soil ejecta arrival times (*left*) and initial peak stress (*right*) for a 1.0 gram Detasheet charge buried in dry sand, 10% saturated sand, 20% saturated sand; and detonated at 10 g. Legend details target height and burial depth.

As shown in Figure 6.63 (*left*), soil saturation accelerates the arrival times of the blast loads and consequent energy transfer in all examined test series. The water constituent augments the soil medium's inter-particle cohesiveness by reducing its overall porosity, substantiated by the

detonation gas flow dynamics depicted in the high-speed videos (Figure 6.57 and 6.58). For moist substrates, less explosive potential energy dissipates to the atmosphere during initial soil deformation and more energy drives the surrounding medium towards the target at accelerated rates, verified by the progressively earlier soil blast impact times with increased moisture content (Figure 6.63, *left*). In contrast, the highly-pressurized detonation gases escape through the air-void spaces in dry sand heaves and thus, explosive potential energy declines. The residual detonation energy converts to kinematic soil ejecta flow and eventual, attenuated kinetic energy transfer to the target.

As previously demonstrated, this in-situ soil moisture-dependence influences the *primary* shock impact phase. The results document that initial peak soil blast stresses exhibit a nonlinear increase with elevated soil saturation (Figure 6.63, *right*). Higher packing densities and faster flow rates in moist soil ejecta heaves significantly increase the inertia granular forcing and subsequent soil blast stress. The diffuse, disaggregate dry sand flows at target impact repeatedly induce the lowest peak soil blast stresses (Figure 6.63, *right*). In addition, initial peak soil blast stresses measured in close-proximity to the soil surface appear more sensitive to mass fraction variations in water content when compared to the gradual change at progressively higher HOTs (Figure 6.63, *right*). This relationship implies that soil properties strongly affect the near-field blast environment, and appear less influential on the far-field blast impact mechanics in the range examined. The simultaneous elevated target height and increased soil heave disaggregation (reduced granular packing density) accounts for this apparent trend.

Figure 6.64 resolves the total blast momentum transferred to the target, derived from a temporal integration of the soil blast stress (Figure 6.62), and further quantifies in-situ moisture effects,

specifically impulse. Moisture content clearly dominates the temporal distribution of impulse over the range investigated.

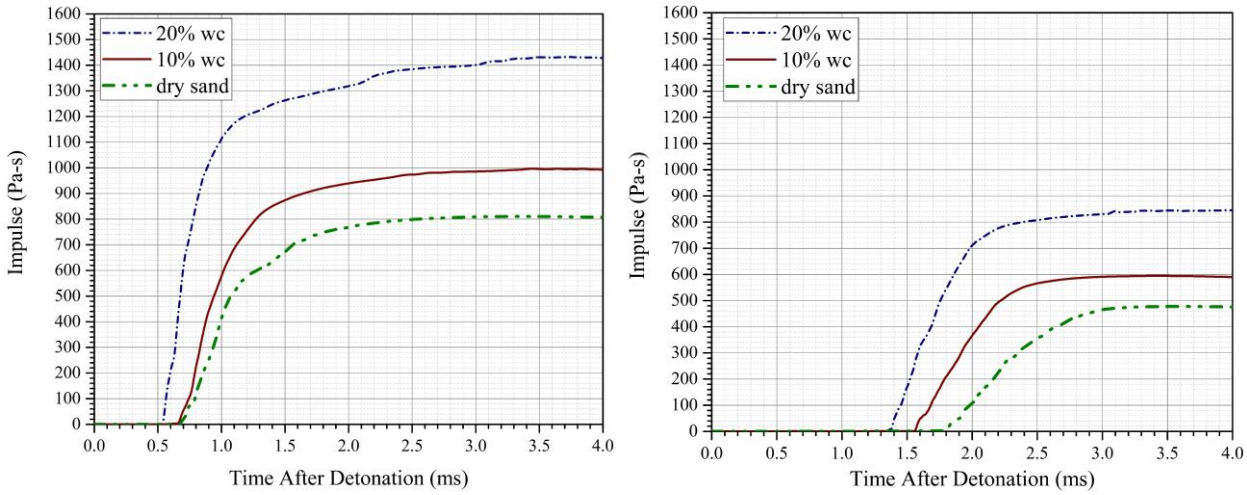

Figure 6.64. Comparisons of the impulse time-histories for a 1.0 gram Detasheet charge buried 5.1 cm in dry sand (*dash-dot-dot-line*), 10% saturated sand (*solid-line*), 20% saturated sand (*dash-dot-line*); and detonated at 10 g. Target positioned (*left*) 0.1 cm and (*right*) 2.5 cm aboveground.

The rate-dependent rise to peak impulse consistently increases with in-situ moisture content which directly relates to the higher initial soil blast stresses induced by partially-saturated soil blast loads (Figure 6.63). Furthermore, the results show that peak impulses induced by wet sand blasts measure higher magnitudes when compared to dry sand explosions, independent of HOT and DOB (Figure 6.64). This apparent trend corresponds to the distinctive constitutive behavior of wet and dry soil, as discussed below.

The data compilation presented in Figure 6.65 compares peak impulse dependence on soil saturation levels at various target heights and burial depths. The results substantiate that the BIRG consistently measures impulses in decreasing peak magnitude: 20% saturated sand, 10% saturated sand, and dry sand, identical to the ordering delineated by both shock wave (Figure 6.61) and soil blast load mechanisms (Figure 6.63).

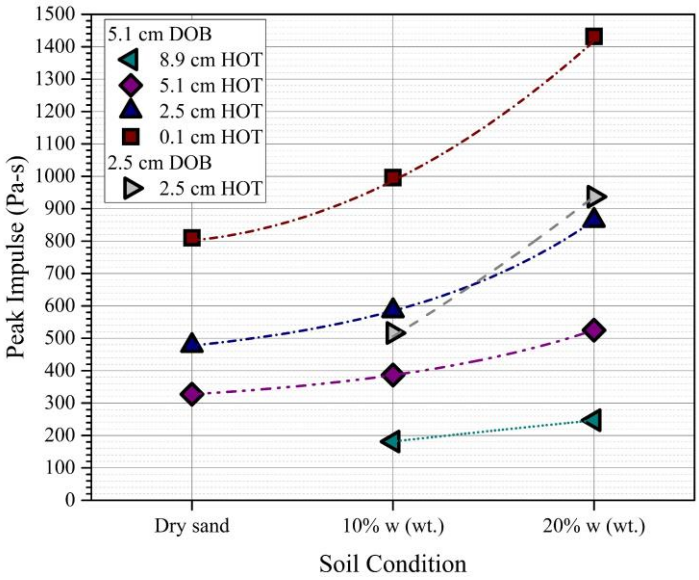

Figure 6.65. Peak impulse as a function of soil saturation for a 1.0 gram Detasheet charge under 2.5 cm and 5.1 cm soil overburdens and detonated at 10 g. Legend details target height and burial depth.

As documented in Section 6.8, increasing standoff distance decreases peak impulse values. Analogous to soil blast peak stress (Figure 6.63), peak impulses measured near the soil-air interface exhibit a more pronounced parabolic increase with soil saturation, and decline with increasing HOT at a constant DOB (Figure 6.65). At the 0.1 cm HOT and 5.1 cm DOB, the total momentum transmitted to the BIRG by dry soil blast loading yields the lowest peak impulse of 810.1 Pa-s (Table 6.23). Increasing in-situ moisture content by 10% increments shows peak impulses increase by 23% and 44%, respectively. With the BIRG's distal surface elevated to a 2.5 cm HOT at the same 5.1 cm DOB, the dry soil ejecta heave yields a lower peak impulse of 477.5 Pa-s (Table 6.23). Consequent 10% additions in moisture content, impulse magnitudes reveal a similar nonlinear rate increase when compared to the 0.1 cm HOT series: 24% and 46%, respectively (Table 6.23). However, beyond this 2.5 cm HOT, increased in-situ moisture content demonstrates less influence on peak impulse. For example, at the 5.1 cm HOT, the peak impulse transferred by dry soil blast loads equate to a reduced 327.5 Pa-s, and increase with saturated sand

intervals by 17% and 36%. And finally, at the maximum 8.9 cm HOT, 20% saturated soil blast loads induce peak impulses 32% higher than 10% saturated soil ejecta heaves. In comparison, the lowest 0.1 cm HOT evidences a greater moisture content dependence. The incremental 10% increase in saturated soil to 20% yields an approximate 45% higher peak impulse value (Table 6.23), and thus, indicates that the mechanistic behavior of partially saturated sand corresponds more closely to the dry sand response as a function of increased HOT. This HOT-sensitivity can attribute to the distinctive differences in the temporal and spatial evolution of gas-soil ejecta loads, with moisture content variance, as shown in the high-speed video images (Figure 6.57 and 6.58). The water constituent significantly affects the soil particle-to-particle dynamics and cohesion: as the wet soil ejecta heave spherically expands, the densified granular regions, or clumps, diffuse and soil annulus packing density decreases. Subsequent increases in radial distance to the overlying target, wet soil ejecta rheology reflects similar dry sand, disperse flow behavior. The data collectively suggests that the moisture content influence lessens with increased HOT in the examined range.

This comprehensive analysis substantiates that soil water content strongly influences the explosive burst characteristics, soil ejecta rheology, shock wave dynamics, and soil blast kinetics. The water constituent decreases the soil skeleton's air-filled void space, and lowers the soil's permeability and shear strength. The inter-particle cohesion impedes the flux of highly pressure denotation gases to the atmosphere as depicted in the high-speed video images (Figure 6.57 and 6.58). More blast energy drives the overlying moist soil at accelerated rates, with a focused directionality towards the target when compared to dry soil blasts. Furthermore, the higher bulk modulus (i.e. lower compressibility) in wet sand flows increases the ejecta annulus packing density, or localized clumping, and correlates to increased soil blast stresses, stagnation pressures,

and peak impulses imparted to the aboveground target. Table 6.23 summarizes *early* and *primary* shock impact times, peak stress and impulse for this moisture-dependent analysis.

Table 6.23. Summary of *early* and *primary* shock phase arrival times and peak stress, in addition to peak impulse for a 1.0 gram Detasheet charge buried 5.1 cm and 2.5 cm in dry and partially-saturated sand and detonated at 10 g. Target positioned at various heights aboveground.

			Arrival time (ms)		Initial Peak Stress (kPa)		
WC	DOB (cm)	HOT (cm)	*Early* shock	*Primary* shock	*Early* Shock	*Primary* shock	Peak Impulse (Pa-s)
Dry			0.49	0.68	5.5	1500.9	810.1
10%	5.1	0.1	0.47	0.64	8.2	2780.2	996.2
20%			0.45	0.52	11.5	4807.5	1431.7
10%	2.5	2.5	0.46	0.66	19.6	1744.4	516.2
20%	2.5	2.5	0.44	0.62	28.9	3661.2	937.0
Dry			0.55	1.80	5.7	802.5	477.5
10%	5.1	2.5	0.53	1.54	8.3	1101.7	585.1
20%			0.51	1.35	11.5	1798.8	864.2
Dry			0.59	2.60	5.7	407.4	327.5
10%	5.1	5.1	0.56	2.42	7.4	662.9	382.6
20%			0.54	2.06	8.5	1200.7	525.0
10%	5.1	8.9	0.73	3.04	4.5	487.4	181.5
20%	5.1	8.9	0.70	2.82	5.1	815.4	246.9

6.16.2 In-situ Clay Constituent Effect

The following parametric analyses provide insight into the inhomogeneous substrate effect on the aboveground blast phenomenon. Air, water, and now a low-plasticity clay constituent fill the inter-particle soil matrix void space. The experimental results from multiple test series clarify the

clay constituent influence on the blast phenomenon and include the 10% saturated sand data, presented before, to augment comparative data analysis.

The first test series used a 1.0 gram Detasheet charge under a 5.1 cm overburden in a testbed composed of 80% sand and 20% clay with 10% saturation (80s20c10w). Target height varies but g-level remains constant (10 g). The dual high-speed images recorded simultaneous to the BIRG measurements in the *primary* shock phase at target impact (Figure 6.66) and subsequent soil dome expansion beyond the target plate (Figure 6.67), illustrate fundamental differences in the heterogeneous soil behavior and evolution of triphasic gas-soil ejecta heaves.

(a)

(b)

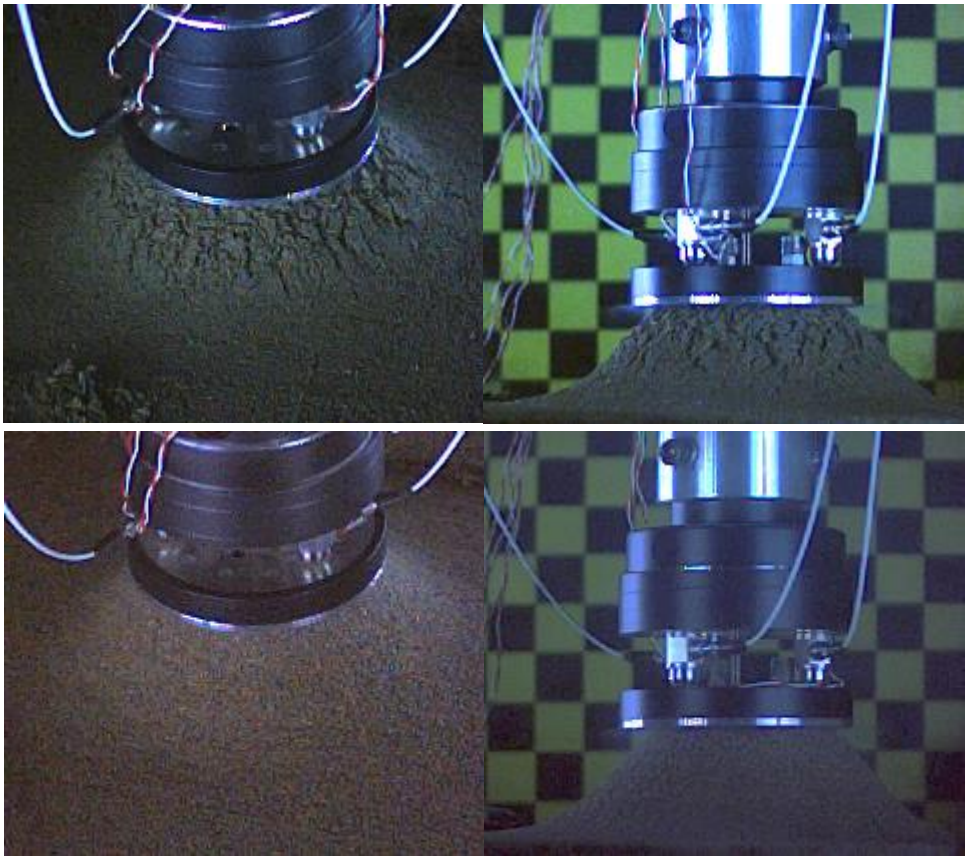

Figure 6.66. Comparison of the soil deformations for a 1.0 gram Detasheet charge buried 5.1 cm in (a) 80% sand, 20% clay with 10% water content (80s20c10w); (b) 10% saturated sand; and detonated at 10 g. Target positioned 5.1 cm aboveground. Frame time after detonation coincides with gas-soil ejecta impact: (a) 2.17 ms; (b) 2.42 ms. Diagonal (*left*) and corresponding lateral (*right*) views provided. Fiducial background 2.2 cm square grid.

(a)

(b)

Figure 6.67. Comparison of the soil deformations for a 1.0 gram Detasheet charge buried 5.1 cm in (a) 80% sand, 20% clay with 10% water content (80s20c10w); (b) 10% saturated sand, and detonated at 10 g. Target positioned 5.1 cm aboveground. Frame time after detonation corresponds to *negligible* target response: (a) 4.80 ms; (b) 4.05 ms. Diagonal (*left*) and corresponding lateral (*right*) views provided. Fiducial background 2.2 cm square grid.

A comparison of the video images clearly shows that the inter-particle organic binders water and clay dominate ejecta heave rheology and surface roughness. Clay-sand ejecta impacts the target's distal surface at 2.17 ms (Figure 6.66a) and precedes the initial 10% saturated sand heave arrival by 0.25 ms (Figure 6.66b). At target impact, both soil domes display a pronounced vertical flow directionality due to the lateral soil confinement and a hemispherical mound growth, characterized by smooth sloping sides (Figure 6.66a, b). However, clay-induced adhesion at the inter-particle contact surfaces causes increased, fissured texturing and visible surface

discontinuities (Figure 6.66 and 6.67a). These irregularly-shaped microstructures physically resemble surface cracks and visibly contrast to the uniform surface contours evidenced in the purely-saturated soil deformations (Figure 6.66 and 6.67b). Subsequent impulsive loading, the soil annulus in both testbeds evolves beyond the target's circumference. The spherically expanding aggregate shell further reflects their characteristic surface features: discrete clumping in clay-sand ejecta (80s20c10w) contrast to coarse granular flows in moist sand (10% saturated sand) (Figure 6.66 and 6.67). Throughout the blast load duration, the cohesive soil front acts as an impermeable membrane and suppresses gas venting throughout the soil annulus.

The high-speed video comparisons delineated the clay constituent's influence on soil deformation rates and rheology (Figure 6.66 and 6.67). To gain insight into the in-situ clay dependence in the *early* shock phase, Figure 6.68 quantifies the detonation wave kinematics (*left*) and kinetics (*right*) as a function of target height for a 1.0 gram Detasheet charge buried 5.1 cm in 80s20c10w and 10% saturated sand.

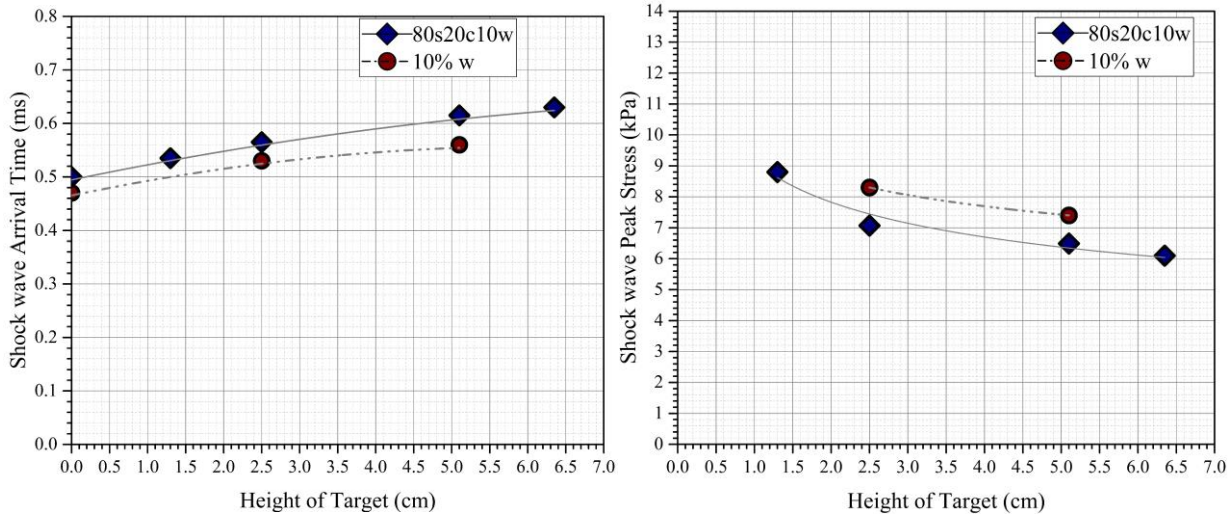

Figure 6.68. Shock wave arrival times (*left*) and peak stress (*right*) as a function of target height for a 1.0 gram Detasheet charge buried 5.1 cm in 10% saturated sand and 80s20c10w. Charge detonated at 10 g. Best-fit regression curves included.

The data indicates that shock wave intensity and propagation rates repeatedly measure lower for 80s20c10w relative to the partially-saturated sand despite variations in HOT (Figure 6.68). At the 0.1 cm HOT, the detonation wave propagating in 10% saturated sand impacts the BIRG at 0.47 ms (Figure 6.68, *left*). This precedes shock wave arrival in 80s20c10w by 20 μs, yielding a 4.5 ms^{-1} difference in wave speed. Likewise, the shock wave impacts the target interface 5.1 cm aboveground approximately 60 μs earlier in 10% partially-saturated sand than clay-sand, a 17.5 ms^{-1} difference in wave speed.

In addition, shock wave peak stresses also demonstrate similar clay-dependent trends (Figure 6.68, *right*). Faster detonation wave speeds evidenced in partially-saturated sand induce elevated shock wave peak stresses, measured by the BIRG. The results confirm the general consensus: shock waves transmit more effectively through 10% partially-saturated soil than 80s20c10w, substantiated by the 17% and 14% higher peak stresses at 2.5 cm and 5.1 cm HOT, respectively (Figure 6.68, *right*). This phenomenon can attribute to the viscoelastic response characteristic of clay-sand mixtures. At the relatively low, 20% mass fraction, the clay constituent adheres to the soil grain interfaces. The heterogenous microstructure enables increased energy attenuation. This material damping mechanism reduces shock wave transmissivity through the granular substrate.

To further assess the clay's influence on the soil blast impact phenomenon, Figure 6.69 contrasts the *primary* shock impact arrival times (*left*) and initial soil blast peak stress (*right*) for the two triphasic mediums as a function of HOT.

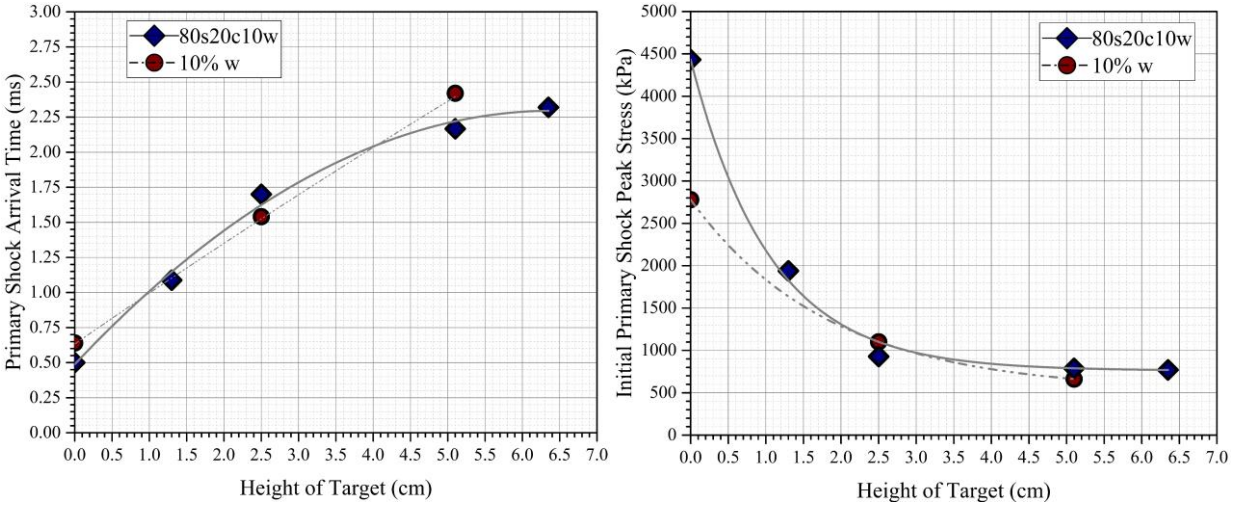

Figure 6.69. *Primary* phase arrival times (*left*) and soil blast peak stress (*right*) as a function of target height for a 1.0 gram Detasheet charge buried 5.1 cm in 10% saturated sand and 80s20c10w. Charge detonated at 10 g. Best-fit regression curves included.

Throughout the examined HOT range, a comparison of the 80s20c10w and partially-saturated sand gas-soil ejecta exhibit close-correspondence, with a nominal deviation of 12% throughout the examined HOT range (Figure 6.69, *left*). This suggests that the in-situ clay content plays a minimal role in the explosive energy conversion to soil ejecta kinematics. The HOT dependence trend continues: the arrival times of the gas-soil ejecta mechanisms lengthen with increasing target height.

The peak stress time-histories in the *primary* shock phase (Figure 6.69, *right*) demonstrate that proximate the soil surface (0.1 cm HOT), the 80s20c10w soil ejecta load mechanisms induce an initial peak stress, 4432.1 kPa, an approximate 1.5 times higher than the partially-saturated loads (Figure 6.69, *right*). After this specific 0.1 cm target height, the initial soil blast peak stresses in both test series decline exponentially until the 2.5 cm HOT (Figure 6.69, *right*). At this point, similar to the shock wave arrival times, the clay constituent appears to have a negligible effect on the initial peak stresses. The two in-situ soil conditions exhibit close-correspondence in peak stress, quantified by a 12.3% mean variance.

Furthermore, soil ejecta heaves containing mass fractions of low-plasticity clay affect the total soil blast momentum. Figure 6.70 compares the peak impulse derived from the temporal and spatial distribution of 80s20c10w and 10% saturated soil blast impacts on the BIRG.

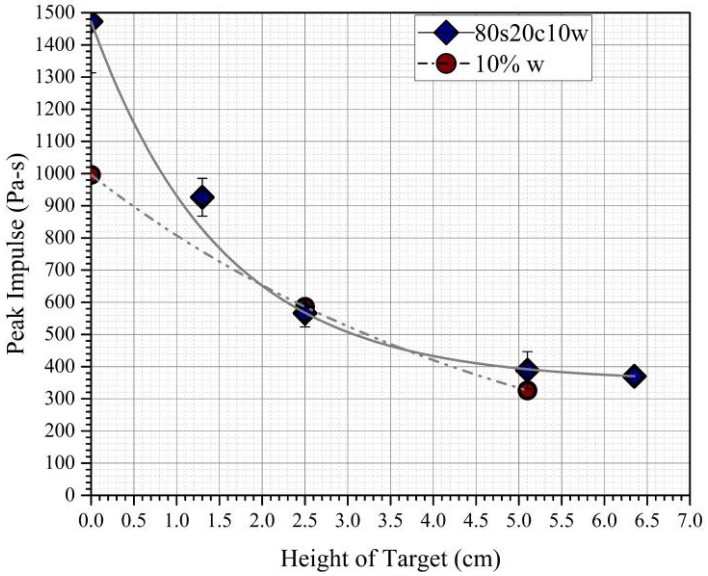

Figure 6.70. Peak impulse as a function of target height for a 1.0 gram Detasheet charge buried 5.1 cm in 10% saturated sand and 80s20c10w. Charge detonated at 10 g. Best-fit regression curves included.

The data confirms the anticipated HOT-dependent trend: impulse magnitudes measure highest at the near-surface HOT and decline nonlinearly with increased vertical distance to the BIRG target plate (Figure 6.70). A closer examination of peak impulse reveals that in-situ soil properties significantly influence the near-field blast kinetic energy. However, the in-situ soil dependence on peak impulse declines with incremental increases in target height. For example, the highest peak impulse, 1473.2 Pa-s, induced by 80s20c10w soil ejecta loads 0.1 cm aboveground, measures nearly 50% higher than the partially-saturated soil blast energy transfer to the target. This phenomenon can attribute 80s20c10w compaction density and cohesive strength when compared to 10% partially-saturated sand. In contrast, at the 2.5 cm and 5.1 cm HOT, soil blast peak impulses differ nominally by 3.2% and 2.8%, respectively (Figure 6.70). As previously discussed,

soil disaggregation increases with elevated target height and reduces the clay constituent effect on the blast momentum transfer. In the near-field environment, the granular heaves behave more like a triphasic particle-continuum, and the soil's bulk material properties play a formative role on the target's dynamic response. At elevated target heights, the soil ejecta heave displays large radial deformations with increased spallation. The compaction density of the load mechanisms declines with consequent reduced blast stress focus on the BIRG target. Therefore, the temporal and spatial distribution of discrete particle impingement on the target surface resolves the total blast momentum. Table 6.24 summarizes the *early* and *primary* shock phases in addition to peak soil blast stress and impulse for the initial in-situ clay constituent analysis.

Table 6.24. Summary of *early* and *primary* shock phase arrival times and peak stress in addition to peak impulse for a 1.0 gram Detasheet charge buried 5.1 cm in 10% saturated sand and 80s20c10w. Charge detonated at 10 g. Target positioned at various heights aboveground.

			Arrival time (ms)		Initial Peak Stress (kPa)		
	DOB (cm)	HOT (cm)	*Early* shock	*Primary* shock	*Early* Shock	*Primary* shock	Peak Impulse (Pa-s)
10% w	5.1	0.1	0.47	0.64	8.2	2780.2	996.2
80s20c10w	5.1	0.1	0.49	0.49		4432.1	1473.2
10% w	5.1	2.5	0.53	1.54	8.3	1101.7	585.1
80s20c10w	5.1	2.5	0.57	1.70	7.1	928.3	566.5
10% w	5.1	5.1	0.56	2.42	7.4	662.9	382.6
80s20c10w	5.1	5.1	0.62	2.17	6.5	788.6	388.7

To further examine the effect of clay on the buried blast impact phenomenon, the experimental results from two individual test series characterize the BIRG response subsequent triphasic soil ejecta blast loads composed of 20% and 50% mass fractions of low-plasticity clay at an equivalent

soil saturation (10% water content). As the mass fraction of clay constituent increases, a predominate clay matrix forms within the soil skeleton's air-void space. This contrasts the micromorphology at lower clay percentages: clay fragments bond directly to individual soil grains. Thus, the addition of low-plasticity clay affects the interfacial granular mechanics, specifically the bulk viscoelastic response of soil blast loads, as discussed below.

The first test series reexamines the dihedral target analysis in Section 6.14 that used a 0.8 gram Detasheet charge buried 2.5 cm and detonated at 10 g. The distance from the V-shape target's apex to the soil surface measures 2.5 cm.

The rate-dependent shock wave propagation in 80s20c10w and 50s50c10w show minimal differences with increased in-situ clay in the *early* shock phase, measured by all tests, occurs at 0.49 ms post-detonation, or an incident wave speed of 102.0 ms^{-1}. Shock wave kinetics, however, exhibit prominent clay-dependent effects. Detonation waves propagating in 80s20c10w yield shock wave peak stresses of 8.14 kPa (135° target) and decrease to 7.33 kPa (90° target). In the 50s50c10w matrix, shock wave peak stresses measure lower, specifically, a reduced 3.6% (135°) compared to 14.2% (90°).

A comparison of the blast stress (Figure 6.71, *left*) and impulse (Figure 6.71, *right*) time-histories demonstrates the clay constituent's formative and consistent influence on the spatial and temporal soil blast load distribution on the BIRG.

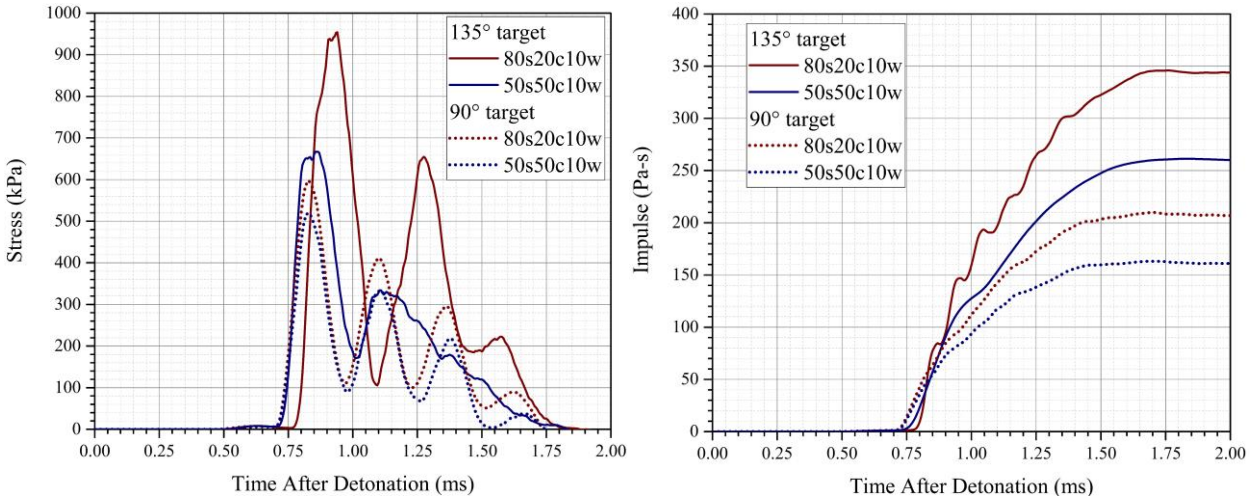

Figure 6.71. Comparisons of the stress (*left*) and impulse (*right*) time-histories for a 0.8 gram Detasheet charge buried 2.5 cm in 10% saturated sand containing 20% and 50% mass fractions of clay and detonated at 10 g. The 135° and 90° dihedral targets positioned 2.5 cm aboveground.

Soil blast stresses and momentum imparted to the target attenuate with progressively higher clay mass fractions. The 80s20c10w soil ejecta blast loads induce initial peak pressures of 954.1 kPa (135°) and 6634.3 kPa (90°). The increasingly damped constitutive behavior of 50s50c10w soil ejecta results in effectively lower initial soil blast peak stresses by approximately 30% and 15% with reduced dihedral target angle. Furthermore, total soil blast momentum transfer to the BIRG exhibits similar clay-induced energy dissipation behavior (Figure 6.71, *right*). The comparative time-histories demonstrate the clay constituent dependence on impulse with the expected inverse proportionality: peak impulses decline with increased in-situ clay content. Specifically, soil ejecta load mechanisms with equal mass fractions of clay and sand induce peak impulses nearly 1.3 times lower than 80s20c10w soil ejecta impacts, independent of target geometry. This apparent dissipative behavior clearly reflects the microstructural mechanical differences in the two heterogeneous soil ejecta heaves.

A second comparative analysis provides additional critical insights on the near-field aboveground flat target response as a function of the same clay mass fractions and includes the

10% saturated and dry sand results to augment data synthesis. This analysis used a 1.0 gram C4 charge buried 0.8 cm and detonated at 10 g. The distance from the target's free surface to the soil-air interface measures 5.1 cm. The data indicates that the shallow, 0.8 cm overburden, the BIRG measures the same force arrival times in both the *early* and *primary* shock impact phases (Figure 6.72, *left*). However, shock impact arrival times demonstrate an in-situ soil dependence.

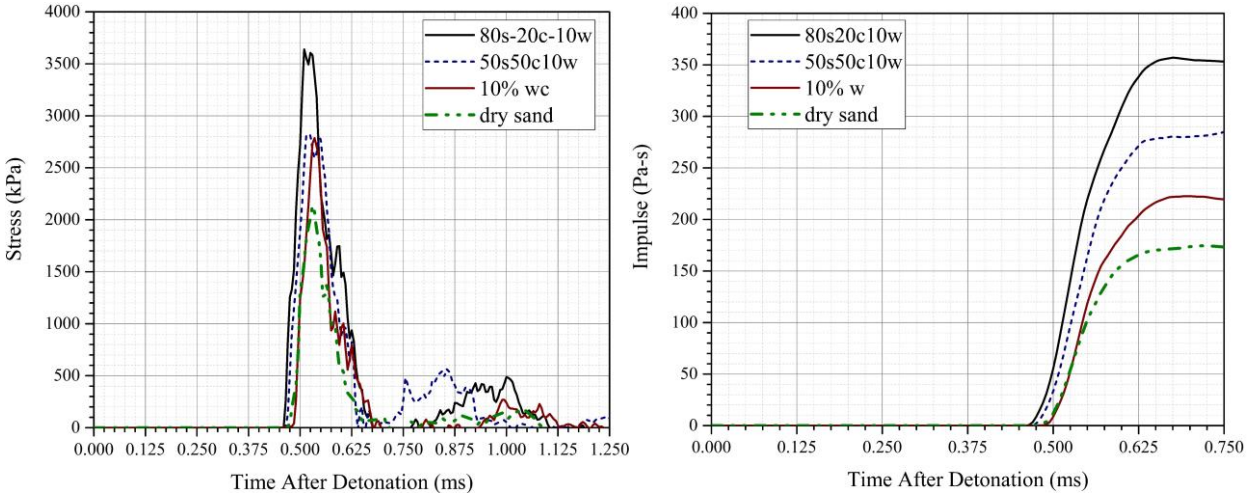

Figure 6.72. Comparison of the stress (*left*) and impulse (*right*) time-histories for a 1.0 gram C4 charge buried 0.8 cm varying degrees of sand-clay and detonated at 13 g. Dry and 10% saturated sand results included. Target positioned 5.1 cm aboveground.

The high-rate shock wave and the 80s20c10w soil blast loads impact the target sooner at 0.46 ms, yielding an incident wave speed of 128.3 ms^{-1}. This arrival of both mechanisms precedes 50s50c10w, dry sand, and 10% saturated sand impacts by 10 µs, 15 µs, and 17 µs, respectively. Immediately after *primary* shock impact, the highly-dense 80s20c10w soil blast load mechanisms induce a maximum peak stress of 3.64 MPa (Figure 6.72, *left*). Sequentially, 50s50c10w and 10% saturated soil blast load mechanisms yield 2.82 MPa and 2.73 MPa, respectively, corresponding to 22.3% and 25.0% reductions in peak value when compared to the 80s20c10w heave. As

anticipated, dry sand heaves induce the lowest peak stress, 2.08 MPa, a 55% difference compared to 80s20c10w ejecta loads (Figure 6.72, *left*).

Furthermore, the highest peak impulse, 356.8 Pa-s, coincides with blast momentum transfer consequent 80s20c10w soil ejecta impulsive loading (Figure 6.72, *right*). The energy imparted by 50% clay-sand blasts measures 284.0 Pa-s, 20% less than 80s20c10w. As the percent clay fines increase, the total blast impulse decreases. The homogenous soil heaves, without clay, transmit the lowest blast energy to the overlying target: the dry sand heave expectedly induces the lowest peak impulse, 174.1 Pa-s, and the partially-saturated sand blast yields an intermediate, 222.7 Pa-s, peak value. This indicates that peak impulse on the target subsequent 10% saturated and dry sand blasts measure 1.6 and 2.0 times less, respectively, relative to 80s20c10w, a notable difference.

In general, the results delineate the influence of the soil microstructure on the aboveground blast impact environment. In addition, the comparative analyses demonstrate that the soil medium's compaction density, permeability, and shear strength collectively affect the mechanistic, buried explosive-induced phenomenon. As the in-soil clay content, or plasticity index, increases, impact energy dissipation increases. Specifically, soil blast stresses and impulses significantly attenuate.

A noteworthy observation, the microstructural differences between the two heterogenous soil models display the similar identified behavior during testbed preparation. The 80s20c10w testbed exhibited noticeably more cohesive properties and resistance to impressible deformation. In contrast, the 50% clay-soil mixture was considerably drier and brittle upon compaction, and its semi-solid response suggests a relatively higher shear strength and diffuse ejecta flow. The results

quantify this reduced soil heave packing density effect upon target impact, with consequent decreased blast energy transfer to the BIRG.

6.17 Analysis of Blast Impulse Scaling Relationships

Past centrifuge soil blast studies primarily documented cratering morphology and the in-situ ground shock response. A need exists to better understand the aboveground blast environment, and specifically, the extrapolation of subscale blast energy to prototype condition. A comprehensive dimensional analysis examines the suitability of conventional centrifuge scaling relationships to predict full-scale buried blast induced loads on an overlying target. The two empirical approaches include 'modeling of models' and a comparison of this study's soil blast peak impulse data, using centrifuge scaling relationships, to past field test impulse results.

6.17.1 Aboveground Blast Impact Modeling of Models

A critical subscale modeling technique, termed modeling of models, compares multiple models of varying physical scale dimensioned via functional centrifuge scaling relationships (Table 2.1) as previously demonstrated in Crater Morphology (Section 4.4). Dynamic similarity requires that gravity-scaled measurements from each centrifuge model experiment simulate the same prototype condition over the examined domain. This evaluates the predictive performance of centrifuge modeling technique to simulate prototype conditions in the absence of larger scale field data.

To enable additional parametric evaluation of this modeling technique, the two test series vary the in-situ soil conditions: dry Mason sand and 80s20c10w. The 1/30, 1/25, and 1/20-scale model results quantify peak blast impulse on a flat target positioned approximately 1 mm aboveground. This HOT precludes target interference with the soil surface and allows minimal soil

disaggregation. Assuming dynamic similitude and equivalent soil conditions, the subscale experiments of distinctly different and arbitrarily chosen target dimensions (Section 2.11.3), explosive masses, burial depths, and g-levels simulate in prototype scale explosive loads induced by: a 13.5 kg charge, buried 1.03 m, with flat target dimensions 3.04 m diameter and 0.04 m thick. Table 6.25 summarizes the experimental constants and values for the three subscale models.

Table 6.25. Summary of the test parameters for 'modeling of models' experiments.

	Model 1	Model 2	Model 3	*scale by*	Prototype
Charge size (gm)	0.50	0.86	1.70	N^3	13.5 kg
Burial Depth (cm)	3.4	4.1	5.1	N	1.03 m
Plate dim. (cm) (*Dia. x thickness*)	10.16 x 1.24	12.19 x 1.49	15.24 x 1.91	N	3.04 m x 0.04 m
G-level N	30	25	20		

Model peak impulses are shown in Figure 6.73 as a function of centrifuge-induced gravity. A comparison of the two test series substantiates the previously discussed soil-dependent trend: clay-sand ejecta impacts yield higher impulse values when compared to dry sand blasts. Furthermore, in both test series, the parallel, best-fit regression curves demonstrate that peak impulse values decrease with elevated gravity, independent of in-situ soil conditions throughout the tested g-level range (Figure 6.73).

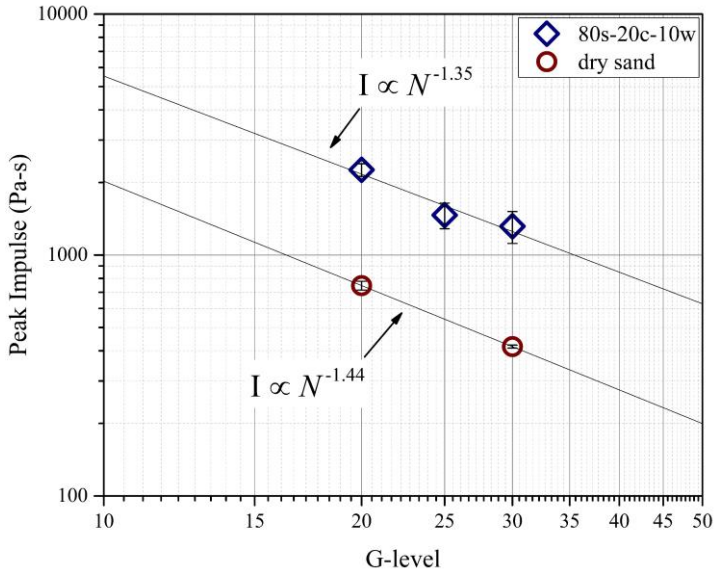

Figure 6.73. Model peak impulse as a function of gravity in *log-log* scale. Prototype condition: 1.36 kg (N^3) charge buried 1.02 m (N) in dry Mason sand and 80s20c10w impacting a 3.04 m diameter (N), 0.04 m thick (N) target positioned 0.1 cm aboveground. Data points represent the average of two individual tests with included error bars. Power law regression curves included (*solid-lines*).

A synthesis of the model peak impulse data for the two test series adheres best to a power-law regression curve in dimensional log-log scale (Figure 6.73). The empirical relationships between model (m) peak impulse $\mathcal{I}_m$ and g-level N for both dry Mason sand and 80s20c10w are respectively:

$$\mathcal{I}_m \propto N^{-1.35} \qquad (80s20c10w) \tag{6.17}$$

$$\mathcal{I}_m \propto N^{-1.44} \qquad (dry\ sand) \tag{6.18}$$

These equations quantify the observed trend: peak impulses display a nonlinear reduction subsequent higher gravity-induced stresses. The power law exponents differ by a nominal 4.6%. This study's empirically-derived relationship between peak impulse and gravity forcing can be approximated as:

$$\mathcal{I}_m \propto N^{-1.4} \tag{6.19}$$

The following formulation derives the centrifuge scaling term, *impulse*. Model (*m*) force F_m multiplied by time t_m and normalized by surface area A_m, defines the total impulse transmitted to the aboveground target, represented as:

$$\mathcal{I}_m = \frac{\mathrm{F}_m \mathrm{t}_m}{A_m} \tag{6.20}$$

Assuming material properties remain constant in model (*m*) and prototype (*p*), F_m, t_m, and A_m, conventionally scale with gravity *N* by:

$$\mathcal{I}_m = \frac{\mathrm{F}_p}{N^2} \tag{6.21}$$

$$\mathrm{t}_m = \frac{\mathrm{t}_p}{N} \tag{6.22}$$

$$\mathrm{A}_m = \frac{\mathrm{A}_p}{N^2} \tag{6.23}$$

Therefore, substituting Equations 6.21-6.23 into Equation 6.20 establishes the centrifuge modeling scale factor for impulse, expressed as:

$$\mathcal{I}_m = \frac{\mathrm{F}_p}{N^2} \frac{\mathrm{t}_p}{N} \frac{N^2}{A_p} = \frac{\mathcal{I}_p}{N} \tag{6.24}$$

A comparison of this study's experimentally-derived $N^{1.4}$ (Equation 6.19) and the centrifuge scale term *N* (for strict adherence to dynamic similitude, Equation 6.24) shows agreeable correspondence within an acceptable variance. Figure 6.74 illustrates the dynamic similitude between the two individual test series in prototype, $N^{1.4}$ scale.

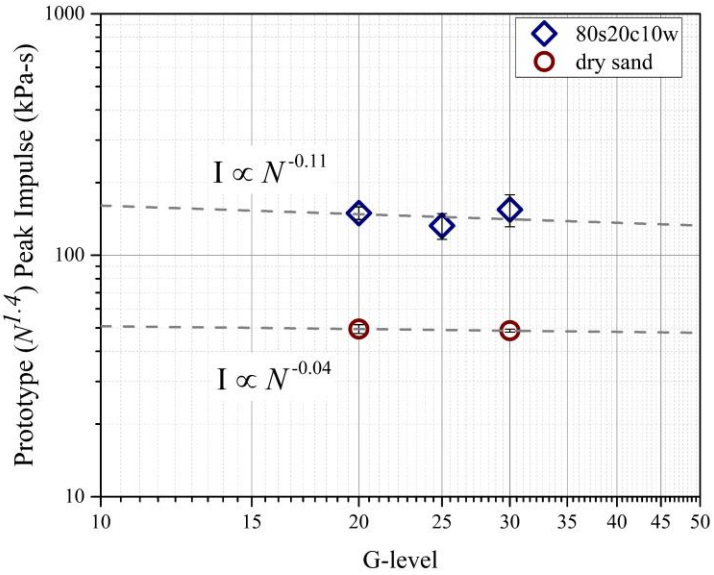

Figure 6.74. Prototype peak impulse ($N^{1.4}$) as a function of gravity in *log-log* scale. Prototype condition: 1.36 kg (N^3) charge buried 1.02 m (N) in dry Mason sand and 80s20c10w impacting a 3.04 m diameter (N), 0.04 m thick (N) target positioned 0.1 cm aboveground. Data points represent the average of two individual tests with included error bars. Power law regression curves included (*dashed-lines*).

Prototype peak impulses, induced by 80s20c10w and dry soil blasts, demonstrate nominal deviation from the sample mean, specifically 6.7% and 1.8%, respectively, and substantiate this study's empirically-derived $N^{1.4}$ to scale the near-field blast impulse (Figure 6.74). The results comply to the 'modeling of models' dynamic similitude requirement and clearly establish that physical models of arbitrarily chosen test parameters can effectively simulate the predicted aboveground full-scale explosive event using geotechnical centrifuge scaling relationships, with the refined $N^{1.4}$ gravity-scale term.

6.17.2 Comparison of Gravity-Scaled Impulse to Field Studies

To further assess the empirically-derived $N^{1.4}$ gravity-scale term and simulate aboveground impulse, the following dimensional analysis compares this study's results to full-scale field test data. The data compilation of 129 model-scale experiments include parametric variations of explosive mass (0.3 gram to 1.7 gram), soil conditions (cohesionless and cohesive), soil

overburdens (surface-tangent to 6.3 cm), target heights (0.1 cm to 8.9 cm), and g-levels (10 g to 30 g).

To address the predictive performance of centrifuge scaling relationships to simulate larger-scale soil blast impulsive loads imparted to an aboveground target, the field tests by Ehrgott [8], Snyman [71], and Gruijicic [72] were selected as suitable datasets because of their comparable experimental configurations. The centrifuge peak impulse results, scaled to prototype condition by $N^{1.4}$, as a function of scaled explosive mass TNT equivalent, show reasonable adherence to the derived power law regression curve and demonstrate this study's self-consistent data throughout three orders of prototype explosive mass magnitude observed in Figure 6.75.

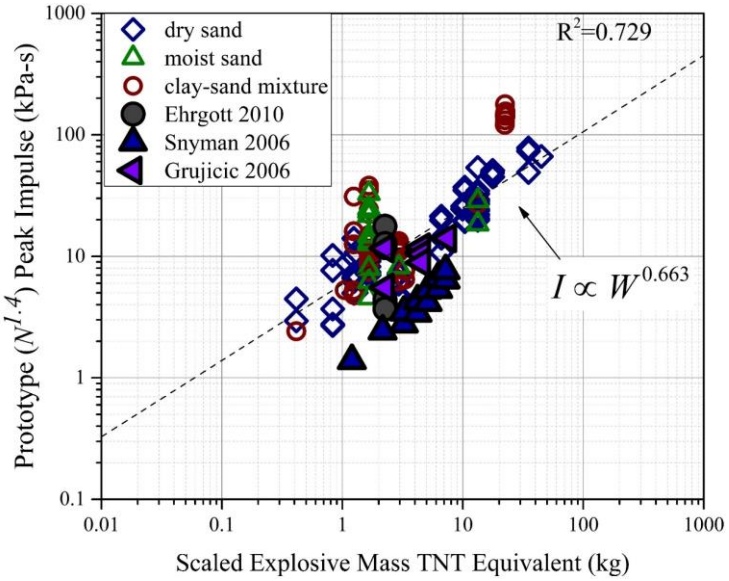

Figure 6.75. Comparison of prototype centrifuge peak impulse ($N^{1.4}$) as a function of scaled mass TNT equivalent to field tests in *log-log* scale. Power law regression curve from this study's 129 data points shown as *dashed-line*. Coefficient of determination (R^2) measured 0.729.

Furthermore, this study's empirically determined, power-dependent relationship between prototype (p) peak impulse $\mathcal{I}_p$ (kPa-s) and charge weight W (kg), represented as:

$$\mathcal{I}_p = \mathrm{W}^{0.663} \tag{6.25}$$

compares favorably to the field results and depicts the expected monotonic behavior: blast peak impulse increases as a function of explosive mass. A closer examination reveals that the data reported by Erghott [15] and Gruijcic [72] correlate well to this work's mid-range data cluster. Specifically, Erghott used a single, 2.27 kg C4 charge size, and varied testbed conditions (dry sand to partially-saturated clay-sand) and burial depth (surface-tangent and 10.16 cm DOB), similar to this study's parametric evaluation. Gruijcic [72] also measured peak impulse subsequent multiple charge size detonations (2.3 kg to 7.5 kg) under different partially-saturated soil overburdens (0.1 m to 0.81 m). Their subsurface data coincides to this study's regression curve. In general, the Snyman [71] data approximates this study's trend line reasonably well. However, their peak impulses remain consistently lower than both the centrifuge and field test results. This under-prediction of the aboveground impulse can attribute to their exclusive surface-tangent detonations which omit lithostatic pressure effects on impulse.

In this dimensional analysis, a new dimensionless constituent term, η, incorporates soil overburden (*DOB*) and target height (*HOT*) effects, defined as:

$$\eta = \left(\frac{HOT}{DOB}\right)^{1/4} \tag{6.26}$$

and further refines the impulse scaling relationships. This constituent term, η, allows enhanced characterization of impulsive soil blast loads on the aboveground targets specific to subsurface detonations. For increasingly shallower burial depths, η approaches infinity and thus, eliminates near-surface and surface-tangent blast measurements. A synthesis of the data compilation (Figure 6.75), and the prototype peak impulse results scaled by the new dimensionless term, η, are shown in Figure 6.76.

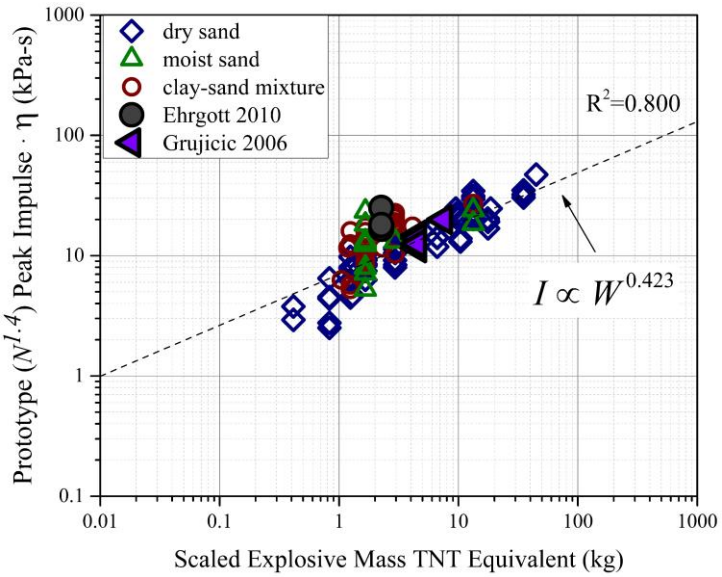

Figure 6.76. Comparison of modified ($N^{1.5}$) prototype scale peak impulse multiplied by dimensionless η as a function of scaled mass TNT equivalent to past larger scale soil blast works in *log-log* scale. Power law regression curve from this study's 121 data points shown as *dashed-line*. Coefficient of determination (R^2) measured 0.800.

Clearly evident, the inclusion of η effectively condenses this study's data, quantified by the increased coefficient of determination (R^2) from 0.729 (Figure 6.75) to 0.800 (Figure 6.76). Furthermore, the peak impulse comparison plot (Figure 6.76) illustrates improved correspondence between centrifuge and field test results. In spite of different test configurations, in-situ soil conditions, and measurement techniques, the subsurface blast impulse data, reported by Ehrgott [8] and Grujicic [72], remains coincident to this study's regression curve and strongly suggests the absence of adverse gravity-related scale effects throughout the range of scaled explosive mass, spanning three orders of magnitude (Figure 6.76).

To expect exact agreement between centrifuge gravity-scaled peak impulse and field experiments remains impractical. However, their close correspondence within an order of peak impulse magnitude indicates similar soil blast impact mechanics in both model and prototype scale (Figure 6.76). Significantly, this empirical analysis substantiates that model-scale soil blast

impacts on aboveground targets at elevated gravity, can simulate full-scale impulsive loads at normal gravity. This confirms the suitability and efficiency of the centrifuge modeling technique to simulate the full-scale, buried blast impact phenomenon using this study's refined scaling relationship.

Chapter 7 Conclusions and Contributions

This dissertation advanced the understanding of the mechanistic phenomenon of buried, explosive-induced dynamic soil responses, with parametric variations of charge size, burial depth, and g-level using geotechnical centrifuge modeling. The innovative experimental regime developed new measurement methodologies that integrated state-of-the art technologies to accurately quantify soil ejecta kinematics and crater morphology. A high-speed imaging system, positioned in close-proximity to the blast, enabled a rigorous in-flight characterization of the transient multiphasic soil blast mechanics including initial soil surface deformation, early soil disaggregation, gas-soil ejecta interactions, and soil dome evolution. These highly-resolved images simulate the same phenomenon apparent in full-scale explosive events and therefore provide a sound physical basis for parametric calibration and validation of iterative computational simulations of soil blast mechanics. The high-speed images in conjunction with particle tracking methods quantified soil ejecta kinematics under accelerated gravity. The empirical derived relationships demonstrated a gravity-dependent reduction in the temporal and spatial evolution of soil ejecta flow.

This research also fully characterized crater morphology. A laser profilometer and monorail encoder system improved conventional measurement techniques and effectively extracted highly-resolved, three-dimensional crater profiles. The results indicated that blast-excavated craters in dry sand remain consistently stable, conical in shape, and adhere to a non-linear reduction subsequent higher gravity-induced stresses. In addition, the data demonstrated an ‘optimal’ burial-depth dependence for maximum final crater dimensions. An in-depth analysis compared this study’s empirical scaling relationships, in both dimensional and dimensionless forms to a compilation of past field and centrifuge results and showed their favorable correlation to full-scale

events and confirmed the centrifuge technique suitability to predict full-scale explosive yields over a wide range of material types and test configurations.

To simultaneously measure buried, explosive-induced ground shock acceleration and stress wave attenuation, this research embedded piezoelectric sensors into testbeds with different clay mass fractions and moisture content. Peak acceleration and stress magnitudes evidenced a power-law reduction with distanced from the buried charge, independent of soil conditions. However, the results showed that incremental additions of the clay and water constituents in the soil matrix significantly increased shock wave transmissivity.

An investigation into the near-field aboveground blast environment led to the design and fabrication of a versatile measurement device, specifically the Blast Impact Response Gage, or BIRG, that directly measured the complex, non-uniform, temporal and spatial distribution of blast loading mechanisms with parametric variations of explosive mass, burial depth, target height, gravity level, target size and geometries, and in-situ soil conditions. The novel, tri-symmetric configuration of shock accelerometers and load cells documented resultant force impacts and rigid-body dynamics, under explosive loads, instead of the conventional, discrete point measurement methodologies. The upgraded, high-speed imaging system, included integration of a second camera that captured at 84,054 frames per second, the interfacial, multiphasic soil blast mechanics and subsequent momentum transfer to the target, apparent in full-scale field tests. The analytic synthesis of the BIRG data correlated to coincident high-speed video images resolved the arrival times and peak magnitudes of the *early* (shock wave) and *primary* (detonation gases-soil ejecta) shock impact phases and delineated the blast load constituents. The results confirmed that gas-soil ejecta impacts transmit most of the kinetic energy to the overlying target. Furthermore, the BIRG accurately determined the eccentricity of load distributions on the target surface. An analysis

of conventional centrifuge relationships demonstrated their suitability to upscale model blast peak impulse to full-scale peak impulse and derived a new dimensionless constitutive scaling term to include target height and burial depth dependence that allowed direct comparisons across studies of different material types and configurations. The highly-resolved and repeatable experimental data base established a benchmark for future parametric investigations and provided a sound physical basis for parametric calibration and stringent validation of advanced, iterative computational simulations of full-scale blast impacts on an overlying target, such as a military vehicle. Thus, this comprehensive experimental program contributes to the development of predictive and preventative technologies to counter the threats of IEDs and landmines.

This research advanced the *in-flight* subsurface and aboveground characterization of the buried blast phenomenon, including soil ejecta kinematics, crater morphology, and kinetic energy transfer to the overlying target, rendering it a truly adaptive technological, experimental platform. Importantly, the new measurement methodologies have potential applications to extended geomechanic fields, such as impact cratering, blast-induced liquefaction, retaining wall stability, surface erosion, and levee performance.

This thesis demonstrates significant research advancements and provides multiple opportunities for future investigations beyond the scope of this study. A shadowgraph visualization system, integrated into the experimental program, offers another method to examine the temporal and spatial resolution of shock wave propagation and the resultant dynamic response of the BIRG. This optical method, based on changes in the index of refraction with fluid density, would further advance the characterization of blast loading mechanisms in the *early* shock phase.

Furthermore, the testing of additional in-situ soil conditions, i.e. layered subgrades and an unbounded granular subbase, remains a worthwhile extension of this research. Testing in model-

scale configuration, feasible and repeatable in the centrifuge controlled laboratory environment, allows simulations of a wide range of natural field conditions, and enables tailoring and testing of models to combat theaters of interest. Extensive research opportunities exist in the mechanistic design optimization of underbody blast shock absorbing and energy attenuation technologies to reduce high-rate impulse target loads. These new technologies could include monolithic pyramid and hemispherical surface target designs, advancing the current limited target geometries, or composite structures, such as pyramid truss core sandwich panels. In addition to these protective mechanistic designs, a biological synthetic gelatin could replace the BIRG dihedral targets to simulate soft muscular tissue subjected to soil blast loading for design of personnel protective equipment.

Similarly, the BIRG design readily adapts to design modifications. An advantageous design of the BIRG would allow the target subassembly to translate vertically, with negligible resistance except for gravity and self-weight. This new mass-piston design configuration would model the free-flight of an aboveground structure or vehicle subjected to blast loading, in a controlled environment. The high-speed video images and motion analysis software quantify the vertical displacement of the known BIRG target mass with substantive correspondence to the accelerometer data. The target's mass and velocity resolves the initial global impulse during translation. The addition of a mechanical stop shaft establishes a fixed upper boundary condition. When the assembly reaches a prescribed peak height, the instrumented BIRG target characterizes the residual blast resultant loads and eccentricity.

Finally, the accurate modeling of the complex, multifaceted buried soil blast phenomenon with direct correspondence to this research's accurate and well-documented experimental data would

advance the development of armoring technologies and the forensic investigation of blast-excavated craters in combat zones or populated urban areas.

Chapter 8 Bibliography

[1] Litowitz JA. The Infernal Machine: The Use of Improvised Explosive Devices (IED) against US Forces. DTIC Document; 2011.

[2] Brown University. Watson Institute International & Public Affairs. Cost of War 2016. http://watson.brown.edu/costsofwar/ (accessed August 12, 2016).

[3] Bergeron D, Tremblay JE. Canadian research to characterize mine blast output. 16th International MABS Symposium, 2000.

[4] NATO. Test Methodologies for Personal Protective Equipment Against Anti-Personnel Mine Blast. France: 2004.

[5] Kutter BL, O'Leary LM, Thompson PY, Lather R. Gravity-scaled tests on blast-induced soil-structure interaction. Journal of Geotechnical Engineering 1988;114:431–47.

[6] Vortman IJ. Cratering experiments with large high-explosive charges. Geophysics 1963;28:351–68.

[7] Genson K. Vehicle shaping for mine blast damage reduction. MS Thesis. Maryland, 2006.

[8] Ehrgott JQ Jr. Influence of soil properties on the aboveground blast environment from a near-surface detonation. Ph.D. Mississippi State University, 2010.

[9] U.S. Marine Corp. MRAP 2016. http://www.marines.com/operating-forces/equipment/vehicles/mrap.

[10] Runciman N, Vagenas N. Evaluation of underground drill and blast mining systems using discrete-event simulation. Mineral Resources Engineering 1998;7:211–20.

[11] Ashford SA, Rollins KM, Lane JD. Blast-induced liquefaction for full-scale foundation testing. Journal of Geotechnical and Geoenvironmental Engineering 2004;130:798–806.

[12] Housen KR, Holsapple KA. Ejecta from impact craters. Icarus 2011;211:856–75.

[13] Goodings DJ, Lin C-P, Dick RD, Fourney WL, Bernold LE. Modeling effects of chemical explosives for excavation on moon. Journal of Aerospace Engineering 1992;5:44–58.

[14] Gault DE, Wedekind JA. Experimental studies of oblique impact. Lunar and Planetary Science Conference Proceedings, vol. 9, 1978, p. 3843–75.

[15] Wünnemann K, Nowka D, Collins GS, Elbeshausen D, Bierhaus M. Scaling of impact crater formation on planetary surfaces: Insights from numerical modeling. Proceedings of the 11th Hypervelocity Impact Symposium, 2011, p. 1–16.

[16] Bull JW, Woodford CH. Camouflets and their effect on runway support. Computers & Structures 1998;69:695–706.

[17] Anirban D, Thomas FZ. Centrifuge modeling of surface blast effects on underground structures. Geotechnical Testing Journal 2007;30:1–5.

[18] Tabatabai H, Bloomquist D, McVay MC, Gill JJ, Townsend FC. Centrifugal Modeling of Underground Structures Subjected to Blast Loading. DTIC Document; 1988.

[19] Parkes J, Kelly H, Munfakh G, Choi S. Analyzing the impacts of explosions on dams and levees. Safety and Security Engineering V 2013;134:307.

[20] Sharp MK, Matheu E, Seda-Sanabria Y. Blast damage assessment and mitigation for dams and navigation locks. Risk Analysis, Dam Safety, Dam Security and Critical Infrastructure Management 2011:381.

[21] Wu C, Hao H, Lu Y, Sun S. Numerical simulation of structural responses on a sand layer to blast induced ground excitations. Computers & Structures 2004;82:799–814.

[22] Roy PP. Technical Note Characteristics of ground vibrations and structural response to surface and underground blasting. Geotechnical & Geological Engineering 1998;16:151–66.

[23] Bleiweis PB, Hart GC, Smith CB, Matthiesen RB. Simulation of strong motion earthquake effects on structures using explosive blasts. Nuclear Engineering and Design 1973;25:126–49.
[24] Rigby SE, Tyas A, Clarke SD, Fay SD, Warren JA, Elgy I, et al. Testing apparatus for the spatial and temporal pressure measurements from near-field free air explosions. Proceedings of the 6th International Conference on Protection of Structures against Hazards, Sheffield; 2014.
[25] Fay SD, Rigby SE, Tyas A, Clarke SD, Reay JJ, Warren JA, et al. Displacement timer pins: An experimental method for measuring the dynamic deformation of explosively loaded plates. International Journal of Impact Engineering 2015;86:124–30.
[26] Pickering EG, Yuen SCK, Nurick GN, Haw P. The response of quadrangular plates to buried charges. International Journal of Impact Engineering 2012;49:103–14.
[27] Defence Research Establishment Suffield., Coffey C, Walker R, Bergeron D. Detonation of 100-gram anti-personnel mine surrogate charges in sand a test case for computer code validation. [Medicine Hat, AB]: Defence Research Establishment Suffield; 1998.
[28] Rooke AD, Carnes BL, Davis LK. Cratering by Explosions: A Compendium and an Analysis. Waterways Experiment Station; 1974.
[29] Drake JL, Little CD, MS AEWESV. Ground Shock from Penetrating Conventional Weapons. Defense Technical Information Center; 1983.
[30] Fox DM, Huang X, Jung D, Fourney WL, Leiste U, Lee JS. The response of small scale rigid targets to shallow buried explosive detonations. International Journal of Impact Engineering 2011;38:882–91. doi:10.1016/j.ijimpeng.2011.05.009.
[31] Taylor LC, Fourney WL, Leiste U, Cheeseman BA. Loading Mechanisms on a Target From Detonation of a Buried Charge. 24th International Symposium on Ballistics, vol. 1, 2008.
[32] Fourney WL, Leiste U, Bonenberger R, Goodings DJ. Mechanism of loading on plates due to explosive detonation. Fragblast 2005;9:205–17. doi:10.1080/13855140500431989.
[33] Johnson SW, Smith JA, Franklin EG, Moraski LK, Teal DJ. Gravity and atmospheric pressure effects on crater formation in sand. Journal of Geophysical Research 1969;74:4838–50. doi:10.1029/JB074i020p04838.
[34] Chabai AJ. On scaling dimensions of craters produced by buried explosives. Journal of Geophysical Research 1965;70:5075–98. doi:10.1029/JZ070i020p05075.
[35] Schmidt R, Holsapple K. Centrifuge cratering scaling experiment I: dry granular soils. Boeing Aerospace Co 1978.
[36] Schmidt RM, Holsapple KA. Theory and experiments on centrifuge cratering. Journal of Geophysical Research: Solid Earth 1980;85:235–52. doi:10.1029/JB085iB01p00235.
[37] Goodings DJ, Fourney WL, Dick RD. Geotechnical Centrifuge Modeling of Explosion Induced Craters-A Check for Scaling Effects. DTIC Document; 1988.
[38] Brownell KC, Charlie WA. Centrifuge modeling of explosion-induced craters in unsaturated sand. DTIC Document; 1992.
[39] Gill JJ, Kuennen ST. Half-space modeling of explosively-formed craters. Proceedings of the International Conference on Centrifuge, 1991, p. 465–72.
[40] Shim H. Response of piles in saturated soil under blast loading. Ph.D Thesis. Colorado, 1995.
[41] Walsh AJ, Charlie WA. Stress Wave Propagation in Unsaturated Sands. Volume 1. Centrifuge Modeling. DTIC Document; 1993.

[42] Ko HY. Summary of the state-of-the-art in centrifuge model testing. Centrifuges in Soil Mechanics 1988:11–8.
[43] Davies MCR. Dynamic soil structure interaction resulting from blast loading. Leung, Lee and Tan (Eds), Centrifuge 1994;94:319–24.
[44] Lenke LR, Pak RY, Ko H-Y. Boundary effects in modeling of foundations subjected to vertical excitation. Centrifuge, vol. 91, 1991, p. 473–80.
[45] Pak RY, Guzina BB. Dynamic characterization of vertically loaded foundations on granular soils. Journal of Geotechnical Engineering 1995;121:274–86.
[46] Svoboda J. Impact of strain rate on the shear strength and pore water pressure generation of clays and sands. UNIVERSITY OF COLORADO AT BOULDER, 2013.
[47] Mun W. Compression Mechanisms of Soils under High Stresses. UNIVERSITY OF COLORADO AT BOULDER, 2016.
[48] Selecting the Right EBW Detonator n.d. http://www.teledynerisi.com/products-services/ebw-detonators/selecting-the-right-ebw-detonator (accessed October 2, 2016).
[49] An J, Tuan CY, Cheeseman BA, Gazonas GA. Simulation of soil behavior under blast loading. International Journal of Geomechanics 2011;11:323–34.
[50] Vision Research Digital High-Speed Cameras Measuring Motion with Imaging Software n.d. https://www.highspeedcameras.com/Solutions/Common-Applications/Motion-Analysis (accessed March 19, 2016).
[51] Cooper P. Explosives Engineering. 1st ed. New York: Wiley-VCH; 1996.
[52] LS-DYNA I. LS-DYNA user's manual. LS-DYNA, Livermore Software Technology Corporation, Livermore, CA, USA 2013;4.
[53] Zukas JA, Walters W, Walters WP. Explosive effects and applications. Springer Science & Business Media; 2002.
[54] Simo JC, Ju J-W, Pister KS, Taylor RL. Assessment of cap model: consistent return algorithms and rate-dependent extension. Journal of Engineering Mechanics 1988;114:191–218.
[55] Chen W-F, Baladi GY. Soil plasticity: theory and implementation. vol. 38. Elsevier; 1985.
[56] Deshpande VS, McMeeking RM, Wadley HNG, Evans AG. Constitutive model for predicting dynamic interactions between soil ejecta and structural panels. Journal of the Mechanics and Physics of Solids 2009;57:1139–64.
[57] Børvik T, Olovsson L, Hanssen AG, Dharmasena KP, Hansson H, Wadley HNG. A discrete particle approach to simulate the combined effect of blast and sand impact loading of steel plates. Journal of the Mechanics and Physics of Solids 2011;59:940–58.
[58] Ehrgott Jr JQ, Akers SA, Windham JE, Rickman DD, Danielson KT. The influence of soil parameters on the impulse and airblast overpressure loading above surface-laid and shallow-buried explosives. Shock and Vibration 2011;18:857–74.
[59] Ehrgott Q. Influence of soil properties on the aboveground blast environment from a near-surface detonation n.d.
[60] Benedetti R. Mitigation of explosive blast effects on vehicle floorboard. ProQuest; 2008.
[61] Clarke SD, Fay SD, Warren JA, Tyas A, Rigby SE, Elgy I. A large scale experimental approach to the measurement of spatially and temporally localised loading from the detonation of shallow-buried explosives. Measurement Science and Technology 2014;26:15001.

[62] Clarke SD, Fay SD, Tyas A, Warren J, Rigby SE, Elgy I, et al. Repeatability of buried charge testing. Proceedings of the 23rd International Symposium on Military Aspects of Blast and Shock, Sheffield; 2014.
[63] Hansen C, Pak RY. Centrifuge Characterization of Buried, Explosive-Induced Soil Ejecta Kinematics and Crater Morphology. Journal of Dynamic Behavior of Materials n.d.:1–20.
[64] Shelton TW, Ehrgott JQ, Moral RJ, Barbato M. Experimental and numerical investigation of the ground shock coupling factor for near-surface detonations. Shock and Vibration 2014;2014.
[65] Snyman IM, Reinecke JD. Measuring the impulse from an explosive charge. Proceedings, 5th South African Ballistics Symposium, OTB, Western Cape, South Africa, vol. 7, 2006.
[66] Yuen SCK, Langdon GS, Nurick GN, Pickering EG, Balden VH. Response of V-shape plates to localised blast load: Experiments and numerical simulation. International Journal of Impact Engineering 2012;46:97–109.
[67] Heider N, Denefeld V, Steinbrenner A, Holzwarth A. Engineering tool for the evaluation of global IED effects. Defence Technology 2016;12:215–23.
[68] Denefeld V, Heider N, Holzwarth A, Sättler A, Salk M. Reduction of global effects on vehicles after IED detonations. Defence Technology 2014;10:219–25.
[69] Westine PS, Morris BL, Cox PA, Polch EZ. Development of computer program for floor plate response from land mine explosions. Contract Report 1985.
[70] Tremblay JE. Impulse on blast deflectors from a landmine explosion. DTIC Document; 1998.
[71] Snyman IM, Reinecke JD. Measuring the impulse from an explosive charge. Proceedings, 5th South African Ballistics Symposium, OTB, Western Cape, South Africa, vol. 7, 2006.
[72] Grujicic M, Pandurangan B, Huang Y, Cheeseman BA, Roy WN, Skaggs RR. Impulse loading resulting from shallow buried explosives in water-saturated sand. Proceedings of the Institution of Mechanical Engineers, Part L: Journal of Materials Design and Applications 2007;221:21–35.
[73] Ehrgott Jr JQ. Tactical Wheeled Vehicle Survivability: Results of Experiments to Quantify Aboveground Impulse. DTIC Document; 2010.

APPENDIX A

Table A.1. Test matrix for free-field soil blast experiments (i.e. no aboveground BIRG target).

Test #	Charge size (gm)	G-level	Burial Depth (cm)	Soil Condition
2013042501	0.069	1	2.5	dry
2013050101	0.069	1	2.5	dry
2013050102	0.069	1	5.1	dry
2013051101	0.069	1	2.5	dry
2013051104	0.069	20	2.5	dry
2013061301	0.069	5	2.5	dry
2013061302	0.069	10	2.5	dry
2013061303	0.069	20	2.5	dry
2013061304	0.069	30	2.5	dry
2013070409	0.069	1	2.5	dry
2014071101	0.069	40	0.2	dry
2014071401	0.069	32	0.2	dry
2013042502	0.203	1	2.5	dry
2013050201	0.203	1	2.5	dry
2013050202	0.203	1	5.1	dry
2013050203	0.203	1	2.5	dry
2013051302	0.203	20	5.1	dry
2013051303	0.203	20	2.5	dry
2013051304	0.203	20	2.5	dry
2014070202	0.203	34	1.5	dry
2014070203	0.203	34	1.5	dry
2014071102	0.203	28	0.4	dry
2014071103	0.203	23	0.4	dry
2013072303	1.0 gram C4	1	5.1	dry
2013072307	1.0 gram C4	20	5.1	dry
2013072308	1.0 gram C4	10	5.1	dry
2013072310	1.0 gram C4	10	5.1	dry
2013090901	1.0 gram C4	30	7.6	dry
2013090902	1.0 gram C4	20	7.6	dry
2013082803	1.0 gram C4	30	5.1	dry
2013082901	1.0 gram C4	30	5.1	dry
2013082902	1.0 gram C4	20	5.1	dry
2013090901	1.0 gram C4	30	7.6	dry
2013090902	1.0 gram C4	20	7.6	dry
2014061701	1.0 gram C4	1	5.1	dry
2014061801	1.0 gram C4	10	5.1	dry
2014061802	1.0 gram C4	20	5.1	dry
2014061803	1.0 gram C4	30	5.1	dry
2014061901	1.0 gram C4	30	5.1	dry

2014062002	1.0 gram C4	30	5.1	dry
2014062003	1.0 gram C4	20	5.1	dry
2014062302	1.0 gram C4	30	1.3	dry
2014062701	1.0 gram C4	20	2.5	dry
2014062703	1.0 gram C4	30	5.1	dry
2014063001	1.0 gram C4	20	5.1	dry
2014063002	1.0 gram C4	10	5.1	dry
2014070101	1.0 gram C4	20	5.1	dry
2014070102	1.0 gram C4	10	5.1	dry
2014071001	1.0 gram C4	20	2.5	dry
2014072201	1.0 gram C4	30	2.5	dry
2014072202	1.0 gram C4	30	2.5	dry
2014072203	1.0 gram C4	30	7.6	dry
2014072301	1.0 gram C4	30	7.6	dry
2014072302	1.0 gram C4	30	10.2	dry
2014072303	1.0 gram C4	30	10.2	dry
2014073001	1.0 gram C4	40	2.0	dry
2014073101	1.0 gram C4	20	1.3	dry
2014073102	1.0 gram C4	1	1.3	dry
2014080401	1.0 gram C4	5	2.0	dry
2015032001	1.0 gram C4	50	5.1	dry
2013082901	1.0 gram Detasheet	30	5.1	dry
2013082902	1.0 gram Detasheet	20	5.1	dry
2014061001	1.0 gram Detasheet	1	5.1	dry
2014061003	1.0 gram Detasheet	1	5.1	dry
2013072004	0.53	10	5.1	dry
2014062601	0.53	30	5.1	dry
2014062602	0.53	20	5.1	dry
2014062603	0.53	10	5.1	dry
2014062702	0.53	25	2.0	dry
2014070201	0.53	25	2.1	dry
2014070301	0.53	34	5.1	dry
2014070701	0.53	20	5.1	dry
2014070702	0.53	10	5.1	dry
2014070703	0.53	1	5.1	dry
2014071103	0.53	20	0.4	dry
2014071403	0.53	17	0.4	dry
2014080501	0.53	35	2.5	dry
2014080502	0.53	35	1.3	dry
2014080503	0.53	35	3.8	dry
2013091001	1.1	30	7.6	dry
2013091002	1.1	20	7.6	dry

2014071801	1.0 gram C4	10	5.1	80s20c10w
2014071802	1.0 gram C4	20	5.1	80s20c10w
2014072501	1.0 gram C4	1	5.1	80s20c10w
2014072502	1.0 gram C4	20	5.1	80s20c10w

Table A.2. Test matrix for soil blast experiments including Blast Impact Response Gage (BIRG).

Test #	Burial Depth (cm)	Target Height (cm)	G-level	Charge Size (gm)	Charge Comp	Soil Condition	Charge Placement	Washer Type	Cameras
2015010401	5.1	5.1	10	1.0	Detasheet	dry sand	centric	rubber	2
2015010501	5.1	5.1	10	0.5	Det. Only	dry sand	centric	rubber	2
2015010601	5.1	5.1	10	0.5	Det. Only	dry sand	1-2 eccentric	rubber	2
2015010602	5.1	5.1	1	0.5	Det. Only	dry sand	1-3 eccentric	rubber	2
2015010701	5.1	5.1	20	1.0	Detasheet	dry sand	centric	metal	2
2015010702	5.1	5.1	1	1.0	Detasheet	dry sand	centric	metal	2
2015010801	2.5	5.1	20	1.0	Detasheet	dry sand	centric	metal	2
2015010901	5.1	5.1	10	1.0	Detasheet	dry sand	centric	metal	2
2015010902	7.6	5.1	10	1.0	Detasheet	dry sand	centric	metal	2
2015011001	5.1	3.8	20	1.0	Detasheet	dry sand	centric	metal	2
2015011002	5.1	2.5	20	1.0	Detasheet	dry sand	centric	metal	2
2015011201	5.1	2.5	20	1.0	Detasheet	dry sand	1-3 eccentric	metal	2
2015011301	5.1	2.5	10	1.0	Detasheet	dry sand	centric	metal	2
2015011302	5.1	1.3	20	0.5	Detasheet	dry sand	centric	metal	2
2015011401	1.3	5.1	20	1.0	Detasheet	dry sand	centric	metal	2
2015011402	1.3	5.1	20	1.0	Detasheet	dry sand	centric	metal	2
2015011501	5.1	5.1	20	1.0	Detasheet	10% wc	centric	metal	2
2015011502	5.1	2.5	20	1.0	Detasheet	10% wc	centric	metal	2
2015033001	5.1	5.1	10	1.0	Detasheet	dry sand	centrc	metal	1
2015033101	5.1	5.1	10	1.0	C4	dry sand	centric	metal	1
2015033102	5.1	5.1	10	0.5	Detasheet	dry sand	centric	metal	1
2015040101	5.1	5.1	10	1.0	Detasheet	dry sand	centric	metal	1
2015040102	5.1	5.1	20	1.0	Detasheet	dry sand	centric	metal	1
2015040201	5.1	2.5	10	1.0	Detasheet	dry sand	centric	metal	1
2015040202	5.1	2.5	10	0.5	Detasheet	dry sand	centric	metal	1
2015040301	5.1	2.5	10	1.0	Detasheet	dry sand	centric	metal	1
2015040302	5.1	3.8	10	1.0	Detasheet	dry sand	centric	metal	1
2015040401	2.5	5.1	10	0.5	Detasheet	dry sand	centric	metal	1
2015041901	5.1	5.1	10	1.0	Detasheet	dry sand	centric	metal	2
2015041902	2.5	5.1	10	1.0	Detasheet	dry sand	centric	metal	2

2015042001	2.5	5.1	10	1.0	C4	dry sand	centric	metal	2
2015042002	2.5	5.1	10	0.5	Detasheet	dry sand	"	"	"
2015042101	5.1	5.1	10	0.8	Detasheet	dry sand	"	"	"
2015042102	2.5	5.1	10	0.8	Detasheet	dry sand	"	"	"
2015042201	7.6	5.1	10	0.8	Detasheet	dry sand	"	"	"
2015042202	7.6	5.1	10	0.5	Detasheet	dry sand	"	"	"
2015042301	5.1	5.1	10	0.5	Detasheet	dry sand	"	"	"
2015042302	5.1	3.8	10	0.8	Detasheet	dry sand	"	"	"
2015042401	5.1	3.8	10	0.5	Detasheet	dry sand	"	"	"
2015042402	5.1	3.8	10	1.0	C4	dry sand	"	"	"
2015042501	2.5	3.8	10	0.8	Detasheet	dry sand	"	"	"
2015042502	2.5	3.8	10	1.0	Detasheet	dry sand	"	"	"
2015042601	5.1	3.8	20	1.0	Detasheet	dry sand	"	"	"
2015042602	2.5	3.8	20	1.0	Detasheet	dry sand	"	"	"
2015042701	5.1	3.8	10	1.0	Detasheet	dry sand	"	"	"
2015042702	2.5	3.8	20	0.5	Detasheet	dry sand	"	"	"
2015042801	2.5	3.8	20	1.0	C4	dry sand	"	"	"
2015042802	2.5	3.8	20	1.0	C4	dry sand	"	"	"
2015042901	3.8	2.5	20	1.0	Detasheet	dry sand	"	"	"
2015042902	2.5	2.5	10	0.8	Detasheet	dry sand	"	"	"
2015043001	2.5	2.5	20	0.5	Detasheet	dry sand	"	"	"
2015043002	3.8	2.5	20	0.8	Detasheet	dry sand	"	"	"
2015050101	2.5	2.5	10	0.3	Detasheet	dry sand	"	"	"
2015050102	5.1	2.5	20	0.8	Detasheet	dry sand	"	"	"
2015050201	2.5	1.3	20	0.5	Detasheet	dry sand	"	"	"
2015050202	5.1	1.3	20	1.0	C4	dry sand	"	"	"
2015050301	2.5	1.3	10	0.5	Detasheet	dry sand	"	"	"
2015050302	2.5	1.3	10	0.8	Detasheet	dry sand	"	"	"
2015050401	2.5	1.3	10	0.3	Detasheet	dry sand	"	"	"
2015050402	5.1	1.3	30	1.0	C4	dry sand	"	"	"
2015050501	5.1	1.3	10	1.0	C4	dry sand	"	"	"
2015050502	5.1	1.3	10	1.0	Detasheet	dry sand	"	"	"
2015050601	5.1	1.3	30	1.0	Detasheet	dry sand	"	"	"
2015050602	5.1	1.3	20	1.0	Detasheet	dry sand	"	"	"
2015050701	3.4	0.2	30	1.0	C4	dry sand	"	"	"
2015050702	3.4	0.1	30	1.0	C4	dry sand	"	"	"
2015050801	5.1	0.1	20	1.0	C4	dry sand	"	"	"
2015050802	5.1	0.2	20	1.0	Detasheet	dry sand	"	"	"
2015050803	2.5	0.1	10	0.5	Detasheet	dry sand	"	"	"
2015050901	3.4	0.1	30	0.5	C4	dry sand	"	"	"
2015050902	3.4	0.1	30	0.5	C4	dry sand	"	"	"
2015050903	5.1	0.1	20	1.0	C4	dry sand	"	"	"

2015051001	5.1	0.1	20	1.7	C4	dry sand	centric	metal	2
2015051002	5.1	0.1	20	1.7	C4	dry sand	"	"	"
2015051003	2.5	2.5	10	0.8	Detasheet	dry sand	"	"	"
2016010701	5.1	5.1	1	1.0	Detasheet	80s20c10w	"	"	"
2016010801	5.1	5.1	10	1.0	Detasheet	80s20c10w	"	"	"
2016011101	2.5	5.1	10	1.0	Detasheet	80s20c10w	"	"	"
2016011201	2.5	5.1	10	1.0	Detasheet	50s50c10w	"	"	"
2016011301	2.5	5.1	10	0.8	Detasheet	50s50c10w	"	"	"
2016011401	5.1	5.1	10	1.0	Detasheet	80s20c10w	"	"	"
2016011501	5.1	5.1	20	1.0	Detasheet	80s20c10w	"	"	"
2016011901	5.1	5.1	10	0.8	Detasheet	80s20c10w	"	"	"
2016012201	2.5	5.1	10	0.6	Detasheet	80s20c10w	"	"	"
2016012601	5.1	5.1	1	0.6	Detasheet	80s20c10w	"	"	"
2016012801	5.1	5.1	10	1.0	Detasheet	80s20c10w	"	"	"
2016020801	5.1	2.5	10	1.0	Detasheet	80s20c10w	"	"	"
2016021001	5.1	2.5	10	1.0	Detasheet	80s20c10w	"	"	"
2016021101	5.1	1.3	10	1.0	Detasheet	80s20c10w	"	"	"
2016021201	5.1	1.3	10	1.0	Detasheet	80s20c10w	"	"	"
2016021501	5.1	1.3	10	1.0	Detasheet	80s20c10w	"	"	"
2016021502	5.1	0	10	1.0	Detasheet	80s20c10w	"	"	"
2016021601	5.1	0	10	1.0	Detasheet	80s20c10w	"	"	"
2016022301	5.1	0	10	1.0	Detasheet	80s20c10w	"	"	"
2016022302	5.1	5.1	10	1.0	Detasheet	80s20c10w	"	"	"
2016022401	2.5	2.5	10	0.8	Detasheet	80s20c10w	"	"	"
2016022402	2.5	2.5	10	0.8	Detasheet	80s20c10w	"	"	"
2016022501	5.1	2.5	10	1.0	Detasheet	80s20c10w	"	"	"
2016022502	5.1	1.3	10	1.0	Detasheet	80s20c10w	"	"	"
2016022601	5.1	0	10	1.0	Detasheet	80s20c10w	"	"	"
2016022602	2.5	2.5	10	1.0	Detasheet	80s20c10w	"	"	"
2016022901	0.0	5.1	20	0.3	Detasheet	80s20c10w	"	"	"
2016030101	0.0	5.1	10	0.3	Detasheet	80s20c10w	"	"	"
2016030102	0.0	5.1	20	0.3	Detasheet	80s20c10w	"	"	"
2016030201	0.8	5.1	13.1	1.0	C4	80s20c10w	"	"	"
2016030202	0.8	5.1	13.1	1.0	C4	80s20c10w	"	"	"
2016030301	0.5	3.8	22.3	0.2	C4	80s20c10w	"	"	"
2016030701	0.5	3.8	22.3	0.2	C4	80s20c10w	"	"	"
2016030801	0.5	3.8	22.3	0.2	C4	80s20c10w	"	"	"
2016030802	0.8	5.1	13.1	1.0	C4	80s20c10w	"	"	"
2016030901	0.8	5.1	13.1	1.0	C4	50s50c10w	"	"	"
2016030902	0.8	5.1	13.1	1.0	C4	50s50c10w	"	"	"
2016031001	0.5	3.8	22.3	0.2	C4	50s50c10w	"	"	"
2016031101	0.5	3.8	22.3	0.2	C4	50s50c10w	"	"	"

2016031102	5.1	0	10	0.8	Detasheet	80s20c10w	centric	metal	2
2016031501	2.5	2.5	10	0.8	Detasheet	80s20c10w	"	"	"
2016031601	3.4	0	30	0.5	Detasheet	80s20c10w	"	"	"
2016031701	2.5	2.5	10	0.8	Detasheet	50s50c10w	"	"	"
2016032201	5.1	6.35	10	1.0	Detasheet	80s20c10w	"	"	"
2016032202	3.4	0	30	0.5	Detasheet	80s20c10w	"	"	"
2016032401	3.4	0	30	0.5	Detasheet	80s20c10w	"	"	"
2016032402	4.1	0	25	0.9	Detasheet	80s20c10w	"	"	"
2016032501	4.1	0	25	0.9	Detasheet	80s20c10w	"	"	"
2016032502	5.1	5.1	10	1.0	Detasheet	80s20c10w	"	"	"
2016032801	5.1	5.1	10	1.0	Detasheet	80s20c10w	"	"	"
2016032901	5.1	0	20	1.7	Detasheet	80s20c10w	"	"	"
2016033001	5.1	0	20	1.7	Detasheet	80s20c10w	"	"	"
2016033002	2.5	6.35	10	1.0	Detasheet	80s20c10w	"	"	"
2016033101	5.1	5.1	10	1.0	Detasheet	80s20c10w	"	"	"
2016040101	2.5	2.5	10	0.8	Detasheet	80s20c10w	"	"	"
2016040102	5.1	2.5	10	1.0	Detasheet	80s20c10w	"	"	"
2016040401	5.1	1.3	10	1.0	Detasheet	80s20c10w	"	"	"
2016040501	5.1	0	10	1.0	Detasheet	80s20c10w	"	"	"
2016040801	2.5	2.5	10	0.8	Detasheet	50s50c10w	"	"	"
2016041101	2.5	2.5	10	1.0	Detasheet	80s20c10w	"	"	"
2016041201	5.1	8.9	10	1.0	Detasheet	80s20c10w	"	"	"
2016041501	2.5	8.9	10	1.0	Detasheet	80s20c10w	"	"	"
2016041801	2.5	2.5	10	0.8	Detasheet	dry sand	"	"	"
2016041802	0.8	5.1	13.1	1.0	C4	dry sand	"	"	"
2016041901	0.8	5.1	13.1	1.0	C4	dry sand	"	"	"
2016041902	0.5	5.1	22.3	0.2	RP-80	dry sand	"	"	"
2016042001	0.5	3.8	22.3	0.2	RP-80	dry sand	"	"	"
2016042002	0.7	3.8	15	0.7	C4	dry sand	"	"	"
2016042101	0.7	5.1	15	0.7	C4	dry sand	"	"	"
2016042102	7.0	11.4	30	1.0	C4	dry sand	"	"	"
2016042201	7.0	12.7	30	0.7	C4	dry sand	"	"	"
2016042501	0.8	5.1	13.1	1.0	C4	10 % wc	"	"	"
2016042502	0.7	5.1	15	0.7	C4	50s50c10w	"	"	"
2016042601	5.1	5.1	10	1.0	Detasheet	10 % wc	"	"	"
2016042602	5.1	2.5	10	1.0	Detasheet	10 % wc	"	"	"
2016042701	2.5	2.5	10	1.0	Detasheet	10 % wc	"	"	"
2016042702	5.1	0.1	10	1.0	Detasheet	10 % wc	"	"	"
2016042801	5.1	0.1	10	1.0	Detasheet	22 % wc	"	"	"
2016042802	5.1	2.5	10	1.0	Detasheet	22 % wc	"	"	"
2016050201	2.5	2.5	10	1.0	Detasheet	22 % wc	"	"	"
2016050301	5.1	5.1	10	1.0	Detasheet	22 % wc	"	"	"

2016050302	5.1	8.9	10	1.0	Detasheet	10 % wc	centric	metal	2
2016050303	5.1	8.9	10	1.0	Detasheet	22 % wc	"	"	"